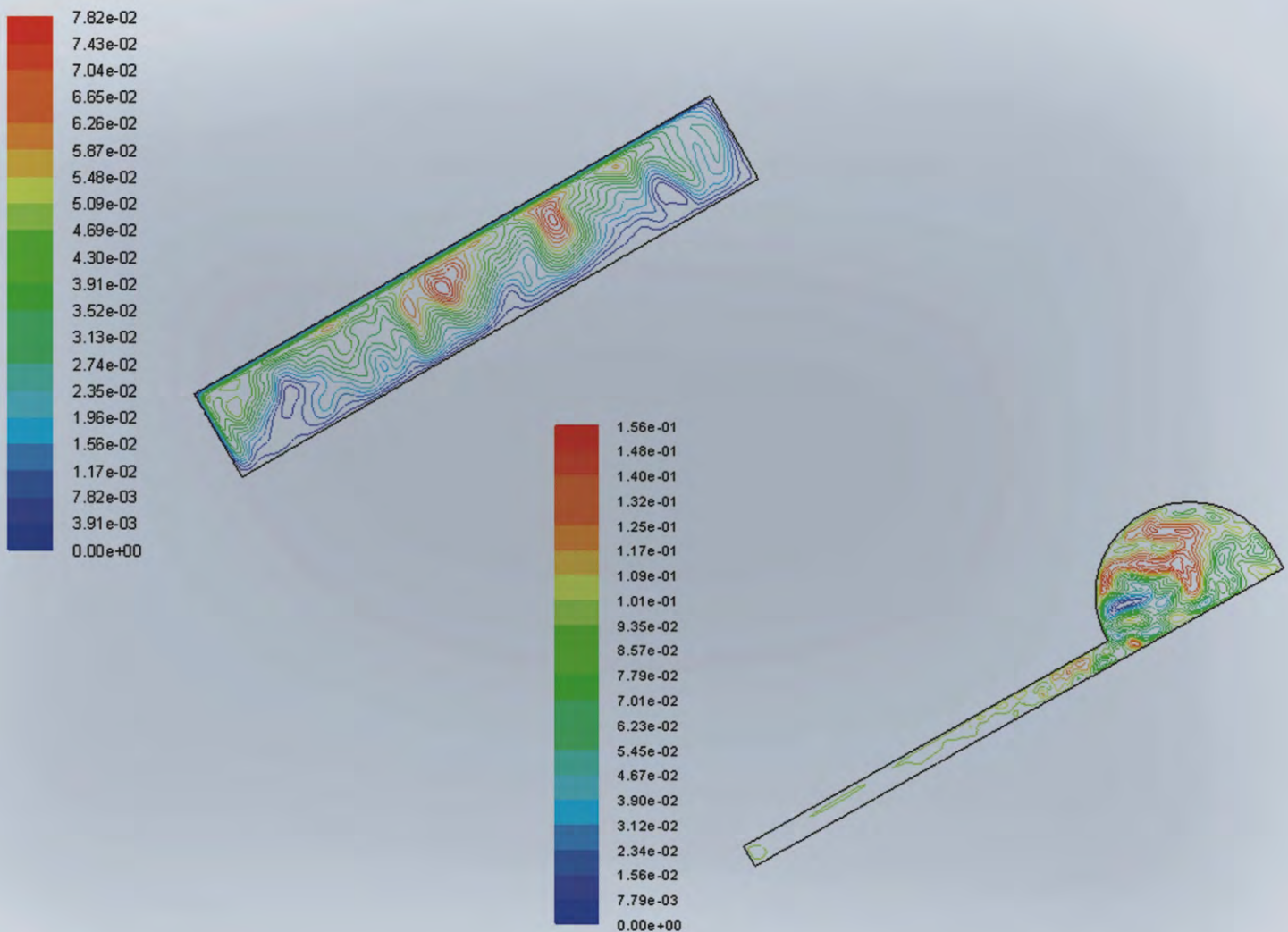




# Engineering

**Prof. David L. Carroll** Wake Forest University, USA



ISSN: 1947-3931



# Journal Editorial Board

ISSN: 1947-3931 (Print), 1947-394X (Online)

<http://www.scirp.org/journal/eng>

---

## Editor-in-Chief

**Prof. David L. Carroll**

Wake Forest University, USA

## Editorial Board

**Dr. Murad Y Abu-Farsakh**

Louisiana State University, USA

**Dr. Mohammad Al-Hwaiti**

Al-Hussein Bin Talal University, Jordan

**Prof. Moh'd A. M. Al-Nimr**

Jordan University of Science and Technology, Jordan

**Prof. Shahnor Basri**

Putra University, Malaysia

**Dr. Hengky Chandralalim**

Swiss Federal Institute of Technology, Switzerland

**Dr. Adinel Gavrus**

National Institut of Applied Sciences Rennes, France

**Dr. Krzysztof Górski**

Technical University of Radom, Poland

**Dr. Zhongwei Guan**

University of Liverpool, UK

**Dr. Kunn Hadinoto**

Nanyang Technological University, Singapore

**Dr. Sung-Cheon Han**

Daewon University College, Korea (South)

**Dr. Yunho Hwang**

University of Maryland, USA

**Prof. Shouetsu Itou**

Kanagawa University, Japan

**Dr. Sushil Kansal**

Panjab University, India

**Prof. Jae Moun Kim**

Inha University, Korea (South)

**Prof. Chui-Chi Lee**

She-Te University, Taiwan (China)

**Dr. Yiyang Li**

The Chinese University of Hong Kong, China

**Dr. Durães Luisa**

Universidade de Coimbra Pólo II, Portugal

**Dr. Vandna Luthra**

University of Delhi, India

**Prof. Yong-Gang Lv**

Chongqing University, China

**Prof. Magdi Mahmoud**

King Fahd University for Petroleum and Minerals, Iran

**Prof. Reinaldo Rodriguez Ramos**

University of Havana, Cuba

**Prof. Yuri Ribakov**

PAriel University Center of Samaria, Israel

**Dr. Arvind K. Srivastava**

NanoSonix Inc., USA

**Prof. Kune Y. Suh**

Seoul National University, Korea (South)

**Prof. Hongbin Sun**

Tsinghua University, China

**Dr. Costin D. Untaroiu**

University of Virginia, USA

**Prof. Baolin Wang**

Harbin Institute of Technology, China

**Dr. Rodrigo Sérgio Wiederkehr**

University of Louisville, USA

**Dr. Yufei Wu**

City University of Hong Kong, China

**Dr. Wei Yan**

Trend Micro, USA

**Prof. Bo Yu**

China University of Petroleum - Beijing, China

**Dr. Lei Zhang**

University of Maryland, USA

**Dr. Ming Zhang**

Smith International, Inc., Uruguay

---

## Editorial Assistant

**Yanna Li**

Scientific Research Publishing, USA

[eng@scirp.org](mailto:eng@scirp.org)

## TABLE OF CONTENTS

**Volume 2    Number 10**

**October 2010**

**Influence of Cutting and Geometrical Parameters on the Cutting Force in Milling**

H. Yangui, B. Zghal, A. Kessentini, G. Chevallier, A. Rivière, M. Haddar, C. Karra.....751

**Modelling and Optimisation of a Spring-Supported Diaphragm Capacitive MEMS Microphone**

N. Mohamad, P. Iovenitti, T. Vinay.....762

**Analysis of the Manufactured Tolerances with the Three-Dimensional Method of Angular Chains of Dimensions Applied to a Cylinder Head of Car Engine**

A. Mezghani, A. Bellacicco, J. Louati, A. Rivière, M. Haddar.....771

**Geometric Inversion of Two-Dimensional Stokes Flows—Application to the Flow between Parallel Planes**

M. Hellou.....780

**Surface Roughness Evaluation in Dry-Cutting of Magnesium Alloy by Air Pressure Coolant**

J.-D. Kim, K.-B. Lee.....788

**Optimization of Surface Milling of Hardened AISI4340 Steel with Minimal Fluid Application Using a High Velocity Narrow Pulsing Jet of Cutting Fluid**

K. L. D. Wins, A. S. Varadarajan, B. Ramamoorthy.....793

**Using Image Analysis for Structural and Mechanical Characterization of Nanoclay Reinforced Polypropylene Composites**

T. P. Mohan, K. Kanny.....802

**Nonlinear Control of an Induction Motor Using a Reduced-Order Extended Sliding**

**Mode Observer for Rotor Flux and Speed Sensorless Estimation**

O. Asseu, M. A. Kouacou, T. R. Ori, Z. Yéo, M. Koffi, X. Lin-Shi.....813

**A Fast Predicating of Nutrient Removal Efficiency in Five Steps Sequencing Batch Reactor System Using Fuzzy Logic Control Model**

S. Abualhail, R. Naseer, A. Ashor, X.-W. Lu.....820

**Effect of Periodic Variation of Sol-Air Temperature on the Performance of Integrated Solar Collector Storage System**

N. H. Saeid, T. J. Wong.....832

---

The figure on the front cover is from the article published in Engineering, 2010, Vol.2, No.10, pp. 832-840, by Nawaf H. Saeid and Tan Jun Wong.

# **Engineering**

## **Journal Information**

### **SUBSCRIPTIONS**

*Engineering* (Online at Scientific Research Publishing, [www.SciRP.org](http://www.SciRP.org)) is published monthly by Scientific Research Publishing, Inc., USA.

#### **Subscription rates:**

Print: \$50 per issue.

To subscribe, please contact Journals Subscriptions Department, E-mail: [sub@scirp.org](mailto:sub@scirp.org)

### **SERVICES**

#### **Advertisements**

Advertisement Sales Department, E-mail: [service@scirp.org](mailto:service@scirp.org)

#### **Reprints (minimum quantity 100 copies)**

Reprints Co-ordinator, Scientific Research Publishing, Inc., USA.

E-mail: [sub@scirp.org](mailto:sub@scirp.org)

### **COPYRIGHT**

Copyright©2010 Scientific Research Publishing, Inc.

All Rights Reserved. No part of this publication may be reproduced, stored in a retrieval system, or transmitted, in any form or by any means, electronic, mechanical, photocopying, recording, scanning or otherwise, except as described below, without the permission in writing of the Publisher.

Copying of articles is not permitted except for personal and internal use, to the extent permitted by national copyright law, or under the terms of a license issued by the national Reproduction Rights Organization.

Requests for permission for other kinds of copying, such as copying for general distribution, for advertising or promotional purposes, for creating new collective works or for resale, and other enquiries should be addressed to the Publisher.

Statements and opinions expressed in the articles and communications are those of the individual contributors and not the statements and opinion of Scientific Research Publishing, Inc. We assumes no responsibility or liability for any damage or injury to persons or property arising out of the use of any materials, instructions, methods or ideas contained herein. We expressly disclaim any implied warranties of merchantability or fitness for a particular purpose. If expert assistance is required, the services of a competent professional person should be sought.

### **PRODUCTION INFORMATION**

For manuscripts that have been accepted for publication, please contact:

E-mail: [eng@scirp.org](mailto:eng@scirp.org)

# Influence of Cutting and Geometrical Parameters on the Cutting Force in Milling

Hedi Yangui<sup>1,2</sup>, Bacem Zghal<sup>1</sup>, Amir Kessentini<sup>1</sup>, Gaël Chevallier<sup>2</sup>,  
Alain Rivière<sup>2</sup>, Mohamed Haddar<sup>1</sup>, Chafik Karra<sup>1</sup>

<sup>1</sup>Unité de Mécanique, Modélisation et Production (U2MP), Ecole Nationale d'Ingénieurs de Sfax (E.N.I.S.),  
route soukra km 4 Sfax – TUNISIE, France

<sup>2</sup>Laboratoire d'Ingénierie des Structures Mécanique et de Matériaux (LISMMA), Institut Supérieur de  
Mécanique de Paris (SUPMECA), 3 rue Fernand Hainaut, 93407 cedex Saint ouen, Paris – France

E-mail: yangui\_hedi@yahoo.fr

Received August 5, 2010; revised August 6, 2010; accepted August 23, 2010

## Abstract

This paper presents a numerical modelling of the dynamic behaviour of the Machine-Tool-Part system (MOP) in milling. The numerical study of such complex structure requires the use of sophisticated method like finite elements one. Simulation is employed to predict cutting forces and dynamic response of Machine-Tool-Part system (MOP) during end-milling operation. Finally, spectral analysis is presented to see the influence of feed direction in the vibration.

**Keywords:** Milling, Modelling, Cutting Force, Finite Element

## 1. Introduction

Milling is frequently employed in manufacturing processes for producing parts with desirable dimensions and shape. However, the quality of the obtained surface is mostly influenced by two vibratory phenomena. In the first hand, the grazing provoked mainly by the mechanism of regeneration of the manufactured surfaces leads to chatter vibration. In the second hand, a forced vibration appears owing to the periodicity of the cut. Models describing cutting tool vibrations began to appear in literature about several decades ago. Tobias [1] and Tlustý [2], almost simultaneously, published papers explaining chatter as a regenerative phenomenon which is widely accepted as a cause of self-excited vibrations on machine tools. Then, large number of dynamic models of cutter and part are presented by authors. In their work Montgomery and Altintas [3,4], use a refined time domain simulation model which incorporates the combined horizontal feed and rotation of the cutter to predict cutting force.

Because, major developments have been designed for aeronautic industry where tools are mostly more flexible than part, Altintas and Budak [5] have proposed an analytic method for computing stability lobes. They analysed the geometrical nonlinearities of the milling proc-

ess. After that, they proposed a solution using Fourier series development and by considering the zero order term. In 1998, they prolonged this work by taking account of the behaviour of the part. These authors worked also on the prediction of the profile defects [7,8]. In these works the study relates the thin wall milling where the defects are due to the static deflections of the tool and the piece and the vibrations are not taken in account. Recently, there have been quite a number of published articles on the bifurcation phenomena in interrupted cutting processes. Indeed, Insperger *et al.* [9], Corpus *et al.* [10], Bayly *et al.* [11], Davies *et al.* [12], Peigné *et al.* [13] proposed analytical way of stability loss in milling processes. All results are approved experimentally by Bayly *et al.* [11], Davies *et al.* [12], Peigné *et al.* [13], Mann *et al.* [14,15] and R.Saffar *et al.* [16].

In fact, the large number of machining operations and the factors that influence each operation lead difficult to develop models for predicting the cutting phenomenon. Since, the concept of the undeformed chip thickness has been used by researchers to predict the cutting forces. In reality, it is very difficult to measure the length of the shear line and to find its relation with other measurable variables such as speed or accelerations. Consequently, the most used model is linear cutting and cutting force is proportional to the undeformed chip thick-

ness. In this work, we start by presenting most popular models. Then, comparison between three models is presented. Finally, variation of cutting forces is presented for different cutting parameters and spectral response is also simulated.

## 2. Dynamic Cutting Force Models

In their study M. T. Zaman *et al.* [17] have simulated peripheral milling to develop a three-dimensional analytical model of cutting force. So it is necessary to determine the analytical expressions for  $F_x$ ,  $F_y$  and  $F_z$  which are presented in **Figure 1**.

Cutting force expressions ( $F_x$  and  $F_y$ ) was extracted from Tlustý *et al.* [7] and Bao *et al.* [18] with little modification. In fact, they introduce in their equations horizontal component of tangential force. Thus, cutting force can be written as below:

$$\begin{aligned} F_{xi} &= (F_{ti} \cos \psi) \sin \phi_i - F_{ri} \cos \phi_i \\ F_{yi} &= -(F_{ti} \cos \psi) \cos \phi_i - F_{ri} \sin \phi_i \\ F_{zi} &= -F_{ti} \sin \psi \\ F_{ci} &= \sqrt{F_{xi}^2 + F_{yi}^2 + F_{zi}^2} \end{aligned} \quad (1)$$

By confronting analytical and experimental study they confirm that tangential cutting force arises when cutting depth arises. Despite, this cutting force model can be used to simulate cutting force with an average of 90%.

In general, cutting force model used is the most classical. In general, cutting force depends on cutting depth. However, in dynamic milling cutting depth depends on tool and part position and the profile of machined surface (Cutting force is presented in **Figure 2**).

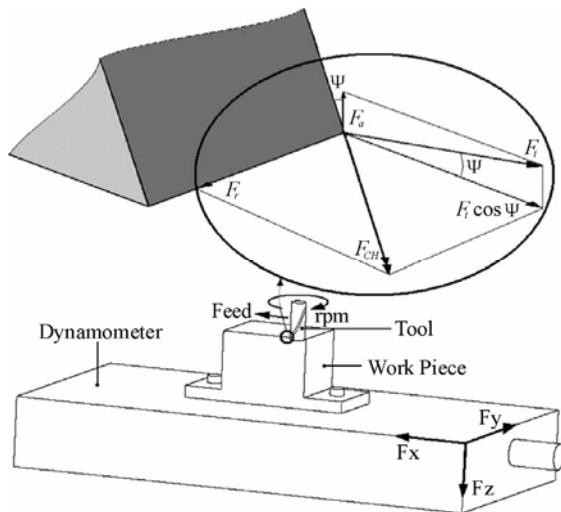


Figure 1. Cutting force component [16].

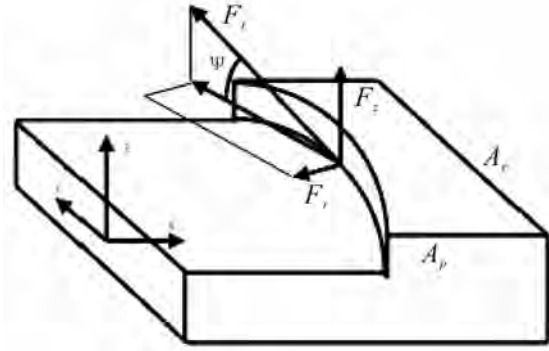


Figure 2. Cutting force model in milling.

$$\begin{aligned} F_{ij} &= K_t \cdot a_p \cdot h(\phi_j) \\ F_{rj} &= K_r F_{ij} \end{aligned} \quad (2)$$

$h$  is the instantaneous cutting thickness

$$h(\phi_j) = g(\phi_j) [\Delta x \sin(\phi_j) + \Delta y \cos(\phi_j)] \quad (3)$$

where

$$\Delta x = x(t) - x(t - \tau)$$

$$\Delta y = y(t) - y(t - \tau)$$

$$\text{And } g(\phi_j) = \begin{cases} 0 & \text{si } \phi_e < \phi_j, \phi_j < \phi_s \\ 1 & \text{si } \phi_e > \phi_j > \phi_s \end{cases}$$

$\phi_j$  is angle of cutter rotation of a point on the cutting edge.

**Figure 3** represents tool position compared with part position,  $e$  is distance between tool and part axis,  $\phi_e$  is entry angle,  $\phi_s$  is leaving angle.

Cutting phase is defined by angles  $\phi_e$  and  $\phi_s$  in the metal. These angles are calculated compared with nominal position. Thus, transitory phases of beginning and end machining are not modeled. However, if the cutting is discontinued, the tool can leave the metal.

In this case, cutting depth is null and cutting forces are also null. This non linearity permits to amplify vibration amplitude.

Angle  $\phi_e$  and  $\phi_s$  are defined as below:

$$\begin{aligned} \cos \phi_e &= \frac{A_e + 2e}{D} \\ \cos \phi_s &= \frac{A_e - 2e}{D} \end{aligned} \quad (4)$$

## 3. Dynamic Response

The first step consists to meshing the Machine-Tool-Part structure. So, voluminal elements are generated for modelling all components of milling machine,

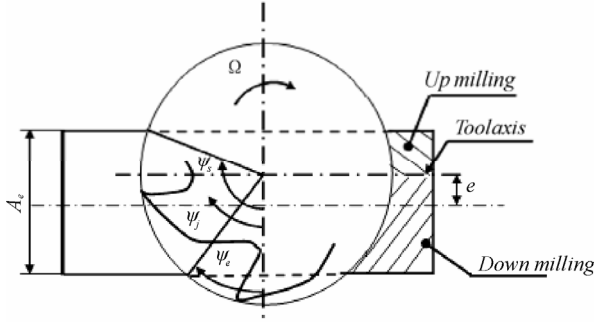


Figure 3. Tool position compared with part one.

tool and part. **Figure 4** shows the photograph and the finite elements modeling of used milling machine.

Generally the dynamic analysis of the system by finite elements is reduced to the resolution of a linear system of the second order differential equations whose rigidity matrix depends on time:

$$[M]\{\ddot{X}(t)\} + [C]\{\dot{X}(t)\} + [K]\{X(t)\} = \{F(t)\} \quad (5)$$

Where  $M$ ,  $C$  and  $K$  are respectively mass matrix, damping matrix and stiffness matrix,  $X$  is generalized displacement vector and  $F(t)$  is cutting force vector. All coefficients of these matrixes are determined from finite element modelisation of the total system tool-machine-part.

$$\begin{aligned} [\phi_r]^T [M] [\phi_r] \{\ddot{q}(t)\} + \\ [\phi_r]^T [K] [\phi_r] \{q(t)\} &= [\phi_r]^T \{F(t)\} \end{aligned} \quad (6)$$

The matrix  $[M]$ ,  $[K]$  and  $[C]$  projected on the basis of the eigenmodes leads to matrix  $[I]$ ,  $[\Lambda]$  and  $[D]$  by:

$$\begin{aligned} [\phi_r]^T [K] [\phi_r] &= [\Lambda] \\ [\phi_r]^T [M] [\phi_r] &= [I] \\ [\phi_r]^T [C] [\phi_r] &= [D] \end{aligned} \quad (7)$$

So dynamic equation projected on the basis of the eigenmodes was reduced to the system of equations in the following form:

$$[I]\{\ddot{q}(t)\} + [D]\{\dot{q}(t)\} + [\Lambda]\{q(t)\} = \{f(t)\} \quad (8)$$

## 4. Numerical Results

The resolution of dynamic Equation (6) by numerical method of resolution like Newmark and Newton raphson permits the determination of the displacement of the tool in the x-y directions. Besides, cutting force variation in time can be predicted.

To validate the developed modelling of milling opera-

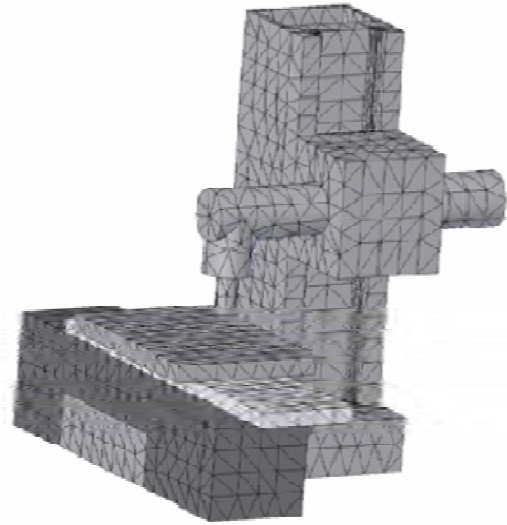
tion, validation test is performed. So, comparison with results of J. Saffar *et al.* [16] is presented in **Figure 5**.

In **Figure 5** variation of cutting force according to rotation angle is presented. We remark a good agreement with J.Saffar's results.

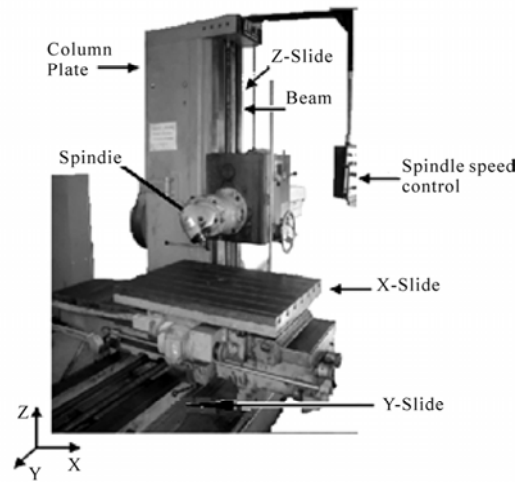
### 4.1. Comparison of Different Cutting Force Models

**Table 1** presents three different model used by authors to quantify cutting force.

In **Figure 6** variation cutting force is presented for three different models. We remark that for the first and third model Cutting component in y and z direction are almost equal. But, for the cutting component in x direction the difference between three models is visible.



Finite elements modeling



Reel machine

Figure 4. Modeling of milling machine.



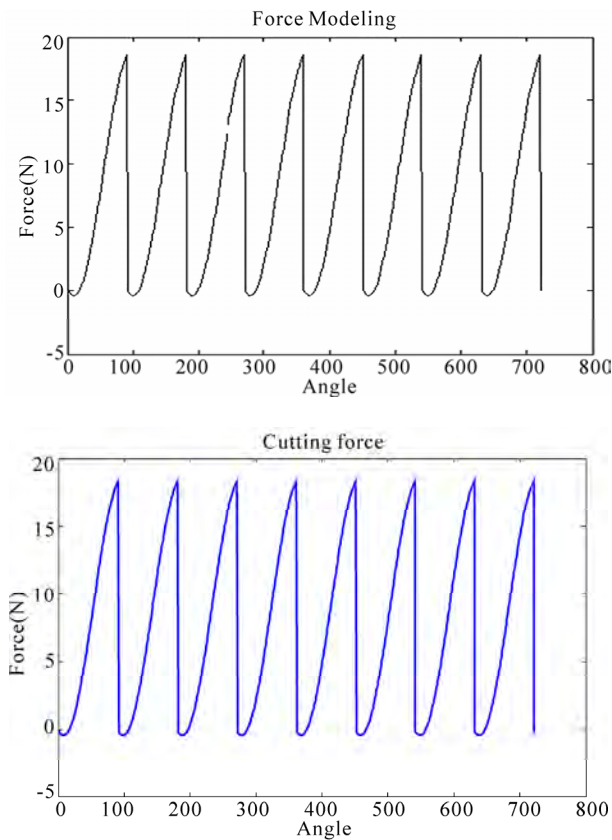


Figure 5. Comparison with saffar results.

## 4.2. Influence of Feed

It is clear from equation that cutting forces are proportional to feed. **Figure 7** represents variation of maximal cutting force according to feed and we remark that cutting forces rise when feed rises. In addition we note that  $F_y$  component rise with an important rate. Besides, **Figure 8** represents variation of instantaneous cutting force. The only difference detected is the amplitude of cutting forces.

$N = 500$  revs. min<sup>-1</sup> ( $A_e = 40$  mm,  $A_p = 1$  mm) for feed ( $f_1 = 0.1$  mm. rev<sup>-1</sup>,  $f_2 = 0.2$  mm rev<sup>-1</sup>,  $f_3 = 0.4$  mm. rev<sup>-1</sup>,  $f_4 = 0.8$  mm. rev<sup>-1</sup>).

## 4.3. Influence of Cutting Depth

**Figure 9** and **Figure 10** show that cutting force increase

Table 1. Different model of cutting force.

Author	Model	
Kienzle (1950)	$F_i = a_p \cdot K_{cl} \cdot h^{1-m}$	
(Altintas, 1998)	$F_i = a_p \cdot K_{ic} \cdot h$ $+ a_p \cdot K_{ie}$	$F_r = a_p \cdot K_{re} \cdot h$ $+ a_p \cdot K_{re}$
(Insperger T., 2000)	$F_i = a_p \cdot K_i \cdot h^{qf}$	$F_r = a_p \cdot K_r \cdot h^{qf}$

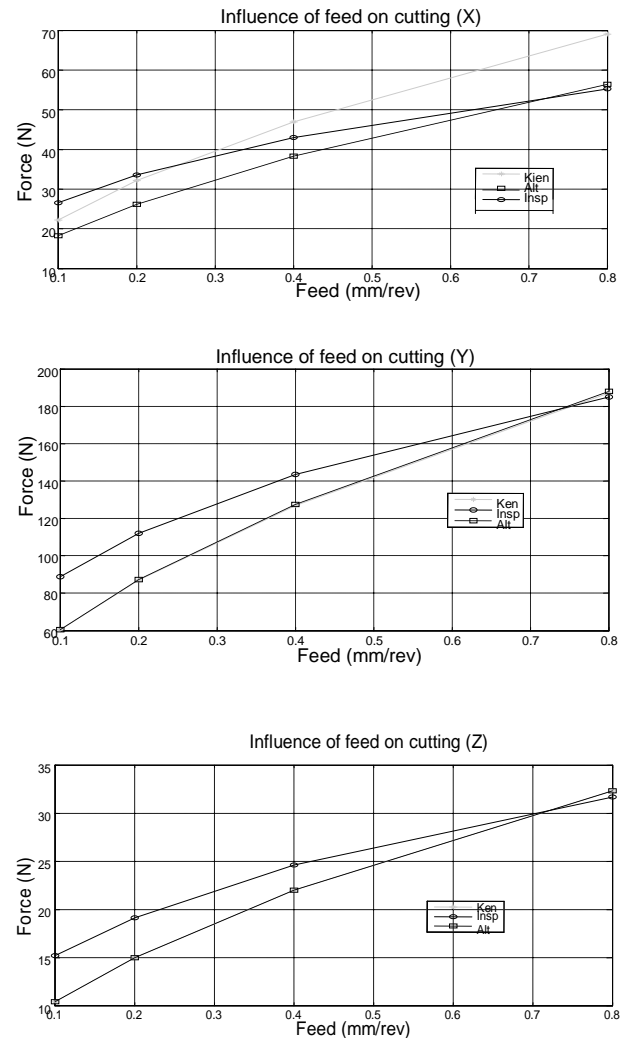


Figure 6. Comparison of different cutting force models.

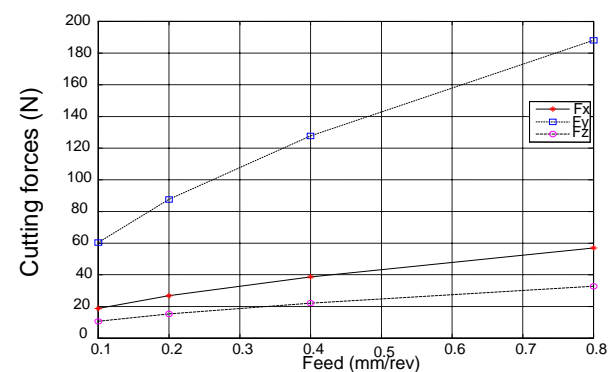


Figure 7. Influence of feed on maximal cutting forces.

when cutting depth increases. This raise is justified by the increase of the width of chip. In fact, it is the largest parameter acting on cutting forces.



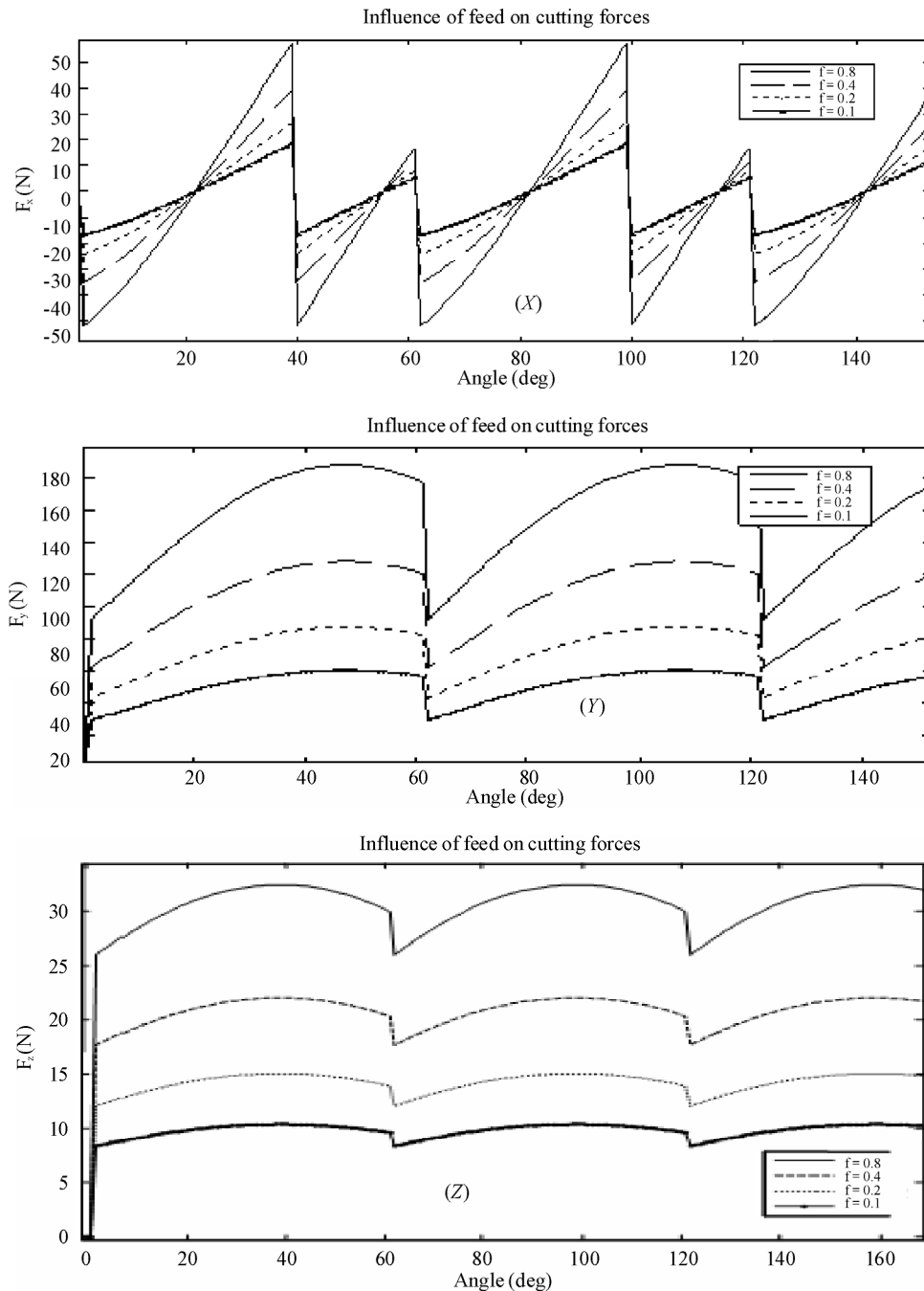


Figure 8. Influence of feed on cutting forces.

Figure 11 shows that rising cutting depth leads to rising vibration amplitude and can lead to chatter vibration. In fact, the dynamic response for Kienzel model with 5mm cutting depth is amplified almost ten times and the response is divergent. For Atlintas model the amplitudes are less than for other model.

#### 4.4. Influence of the Beginning Angle $\varphi_e$

Increasing the spacing between the tool and the piece

caused a slight increase in the cutting force. Figure 12 shows the influence of the angle of entry on the cutting forces because the period of machining for each tooth has increased (for  $e = 20$  mm and  $e = -20$  mm).

#### 4.5. Influence of Teeth Number in Beginning

Figure 13 shows the influence of numbers of teeth in attack that affects the shapes of the cutting forces and

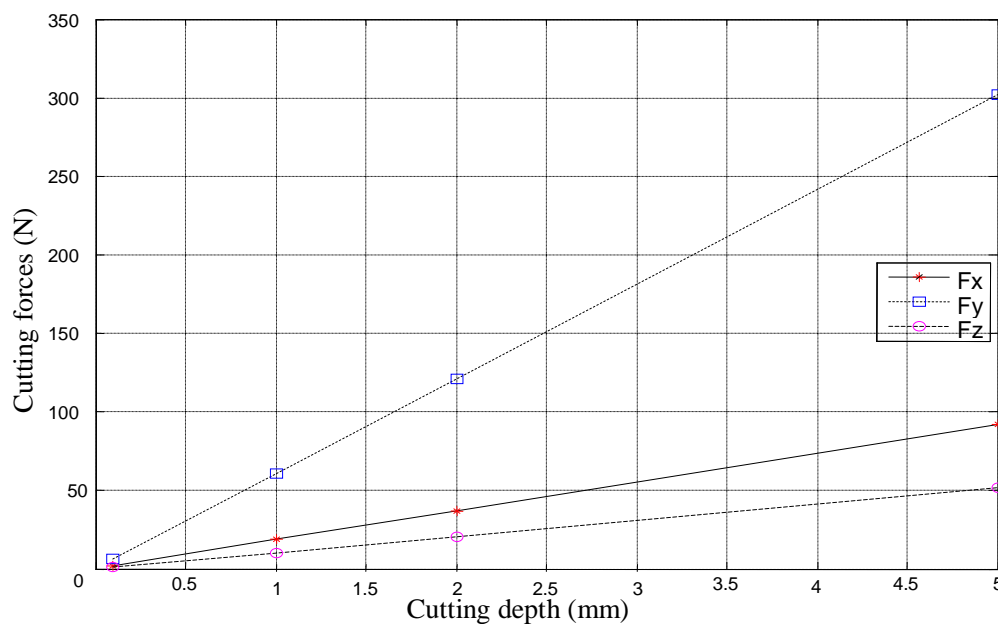
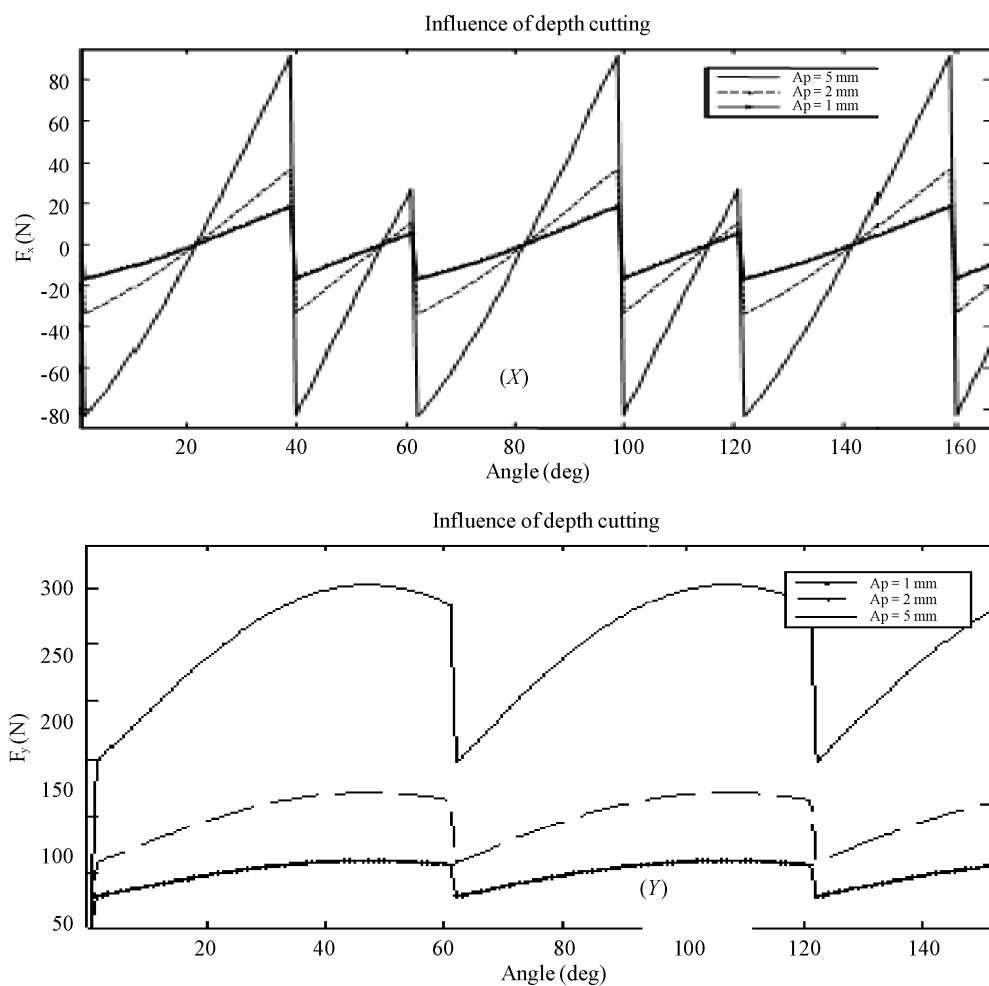


Figure 9. Influence of cutting depth on cutting force  $f = 0.1$  mm/rev;  $N = 500$  rev/min and  $Z = 6$  teeth.



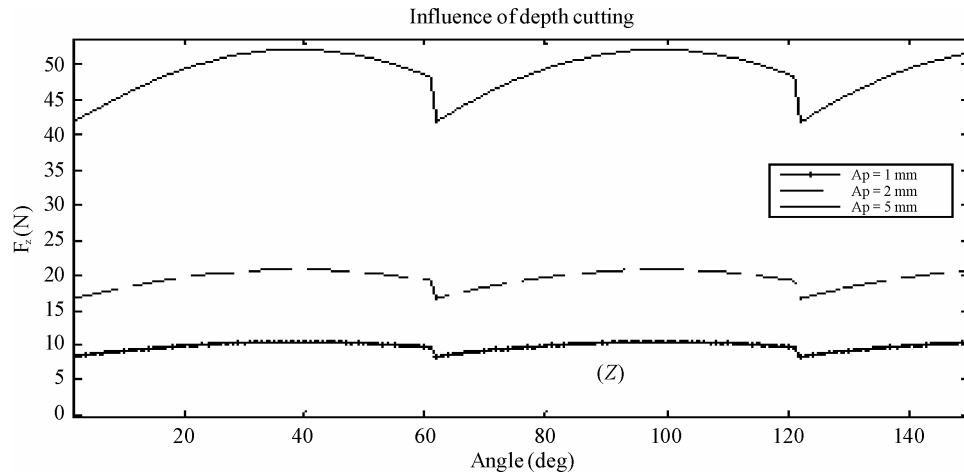
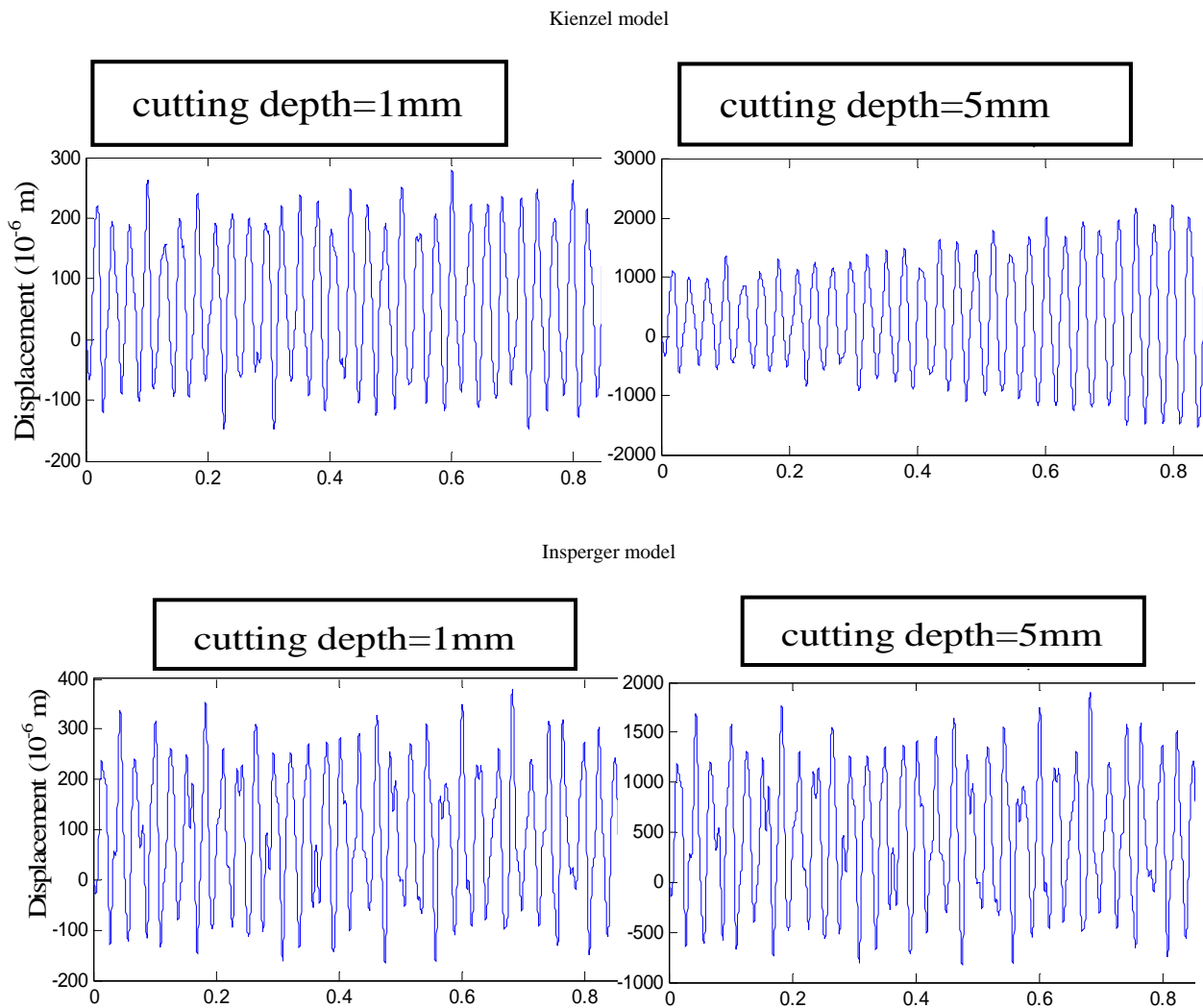
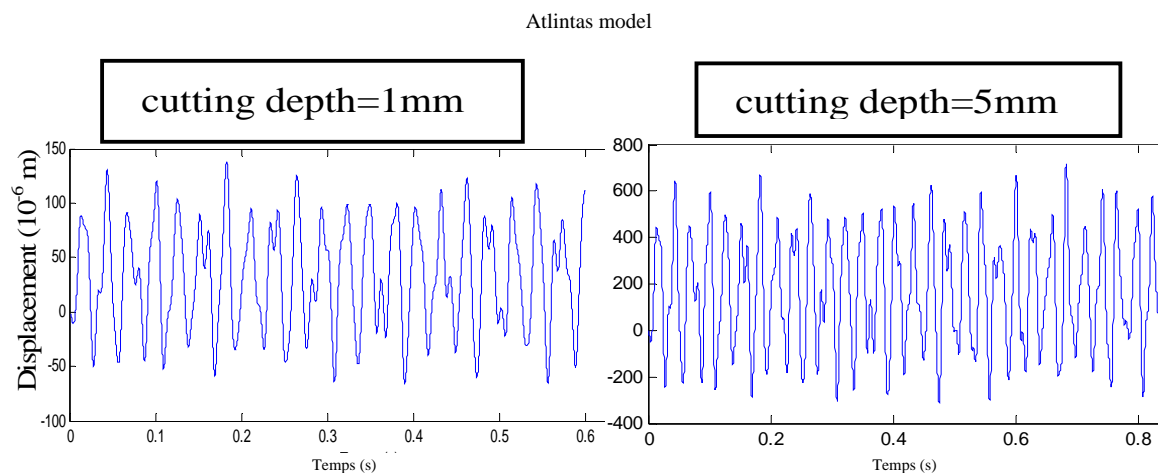
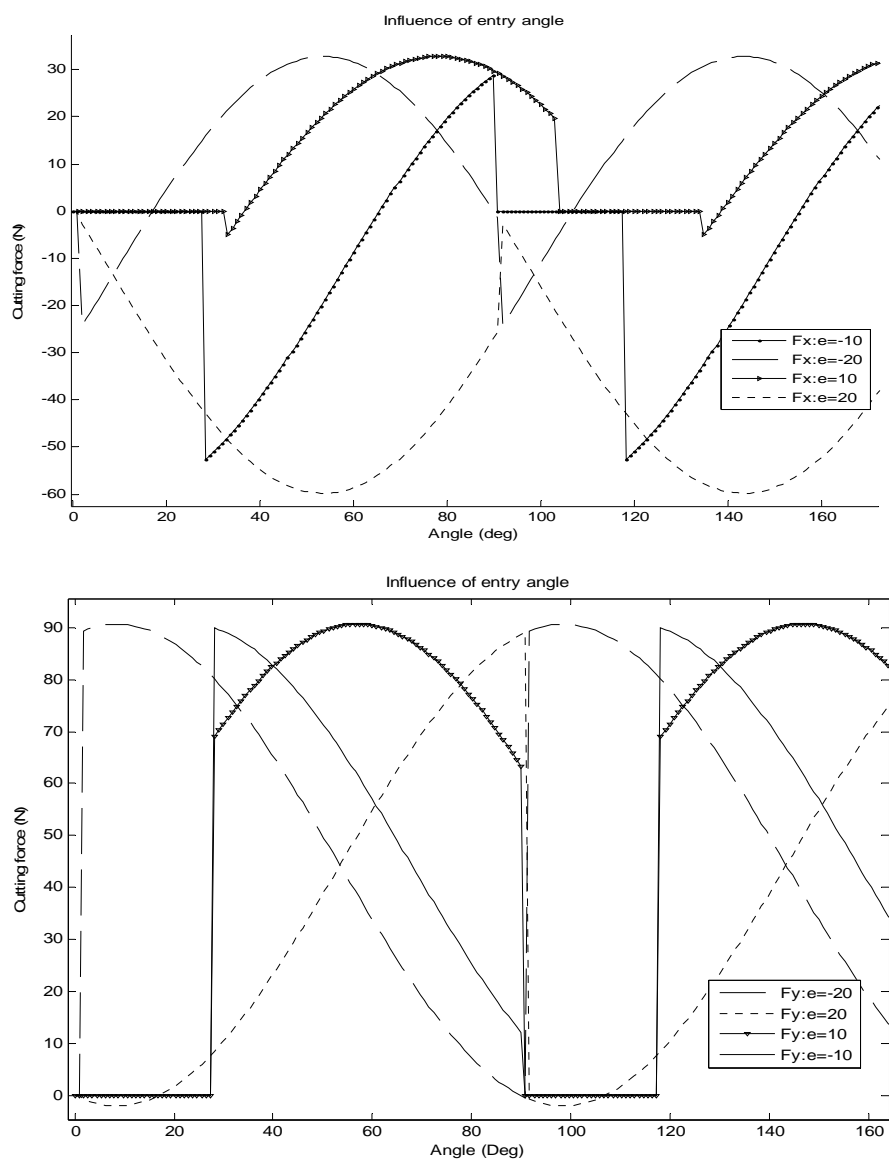


Figure 10. Influence of cutting depth on cutting force.





**Figure 11. Influence of cutting depth on dynamic response ( $f = 0.1$  mm/rev;  $N = 500$  rpm;  $Z = 6$ ).**



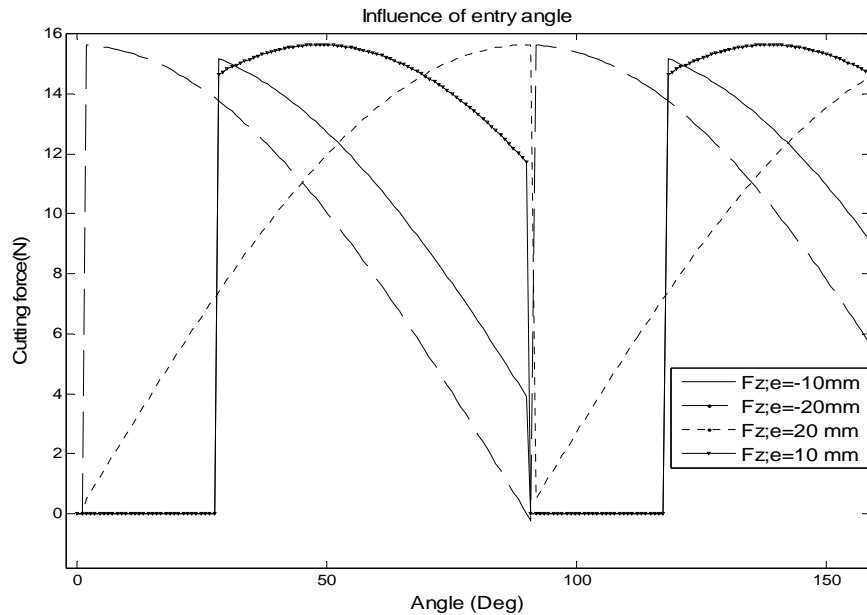


Figure 12. Influence of entry angle on cutting forces.

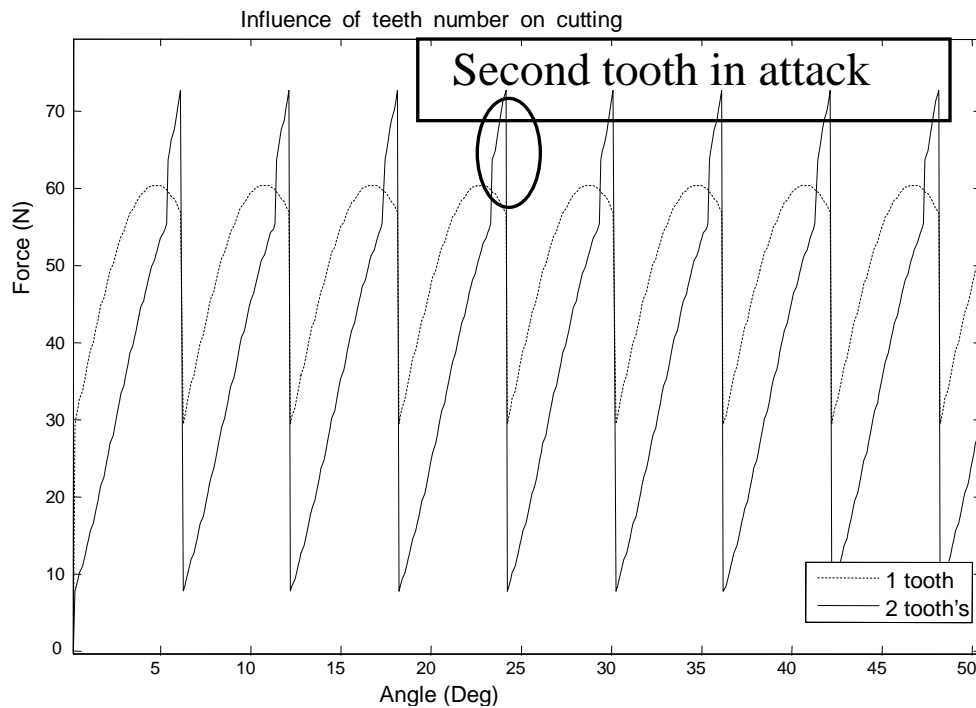


Figure 13. Influence of teeth number on cutting forces.

their value because the summation of forces of two teeth in attack.

**Figure 14** proposes the two modes of milling up milling and down milling. **Figure 15** gives the results obtained during two simulations carried out under the same cutting conditions, except the mode of selected milling: the first is in configuration of up milling and the second

in configuration of down milling.

We remark that for down milling frequency of vibration rises. Besides, amplitude seems to be little changed.

## 5. Spectral Response

The spectral representation of displacement following

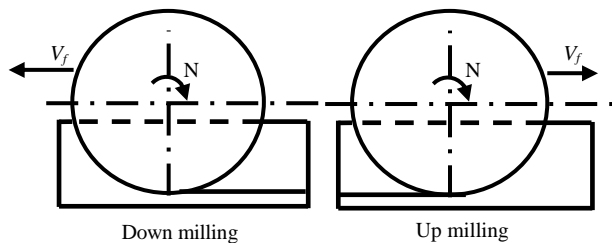


Figure 14. Two modes of milling.

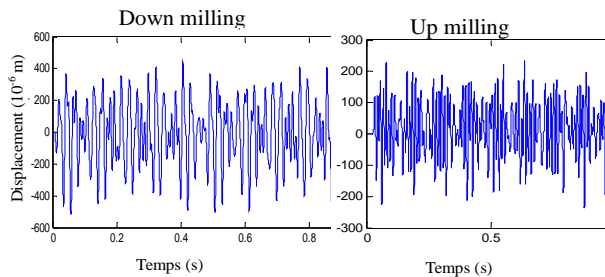


Figure 15. Numerical results for the two modes of milling.

axis X, Y in **Figure 16** proves that there are dominant vibrations due to periodical cutting pressure at the frequencies of passage of the teeth (TPF, 2TPF and 3TPF) and the maximum vibration is in the feed direction. In the feed direction (X), simulation shows the unstable frequencies for the cut with approximately 37 Hz, 60 Hz and 85 Hz, which is almost one of the natural frequencies of the system.

TPF: Frequency of teeth passage

FP: Eigen frequency

## 6. Conclusions

In this work, numerical study is conducted to predict

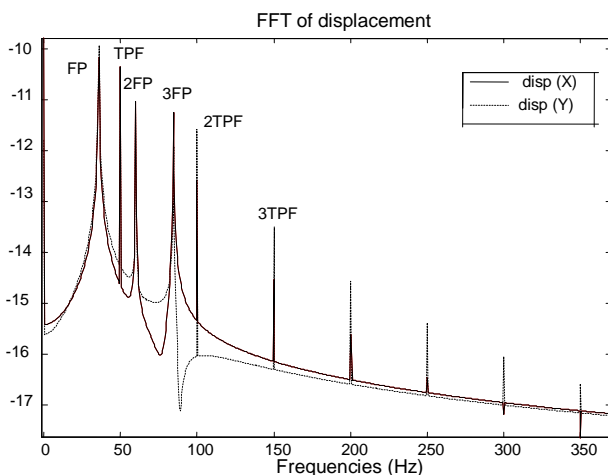


Figure 16. Spectral response.

cutting forces variation according to cutting parameters in milling operation. So, dynamic equation is established using finite element method and projected on the basis of the eigenmodes. The resolution of the obtained equation by numerical method gives dynamic response and cutting force variation. The main objective of this method is to take the influence of machine, tool and part simultaneously. Results showed that most influenced parameters are feed and cutting depth. In fact, clear influence appears on dynamic response for little variation of these parameters. Indeed, simulation reveals that the adopted cutting models have an effect on dynamic response of the system. Besides predicted spectral response of the system machine-tool-part showed that frequency vibrations are due to frequencies of passage of the teeth and eigen frequency of the system.

Finally, modelling milling operations, by finite element method represents a very useful tool for the prediction of the behaviour of the system. So, the need for establishing extensive cutting experiments is reduced.

## 7. References

- [1] S. A. Tobias and W. Fishwick, "A theory of Regenerative chatter," The Engineer-London, 1958.
- [2] J. Tlustý and M. Poláček, "The Stability of Machine Tools against Self Excited Vibrations in Machining," *International research in production engineering, ASME*, 1963, pp. 465-474.
- [3] D. Montgomery and Y. Altintas, "Mechanism of Cutting Force and Surface Generation in Dynamic Milling," *ASME, Journal of Engineering for Industry*, Vol. 113, No. 2, 1991, pp. 160-168.
- [4] Y. Altintas, D. Montgomery and E. Budak, "Dynamic Peripheral Milling of Flexible Structures," *ASME Journal of Engineering for Industry*, Vol. 114, No. 2, 1992, pp. 137-145.
- [5] E. Budak and A. Altintas, "Modelling and Avoidance of Static form Errors in Peripheral Milling of Plates," *International Journal of Machine Tools and Manufacture*, Vol. 35, No. 3, 1993, pp. 459-476.
- [6] E. Budak and Y. Altintas, "Analytical Prediction of Chatter Stability in Milling—Part I: General Formulation," *Journal of Dynamic Systems, Transactions of the ASME*, Vol. 120, No. 1, 1998, pp. 31-36.
- [7] Y. Altintas and E. Budak, "Analytical Prediction of Stability Lobes in Milling," *Annals of the CIRP*, Vol. 44, No. 1, 1995, pp. 357-362.
- [8] Y. Altintas, "Manufacturing Automation—Metal Cutting Mechanics, Machine Tool Vibration and CNC Design," Cambridge University, 2000. ISBN-13: 978-0521659734.
- [9] T. Insperger and G. Stépán, "Stability of High-Speed Milling," *Proceedings of the 2000 ASME International Mechanical Engineering Congress and Exposition*, No. AMD-241, Orlando, Florida, 2000, pp. 119-123.

- [10] W. T. Corpus and W. J. Endres, "A High Order Solution for the Added Stability Lobes in Intermittent Machining," in *Proceeding of the Symposium on Machining Processes*, No. MED-11, 2000, pp. 871-878. Paper number DETC97/VIB-4021.
- [11] P. V. Bayly, J. E. Halley, B. P. Mann and M. A. Davies, "Stability of Interrupted Cutting by Temporal Finite Element Analysis," *Journal of Manufacturing Science and Engineering*, Vol. 125, No. 2, 2003, pp. 220-225.
- [12] M. A. Davies, J. R. Pratt, B. Dutterer and T. J. Burns, "Stability Prediction for Low Radial Immersion Milling," *Journal of Manufacturing Science and Engineering*, Vol. 124, No. 2, 2002, pp. 217-225.
- [13] G. Peigné, H. Paris, D. Brissaud and A. Gouskov, "Simulation numérique d'une opération de fraisage à grande vitesse : étude de la stabilité", " 16ème Congrès Français de Mécanique, Nice, 2003.
- [14] B. P. Mann, T. Insperger, P. V. Bayly and G. Stépán, "Stability of Up-Milling and Down-Milling, Part 2: Experimental Verification," *International Journal of Machine Tools & Manufacture*, Vol. 43, No. 1, 2003, pp. 35-40.
- [15] B. P. Mann, P. V. Bayly, M. A. Davies and J. E. Halley, "Limit Cycles, Bifurcations, and Accuracy of the Milling Process," *The Journal of Sound and Vibration*, Vol. 277, No. 1-2, 2004, pp. 31-48.
- [16] R. J. Saffar, M. R. Razfar, O. Zarei and E. Ghassemieh, "Simulation of Three-Dimension Cutting Force and Tool Deflection in the End Milling Operation Based on Finite Element Method," *International Journal of the Federation of European Simulation Societies: Simulation Modeling Practice and Theory*, Vol. 16, No. 10, 2008, pp. 1677-1688.
- [17] M. T. Zaman, A. S. Kumar, M. Rahman and S. Sreeram, "A Three-Dimensional Analytical Cutting Force Model for Micro End Milling Operation," *International Journal of Machine Tools & Manufacture*, Vol. 46, No. 3-4, 2006, pp. 353-366.
- [18] W. Y. Bao and I. Tansel, "Modeling Micro End Milling Operations, Part I: Analytical Cutting Force Model," *International Journal of Machine Tool and Manufacture*, Vol. 40, No. 15, 2000, pp. 2155-2173.



# Modelling and Optimisation of a Spring-Supported Diaphragm Capacitive MEMS Microphone

Norizan Mohamad<sup>1</sup>, Pio Iovenitti<sup>1</sup>, Thurai Vinay<sup>2</sup>

<sup>1</sup>Faculty of Engineering and Industrial Sciences, Swinburne University of Technology, Hawthorn, Australia

<sup>2</sup>School of Electrical and Computer Engineering, RMIT University, Melbourne, Australia

E-mail: [norizan@utem.edu.my](mailto:norizan@utem.edu.my)

Received June 9, 2010; revised September 6, 2010; accepted September 21, 2010

## Abstract

Audio applications such as mobile communication and hearing aid devices demand a small size but high performance, stable and low cost microphone to reproduce a high quality sound. Capacitive microphone can be designed to fulfill such requirements with some trade-offs between sensitivity, operating frequency range, and noise level mainly due to the effect of device structure dimensions and viscous damping. Smaller microphone size and air gap will gradually decrease its sensitivity and increase the viscous damping. The aim of this research was to develop a mathematical model of a spring-supported diaphragm capacitive MEMS microphone as well as an approach to optimize a microphone's performance. Because of the complex shapes in this latest type of diaphragm design trend, analytical modelling has not been previously attempted. A novel diaphragm design is proposed that offers increased mechanical sensitivity of a capacitive microphone by reducing its diaphragm stiffness. A lumped element model of the spring-supported diaphragm microphone is developed to analyze the complex relations between the microphone performance factors and to find the optimum dimensions based on the design requirements. It is shown analytically that the spring dimensions of the spring-supported diaphragm do not have large effects on the microphone performance compared to the diaphragm and backplate size, diaphragm thickness, and air-gap distance. A 1 mm<sup>2</sup> spring-supported diaphragm microphone is designed using several optimized performance parameters to give a -3 dB operating bandwidth of 10.2 kHz, a sensitivity of 4.67 mV/Pa (-46.5 dB ref. 1 V/Pa at 1 kHz using a bias voltage of 3 V), a pull-in voltage of 13 V, and a thermal noise of -22 dBA SPL.

**Keywords:** Capacitive Microphone, Spring-Supported Diaphragm, Microphone Modelling

## 1. Introduction

The silicon capacitive microphone has been studied and shown to potentially replace the existing and widely used piezoelectric microphone due to its high sensitivity, long term stability and ability to withstand a high temperature soldering process [1,2]. This type of microphone has been designed to use various diaphragm materials including silicon nitride, polysilicon, aluminum, and polyimide [3-6]. A different diaphragm material was chosen to suit the intended application based on the required dimension, sensitivity, and operating frequency range. Open-circuit sensitivity of a capacitive microphone can be increased by applying a higher bias voltage or reducing the diaphragm stiffness. Since many small size audio applications prefer a low voltage operation, the microphone sensitivity needs to be increased by reducing the

diaphragm stiffness alone. The diaphragm stiffness can be reduced by using a low stress material, perforated diaphragm or as a combination with corrugated or spring type diaphragm [4,6-12]. However, the reduction in diaphragm stiffness will cause the reduction in its operating frequency range and pull-in voltage. Moreover, the desired smaller device size and capacitor air-gap thickness will increase the thin film air damping effect which will decrease its open-circuit sensitivity further. Due to the trade-offs relation between these performance factors, the optimization of the microphone parameters is always required depending on the design requirements.

Previous research has been carried out using various spring type diaphragm to increase the sensitivity of a capacitive MEMS microphone. Kim *et al.* [11] has demonstrated the use of a flexure hinge diaphragm to achieve 0.2 m diaphragm centre deflection with a flat frequency

range of up to 20 kHz. Weigold *et al.* [13] was using a spring-supported, thin polysilicon diaphragm fabricated on silicon on insulator (SOI) wafer to achieve a sensitivity of  $-47$  dB (ref 1V/Pa) with the amplifier circuit. Another high sensitivity of up to 8.2 mV/Pa was reported by Fuldner *et al.* [9] using a spring type diaphragm membrane of 1 mm in diameter and low bias voltage of 1 V. Mohamad *et al.* [12,14] has also demonstrated that a specially designed spring-supported diaphragm can easily achieve up to 100 times higher mechanical sensitivity and 1.5 times higher capacitance change compared to the edge-clamped diaphragm of the same size.

The behaviour of a capacitive microphone can be simplified and represented using linear lumped elements in a reduced-order network modelling. An accurate model will speed-up design analysis and parameters optimization using finite element analysis (FEA). In network modelling method, the electrical linear lumped elements were determined from the acoustical and mechanical structure of the microphone. The diaphragm compliance has the greatest influence on the microphone sensitivity, thus its analytical expression needs to be determined accurately. A detailed analysis to determine the compliance of a circular spring diaphragm has been reported by Fuldner *et al.* [9].

A novel spring type diaphragm design is proposed that provides increased mechanical sensitivity of a capacitive microphone by reducing its diaphragm stiffness compared to traditional designs. This paper aims to develop a mathematical model of the spring supported diaphragm microphone design and optimize its performance. Spring type diaphragms are the latest design approaches in capacitive microphone research, and analytical modelling of this type diaphragm has not been previously attempted because of the complex shapes. A lumped element model of the spring-supported diaphragm microphone is derived to analyze the complex relations between the microphone performance factors and to find its optimum parameters setting based on the design requirements.

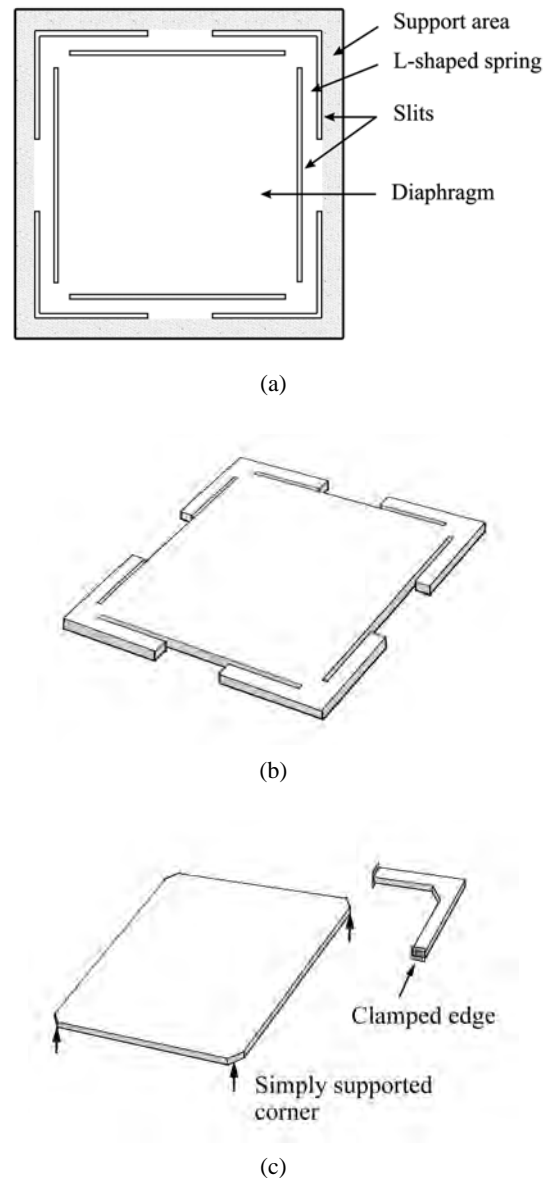
## 2. Microphone Design and Modelling

This section first describes the development of equations to model the centre deflection of the diaphragm, and then determines equations for the open-circuit sensitivity, frequency response, pull-in voltage and the mechanical thermal noise of the microphone.

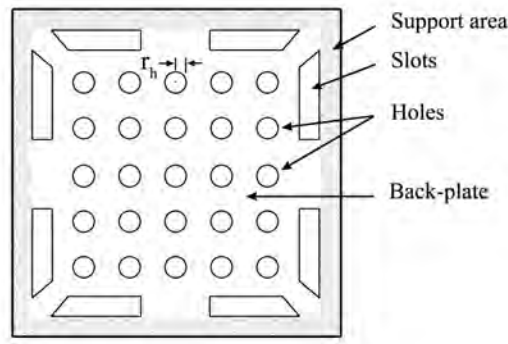
The spring-supported diaphragm presented in this paper has a structure as shown in **Figure 1**. The square diaphragm is suspended by four L-shape spring at its four corners. Its matched size backplate with several perforated holes is shown in **Figure 2**. The cross-section

tional view of the microphone structure is shown in **Figure 3**. A mathematical model to describe the diaphragm movement under an oscillating sound pressure was developed by dividing the diaphragm in **Figure 1(a)** into two main parts:

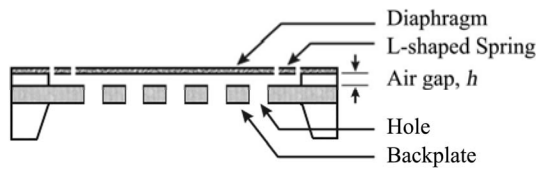
- 1) A diaphragm with four corners simply supported by a fixed point in **Figure 1(c)** (see **Figure 4**), and
- 2) Four doubly clamped L-shaped springs in **Figure 1(c)** (see **Figure 6**).



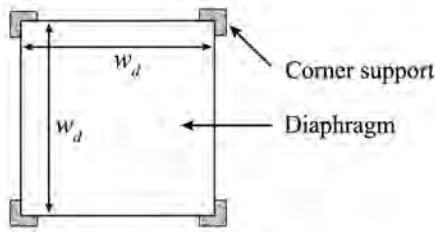
**Figure 1. Microphone diaphragm structure showing a square diaphragm with four L-shaped springs attached: (a) top-view and (b) 3D view, and (c) a square diaphragm with four simply supported corners and one of the four L-shaped springs with its clamped edges.**



**Figure 2.** Microphone back-plate structure with perforated holes.



**Figure 3.** Microphone cross-sectional view.



**Figure 4.** Corner supported diaphragm.

Assuming a linear displacement, the corner-supported diaphragm's center deflection,  $w_1$  in **Figure 4** is given by [15]:

$$w_1 = \frac{0.12P(w_d)^4(1-\nu^2)}{Eh^3} \quad (1)$$

where  $P$  is the sound pressure perpendicular to the top of the diaphragm in Pascal,  $h$  is the diaphragm thickness,  $w_d$  is the diaphragm length and width.  $E$  and  $\nu$  are the modulus of elasticity, and Poisson's ratio of the diaphragm material respectively.

The deflection of an L-shaped spring is derived from a doubly-clamped beam center deflection [16]. Assuming small and linear diaphragm deflection, a center beam deflection,  $w_{bc}$  in **Figure 5** is given by:

$$w_{bc} = \frac{P_b(w_b)^2(L_b)^3}{C_b E w_b h^3} \quad (2)$$

where  $w_b$  is the beam width,  $h$  and  $L_b$  are the beam thickness and beam length respectively. The constant

factor  $C_b$  was determined using Coventor MEMS design software by varying the beam thickness, width, and length to give  $C_b \approx 17.4$ . Modifying (2) by introducing a factor  $C_1$  to compensate the differences between the doubly-clamped beam and the L-shaped spring deflection in **Figure 6** gives:

$$w_2 = \frac{P_s(w_s)^2(2L_s - w_s)^3}{17.4C_1 E w_s h^3} \quad (3)$$

where  $w_2$  is the L-shaped spring center deflection,  $h$ ,  $w_s$ , and  $L_s$  are the spring thickness, spring width, and spring length respectively.

Since the microphone diaphragm's corner is attached to the center of the L-shaped spring, (3) was modified to include the effect of diaphragm's corner deflection to give:

$$w_2 = \frac{P(w_d)^2(2L_s - w_s)^3}{17.4C_1 E w_s h^3} \quad (4)$$

The centre deflection of the square spring-supported diaphragm,  $w_c$  for small diaphragm deflection ( $w_c < h$ ) is given by the sum of the diaphragm deflection in (1) and L-shaped spring deflection in (4):

$$w_c = \frac{0.12P(w_d)^4(1-\nu^2)}{Eh^3} + \frac{P(w_d)^2(2L_s - w_s)^3}{17.4C_1 E w_s h^3} \quad (5)$$

**Figure 7** shows the numerical relationship of factor,  $C_1$  with the diaphragm thickness. The relationship was found using the Coventor to model a spring diaphragm microphone with parameters in **Table 1**. A linear curve fitting on the graph gives:

$$C_1 = 5.802 - 0.056h \quad (6)$$

## 2.1. Open-Circuit Sensitivity

A capacitive microphone operates using the principle of a variable capacitor which produces a variable output voltage when one of its charged capacitor plate is moving parallel to the other plate, thus varying its plate gap. The open-circuit sensitivity (in Volt per Pascal) of a capacitive microphone is given by [17]:

$$S = \frac{V_b}{\Delta P} \cdot \frac{\Delta h_g}{h_g} \cdot \frac{1}{(1 + C_s / C_o)} \quad (7)$$

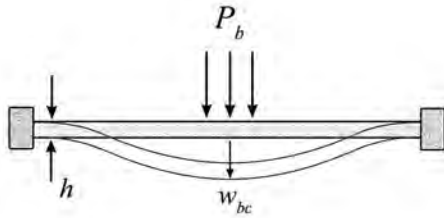
where  $V_b$  is the bias voltage (in volt),  $h_g$  is the sound pressure change,  $C_o$  is the initial air gap distance (in meter) between microphone diaphragm and its back plate, and  $C_s$  are the microphone initial capacitance and stray capacitance (in Farad) respectively. The initial or working capacitance can be calculated using the parallel-plate capacitor equation. The narrow air gap in this microphone leads to an increase in the viscous damping. A

number of back plate holes was used to reduce the viscous damping effect [18,19] (see **Figure 2**). Subtracting the back plate holes from the back plate area and assuming a flat diaphragm deflection, the initial capacitance,  $C_o$  is given by:

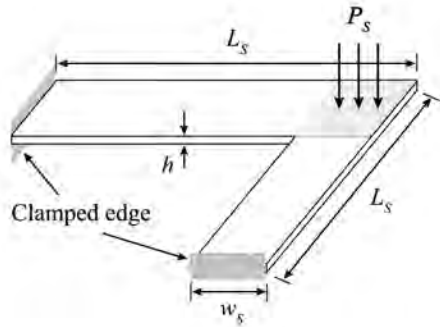
$$C_o = \frac{\epsilon_r \epsilon_o (w_d^2 - n\pi r_h^2)}{h_g} \quad (8)$$

where  $\epsilon_r$  is the dielectric constant of the air gap ( $\epsilon_r \approx 1$  for air),  $\epsilon_o$  is the absolute permittivity of a vacuum,  $n$  and  $r_h$  are the number of back-plate holes and hole radius respectively.

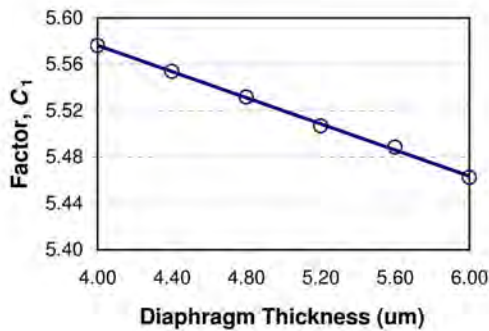
Substituting (5) for the  $\Delta h_g$  into (7) yields a frequency dependent open-circuit sensitivity of a spring diaphragm microphone:



**Figure 5. Doubly-clamped beam center deflection.**



**Figure 6. L-shaped spring dimensions.**



**Figure 7. A linear curve fitting for factor  $C_1$  vs. diaphragm thickness.**

$$S_{OC} = \left[ \frac{0.12(w_d)^4(1-\nu^2)}{Eh^3} + \frac{(w_d)^2(2L_s - w_s)^3}{17.4C_1Ew_s h^3} \right] \times \frac{V_b}{h_g(1 + C_s/C_o)} \quad (9)$$

## 2.2. Frequency Response

A capacitive microphone is often designed to operate in a desired operating frequency range. The frequency response of the microphone must be flat within the desired range to reproduce a good quality sound. In this paper, the microphone will be designed to operate in an audio operating bandwidth of up to 20 kHz. **Table 1** shows the optimized parameters for the microphone design discussed in Section 3.

The frequency response of a condenser microphone can be analyzed using linear lumped elements in a network modelling. **Figure 8** shows an equivalent circuit diagram to represent various lumped elements of a condenser MEMS microphone where  $F_s$  is the sound pressure force, and  $V_m$  is the sound velocity.

The mechanical compliance,  $C_m$  of the diaphragm is given by [17]:

$$C_m = \frac{\Delta h}{\Delta P \cdot w_d^2} \quad (10)$$

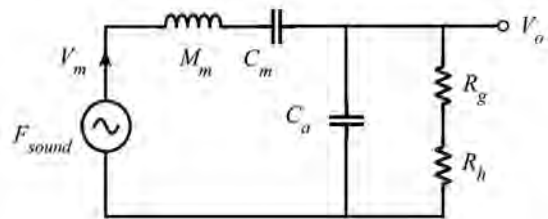
Substituting (5) for  $\Delta h$  into (10) gives a spring-supported diaphragm compliance (in meter/Newton):

$$C_m = \frac{0.12(w_d)^2(1-\nu^2)}{Eh^3} + \frac{(2L_s - w_s)^3}{17.4C_1Ew_s h^3} \quad (11)$$

The lumped effective mass,  $M_m$  (in kg) of the microphone can be approximated by the total diaphragm and L-shaped spring mass:

$$M_m = \rho h w_d^2 + 4\rho h w_s(2L_s - w_s) \quad (12)$$

where  $\rho$  is the polysilicon density for both diaphragm and L-shaped spring. The air gap viscosity loss,  $R_g$  (in N.s/m) and its compliance,  $C_a$  (in m/N) can be expressed as [20]:



**Figure 8. Equivalent circuit diagram of a MEMS microphone.**

**Table 1. Microphone parameters used for the numerical simulations.**

Parameter	Symbol	Value
Poisson's Ratio	$\nu$	0.3
Young's Modulus	$E$	$1.7 \times 10^5$ MPa
Polysilicon density	$\rho$	2230 kg.m <sup>-3</sup>
Air density (20°C)	$\rho_o$	1.2 kg.m <sup>-3</sup>
Air viscosity (20°C)	$\mu_o$	$1.84 \times 10^{-5}$ kg/m-s
Sound velocity (20°C)	$c$	343 ms <sup>-1</sup>
Boltzmann constant	$k_B$	$1.38 \times 10^{-23}$ JK <sup>-1</sup>
Diaphragm thickness	$h$	4 $\mu$ m
Diaphragm width	$w_d$	4 mm
Backplate hole radius	$r_h$	25 $\mu$ m
Backplate thickness	$h_b$	8 $\mu$ m
Backplate width	$w_b$	1 mm
Backplate holes count	$n$	25
Initial air gap distance	$h_g$	4 $\mu$ m
Spring length	$L_s$	0.4 mm
Spring width	$w_s$	0.1 mm
Bias voltage	$V_b$	3 V

$$R_g = \frac{12\mu_o w_d^2}{\pi n h_g^3} \left[ \frac{\alpha}{2} - \frac{\alpha^2}{8} - \frac{\ln \alpha}{4} - \frac{3}{8} \right] \quad (13)$$

$$C_a = \frac{h_g}{\rho_o c^2 \alpha^2 w_d^2} \quad (14)$$

where  $\mu_o$  and  $\rho_o$  are the viscosity and density of air respectively,  $n$  is the number of backplate holes,  $h_g$  is the air-gap distance with zero bias voltage,  $\alpha$  is the surface fraction occupied by the backplate holes, and  $c$  is the sound velocity at room temperature. The backplate holes viscosity loss,  $R_h$  (in N.s/m) is given by [17]:

$$R_h = \frac{8\mu_o h_b w_d^2}{n\pi r_h^4} \quad (15)$$

The total impedance,  $Z_t$  of the circuit in **Figure 8** can be expressed as:

$$Z_t = j\omega M_m + \frac{1}{j\omega C_m} + \frac{R_g + R_h}{1 + j\omega(R_g + R_h)C_a} \quad (16)$$

Thus, the frequency dependent sensitivity and frequency response of the microphone (in Volt/Pascal) can be calculated as:

$$S(\omega) = \frac{V_o(\omega)}{P} = \frac{V_b w_d^2}{j\omega h_g Z_t} \quad (17)$$

### 2.3. Pull-In Voltage

A capacitive microphone's pull-in voltage is caused by

the attractive force between the diaphragm and backplate when a constant bias voltage is applied during its operation. Its value is mainly determined by the spring restoring force of the diaphragm [21] and the L-shaped spring in this paper. Assuming a linear spring restoring force, the net force,  $F_{\text{net}}$  acting on upper plate (diaphragm and L-shaped spring) is given by [16]:

$$F_{\text{net}} = k(h_g - h_d) - \frac{\epsilon_o A V_b^2}{2h_d^2} \quad (18)$$

where spring constant,  $k$  can be calculated from the inverse of the spring-supported diaphragm compliance ( $k = 1/C_m$ ),  $h_g$  and  $h_d$  are the air-gap distance with zero and constant bias voltage respectively.  $A$  is the effective parallel plate area (backplate area minus area occupied by the holes). The first part of the expression in (18) is the spring upward force by the diaphragm and L-shaped spring, and the second part of the expression is the downward electrostatic force caused by the constant bias voltage. At equilibrium, the net force is equal to zero:

$$F_{\text{net(PI)}} = 0 \quad (19)$$

The pull-in occurs at the air-gap distance [16]:

$$h_{\text{net(PI)}} = \frac{2}{3} h_g \quad (20)$$

Equating (18) and (19), and substituting (20) for the pull-in air-gap yields:

$$k = \frac{\epsilon_o A V_{\text{PI}}^2}{h_{\text{PI}}^3} \quad (21)$$

where  $V_{\text{PI}}$  is the pull-in voltage at pull-in air-gap distance,  $h_{\text{PI}}$ . Substituting (20) into (21) yields the pull-in voltage,  $V_{\text{PI}}$  expression:

$$V_{\text{PI}} = \sqrt{\frac{8kh_g^3}{27\epsilon_o(w_d^2 - n\pi r_h^2)}} \quad (22)$$

### 2.4. Mechanical Thermal Noise

A good capacitive microphone is designed to pick up the lowest possible sound pressure which is limited by the mechanical thermal noise and the preamplifier noise of the microphone [19]. The A-weighted mechanical thermal noise,  $S_N$  (in Pascal) can be calculated by [19]:

$$S_N = \sqrt{\int_{f_1}^{f_2} 4k_B T (R_g + R_h) A^2(f) df} \quad (23)$$

where  $f_1$  and  $f_2$  are 20 Hz and 20 kHz respectively,  $T$  is the Boltzmann constant, and  $A(f)$  is the absolute temperature (in Kelvin). The A-weighted filter function, is given by:

$$A(f) = \frac{12200^2 \cdot f^4}{(f^2 + 20.6^2)(f^2 + 12200^2)} \times \frac{1}{\sqrt{(f^2 + 107.7^2)(f^2 + 737.9^2)}} \quad (24)$$

where  $f$  is the sound pressure frequency in Hertz.

It can be seen in (23) that a mechanical thermal noise can be reduced by reducing the backplate holes viscous damping. However, the viscous damping reduction will increase the resonant peak of the microphone diaphragm. Thus, optimum parameters need to be calculated to get the lowest mechanical thermal noise according to the frequency response requirements.

### 3. Performance Analysis

A capacitive MEMS microphone performance factors such as sensitivity, operating bandwidth, pull-in voltage, and thermal noise can be analyzed by varying some of its structural parameters. **Table 2** shows the microphone parameters' change from a low to a higher value which was shown as a percentage parameter change in the analysis graphs throughout this section. Since only one parameter is changed at a time, all other parameters used in the performance analysis simulations are fixed at a reference value as shown in **Table 1**.

The following sections analyses the effect of viscous damping and structure dimensions on bandwidth, sensitivity, pull-in voltage and thermal noise. The results are then used to determine optimised parameters and the frequency response of the diaphragm.

#### 3.1. Viscous Damping

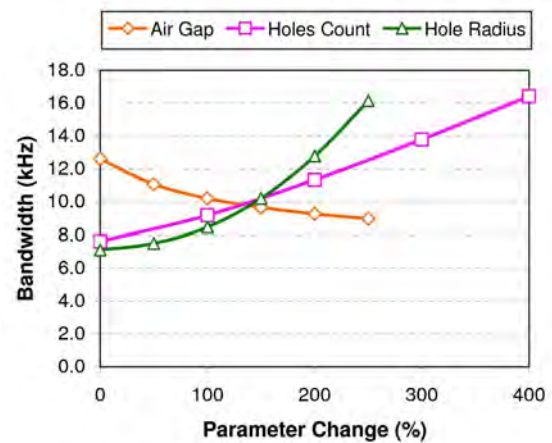
Viscous damping of a MEMS microphone is largely affected by the air gap and backplate viscosity loss as in Equations (13) to (15). In this section, the spring-supported microphone's air gap distance, backplate hole count and hole radius were varied as in **Table 2** to observe its performance effects. **Figure 9** shows that the -3dB operating bandwidth of the microphone can be increased gradually by increasing the backplate hole radius and hole count. Although a larger operating bandwidth can easily be achieved by having more backplate holes and larger hole radius, this decreases the microphone sensitivity as shown in **Figure 10**. Also, these two parameters changes have negligible effect on the pull-in voltage value (see **Figure 11**).

An increase in air gap on the other hand reduces the operating bandwidth (**Figure 9**) even though it increases the pull-in voltage gradually as shown in **Figure 11**. The aim of a microphone design is to achieve the highest

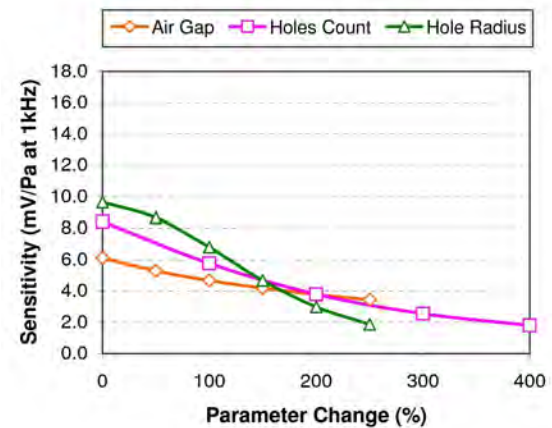
sensitivity, adequate operating bandwidth (20 kHz for an audio applications), and at least 3 times higher pull-in voltage than its bias voltage to prevent the diaphragm from collapsing to the backplate during microphone normal operation.

**Table 2. Microphone parameters' changes used for the performance analysis simulations.**

Parameter	Symbol	Value (low-high)
Diaphragm thickness	$h$	1 $\mu\text{m}$ – 5 $\mu\text{m}$
Diaphragm width	$w_d$	0.8 mm – 1.8 mm
Backplate hole radius	$r_h$	10 $\mu\text{m}$ – 35 $\mu\text{m}$
Backplate width	$w_b$	0.8 mm – 1.8 mm
Backplate holes count	$N$	10 – 50
Initial air gap distance	$h_g$	2 $\mu\text{m}$ – 7 $\mu\text{m}$
Spring length	$L_s$	0.1 mm – 0.5 mm
Spring width	$w_s$	50 $\mu\text{m}$ – 175 $\mu\text{m}$

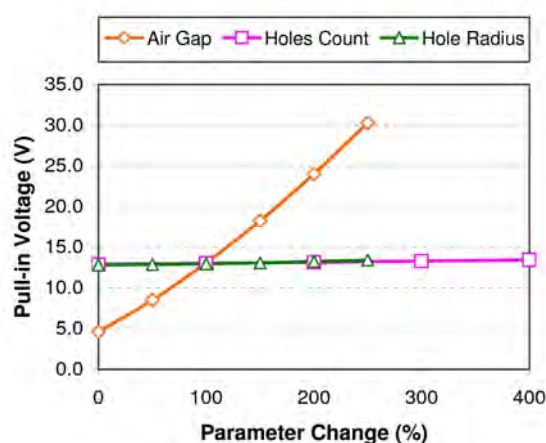


**Figure 9. Microphone bandwidth with air-gap distance, number of backplate holes (holes count), and backplate hole radius change.**



**Figure 10. Microphone sensitivity with air-gap distance, number of backplate holes (holes count), and backplate hole radius change.**





**Figure 11.** Microphone pull-in voltage with air-gap distance, number of backplate holes (holes count), and backplate hole radius change.

The A-weighted mechanical thermal noise of the spring-supported microphone is shown to be decreasing with the decrease of viscous damping (see **Figure 12**). Also, the noise value is shown to be several dBs below the lowest hearing threshold (0 dBA SPL) even at the higher viscous damping values.

### 3.2. Structure Dimensions

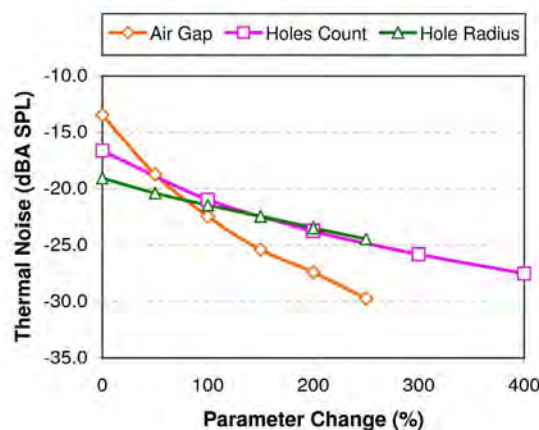
A microphone's open-circuit sensitivity and its frequency response are dependent on viscous damping, as discussed previously, as well as its structure dimensions as in Equations (9) and (17). **Figure 13** shows that an increase in spring width has little effect on the operating bandwidth, but slowly reduces the sensitivity as shown in **Figure 14**. The increase in spring width, however, does raise the pull-in voltage slightly (see **Figure 15**). In contrast, the use of a longer spring in a spring-supported MEMS microphone reduces the microphone operating bandwidth and pull-in voltage slightly (see **Figure 13** and **Figure 15**) even though it causes a small increase in microphone sensitivity (**Figure 14**).

Significant microphone performance effects can be seen by varying the diaphragm and backplate width, as well as the diaphragm thickness. Increasing the diaphragm and backplate width will obviously increase the capacitor effective area thus increasing its capacitance. This is reflected by the large increase in microphone sensitivity as shown in **Figure 14**. However, the diaphragm width increase will also reduce its spring constant, thus gradually reducing the microphone operating bandwidth (**Figure 13**), as well as the pull-in voltage (**Figure 15**).

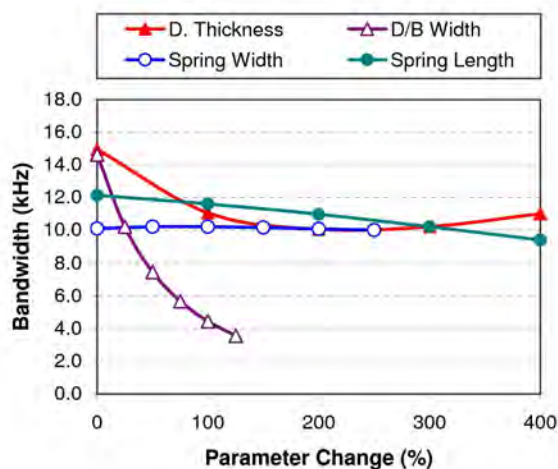
Increasing a diaphragm's thickness will increase its

spring constant, however this will reduce its operating bandwidth up to about 200% thickness change before the bandwidth begins to increase slightly (see **Figure 13**). A thicker microphone diaphragm gives a higher pull-in voltage (**Figure 15**) but reduces the sensitivity due to a higher spring constant (**Figure 14**).

The A-weighted mechanical thermal noise is shown not to be affected by variations in diaphragm thickness, spring width and spring length, however the noise becomes greater with the increase in diaphragm and backplate width due the increased in the capacitor area which will increase the microphone's air gap and the backplate holes viscosity loss (see **Figure 16**). Similar to the viscous damping case, the noise value here is shown to be more than 10 dB below the lowest hearing threshold (0 dBA SPL).



**Figure 12.** Microphone thermal noise with air-gap distance, number of backplate holes (holes count), and backplate hole radius change.



**Figure 13.** Microphone bandwidth with diaphragm thickness, diaphragm and backplate width, spring width, and spring length change.



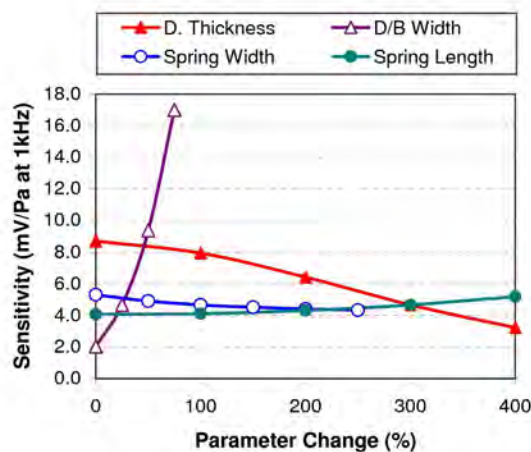


Figure 14. Microphone sensitivity with diaphragm thickness, diaphragm and backplate width, spring width, and spring length change.

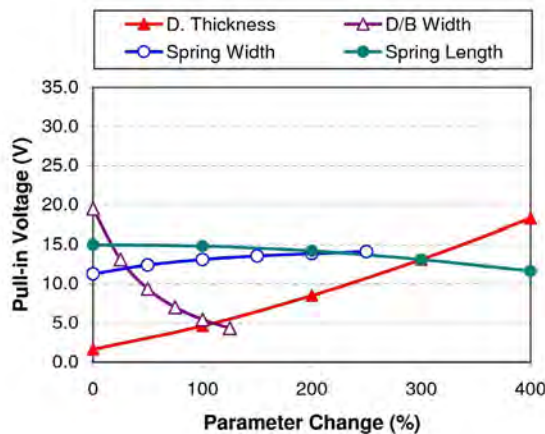


Figure 15. Microphone pull-in voltage with diaphragm thickness, diaphragm and backplate width, spring width, and spring length change.

### 3.3. Parameters Optimization

Parameters optimization is required to achieve the best microphone performance given various design and application constraints such as smaller device size, wider operating bandwidth, and minimum electrical power usage. In this paper, a spring-supported diaphragm microphone requires 20 kHz operating bandwidth with highest sensitivity and pull-in voltage, as well as the lowest possible thermal noise.

Based on the complex parameters relationships as discussed in previous sections, an optimised microphone design was achieved using the parameter values shown in **Table 1**. The design gives a -3dB operating bandwidth of 10.2 kHz, a sensitivity of 4.67 mV/Pa (-46.5 dB ref. 1 V/Pa at 1 kHz using a bias voltage of 3 V), a pull-in

voltage of 13 V, and a thermal noise of -22 dBA SPL. The theoretical frequency response of the microphone was calculated using (17) and is shown in **Figure 17**.

## 4. Conclusions

The design of a spring-supported microphone is governed by a complex relations and trade-offs between several performance factor parameters. Since optimum parameter values are required for a microphone's performance, a lumped element model is developed to assist in achieving this goal. The model is applied to a novel spring-supported diaphragm capacitive microphone design, and it is concluded that the spring width and length in the spring-support do not have a large effect on the microphone's operating bandwidth, sensitivity, pull-in voltage, and thermal noise.

An optimum set of parameter values are used for the new spring-supported diaphragm microphone to give a -3

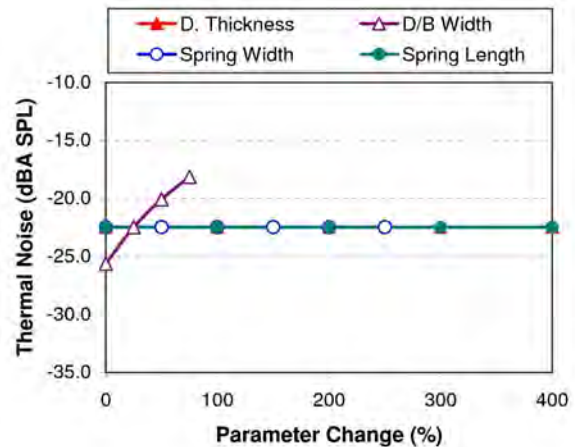


Figure 16. Microphone thermal noise with diaphragm thickness, diaphragm and backplate width, spring width, and spring length change.

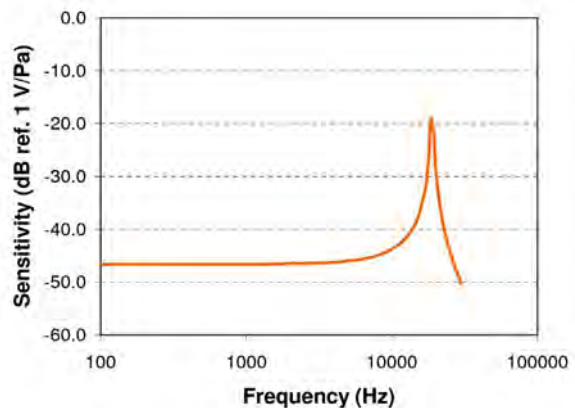


Figure 17. Theoretical frequency response of a new microphone design using parameters in Table 1.

dB operating bandwidth of 10.2 kHz, a sensitivity of 4.67 mV/Pa (−46.5 dB ref. 1 V/Pa at 1 kHz using a bias voltage of 3 V), a pull-in voltage of 13 V, and a thermal noise of −22 dBA SPL. The operating bandwidth of the microphone can be increased further by using a thicker diaphragm size with a trade-off of lowering its sensitivity. However, a lower sensitivity can easily be increased by using a higher bias voltage if it is permitted by the intended application and does not exceed the pull-in voltage threshold of the diaphragm.

## 5. References

- [1] C. P. R. Scheeper, A. G. H. Van Der Donk, W. Olthuis and P. Bergveld, "Review of silicon microphones," *Sensors and Actuators, A: Physical*, Vol. 44, No. 1, 1994, pp. 1-11.
- [2] P. Rombach, M. Mullenborn, U. Klein and K. Rasmussen, "The First Low Voltage, Low Noise Differential Silicon Microphone, Technology Development and Measurement Results," *Sensors and Actuators, A: Physical*, Vol. 95, No. 2-3, 2002, pp. 196-201.
- [3] P. R. Scheeper, W. Olthuis and P. Bergveld, "Silicon Condenser Microphone with a Silicon Nitride Diaphragm and Backplate," *Journal of Micromechanics and Microengineering*, Vol. 2, No. 3, 1992, pp. 187-189.
- [4] A. Torkkeli, O. Rusanen, J. Saarihahti, H. Seppa, H. Sipola and J. Hietanen, "Capacitive Microphone with Low-Stress Polysilicon Membrane and High-Stress Polysilicon Backplate," *Sensors and Actuators, A: Physical*, Vol. 85, No. 1-3, 2000, pp. 116-123.
- [5] M. Pedersen, R. Schellin, W. Olthuis and P. Bergveld, "Electroacoustical Measurements of Silicon Microphones on Wafer Scale," *Journal of the Acoustical Society of America*, Vol. 101, No. 4, 1997, pp. 2122-2128.
- [6] B. A. Ganji and B. Y. Majlis, "Design and Fabrication of a New MEMS Capacitive Microphone Using a Perforated Aluminum Diaphragm," *Sensors and Actuators, A: Physical*, Vol. 149, No. 1, 2009, pp. 29-37.
- [7] P. R. Scheeper, W. Olthuis and P. Bergveld, "Design, Fabrication, and Testing of Corrugated Silicon Nitride Diaphragms," *Journal of Microelectromechanical Systems*, Vol. 3, No. 1, 1994, pp. 36-42.
- [8] X. Li, R. Lin, H. Kek, J. Miao and Q. Zou, "Sensitivity-Improved Silicon Condenser Microphone with a Novel Single Deeply Corrugated Diaphragm," *Sensors and Actuators, A: Physical*, Vol. 92, No. 1-3, 2001, pp. 257-262.
- [9] M. Fuldner, A. Dehe and R. Lerch, "Analytical Analysis and Finite Element Simulation of Advanced Membranes for Silicon Microphones," *IEEE Sensors Journal*, Vol. 5, No. 5, 2005, pp. 857-862.
- [10] B. A. Ganji and B. Y. Majlis, "Design and Fabrication of a Novel Single-Chip MEMS Capacitive Microphone Using Slotted Diaphragm," *Journal of Micro/Nanolithography, MEMS, and MOEMS*, Vol. 8, No. 2, 2009.
- [11] H. J. Kim, S. Q. Lee and K. H. Park, "A Novel Capacitive Type Miniature Microphone with a Flexure Hinge Diaphragm," *Proceedings of SPIE—The International Society for Optical Engineering*, Vol. 6374, Boston, 2006.
- [12] N. Mohamad, P. Iovenitti and T. Vinay, "High sensitivity capacitive MEMS microphone with spring supported diaphragm," *Proceedings of SPIE—The International Society for Optical Engineering*, SPIE, Canberra, Australia, 2008, pp. 68001T-1 until 68001T-9.
- [13] J. W. Weigold, T. J. Brosnihan, J. Bergeron and X. Zhang, "A MEMS Condenser Microphone for Consumer Applications," *Proceedings of the IEEE International Conference on Micro Electro Mechanical Systems (MEMS)*, Istanbul, 2008, pp. 86-89.
- [14] N. Mohamad, P. Iovenitti and T. Vinay, "Effective Diaphragm Area of Spring-Supported Capacitive MEMS Microphone Designs," *Proceedings of SPIE—The International Society for Optical Engineering*, SPIE, Melbourne, Australia, 2008, pp. 726805-1 until 726805-7.
- [15] S. Timoshenko and S. Woinowsky-Krieger, "Theory of Plates and Shells," McGraw-Hill, New York, 1959, pp. 180-228.
- [16] S. D. Senturia, "Microsystem Design," Kluwer Academic, Boston; London, 2001, pp. 239-265.
- [17] J. Bergqvist, "Finite-Element Modelling and Characterization of a Silicon Condenser Microphone with a Highly Perforated Backplate," *Sensors and Actuators, A: Physical*, Vol. 39, No. 3, 1993, pp. 191-200.
- [18] J. Bergqvist, F. Rudolf, J. Maisano, F. Parodi and M. Rossi, "A Silicon Condenser Microphone with a Highly Perforated Backplate," *IEEE International Conference on Solid-State Sensors and Actuators*, San Francisco, CA, USA, 1991, pp. 266-269.
- [19] C. W. Tan, Z. Wang, J. Miao and X. Chen, "A Study on the Viscous Damping Effect for Diaphragm-Based Acoustic MEMS Applications," *Journal of Micromechanics and Microengineering*, Vol. 17, No. 11, 2007, pp. 2253-2263.
- [20] P. C. Hsu, C. H. Mastrangelo and K. D. Wise, "High Sensitivity Polysilicon Diaphragm Condenser Microphone," *Proceedings of the IEEE Micro Electro Mechanical Systems (MEMS)*, Heidelberg, Germany, 1998, pp. 580-585.
- [21] S. Chowdhury, M. Ahmadi and W. C. Miller, "Nonlinear Effects in MEMS Capacitive Microphone Design," *Proceedings International Conference on MEMS, NANO and Smart Systems*, 2003, pp. 297-302.

# Analysis of the Manufactured Tolerances with the Three-Dimensional Method of Angular Chains of Dimensions Applied to a Cylinder Head of Car Engine

Aida Mezghani<sup>1,2</sup>, Alain Bellacicco<sup>2</sup>, Jamel Louati<sup>1</sup>, Alain Rivière<sup>2</sup>, Mohamed Haddar<sup>1</sup>

<sup>1</sup>Mechanics Modelling and Production Research Unit, ENIS, TUNISIA

<sup>2</sup>Laboratoire d'Ingénierie des Structures Mécaniques et des Matériaux, SUPMECA Paris, FRANCE

E-mail: mezghani\_aida@yahoo.fr

Received May 4, 2010; revised July 21, 2010; accepted August 16, 2010

## Abstract

This paper proposes an analysis method of the manufactured tolerances applied to a cylinder head of car engine. This method allows to determine the manufacturing tolerances in the case of angular chains of dimensions and to check its correspondence with the functional tolerances. The objective of this work is to analyze two parameterized functions: the angular defect  $\Delta\alpha$  and the projected length  $lg$  of the toleranced surface. The angular defects are determined from the precision of the machine tools, we consider only the geometrical defects (position and orientation of surfaces), making the assumption that the form defects are negligible. The manufactured defect is determined from these two parameterized functions. Then it will be compared with the functional condition in order to check if the selected machining range allows, at end of the manufacturing process, to give a suitable part.

**Keywords:** Three-Dimensional Tolerancing, Manufacturing Process, Toleranced Surface, Angular Defect.

## 1. Introduction

Today, the manufacturing engineers face the problem of selecting the appropriate manufacturing process (machining processes and production equipments) to ensure that design specifications are satisfied. Developing a suitable process is complicated and time-consuming.

To verify the capacity of a manufacturing process to make the corresponding parts it is necessary to simulate the defects that it generates and to analyze the correspondence of produced parts with the functional tolerances. In order to check the capability of a manufacturing process to carry out suitable parts, it is necessary to analyze each functional tolerance. In the literature available on this subject, the evaluation of a process in terms of functional tolerances is called the tolerance analysis, [1-5].

The best way to analyze the tolerances is to simulate the influence of parts deviations on the geometrical requirements. Usually, these geometrical requirements limit the gaps or the displacements between product surfaces. For this type of geometrical requirements, the influences of parts deviations can be analyzed by different ap-

proaches as Variational geometry [6,7], Vectorial tolerancing [8,9], Clearance space and deviation space [10-13], Gap space [14], quantifier approach [15,16], kinematic models [17,18], Inertial Tolerancing [19].

In this paper the three-dimensional method of angular chains of dimensions is used for simulating the manufacturing process and then manufactured tolerancing is determined to carry out tolerance analysis

## 2. Description of the Method

The three-dimensional method of angular chains of dimensions, initiated by [20], allows the optimization of the calculation of three-dimensional angular dispersions. This method also allows the validation of the manufacturing range by taking into account the processes precision.

The objective of this work is to analyze two parameterized functions: the angular defect  $\Delta\alpha$  and the projected length  $lg$  of the toleranced surface. The angular defects are determined from the precision of the machine tools, only the geometrical defects are considered (position and orientation of surfaces), making the assumption

that the form defects are negligible. The manufactured defect is first determined from these two parameterized functions. Then it is compared with the functional condition in order to check if the selected machining range allows, at the end of the manufacturing process, to give a suitable part.

## 2.1. The Angular Defect

The angular defect can be determined through two methods: the 2D method used currently in the industries and the new 3D method, in order to compare the results given by both methods.

### 2.1.1. 2D Approach

To determine the angular defect of a surface with the 2D method, it is necessary to choose two projection plans (perpendicular to the tolerated surface). Then the angular defect in each plan is determined by the 1D method of angular chains of dimensions. The angular defect of the tolerated surface is given by the combination of both angular defects found in the analysis plans.

If the angular chains of dimensions are made in two projection plans (H and V for example), perpendicular between them, the defect in the plan V lies between zero and an angle  $\Phi_1$ . It will combine with a defect, manufactured in the plan H, located between zero and  $\Phi_2$ .

The greatest angular defect  $\Delta\alpha_{max}$ , resulting from the combination of the two defects, is given by:

$$\Delta\alpha_{max} = \sqrt{\Phi_1^2 + \Phi_2^2} \quad (1)$$

$\Delta\alpha_{max}$  is located in the direction which forms an angle  $\theta$  with the plan V.

$$\theta = \text{Atan}(F_2 / F_1) \quad (2)$$

The diagram of the angular defects is shown in **Figure 1**.

Referring to this diagram, the angular defect  $\Delta\alpha$  is given in each analysis direction in accordance with  $\theta$ . The value of the angular defect is equal to the length of the segment OA.

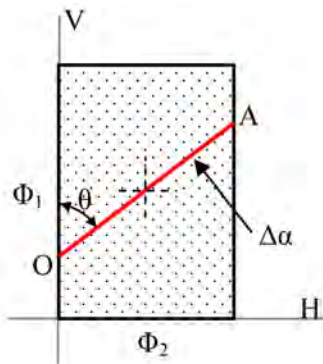


Figure 1. Diagram of the angular defects (2D method).

### 2.1.2. 3D Approach

In reality, the normal vectors  $\vec{n}$ , of the various machined surfaces, is contained in a volume forming a conical zone of tolerance. These zones of tolerance constitute solid angles.

The method consists in cumulating the solid angles which represent the angular defects of the part's surfaces in the aim of finding the angular defect of the tolerated surface.

For a given machining range, it is necessary to determine the locus of each manufactured defect, from the 1st phase until the nth phase. The combination of these defects gives a solid angle comparable to a right cone with an oblong form directrix. The manufactured defects diagram will have an oblong form instead of a rectangular one.

A parameterized diagram is drawn on a CATIA file related to a table of parameter setting. This parameter setting makes it possible to change the shape of the diagram according to the machine precision and the orientation of positioning surfaces (**Figure 2**).

Referring to this diagram, the angular defect  $\Delta\alpha$  is given in each analysis direction in accordance with  $\theta$ . The value of the angular defect is equal to the length of the segment BC. To determine the value of  $\Delta\alpha$  the CATIA macros are used. For each value of  $\theta$ ,  $\Delta\alpha$  is measured then transferred towards an EXCEL file.

## 2.2. The Manufactured Defect

The manufactured defect tf is the greatest height measured between the tolerated element, surface S considered plane, and the associated exact theoretical plan.

The measured defect tf is given by the Equation (3)

$$tf(\theta) = \Delta\alpha(\theta) \times \lg(\theta) \quad (3)$$

with

$\Delta\alpha(\theta)$ : the angular defect of the tolerated surfaces in each analysis plan.

$\lg(\theta)$ : the projected length of the tolerated surface in each analysis plan.

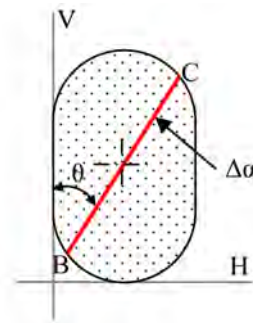


Figure 2. Diagram of the angular defects (3D method).

When  $S$  surface has a particular form (**Figure 3**), the projected length  $lg$  is not uniform in all the analysis directions. To determine the various values of the projected length according to  $\theta$  we use software CATIA. The values of  $lg$  are extracted from the CAD model of the part. The projected surface length is measured for each value of  $\theta$  then automatically transferred from CATIA towards an Excel file. Then we obtain a table which contains all the values of  $lg$  for a sweeping of  $\theta$ .

The projected length and the angular defect  $\Delta\alpha$  are given for a sweeping of  $\theta$  then the manufactured defect  $tf$  can be deduced.  $tf_{max}$  will be compared with the functional condition.

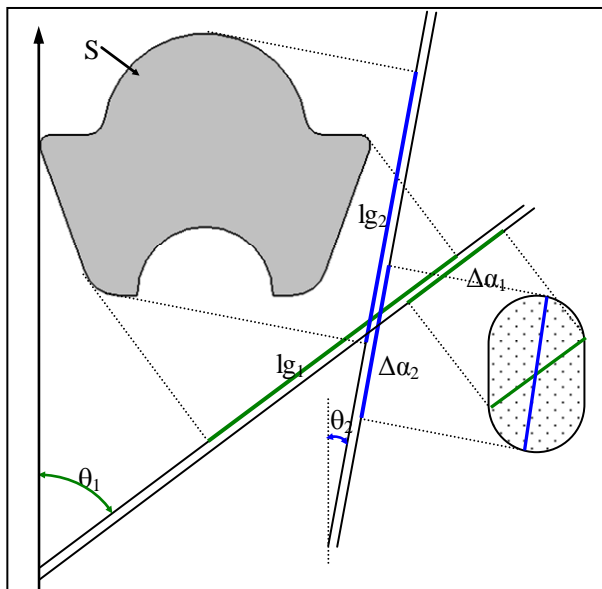
### 3. Case Study: A Cylinder Head of Car Engine

In this paper, the studied example is a cylinder head of car engine. The functional geometrical conditions of orientation are checked by using the method of three-dimensional angular chains of dimensions.

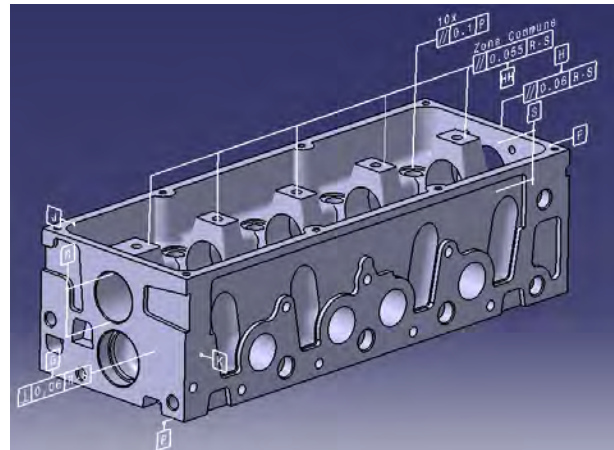
The geometrical orientation conditions, such as parallelism, perpendicularity and angularity will be treated in order to check their respect according to the machining processes precision.

**Figure 4** represents the Digital Mock-Up (DMU) of the cylinder head made with the geometrical orientation conditions to study.

Digital Mock Up or DMU allows real-time visualization of the complete product in 3 dimensions and to describe it during its life cycle. The DMU is a virtual version of the product that makes it possible to create all the



**Figure 3.** Case of particular form surface.



**Figure 4.** Digital Mock-Up (DMU) of the cylinder head with the orientation geometrical conditions.

simulations needed for product development, manufacturing and the aftermarket.

The DMU enables the simulation of the product with the intention of knowing future and to replace the physical prototypes with the virtual ones.

The cylinder head machining range comprises three phases. **Table 1** summarizes them. This table highlights the manufactured and positioning surfaces in each phase.

We will study the feasibility of the DD condition: parallelism of  $H$  relative to  $R-S$ . The angular defect is determined by the 2D method then the 3D or the spatial method.

The precision of the used machine is 0.007 mm. This corresponds to an angular defect  $\Delta\alpha = 0.07$  mrd for 100 mm length and in any direction.

**Table 1.** Machining range of the head cylinder.

Operation	Positioning surfaces			Machined surfaces
OP 20	W	V	Y	P
	P	V	Y	H and HH
OP30	P	V	F'	J
	P	J	F'	K
	P	K	Y	F and G
	P	K	F	A-B
	P	542 (cylindrical pins)	A (milled pins)	601-610
OP40	P	542 (cylindrical pins)	515 (milled pins)	Spot-facing 601-610
	P	542 (cylindrical pins)	515 (milled pins)	R-S



### 3.1. The Angular Defect

#### 3.1.1. 2D Approach

In order to determine the angular defect generated by the manufacturing process, in each projection plan, we use the 1D angular chains of dimensions.

The machining range proposed for the cylinder head manufacturing indicates that the tolerated surface is machined before the reference element, which explains the need for a tolerances transfer.

**Figures 5 and 6** show the 1D dimensions chains plot on the projection plans (PL1 Parallel to G and F, PL2 Parallel to K and J).

The cumulated defect in the projection plan can be deduced from this chain of dimensions:

- in PL1 the cumulated angular defect is  $\Delta\alpha = 0.14$  mrd.
- in PL2 the cumulated angular defect is  $\Delta\alpha = 0.07$  mrd.

Then the diagram of the angular defect is represented in **Figure 7** with  $\Phi_1 = 0.07$  mrd and  $\Phi_2 = 0.14$  mrd.

Referring to this diagram the angular defect  $\Delta\alpha$  can be given in each analysis direction in accordance with  $\theta$ . The value of the angular defect is equal to the length of the segment OA. So we obtain the result of **Figure 8** which represents the angular defect  $\Delta\alpha$  in each analysis direction.

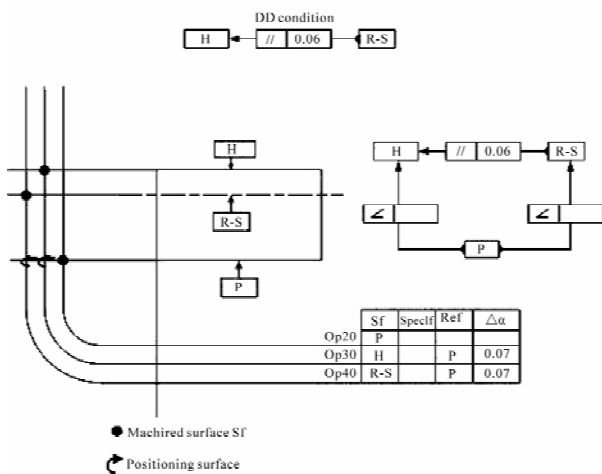
According to this result the maximum angular defect is 0.155 mrd. It's located in the analysis direction which has  $\theta = 1.11$  rd

This result can be found using calculation since

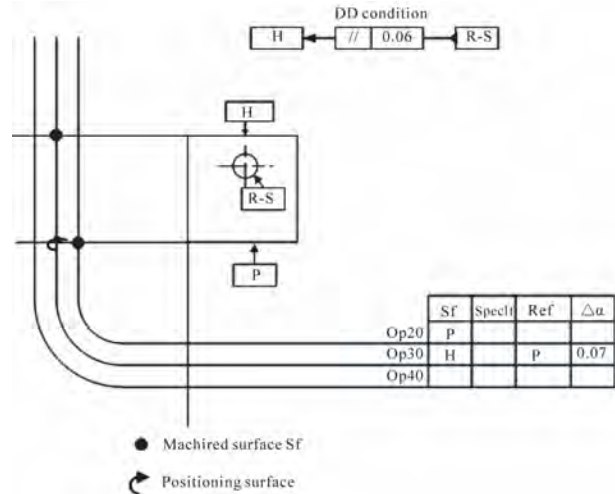
$$\Delta\alpha_{max} = \sqrt{\Phi_1^2 + \Phi_2^2} = 0.156 \text{ mrd.}$$

#### 3.1.2. 3D Approach

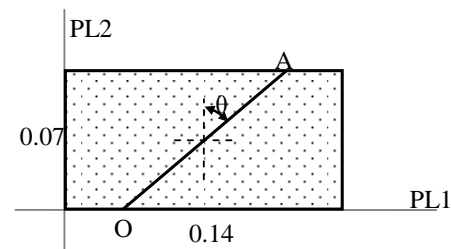
To determine the resulting angular defect, it's necessary to cumulate the solid angles and the plan angles which represent the angular defects of the manufactured surfaces.



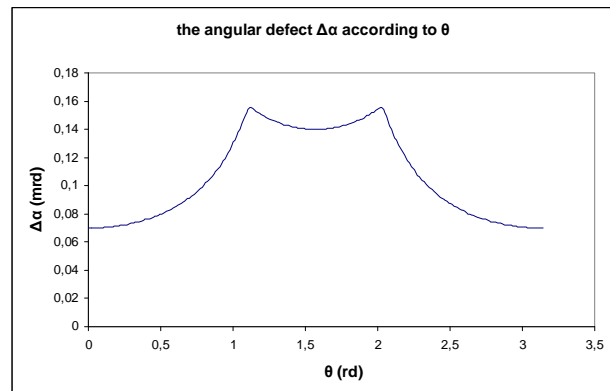
**Figure 5. 1D angular dimensions chain in PL1.**



**Figure 6. 1D angular dimensions chain in PL2.**



**Figure 7. The angular defect diagram (2D Method).**


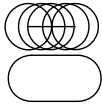


**Figure 8. The angular defect of the tolerated surface according to  $\theta$ . (2D method).**

The defect associated to the tolerated surface (normal vector  $\vec{z}$ ) is modeled by a solid angle which the directrix diameter depends of the precision of the machine. The direction vector for R-S is  $\vec{x}$ , therefore only the angular defect of rotation according to  $\vec{y}$  is considered. The angular defect of rotation according to  $\vec{z}$  does not have influence on the respect of the parallelism condition.

**Table 2** summarizes the method of determination of the angular defects diagram.

**Table 2. Directrix of the cumulated defect.**

phase	Manufactured surface	Locus of the manufactured defect	Directrix of the cumulated defect
30	H	Angle solide	Cercle $\varnothing 0.07$ 
40	R-S	Angle plan	Oblong $0.14 \times 0.07$ 

**Figure 9** presents the diagram of the angular defect  $\Delta\alpha$  given by the 3D method. The manufactured defects diagram has an oblong form instead of a rectangular form.

Referring to this diagram the angular defect  $\Delta\alpha$  can be given in each analysis direction in accordance with  $\theta$ . The value of the angular defect is equal to the length of the segment BC. We obtain the result of **Figure 10** which represents the angular defect  $\Delta\alpha$  in each analysis direction.

The greatest defect is equal to 0.14 mrd. It's located in the analysis direction which has  $\theta = 1.57$  rd. It is noticed that the angular defect determined by the 3D approach is smaller than the angular defect found by the 2D method. After that we will use the results of **Figure 8** and **Figure 10** to determine the manufactured tolerances in both cases and to compare them with the functional specifications.

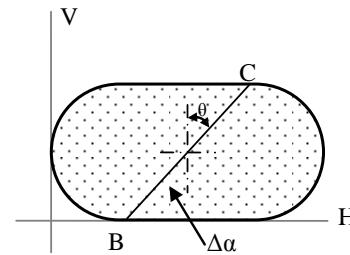
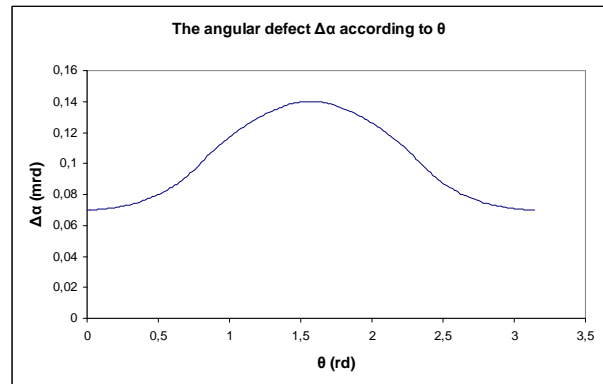
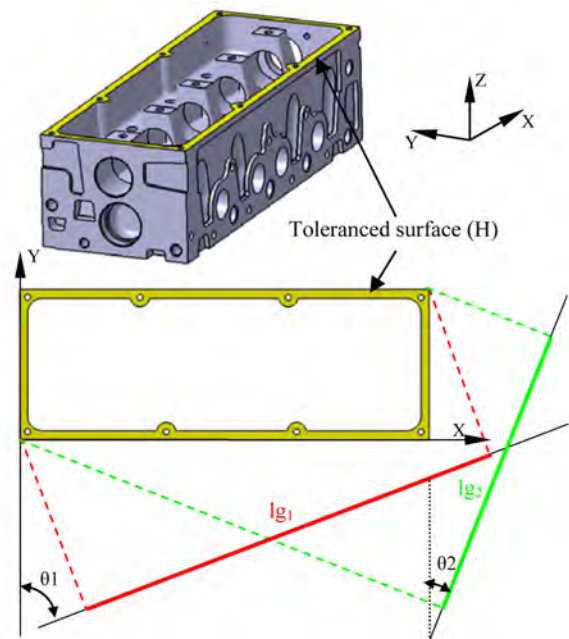
### 3.2. The Manufactured Defect

The method requires geometrical data relative to the tolerated surface. These data are extracted from the CAD model of the cylinder head. **Figure 11** represents the form of the tolerated surface.

We use CATIA to determine the projected length in each analysis direction that is shown in **Figure 12**.

To determine the critical defect, it is necessary to express the measured defect  $t_f$  according to the two independent variables: the angular defect  $\Delta\alpha(\theta)$  and the projected length  $lg(\theta)$ . **Figure 13** and **Figure 14** present the manufactured defect determined respectively by the 2D method and 3D method.

The result of **Figure 13** shows that the maximum manufactured defect is equal to 0.067 mm. It's exceeded the limits imposed by the functional requirement (parallelism of 0.06 mm according to R-S). So the used machine cannot satisfy the parallelism condition. We must use a more precise machine. This increases the production cost of the part.

**Figure 9. The angular defect diagram (3D Method).****Figure 10. The angular defect of the tolerated surface according to  $\theta$ . (3D method)****Figure 11. Form of the tolerated surface.**

On the other hand, the result given by the 3D method shows that the maximum manufactured defect is equal to 0.058 mm. The parallelism condition is checked. The use of a machine the precision of which is 0.007 mm makes it possible to satisfy the DD condition.



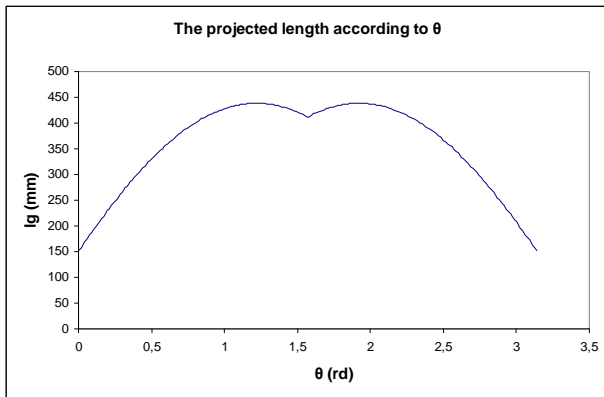


Figure 12. The projected length of the tolerated surface according to  $\theta$ .

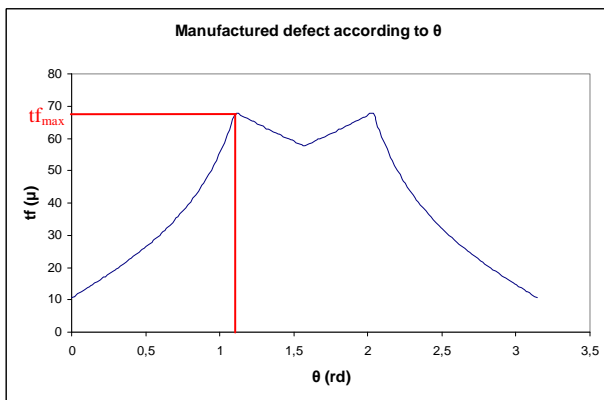


Figure 13. The manufactured defect of the tolerated surface (H) according to  $\theta$  (2D method).

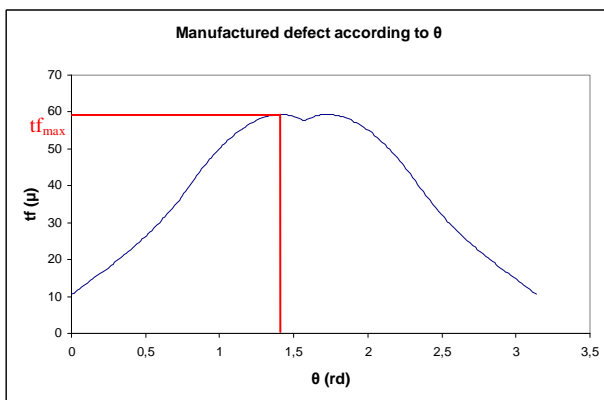


Figure 14. The manufactured defect of the tolerated surface (H) according to  $\theta$  (3D method).

The 3D method allows to optimize the manufactured tolerance intervals and to check the feasibility of the parts according to the machine precision. We will be able to choose a less precise machine and to reduce the production cost.

Next we present the results for several orientation con-

ditions. The same methodology is used to check the correspondence of these conditions with the functional specifications according to the machine precision.

**Condition 2:** parallelism of R-S relative to datum surface P.

In this case the tolerated element is machined directly relative to the datum surface P. it doesn't need a tolerance transfer. At worst the manufactured tolerance must be equal to the value of the tolerance interval of the DD requirement (0.04 mm). The parametric function  $lg(\theta)$  is a constant equal to the length of the axis R-S. As a result, the precision machine needed to satisfy the functional specification is of  $p = 0.097$  mm.

**Condition 3:** parallelism of HH relative to datum axis R-S.

Figure 15 and Figure 16 present the manufactured defect determined respectively by the 2D method and 3D method for  $p = 0.007$  mm.

Both methods show that the use of a machine, which precision is 0.007 mm, makes it possible to satisfy the functional specification (parallelism of 0.055 mm relative to R-S).

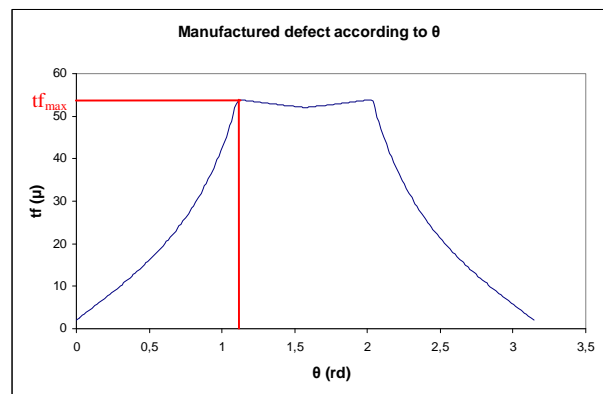


Figure 15. The manufactured defect of the tolerated surface according to  $\theta$  (2D method).

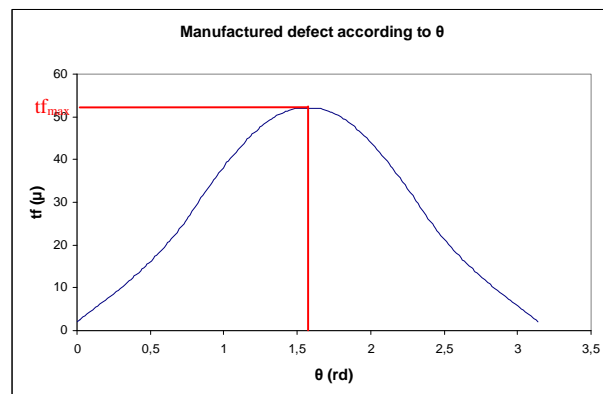


Figure 16. The manufactured defect of the tolerated surface according to  $\theta$  (3D method).

- 2D method:  $tf_{\max} = 0.052$  mm
- 3D method:  $tf_{\max} = 0.054$  mm

**Condition 4:** parallelism of the melts of spot facing relative to the datum surface P.

The tolerated element is machined directly relative to the datum surface. Only the defect generated by the machining of the tolerated element is considered. Consequently, the diagram of the angular defect determined by the 2D and 3D method has respectively a square form and a circular form.

The tolerated surface has a circular form, so  $lg(\theta)$  is constant and equal to the diameter of the surface, which explains the result of the **Figure 18**. The manufactured defect is a constant for any value of  $\theta$ .

**Figure 17** and **Figure 18** present the manufactured defect determined respectively by the 2D method and 3D method for  $p = 0.45$  mm.

The DD condition is checked only with the 3D method. This method allows the optimization of the choice of the machine compared to the 2D method.

We notice that the precision  $p = 0.45$  mm is justified by tow facts:

- The dimensions of the tolerated surface are smaller than the dimensions of the other tolerated surfaces studied previously.

- The tolerated element is machined directly relative to the datum surface

**Condition 5:** perpendicularity of G relative to the datum axis R-S.

In the same way, the condition of perpendicularity is analyzed. **Figure 19** and **Figure 20** present the manufactured defect determined respectively by the 2D method and 3D method for  $p = 0.01$  mm.

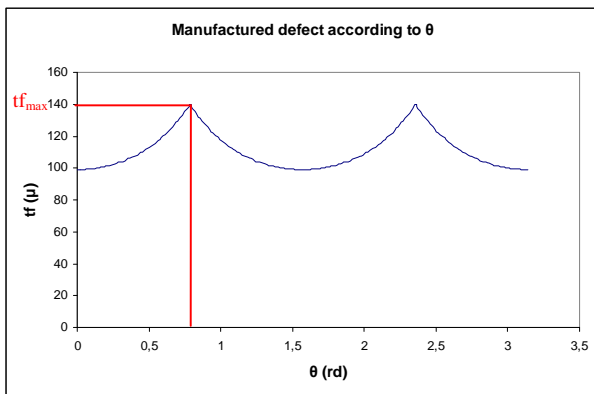
We find the following results:

- 2D method:  $tf_{\max} = 0.052$  mm
- 3D method:  $tf_{\max} = 0.037$  mm

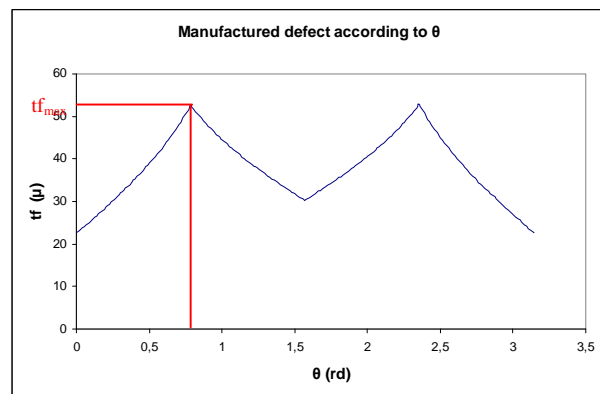
The result find with the 3D method shows that the condition of perpendicularity of G relative to R-S can be respected if  $p = 0.01$  mm

It is noticed that dimensions of the tolerated surfaces have a great influence on the choice of the machine. It is always delicate to respect the tight tolerance interval relative to large-sized tolerated surfaces.

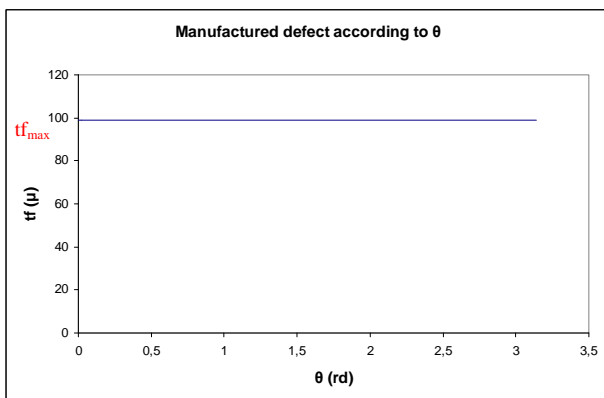
**Table 3** summarizes the results find with the 3D method.



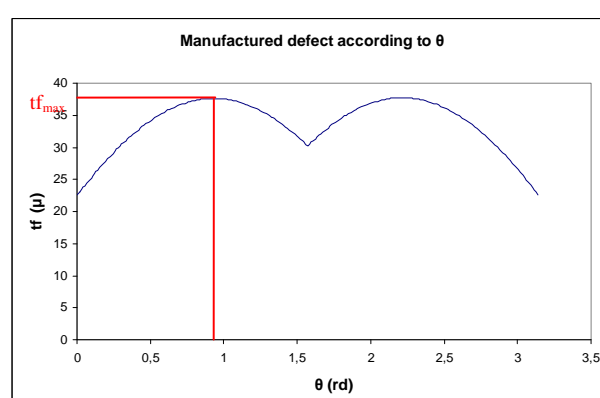
**Figure 17.** The manufactured defect of the tolerated surface according to  $\theta$  (2D method).



**Figure 19.** The manufactured defect of the tolerated surface according to  $\theta$  (2D method).



**Figure 18.** The manufactured defect of the tolerated surface according to  $\theta$  (3D method).



**Figure 20.** The manufactured defect of the tolerated surface according to  $\theta$  (3D method).

**Table 3. Summary of the results.**

DD condition	Form and dimension of the toleranced surface	Manufactured defect find with the 3D method	Machine precision
<b>Condition 1</b>			
H // 0.06 R-S	Rectangular form 151 × 411.5 mm	$tf_{max} = 0.058$ mm	$p = 0.007$ mm
<b>Condition 2</b>			
R-S // 0.04 P	Axis 411.5 mm	$tf_{max} = 0.04$ mm	$p = 0.097$ mm
<b>Condition 3</b>			
Common zone HH // 0.055 R-S	Rectangular form 371.5 × 27 mm	$tf_{max} = 0.054$ mm	$p = 0.007$ mm
<b>Condition 4</b>			
$\frac{10}{x}$ // 0.1 P	Circular form Ø22 mm	$tf_{max} = 0.099$ mm	$p = 0.45$ mm
<b>Condition 5</b>			
G ⊥ 0.05 R-S	Rectangular form 150 × 113 mm	$tf_{max} = 0.037$ mm	$p = 0.01$ mm

The machining of surfaces H and HH requires a more precise machine compared with the other part surfaces. That is explained by two reasons: on the one hand, the tolerance intervals of the functional specifications are too tight; on the other hand, the toleranced surfaces have larger dimensions. Moreover, in both cases, toleranced surfaces are not machined directly relative to the datum. Consequently the accumulation of the defects generated in each phase of the manufacturing range increases the manufactured defect.

## 4. Conclusions

In this paper, we have presented a three-dimensional method of manufactured tolerances analysis applied to a cylinder head of a car engine. This method makes it possible to evaluate the validity of a manufacturing process and to analyze the defects which occur in the various production phases. The use of CATIA macros decreases considerably the processing time of the examples and facilitates the treatment of the geometrical conditions.

We showed here an example of a cylinder head of a car engine in which we can see that the choice of the machine precision depends on the dimensions of the toleranced surfaces and the interval of tolerance required by the Design Department. This method is not a specific one, but a general one. It can be used in the case of industrial complex examples.

## 5. References

- [1] F. Germain, D. Denimal and M. Giordano, "A Method for Three Dimensional Tolerance Analysis and Synthesis Applied to Complex and Precise Assemblies," in IFIP International Federation for Information Processing, Volume 260, Micro-Assembly Technologies and Applications, Springer, Boston, 2008, pp. 55-65.
- [2] F. Villeneuve and F. Vignat, "Manufacturing Process Simulation for Tolerance Analysis and Synthesis," *Proceedings of IDMMME*, 2004, Bath, 10 pages.
- [3] M. H. Kyung and E. Sacks, "Nonlinear Kinematic Tolerance Analysis of Planar Mechanical Systems," *Computer Aided Design*, Vol. 35, No. 10, 2003, pp. 901-911.
- [4] R. J. Gerth and W. M. Hancock, "Computer Aided Tolerance Analysis for Improved Process Control," *International Journal of Computers and Industrial Engineering*, Vol. 38, No. 1, 2000, pp. 1-19.
- [5] Z. Shen, G. Ameta, J. J. Shah and J. K. Davidson, "A Comparative Study of Tolerance Analysis Methods," *Journal of Computing and Information Science in Engineering*, Vol. 5, No. 3, 2005, pp. 274-284.
- [6] J. Hu, G. Xiong and Z. Wu, "A variational Geometric Constraints Network for a Tolerance Types Specification," *International Journal of Advanced Manufacture Technology*, Vol. 24, No. 3-4, 2004, pp. 214-222.
- [7] U. Roy and B. Li, "Representation and Interpretation of Geometric Tolerances for Polyhedral Objects," *Computer Aided Design*, Vol. 31, No. 4, 1999, pp. 273-285.
- [8] J. Y. Dantan, J. Bruyere, J. P. Vincent and R. Bigot, "Vectorial Tolerance Allocation of Bevel Gear by Discrete Optimization," *Mechanism and Machine Theory*, Vol. 43, No. 11, 2008, pp. 1478-1494.
- [9] E. Ballot and P. Bourdet, "A Computation Method for the Consequences of Geometric Errors in Mechanisms," *Proceedings of CIRP Seminar on Computer Aided Tolerancing*, Toronto, Canada, April 1997, pp. 197-207.
- [10] M. Giordano, S. Samper and J. P. Petit, "Tolerance Analysis and Synthesis by Means of Deviation Domains, Axis-Symmetric Cases" of the 9th CIRP International Seminar on Computer Aided Tolerancing, Tempe (US), April, 2005, pp. 85-94.
- [11] A. Mujezinovic, J. K. Davidson and J. J. Shah, "A New Mathematical Model for Geometric Tolerances as Applied to Polygonal Faces," *Transaction of the ASME, Journal of Mechanical Design*, Vol. 126, No. 4, 2004, pp. 504-518.
- [12] J. P. Petit, S. Samper and M. Giordano, "Minimum Clearance for Tolerance Analysis of a Vacuum Pump," *Proceedings of the 8th CIRP seminar on computer aided design*, Charlotte (US), 2003, pp. 43-51.
- [13] S. Bhide, G. Ameta, J. K. Davidson and J. J. Shah, "Tolerance-Maps Applied to the Straightness and Orientation of an Axis" of the 9th CIRP International Seminar on Computer Aided Tolerancing, Tempe (US), April 2005, pp. 45-54.
- [14] Z. Zou and E. P. Morse, "A Gap-Based Approach to Capture Fitting Conditions for Mechanical Assembly," *Computer Aided Design*, Vol. 36, No. 8, 2004, pp. 691-700.
- [15] J. Y. Dantan, L. Mathieu, A. Ballu and P. Martin, "Tolerance Synthesis: Quantifier Notion and Virtual Boundary," *Computer Aided Design*, Vol. 37, No. 2, 2005, pp. 231-240.

- [16] S. Tichadou, O. Legoff and J. Y. Hascoet, "Quantification of Machining and Fixture Errors: 3d Method and Analysis of Planar Mechanical Systems," *Computer Aided Design*, Vol. 35, No. 10, 2003, pp. 901-911.
- [17] E. Sacks and L. Joskowicz, "Parametric Kinematic Tolerance Analysis of Planar Mechanisms," *Journal of Computer Aided Design*, Vol. 29, No. 5, 1997, pp. 333-342.
- [18] M. Kyung and E. Sacks, "Nonlinear Kinematic Tolerance Analysis of Planar Mechanical Systems," *Computer Aided Design*, Vol. 35, No.10, 2003, pp. 901-911.
- [19] M. Pillet, "Inertial Tolerancing," *The Total Quality Magazine*, Vol. 16, No. 3, 2004, pp. 202-209.
- [20] R. Pauliac and A. Bellacicco, "Cours chaîne de cotes Process Angulaire," Lycée Dorian Paris, 2007.

# Geometric Inversion of Two-Dimensional Stokes Flows – Application to the Flow between Parallel Planes

Mustapha Hellou

Université Européenne de Bretagne, France  
INSA, LGCGM, EA3913, F-35708 RENNES

E-mail: [mustapha.hellou@insa-rennes.fr](mailto:mustapha.hellou@insa-rennes.fr)

Received May 17, 2010; revised July 21, 2010; accepted September 25, 2010

## Abstract

Geometric inversion is applied to two-dimensional Stokes flow in view to find new Stokes flow solutions. The principle of this method and the relations between the reference and inverse fluid velocity fields are presented. They are followed by applications to the flow between two parallel plates induced by a rotating or a translating cylinder. Thus hydrodynamic characteristics of flow around circular bodies obtained by inversion of the plates are thus deduced. Typically fluid flow patterns around two circular cylinders in contact placed in the centre of a rotating or a translating circular cylinder are illustrated.

**Keywords:** Inversion Transformation, Geometric Inversion, Stokes Flow, Viscous Eddies, Flow around a Cylinder, Microflow

## 1. Introduction

Geometric inversion is a type of transformation of the Euclidean plane. This transformation preserves angles and map generalized circles into generalized circles, where a generalized circle means either a circle or a line (a circle with infinite radius). One of the main properties of this method is the transformation of a straight line to a circle. Many difficult problems in geometry become much more tractable when an inversion is applied.

In engineering, the geometric inversion could be very useful to solve complex problems. For example, in fluid mechanics, the equation of two-dimensional Stokes flow remains valid in the new coordinates system obtained by inversion. Thus two-dimensional Stokes flow around certain bodies presenting circular shape appears less difficult to calculate by inversion of flow in channels of parallel walls than by direct calculation using polar coordinates. Although this method is rather general, we will apply it to the case of cellular flows (recirculation flow) presenting viscous eddies. In fact these flows are characterized by the presence of dividing streamlines (separating streamlines) which also give by inversion in the new geometry dividing streamlines.

Much attention has been paid to the steady viscous flow between parallel plates at low Reynolds number (Stokes flow) because of its theoretical importance and

also its engineering applications. The particular case of the flow with vanishing velocity to zero when  $\vec{x} \rightarrow \infty$  (i.e. flow with mean rate equal zero) has been widely studied by authors motivated among others by separation phenomena. Thus, after the pioneering work of [1] who presented predictions of cellular motion in Stokes regime between parallel walls, theoretical works like those of [2] and [3] demonstrate the existence of such cellular flow. The corresponding authors showed that, independently of the motion source, any two-dimensional flow with mean rate null in a channel presented necessarily cellular motion composed by successive counter rotating eddies bounded by separating streamlines reattaching the walls. In order to examine the influence of the motion source, accurate computations for various motion sources have been performed [4-16]. Stokes flows and particularly cellular flows could be encountered in numerous applications in physics, biophysics, chemistry and MEMS (Micro and ElectroMechanical Systems) where microflows appear. The particularity of these applications is that they use microchannels [17-19]. Thus, several theoretical and numerical results are available. They could be useful to obtain by inversion transformation the structure and the features of Stokes flows around bodies of circular shape. This transformation is also useful to obtain flow around bodies with complex shape for which the direct calculation could be tiresome.

## 2. Geometric Inversion-Definitions and Properties

Inversion is the process of transforming points  $M$  to a corresponding set of points  $N$  known as their inverse points. Two points  $M$  and  $N$  drawn in **Figure 1** are said to be inverses with respect to an inversion circle having inversion centre  $O$  and inversion radius  $R_0$  if  $N$  is the perpendicular foot of the altitude of the triangle  $OQM$ , where  $Q$  is a point on the circle such that  $OQ \perp QM$ .

If  $M$  and  $N$  are inverse points, then the line  $L$  through  $M$  and perpendicular to  $OM$  is called a “polar” with respect to point  $N$ , known as the “inversion pole”. In addition, the curve to which a given curve is transformed under inversion is called its inverse curve (or more simply, its “inverse”).

From similar triangles, it immediately follows that the inverse points  $M$  and  $N$  obey to:

$$\frac{OM}{R_0} = \frac{R_0}{ON} \quad \text{or} \quad R_0^2 = OM \times ON \quad (1)$$

where the quantity  $R_0^2$  is known as the circle power or inversion power [20].

The general equation for the inverse of the point  $M(x, y)$  relative to the inversion circle with inversion centre  $O(x_0, y_0)$  and inversion radius  $R_0$  is given by

$$\begin{aligned} x' &= x_0 + \frac{R_0^2(x - x_0)}{(x - x_0)^2 + (y - y_0)^2}, \\ y' &= y_0 + \frac{R_0^2(y - y_0)}{(x - x_0)^2 + (y - y_0)^2} \end{aligned} \quad (2)$$

Note that a point on the circumference of the inversion circle is its own inverse point. In addition, any angle inverts to an opposite angle.

Treating lines as circles of infinite radius, all circles invert to circles. Furthermore, any two nonintersecting circles can be inverted into concentric circles by taking the inversion centre at one of the two so-called limiting points of the two circles [20], and any two circles can be inverted into themselves or into two equal circles. Or-

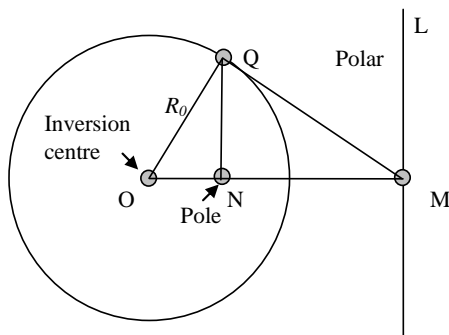


Figure 1. Geometric inversion – definition.

thogonal circles invert to orthogonal circles. The inversion circle itself, circles orthogonal to it, and lines through the inversion centre are invariant under inversion. Furthermore, inversion is a conformal map, so angles are preserved. Note that a point on the circumference of the inversion circle is its own inverse point. In addition, any angle inverts to an opposite angle.

The property that inversion transforms circles and lines to circles or lines (and that inversion is conformal) makes it an extremely important tool of plane analytic geometry. **Figure 2** shows a simple example of application of geometric inversion.

The circle with dashed lines is the inversion circle of centre  $O$  and radius  $R_0$ . Let take for example  $R_0 = 1$ , the distance  $OM = 2$  and the distance  $OP = 0.5$ . Let's make inversion of the straight lines  $L$  and  $L'$  with centre  $O$  and power  $R_0^2$ , we obtain the circles  $C$  and  $C'$ . The points  $N$  and  $Q$  are respectively the inverse images of the points  $M$  and  $P$ . The distances  $ON$  and  $OQ$ , calculated by using Equation (1), are  $ON = 0.5$  and  $OQ = 2$ . Thus the radii of the circles  $C$  and  $C'$  are respectively  $R = 0.25$  and  $R' = 1$ .

In **Figure 3** we present the classical example of inversion of a square relatively to a circle inscribed in this square. This inversion image becomes more complex if the number of squares is increased (see Mathematica Notebook presenting inversion of a grid).

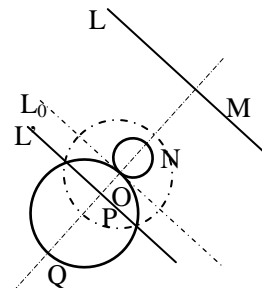


Figure 2. Inversion of two parallel straight lines.

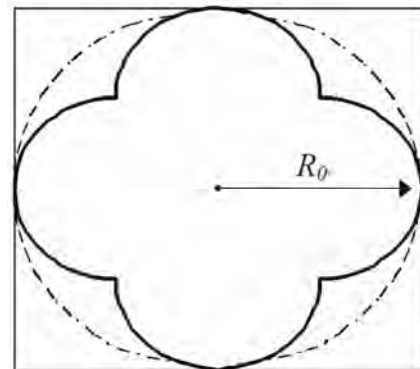


Figure 3. Inversion of a square. The inversion centre coincides with the square centre.

**Figure 4** illustrates the inversion of parabola. This transformation leads to a cardioid defined in **Figure 4(c)**. It's worth to note that the change of the inversion centre leads to other figures of inversion.

### 3. Inversion Transformation of Stokes Flow

Let  $\psi(z)$  be the stream function of a plane Stokes flow denoted  $F_0$  where  $z = r \exp(i\theta)$ . This flow is governed by the biharmonic equation:

$$\Delta\Delta\psi = 0 \quad (3)$$

The function  $\psi(z)$  is necessarily expressed by:

$$\psi(z) = z\bar{\phi}(z) + \bar{z}\phi(z) + X(z) + \bar{X}(\bar{z}) \quad (4)$$

(see[21]). Introducing the complex variable  $Z = \frac{a^2}{z}$ , it

follows that the function  $\varphi(Z) = \frac{Z\bar{Z}}{a^2}\psi(z)$  can be written

in a form similar to Equation (3). Consequently  $\varphi(Z)$  is likewise biharmonic and represents therefore the stream function of an other Stokes flow denoted thereafter  $F_I$ .

Let  $M(r, \theta)$  be a point of  $F_0$  and  $N(\rho, \theta)$  its homologous in the flow field  $F_I$  obtained by the positive inversion transformation of power  $a$  and centre  $O$  defined by Equation (1). It follows:

$$r\rho = a^2 \quad (5)$$

And it's easy to show that :

$$\varphi(N) = \frac{\rho^2}{a^2}\psi(M) \quad (6)$$

The velocity components in polar coordinates framework of centre  $O$  on the homologous points are readily found to be:

$$V_\rho(N) = V_r(M) ; \quad V_\theta(N) = -V_\theta(M) - \frac{2\psi(M)}{r} \quad (7)$$

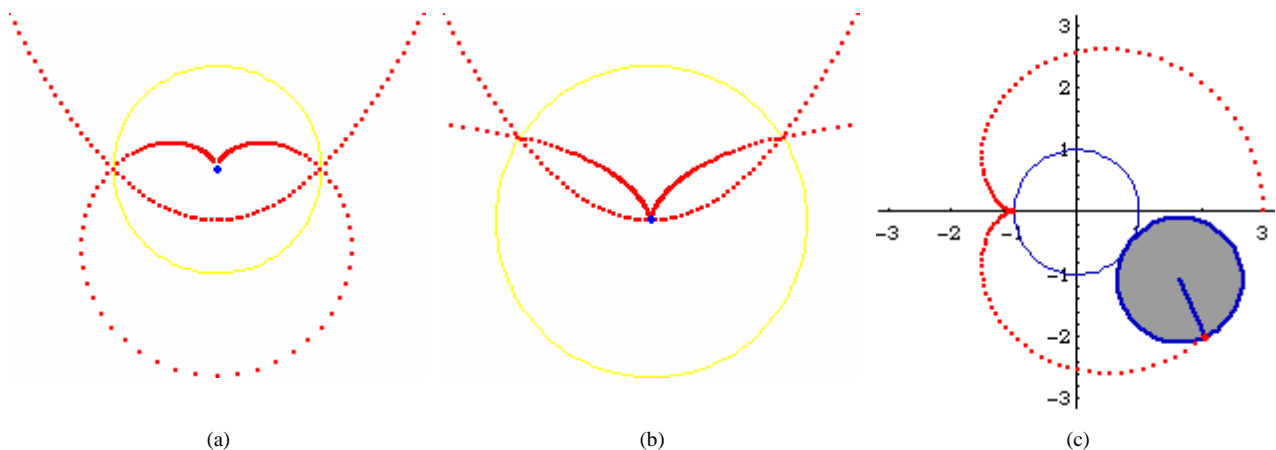
Hereafter, flow on which we apply the inversion method (Flow  $F_0$ ) is called reference flow. Now let  $F_0$  be a reference flow around a fixed body  $C_0$  and  $F_I$  is the equivalent flow in the proximity of the inverse fixed body  $C_I$ . Assuming that the body  $C_I$  is at rest, by virtue of Equation (7), the non slip conditions on  $C_I$  are satisfied only for  $\psi = 0$  on  $C_0$ . However, we can add a constant which yields  $\psi = 0$  on this body without modifying  $F_0$ . In this condition, an additional velocity is therefore added to  $F_I$  in order to ensure the non slip conditions on  $C_I$ . Hence, the knowledge of the stream function field of  $F_0$  permits to determine the features of  $F_I$ . Nevertheless, the inversion of a streamline of  $F_0$  does not give a streamline of  $F_I$  unless this streamline is a circle or of value  $\psi = 0$ . Thus in order to draw the streamlines, it would be necessary to calculate the stream function field of  $F_I$  by using Equation (6) and one can deduce straightforward the desired streamlines of  $F_I$ . It is worth noting that the relations of equivalence between  $F_0$  and  $F_I$  for the other physical quantities (velocity, pressure, vorticity,...) can be determined without any particular problem.

### 4. Characteristics of the Cellular Flow between Parallel Plane Walls

The stream function of two dimensional Stokes flow with zero mean rate between parallel walls of a long rectangular channel has been found by [3], [5], [7] and [8] to be:

$$\psi(x, y) = \sum_n C_n e^{-\alpha_n x} G_n(y) \quad (8)$$

where the functions  $G_n(y)$  have the following expressions according to the flow is antisymmetric



**Figure 4. Inversion of a parabola (1996 © 2010 by Xah Lee).** (a) inversion centre coincides with the focus of the parabola; (b) inversion centre coincides with the cusp of the parabola; (c) Cardioid can be defined as the trace of a point on a circle that rolls around a fixed circle of the same size without slipping.



$\psi(x, y) = \psi(x, -y)$  (Equation (9)), respectively symmetric  $\psi(x, y) = -\psi(x, -y)$  (Equation (10)):

$$G_n(y) = y_0 \sin \alpha_n y_0 \cos \alpha_n y - y \cos \alpha_n y_0 \sin \alpha_n y \quad (9)$$

$$G_n(y) = y \sin \alpha_n y_0 \cos \alpha_n y - y_0 \cos \alpha_n y_0 \sin \alpha_n y \quad (10)$$

The linear combination of these basic flows can compose the stream function of a more general flow. The coefficients  $C_n$  are arbitrary complex coefficients to be determined by the boundary conditions and  $2y_0$  represents the width of the channel. The parameters  $\alpha_n = \lambda_n + i\mu_n$  are the complex roots of the following equations coming from the non slip conditions on the channel walls.

$$\sin 2\alpha y_0 = -2\alpha y_0 \quad (\text{antisymmetric flow}) \quad (11)$$

$$\sin 2\alpha y_0 = +2\alpha y_0 \quad (\text{symmetric flow}) \quad (12)$$

The real coefficients  $\lambda_n$  and  $\mu_n$  have been accurately computed by Bourot & Moreau [5]; their sign is chosen here such as  $\psi \rightarrow 0$  for  $x \rightarrow \infty$ .

Each term of the stream function of Equation (8) denoted  $\psi_n$  is null infinitely many times as  $x \rightarrow \infty$  whatever the motion source may be. There is an infinity of dividing streamlines of value  $\psi_n = 0$  which attach the parallel walls where the stream function is likewise zero and divide thus the flow on successive eddies. The equation of these dividing streamlines is given by:

$$\tan \mu_n x = \frac{P_n(y)}{Q_n(y)} \quad (13)$$

where  $P_n(y)$  and  $Q_n(y)$  represent the real and imaginary parts of  $G_n(y)$ .

The Equation (13) means that the location of the dividing streamlines is periodic in the longitudinal direction. Hence, the axial length of each class  $n$  of eddies is constant and readily given by:

$$L_n = \frac{\pi}{|\mu_n|} \quad (14)$$

Furthermore, angle at which the separating streamlines detach from the walls, *i.e.* the separation angle (angle T indicated in **Figure 5**), satisfies the equation:

$$\tan \alpha_n = -\frac{3}{\tan 2\lambda_n} \quad (15)$$

For  $n = 1$ , the separation angle is  $58^\circ 61'$  for an antisymmetric structure and  $46^\circ 25'$  for a symmetric one.

The ratio of the velocity on homologous points, *i.e.* points as  $S(x, y)$  and  $S'(x+L_n, y)$  (for example points S and S' indicated in **Figure 5**), is given by:

$$K_n = \exp \frac{\pi |\lambda_n|}{|\mu_n|} \quad (16)$$

For the same value of  $n$ , the velocity of the symmetric flow decays more than the velocity of the antisymmetric one. Thus, practically an arbitrary Stokes flow of zero mean rate between parallel plates becomes antisymmetric far from the motion source except when this source is strictly symmetric. Of course, numerical calculation of this arbitrary flow in the proximity of the motion source requires to conserve a sufficient number of terms  $\psi_n$  of the stream function,  $n = 20$  or more ([5], [7] and [8]).

**Figure 5** shows the streamlines of the theoretical flow corresponding to  $n = 1$  for antisymmetric and symmetric conditions between parallel plates. The sequences of the dividing streamlines drawn in **Figure 5** are located arbitrary since the motion source is not yet considered.

The stream function of the separating streamlines is zero hence they can be directly transformed. Thus associating to a point  $M(r, \theta)$  of a separating streamline of

$F_0$  a point  $N(\frac{a^2}{r}, \theta)$ , we obtain a point of the corre-

sponding separating streamline of the new flow  $F_1$ . Consequently, the infinite cellular flow between parallel plates leads by inversion transformation to a finite cellular flow within the corners between the transformed bodies which the shape depends closely on the position of the inversion centre.

## 5. Applications

Antisymmetric and symmetric Stokes flows between parallel walls can be concretely realized by the uniform rotation respectively the uniform longitudinal translation of a cylinder midway between the parallel walls of a long rectangular channel filled with a viscous oil. The boundary conditions are the non slip conditions on the cylinder boundary and the matching conditions at  $x = 0$  between the two semi-infinite domains. Precisely, these conditions are written as following:

*Antisymmetric flow induced by a rotating cylinder*

$$u(x_{C_0}, y_{C_0}) = -V_0 \sin \theta, \quad v(x_{C_0}, y_{C_0}) = V_0 \cos \theta \quad \text{with}$$

$$x_{C_0}^2 + y_{C_0}^2 = R_0^2, \quad 0 \leq \theta \leq \frac{\pi}{2},$$

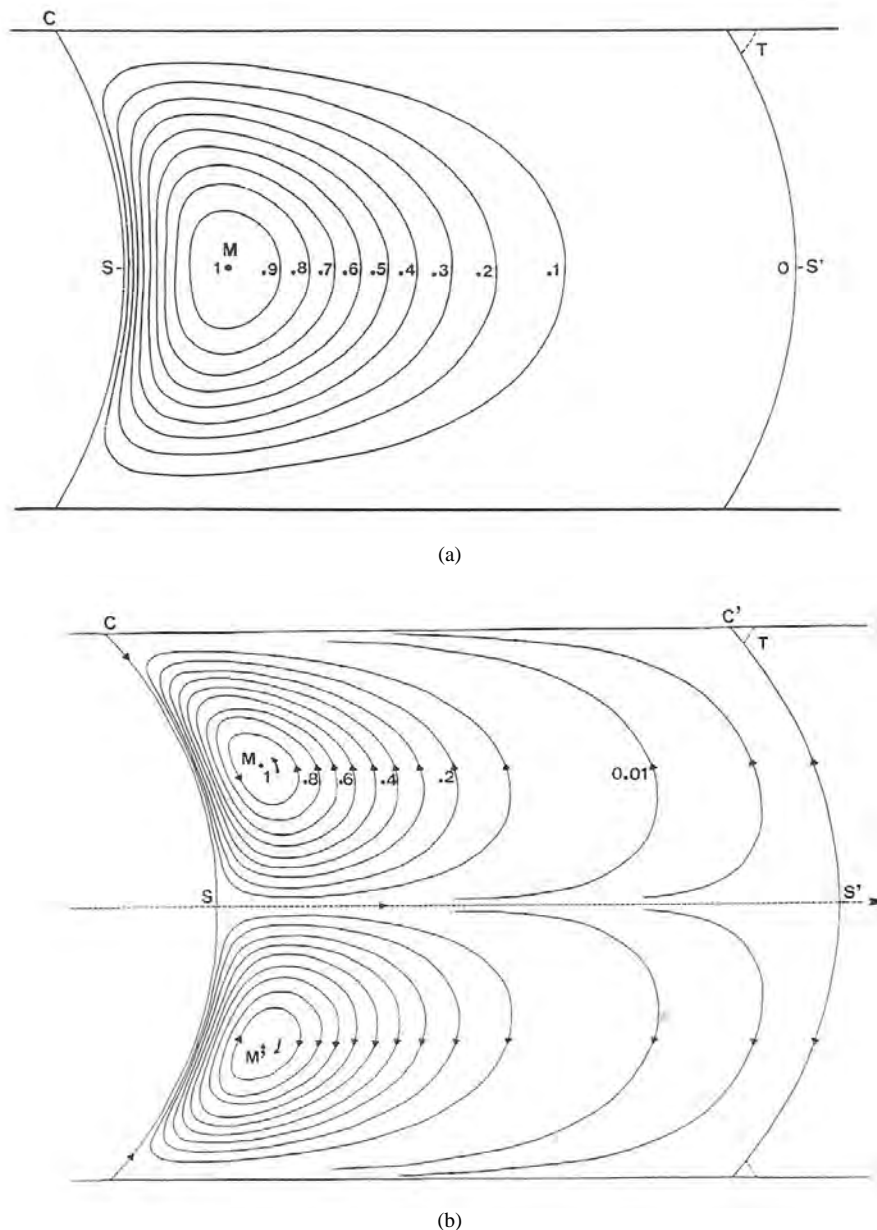
$$v(0, y) = 0, \quad R_0 < y < y_0,$$

$$p(0, y) = 0, \quad R_0 \leq y \leq y_0 \quad (17)$$

where  $R_0$  represents the cylinder radius,  $V_0$  the cylinder velocity,  $u, v$  the Cartesian components of the velocity and  $p$  the pressure (see **Figure 6** for the notations).

*Symmetric flow induced by a translating cylinder along the channel axis*

$$u(x_{C_0}, y_{C_0}) = V_0, \quad v(x_{C_0}, y_{C_0}) = 0, \quad 0 \leq \theta \leq \frac{\pi}{2}$$



**Figure 5. Theoretical flow between parallel walls [3]; (a) antisymmetric flow between parallel walls; (b) symmetric flow between parallel walls.**

$$v(0, y) = 0, \quad R_0 < y < y_0,$$

$$\frac{\partial p(0, y)}{\partial y} = 0, \quad R_0 \leq y \leq y_0 \quad (18)$$

These flows, produced by rotating or translating cylinder, have been previously computed and examined by [22] and [8].

Now let apply the positive inversion to the domain bounded by parallel infinite walls. The centre of the cylinder is chosen as the inversion centre. The choice of the

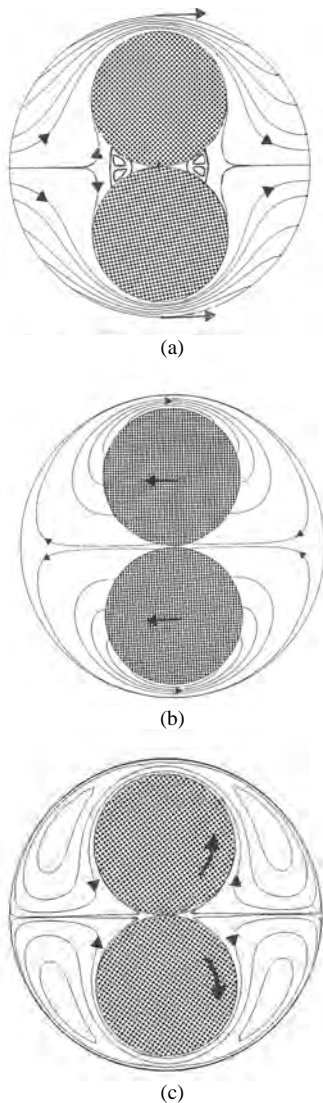
power  $a$  is not important. This parameter modify only the scale of the inverse field; let take  $a = y_0$  here. The transformation of the lines  $b_0$  and  $d_0$  representing the parallel walls leads to the tangent circles  $b_1$  and  $d_1$  (**Figure 6**). The rotating circle  $C_0$  of radius  $R_0$  gives a circle  $C_1$  of

radius  $R_1 = \frac{y_0^2}{R_0}$  which rotates with the velocity

$$V_1 = -V_0 - \frac{2\psi_0}{R_0} \quad \text{where } \psi_0 \text{ is the stream function on } C_0.$$



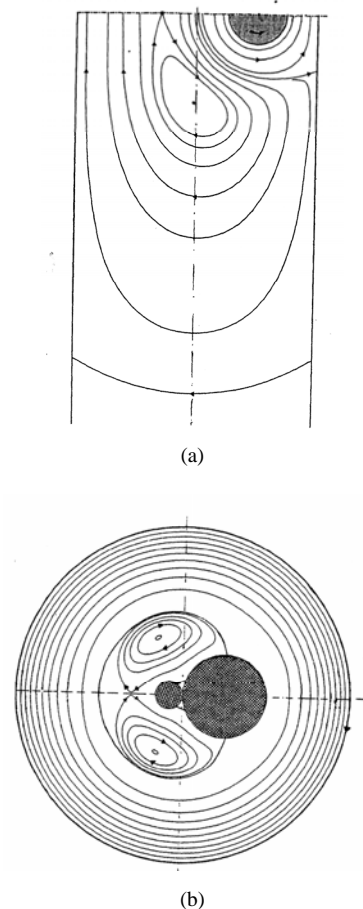
In the case of the translating cylinder, two configurations seem to be possible depending on whether the framework is absolute or relative. The inversion of the stream visualized by an observer attached to the absolute framework gives an instantaneous image of the flow around two cylinders in contact placed in the centre of the fluid domain bounded by a cylinder translating in the direction parallel to the contact plane, **Figure 8(a)**. We see a symmetric cellular flow with an extent relatively small



**Figure 8.** Streamlines around two cylinders in contact of radius  $R_1$  centred inside an outer cylinder of radius  $R_1$  ( $\frac{R_1}{R_1} = 2.22$ ). The point of contact is located at the enclosure centre; (a) Two cylinders in contact fixed in a translating one; (b) Two cylinders in contact translating in the direction of the contact plane inside a fixed cylinder enclosure; (c) Two cylinders in contact rotating inside a fixed cylinder enclosure.

compared to the antisymmetric one. Note that adding the constant  $-V_0 \bar{x}$ , leads to the more practical problem of two cylinders in contact translating in a fixed cylindrical enclosure whose the streamlines are presented in **Figure 8(b)**. The relative reference flow regarded by an observer attached to the translating cylinder centre is equivalent to the flow around a fixed cylinder induced by translation of the walls. The inversion of this flow leads to the flow produced by two counter rotating cylinders in a fixed cylindrical enclosure, **Figure 8(c)**. There is no separating streamlines because the corresponding reference stream is not of zero mean rate.

**Figure 9(a)** present an example of a flow obtained by a rotating cylinder decentred from the axis of a channel of parallel plates with the distance  $\delta$ . If the inversion centre coincides with the cylinder centre, the inversion of the parallel walls leads to two cylinders in contact of different radius. The inversion of the flow leads to the flow drawn in **Figure 9(b)**.



**Figure 9.** Inversion of the fluid flow between parallel walls due to a rotating cylinder of radius  $R_1 = 0.25y_0$  decentred with the quantity  $\delta = 0.5y_0$ . Inversion of this flow; (a) Original flow; (b) Inversion of this flow.

## 6. Conclusions

For a two dimensional Stokes field corresponds theoretically by inversion an infinity of Stokes flows because the inversion centre can be any point of the  $(O, \bar{x}, \bar{y})$  plane. For example, in the case of the flow between parallel plates, choosing this centre position on the  $\bar{y}$  axis normal to the parallel plates, provide solutions to flows around two unequal cylinders in contact internally or externally or around a cylinder in contact with a plane. Nevertheless, this centre would be suitably chosen otherwise the motion source obtained by inversion can be out of physical sense. For example, the inversion of the flow relatively to a point which is not the centre of a rotating cylinder leads to a flow across the inverse cylinder. Thus, useful configurations seem to be obtained essentially when the inversion centre coincides with the cylinder centre. From a general point of view, the inversion transformation is an interesting method which can be wide with various problems even apart from the fluid mechanics (electricity, chemistry, engineering processes, ...) but a precaution in the choice of the position of the centre of inversion is necessary.

## 7. References

- [1] H. K. Moffatt, "Viscous and Resistive Eddies near a Sharp Corner," *Journal of Fluid Mechanics*, Vol. 18, No. 1, 1964, pp. 1-18.
- [2] M. E. O' Neill, "On Angles of Separation in Stokes Flow," *Journal of Fluid Mechanics*, No. 133, 1983, pp. 427-442.
- [3] J. M. Bourot, "Sur la structure cellulaire des écoulements plans de Stokes, à débit moyen nul, en canal indéfini à parois parallèles," *Comptes rendus de l'Académie des sciences*, Vol. 298, Serie II, 1984, pp. 161-164.
- [4] C. Shen and J. M. Floryan, "Low Reynolds Number Flow over Cavities," *Physics of Fluids*, Vol. 28, No. 11, 1985, pp. 3191-3202.
- [5] J. M. Bourot and F. Moreau, "Sur l'utilisation de la série cellulaire pour le calcul d'écoulements plans de Stokes en canal indéfini: Application au cas d'un cylindre circulaire en translation," *Mechanics Research Communications*, Vol. 14, No. 3, 1987, pp. 187-197.
- [6] P. Carbonaro and E. B. Hansen, "Transient Stokes Flow in a Channel Driven by Moving Sleeves," *ASME Journal of Applied Mechanics*, Vol. 57, No. 4, 1990, pp. 1061-1065.
- [7] M. Hellou and M. Coutanceau, "Cellular Stokes Flow Induced by Rotation of a Cylinder in a Closed Channel," *Journal of Fluid Mechanics*, No. 236, 1992, pp. 557-577.
- [8] F. Moreau and J. M. Bourot, "Écoulements cellulaires de Stokes produits en canal plan illimité par la rotation de deux cylindres," *Journal of Applied Mathematics and Physics*, Vol. 44, No. 5, 1993, pp. 777-798.
- [9] P. N. Shankar and M. D. Deshpande, "Fluid Mechanics in the Driven Cavity," *Annual Review of Fluid Mechanics*, No. 32, 2000, pp. 93-136.
- [10] J. T. Jeong, "Slow Viscous Flow in a Partitioned Channel," *Physics of Fluids*, Vol. 13, No. 6, 2001, pp. 1577-1582.
- [11] M. Hellou, "Structures d'écoulements de Stokes dans une jonction bidimensionnelle de canaux," *Mécanique & Industries*, Vol. 4, No. 5, 2003, pp. 575-583.
- [12] C. Y. Wang, "Slow Viscous Flow between Hexagonal Cylinders," *Transport in Porous Media*, Vol. 47, No. 1, 2002, pp. 67-80.
- [13] C. Y. Wang, "The Recirculating Flow due to a Moving Lid on a Cavity Containing a Darcy-Brinkman Medium," *Applied Mathematical Modelling*, Vol. 33, No. 4, 2009, pp. 2054-2061.
- [14] A. H. Abd El Naby and M. F. Abd El Hakeem, "The Flow Separation through Peristaltic Motion of Power-Law Fluid in Uniform Tube," *Applied Mathematics Sciences*, Vol. 1, No. 26, 2007, pp. 1249-1263.
- [15] D. van der Woude, H. J. H. Clercx, G. J. F. van Heijst and V. V. Meleshko, "Stokes Flow in a Rectangular Cavity by Rotlet Forcing," *Physics of Fluids*, Vol. 19, No. 8, 2007, pp. 083602-083602-19.
- [16] M. Zabarankin, "Asymetric Three-dimensional Stokes Flows about Two Fused Equal Spheres," *Proceedings of the Royal Society A: Mathematical, Physical and Engineering Sciences*, Vol. 463, No. 2085, 2007, pp. 2329-2350.
- [17] J. P. Brody, P. Yager, R. E. Goldstein and R. H. Austin, "Biotechnology at Low Reynolds Numbers," *Biophysical Journal*, Vol. 71, No. 6, 1996, pp. 3430-3441.
- [18] J. Yeom, D. D. Agonafer, J.-H. Han and M. A. Shannon, "Low Reynolds Number Flow across an Array of Cylindrical Microposts in a Microchannel and Figure-Of-Merit Analysis of Micropost-Filled Microreactors," *Journal of Micromechanics Microengineering*, Vol. 19, No. 6, 2009.
- [19] C. Y. Wang, "Flow through a Finned Channel Filled with a Porous Medium," *Chemical Engineering Science*, Vol. 65, No. 5, 2010, pp. 1826-1831.
- [20] H. S. M. Coxeter, "Introduction to Geometry," 2nd edition, Wiley, New York, 1969, pp. 77-83.
- [21] M. A. Laurentiev and B. V. Chabat, "Les méthodes de la théorie des fonctions de la variable complexe," traduit du russe par Damadian H., Ed., Mir 1972, 1977.
- [22] R. Bouard and M. Coutanceau, "Étude théorique et expérimentale de l'écoulement engendré par un cylindre en translation uniforme dans un fluide visqueux en régime de Stokes," *Journal of Applied Mathematics and Physics*, Vol. 37, No. 5, 1986, pp. 673-684.

# Surface Roughness Evaluation in Dry-Cutting of Magnesium Alloy by Air Pressure Coolant

Jeong-Du Kim<sup>1\*</sup>, Keon-Beom Lee<sup>2</sup>

<sup>1</sup>Department of mechanical Engineering, Sejong University, Seoul, South Korea

<sup>2</sup>Department of mechanical Engineering, Korea Polytechnic College IV, Daejeon, South Korea

E-mail: [jdkim@sejong.ac.kr](mailto:jdkim@sejong.ac.kr)

Received July 12, 2010; revised September 1, 2010; accepted September 19, 2010

## Abstract

In this paper, a studying of surface roughness in dry milling with air pressure coolant of wrought magnesium alloy AZ31B will be carried out. The effects of air flow, feed-rate per tooth, cutting velocity and number of inserts in a cutting tool on surface roughness have been examined. Surface roughness increases with increasing feed-rate per tooth and increasing number of inserts in the cutting tool. However, it is nearly unchanged under a specific range of cutting velocity in the experiment and improved by the flow of air cooling.

**Keywords:** Machinability, Surface Roughness, Number of Inserts, Dry Milling, Air Pressure Coolant

## 1. Introduction

Magnesium alloy is one of the lightest materials and is attractive in many applications such as aircraft engines, airframes, helicopter components, cars, light trucks, automotive parts, computers and so much more [1]. Following the recent trend in using magnesium material, B. L. Mordike and T. Ebert show that many researches in magnesium alloy have been made, [2] and obviously include the machining process.

In 1997, H. K. Tönshoff and J. Winkler researched the interactions between work-piece material AZ91HP, tool material and coating [3].

In 2005, F. Z. Fang, L. C. Lee and X. D. Liu measured the mean flank temperature in dry milling magnesium alloy AZ91 [4]. They recognize that when the maximum temperature is 302°C, it occurs at cutting speed 816 m/min and under-formed chip thickness 9 µm.

Wrought magnesium alloy has good behavior during crashes and is utilized in parts with high safety concerns. When machining magnesium alloy with a water-base coolant, water will react with magnesium to create hydrogen. It is very dangerous because hydrogen is flammable and potentially explosive [5,6]. In addition, coolants and lubricants represent 16-20% of manufacturing costs, which should be diminished [7]. Cutting fluids are also harmful for the environment and costs for waste disposal, so air pressure coolant has been chosen to investigate.

In this paper, I will study the surface roughness in high-speed end milling of wrought magnesium alloy AZ31B with carbide inserts under effects of air coolant and number of cutting tool inserts.

## 2. Effects of the Number of Inserts

In this case, cutting edge is straight. The length of cutting edge, the number of inserts in the cutting tool and the feed-rate per revolution affect surface roughness profile.

$$\text{We consider } f' = n_t \cdot f_t \quad (1)$$

$$f' = \frac{f}{n} \quad (2)$$

In the multipoint cutting tool, we use more than one insert. **Figure 1** shows the effects of insert run-out errors on the surface roughness profile. Whenever the feed-rate per revolution is smaller than length of the cutting edge, the lowest insert mainly forms the surface roughness profile. Using multiple inserts in face milling will generate axial and radial run-out errors. These errors will change the cutting force acting on the cutting tool and work-piece. These cutting forces in turn will generate more vibration and increase surface roughness.

Consider z-direction, the higher inserts will contact and cut the material, but the lowest insert will cut once again and negate the effects of higher inserts.

Cutting force in vertical direction  $F_T$  [8]

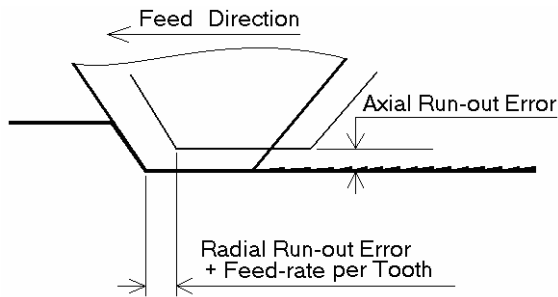


Figure 1. Effects of run-out errors on surface roughness profile.

$$F_T = \frac{k \cdot w \cdot \sin(\lambda - \alpha)}{\sin \phi \cos \theta} t \quad (3)$$

Where:

$$\theta = \phi + \lambda - \alpha \quad (4)$$

From Figure 2, we obtain chip ratio:

$$r = \frac{t}{t_c} = \frac{\sin \phi}{\cos(\phi - \alpha)} \quad (5)$$

where

Real under-formed chip thickness

$$t = f_i \sin \phi \quad (6)$$

Consider multi-point milling tool with six inserts as shown in Figure 3.

At the same cutting velocity and same feed-rate per tooth, changing the number of inserts in the cutting tool will change the contacting frequency between cutting tool and work-piece.

The contact angle will also affect cutting force profile. The contact angle:

$$\beta = 2 \cdot \arcsin\left(\frac{w_w}{r_i}\right) \quad (7)$$

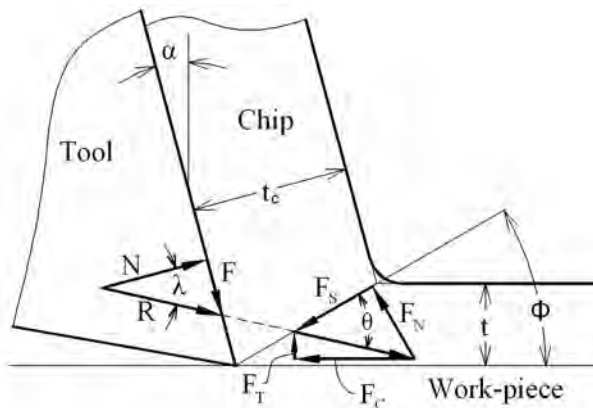


Figure 2. Orthogonal chip model.

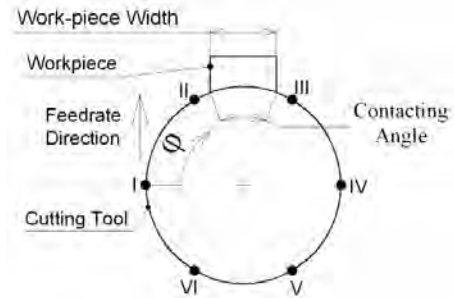


Figure 3. Contacting angle between cutting tool and work-piece.

The cutting force profile in the z-direction for one insert within half revolution is a thin curve in Figure 4. The cutting force will force the work-piece and cutting tool to vibrate at the same frequency to cutting force's frequency.

As shown in Figure 4, with only one insert in the cutting tool, if the contact angle is equal to 180°, the cutting force profile in z-direction will continue as a thin curve from 0° to 180°. When the contact angle is smaller than 180°, there is a suddenly a change at the entry and exit points as shown in this figure. This change will increase the vibrations of the system.

Increasing the number of inserts in the cutting tool will decrease angle between two consecutive sections. Therefore, vibration frequency will increase. This factor will increase the number of peaks and valleys on the surface roughness profile.

Increasing the feed-rate per tooth  $f_i$  will increase the value on the cutting forces; and so increase the amplitude of vibration. This factor will increase the distance between the peaks and valleys of the surface roughness profile. As we can see in Equations (3) and (5), the cutting force and feed-rate per tooth have linear dependence. However, the cutting energy required to remove a unit volume of magnesium alloy is small, increasing the feed-rate per tooth when machining magnesium alloy will increase small amount of cutting force compare with other materials.

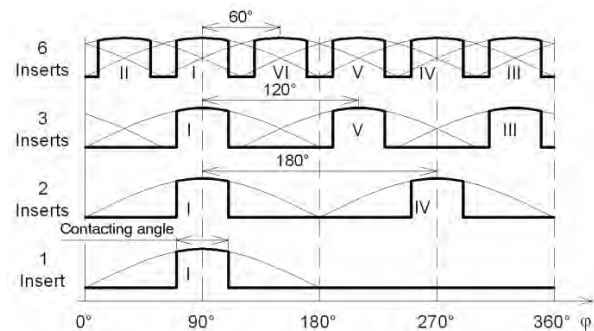


Figure 4. Cutting force in z-direction.



### 3. Experimental Conditions

This experiment uses a milling machine, HMV-F-1100N. The maximum spindle speed and feed-rate are respectively 1400 rpm and 720 mm/min. The cutting tool diameter is  $\Phi 100$  mm. The uncoated carbide inserts, TPKN 2204 (follow ISO standard), are supplied by Taegu-Tech manufacturing, South Korea.

Magnesium alloy AZ31B by Doowon Korea. The chemical composition is 3% aluminum, 1% zinc, 0.2% manganese, 0.1% copper, 0.01% ferrite. Density is  $1.77 \text{ g/cm}^3$ [9]. The work-piece dimension is 34 mm.

Air pressure is  $4.5 \text{ kg/cm}^2$ . Airflow at room temperature sprays directly to the machining zone as shown in **Figure 5**.

The experiment will check two cases: case 1 is dry milling, case 2 is air-coolant milling with incline angle  $45^\circ$ , distance from the nozzle to cutting point is  $d_a = 25 \pm 2$  mm. The nozzle diameter is 5.5 mm.

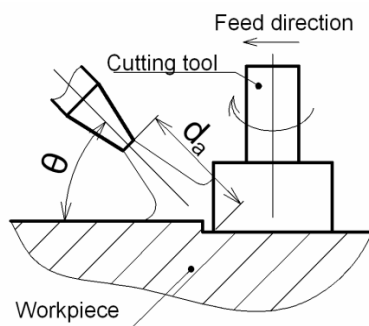
**Table 1** shows cutting parameters.

There are four cutting velocities, four feed-rates at a 0.2 mm depth of cut and only one insert the in cutting tool.

The cutting parameter is shown in **Table 2**. There are two cutting velocities, two feed-rates and four numbers of inserts in the cutting tool at depth of 0.2 mm.

The surface test equipment SJ-301 of Mitutoyo manufacturer has been used to check the surface roughness. The measurement process is performed at three positions and an average value will be calculated to represent for surface roughness.

Point micrometer and dial test indicator of Mitutoyo manufacturing are used to measure chip thickness, and a microscope is used to examine the chip shape.



**Figure 5.** Air coolant flow setting.

**Table 1.** First cutting parameters.

$V$	116; 163; 236; 311 m/min
$f_t$	0.04; 0.08; 0.17; 0.25 mm/tooth
$d$	0.2 mm

**Table 2.** Second cutting parameters.

$V$	116; 236 m/min
$f$	0.06; 0.12 mm/tooth
$d$	0.2 mm
Number of inserts ( $n_i$ )	1; 2; 3; 6

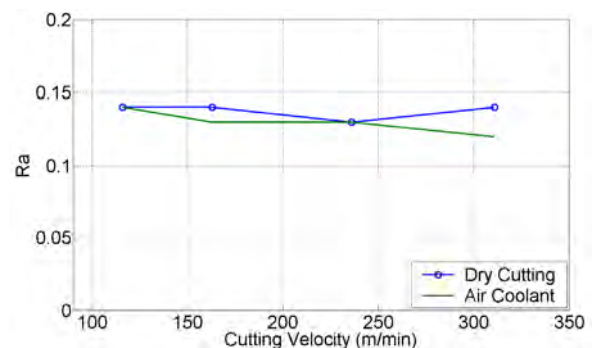
### 4. Results and Discussion

**Figure 6** is surface roughness at a feed-rate of  $f = 0.08$  mm/tooth. In dry cutting, the surface roughness is also nearly unchanged. Airflow has a small effect in improving the surface roughness.

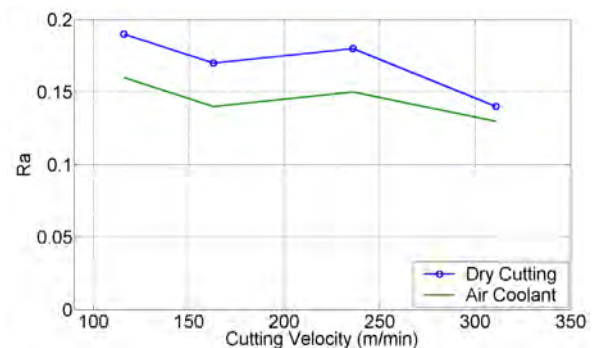
**Figure 7** shows that air coolant has a similar effect at various cutting velocities.

The air coolant cutting slightly improves the surface roughness. Magnesium alloy machining produces low cutting pressure, so the cutting energy and temperature are low. In addition, it also has a high thermal conductivity. This will dissipate heat rapidly. Because of this, the temperature difference between work-piece and airflow is small. This will reduce the cooling effect of air flow.

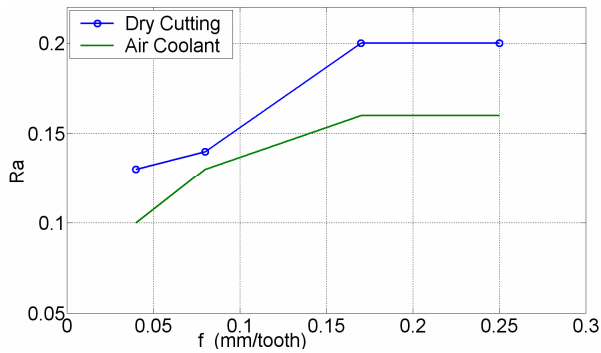
**Figure 8** shows the surface roughness under changing feed-rate per tooth at the same cutting velocity  $V = 116$  m/min.



**Figure 6.** Surface roughness at  $d = 0.2$  mm,  $f_t = 0.08$  mm/tooth. Air pressure:  $4.5 \text{ kg/cm}^2$ .



**Figure 7.** Surface roughness at  $d = 0.2$  mm and  $f_t = 0.17$  mm/tooth. Air pressure:  $4.5 \text{ kg/cm}^2$ .



**Figure 8.** Surface roughness at  $V = 116$  m/min and  $d = 0.2$  mm. Air pressure:  $4.5 \text{ kg/cm}^2$ .

From  $f = 0.04$  mm/tooth to  $0.17$  mm/tooth,  $Ra$  increases rapidly, but from  $f = 0.17/0.25$  mm/tooth, it is nearly unchanged. We use insert TPKN 2204. Insert corner is flat; this will leave feed marks by cutting tool work-piece vibrations.

Surface roughness also depends on the number of teeth in the cutting tool peripheral. **Figure 9** shows the surface roughness at a cutting speed of  $V = 116$  m/min, feed-rate  $f = 0.12$  mm/tooth and depth of cut  $d = 0.2$  mm.

Best result can achieve with one insert in the cutting tool. It gradually increases with two teeth and rapidly changes with three teeth. The value of  $Ra$  at six inserts is nearly four times larger than at one tooth.

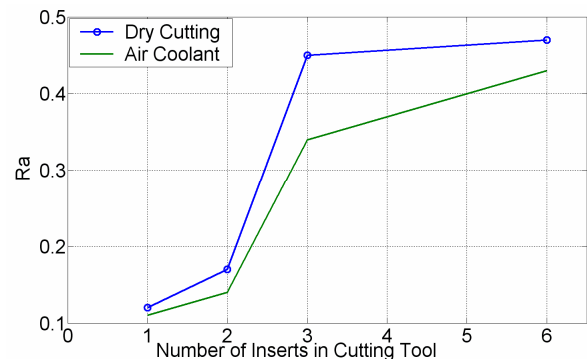
Fewer inserts in the cutting tool will increase chip clearance. This will make chips easier to move out, transfers cutting heat and decreases frictional heat. It also decreases scratches on the finish surface from the chips. Hence, we obtain a better surface.

In **Figure 10**, at three and six inserts, airflow has better effect than the others.

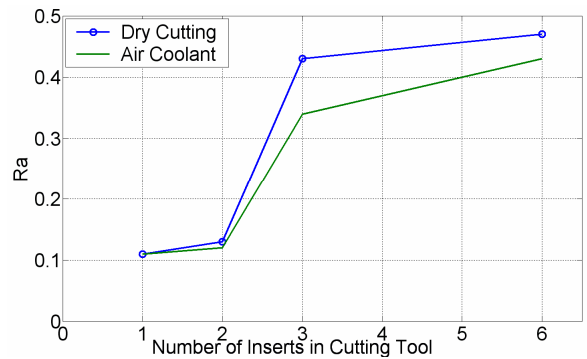
At a higher cutting speed and a smaller feed-rate, the air coolant has small effect because at a high cutting speed, a lower percent of cutting heat is transferred to the work-piece. Hence the cooling effect of airflow decreases.

In second experiment, a microscope is used to examine chip shape. **Figure 11** is chip shape at difference numbers of inserts in dry cutting at  $V = 116$  m/min,  $f = 0.06$  mm/tooth and  $d = 0.2$  mm. The side in contact with the cutting tool has a continuous edge. While the other side has a jagged edge or saw-tooth formation. At a larger number of inserts in cutting tool, the dimension of saw-tooth is smaller.

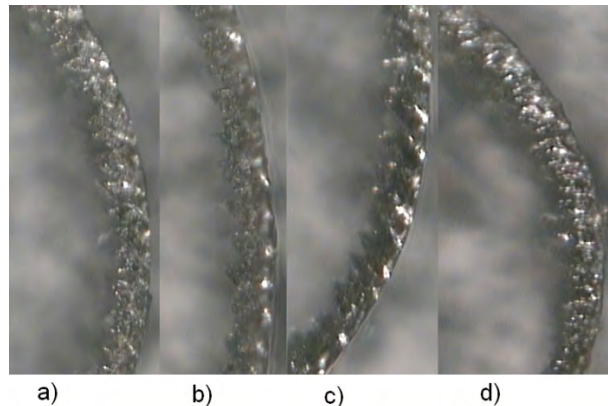
The shear angle is calculated by measuring chip thickness  $t_c$ , and its value is shown in **Figure 12**. With a larger number of inserts in the cutting tool, the shear angle decreases. Increasing the number of inserts will increase the cutting temperature, increasing the friction between tool and chip and decreasing the shear angle.



**Figure 9.** Surface roughness at  $V = 116$  m/min,  $f_t = 0.12$  mm/tooth and  $d = 0.2$  mm. Air pressure:  $4.5 \text{ kg/cm}^2$ .



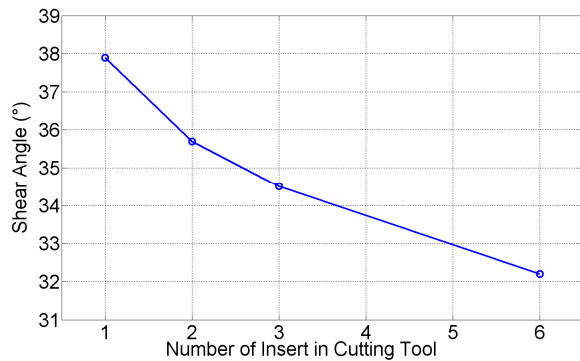
**Figure 10.** Surface roughness at  $V = 236$  m/min,  $f_t = 0.12$  mm/tooth and  $d = 0.2$  mm. Air pressure:  $4.5 \text{ kg/cm}^2$ .



**Figure 11.** Chip shape in dry cutting at  $V = 116$  m/min,  $f_t = 0.06$  mm/tooth and  $d = 0.2$  mm. (a) 1 insert (b) 2 inserts (c) 3 inserts (d) 6 inserts.

Changing feed-rate per tooth at the same cutting velocity will increase the surface roughness because increased cutting forces. Increasing the feed-rate will increase the cutting force amplitude and increase the height between peaks and valleys on the surface roughness profile.

Airflow decreases cutting temperature by convection. Higher feed-rates will generate more cutting heat, this



**Figure 12. Shear angle in dry cutting at  $V = 116$  m/min,  $f_t = 0.06$  mm/tooth and  $d = 0.2$  mm.**

will increase the temperature deviation between air flow and the work-piece, so affects of air flow are clearer. However, it is not a significant effect because the cutting temperature is not high.

In the second experiment, the width of the work-piece is 34 mm. The contact angle is  $40^\circ$ . Changing the number of inserts in the cutting tool will significantly increase the surface roughness. This is because of the increasing frequency of cutting forces. A significant change on clearance angle is the main cause of significantly increased vibrations. As a result, the number of peaks and valleys in a unit length of surface will increase, and so increase the surface roughness.

Two inserts in the cutting tool, increases vibration and lowers the tool-chip friction and changes the surface roughness slowly. Three inserts, time to transfer cutting heat is enough, tool-chip friction increases little. Vibrations play the main role in increasing surface roughness. Six inserts significantly increases both the vibration and tool-chip friction, so the arithmetic mean value increases significantly.

## 5. Conclusions

Having milled magnesium alloy, we have drawn some conclusions:

1) When the cutting velocity changes from 116 m/min to 311 m/min, the surface roughness is nearly unchanged.

2) Air pressure flow at room temperature has a remarkable effect on the surface roughness with a large number of inserts in the cutting tool.

3) Surface roughness changes significantly with changing of number of inserts in the cutting tool. It is better to use one-third as many as used during conventional cutting.

## 6. Acknowledgements

This work was supported by the faculty research fund of Sejong University in 2008

## 7. References

- [1] D. Eliezer, E. Aghion and F. H. (Sam) Froes, "Advanced Performance Materials," *Magnesium Science, Technology and Applications*, Vol. 5, No. 3, 1998, pp. 201-212.
- [2] B. L. Mordike and T. Ebert, "Magnesium: Properties-Applications-Potential," *Materials Science and Engineering A*, Vol. 302, No. 1, 2001, pp. 37-45.
- [3] H. K. Tönshoff and J. Winkler, "The Influence of Tool Coatings in Machining of Magnesium," *Surface and Coatings Technology*, Vol. 94-95, No. 10, 1997, pp. 610-616.
- [4] F. Z. Fang, L. C. Lee and X. D. Liu, "Mean Flank Temperature Measurement in High Speed Dry Cutting of Magnesium Alloy," *Journal of Materials Processing Technology*, Vol. 167, No. 1, 2005, pp. 119-123.
- [5] M. M. Advedesian and H. Baker, "Magnesium and Magnesium Alloys – ASM Specialty Handbook," ASM International, Ohio, 1999, pp. 127-129.
- [6] K. U. Kainer, "Magnesium-Alloys and Technology," WILEY-VCH, Weinheim, 2003, pp. 130-132.
- [7] P. S. Sreejith and B. K. A. Ngoi, "Dry Machining: Machining of the Future," *Journal of Materials Processing Technology*, Vol. 101, No. 1-3, 2000, pp. 287-291.
- [8] H.-T. Young, P. Mathew and P. L. B. Oxley, "Predicting Cutting Forces in Face Milling," *International Journal of Machine Tools and Manufacture*, Vol. 34, No. 6, 1994, pp. 771-783.
- [9] T. L. Jones, R. D. DeLorme, M. S. Burkins and W. A. Gooch, "Ballistic Evaluation of Magnesium Alloy AZ31B," U.S. Army Research Laboratory, Project Number 1L162 618AH80, Report Number ARL-TR-4077, 2006, pp. 2-3.

## Nomenclature

$\alpha$	rake angle ( $^\circ$ )
$d$	depth of cut (mm)
$d_a$	distance from nozzle to cutting point (mm)
$f$	feed-rate per minute (mm/min)
$f_t$	feed-rate per tooth (mm/tooth)
$f^*$	feed-rate per revolution (mm/rev)
$F_C$	orthogonal cutting force in cutting direction
$F_T$	normal cutting force in cutting direction
$F_N, F_S$	normal force and shear force on shear plane
$k$	shear flow stress on shear plane
$n$	spindle speed (rpm)
$n_i$	number of insert in cutting tool
$N, F$	normal force and tangent force at tool-chip interface
$r$	chip ratio
$r_t$	radius of cutting tool
$R$	resultant force
$t, t_c$	real under-formed chip thickness and chip thickness
$w, w_w$	width of cut and width of work-piece
$\phi$	shear angle
$\beta$	contacting angle
$\theta$	angle made by resultant force R with AB
$\lambda$	mean friction angle at tool-chip interface
$\varphi$	rotate angle of cutting tool

# Optimization of Surface Milling of Hardened AISI4340 Steel with Minimal Fluid Application Using a High Velocity Narrow Pulsing Jet of Cutting Fluid

K. Leo Dev Wins<sup>1</sup>, A. S. Varadarajan<sup>1</sup>, B. Ramamoorthy<sup>2</sup>

<sup>1</sup>*School of Mechanical Sciences, Karunya University, Coimbatore, Tamilnadu, India*

<sup>2</sup>*Department of Mechanical Engineering, IIT Madras, Chennai, India*

*E-mail: leodevins@gmail.com, varadarajan\_as@yahoo.co.in*

*Received July 26, 2010; revised September 28, 2010; accepted October 13, 2010*

## Abstract

Surface milling of hardened steel is carried out with copious supply of cutting fluid and is obviously associated with problems related to procurement and storage of cutting fluid. The disposal of cutting fluid has to comply with environmental legislation such as OSHA regulations. The present investigation proposes an environment friendly minimal pulsed jet cutting fluid application scheme for surface milling of AISI4340 steel with a hardness of 45 HRC using commercially available carbide tools. This scheme can be implemented as such on the shop floor with out the need for any major alternations on the existing facilities and it was observed that the new scheme is not only environment friendly but also provided better cutting performance when compared to conventional wet milling which requires copious supply of cutting fluid.

**Keywords:** Environment Friendly, Pulsed Jet, Minimal Cutting Fluid Application

## 1. Introduction

Conventional surface milling of hardened steel needs application of large quantities of cutting fluid. Procurement, storage and disposal of cutting fluid incur expenses and large scale use of cutting fluid causes serious environmental and health hazards on the shop floor. Apart from the fact that it gives a foul smell, disposal of cutting fluid is a problem and one has to comply with environmental legislation.

In this context, dry milling is a logical alternative which is totally free from the problems associated with storage and disposal of cutting fluid. But it is difficult to implement on the existing shop floor as it needs ultra hard cutting tools and extremely rigid machine tools. Ultra hard cutting tools may be introduced but the existing machine tools may not be rigid enough to support dry hard milling. In this context the best alternative is to introduce pseudo dry milling or milling with minimal fluid application. In this method, extremely small quantity of cutting fluid is introduced at high velocity (70 m/s) in the form of tiny droplets at critical zones so that for all practical purposes it resembles dry machining. [1-4].

It is reported that minimal cutting fluid application can improve cutting performance during turning [5]. Some

fundamental work is reported in the field of fluid minimization during turning. But very less work is reported in the area of fluid minimization during milling [6-8]. The present work aims at a systematic investigation on the viability of cutting fluid minimization during surface milling of AISI 4340 steel with a hardness of 45 HRC by developing a fluid application system that can deliver a high velocity narrow pulsed jet of cutting fluid through fluid application nozzles that can be located with the help of fixtures so that cutting fluid particles can reach critical zones and offer better cooling and lubrication. The most important aspect of this scheme is that it can be easily implemented on the shop floor and offers better cutting performance when compared to conventional wet milling while using very small quantities of cutting fluid (about 5-15 ml/min).

### 1.1. Selection of Work Material

A through hardenable AISI4340 steel was selected as work material. It was hardened to 45 HRC by heat treatment. It is a general purpose steel having a wide range of applications in automobile and allied industries by virtue of its good hardenability. Plates of 125mm length, 75mm breadth and 20 mm thickness were used for the present investigation. The composition of the work material is

shown in **Table 1**.

## 1.2. Selection of Cutting Tool

Carbide inserts with the specification AXMT 0903 PER-EML TT8020 of TaeguTec was used in the investigation along with a tool holder with the specification TE90AX 220-09-L.

## 1.3. Formulation of Cutting Fluid

Since the quantity of cutting fluid used is extremely small, a specially formulated cutting fluid was employed in this investigation. The base was a commercially available mineral oil and the formulation contained other ingredients [9]. It acted as oil in water emulsion.

## 1.4. Fluid Application System

A special fluid application system was developed for this purpose [1]. It consists of a P-4 fuel pump (Bosch make) coupled to an infinitely variable electric drive. An injector nozzle of single hole type with a specification DN0SD151 with a spray angle of  $0^\circ$  was used in the investigation. The fluid application system facilitated independent variation of pressure at fluid injector (P), frequency of pulsing (F) and the rate of fluid application (Q). The system can deliver cutting fluid through four outlets simultaneously so that cutting fluid could be applied to more than one location or more than one machine tool at the same time. By selecting proper settings, the rate of fluid application could be made as small as 0.25ml/min. The frequency of pulsing is determined by the speed of rotation of the DC variable speed motor that drives the fluid pump.

The fluid applicator delivers cutting fluid in the form of pulsed spray at the rate of one pulse per revolution. This facility enables application of less amount of cutting

fluid per pulse. The quantity per pulse is adjusted by a plunger with helical groove arrangement which is present in the fluid pump which can be rotated about its axis and the angle through which the plunger is rotated determines the quantity of fluid delivered per stroke. In this system, it is possible to deliver cutting fluid at the same rate of fluid application with different frequencies of pulsing. For example, if Q is the rate of fluid application in ml/min and F is the frequency of pulsing in pulses/min, fluid applied per pulse is given by  $Q/F$ . Pulsing jet aids in fluid minimization without compromising the velocity of individual particles as the pressure at the fluid injector remains constant. By varying the frequency, the rate of fluid delivered per pulse can be controlled. For example if Q is 1 ml/min and F is 1000 pulses/min and the pressure at the fluid injector is set at 100 bar, then fluid delivered per pulse is equal to  $1/1000 = 0.001$  ml while the velocity of the individual fluid particles will be approximately equal to 70 m/sec [10,11].

A schematic view of the fluid applicator is shown in **Figure 1**. Special fixtures were designed so that the injector nozzle could be located in any desired position without interfering the tool or work during actual cutting.

## 2. Experimentation

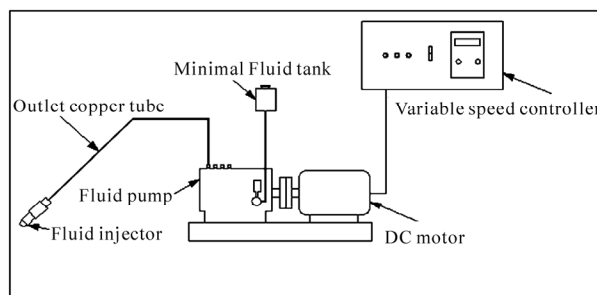
The minimal pulsed jet fluid applicator (MPFA) developed in the Centre for Research in Design and Manufacturing Engineering (CRDM) of Karunya University for carrying out this research work was characterized by the following fluid application parameters which can be varied independently.

- 1) Pressure at the fluid injector (P) in bar.
- 2) Frequency of pulsing (F) in pulses/min.
- 3) Rate of fluid application (Q) in ml/min.
- 4) Mode of fluid application (N)

It was decided to explore the relative significance of these fluid application parameters along with one cutting fluid parameter namely the composition of the cutting fluid on the cutting performance. The fluid application and fluid composition parameters were varied at two levels as summarized in **Table 2**.

**Table 1. Chemical composition of work material.**

Element	Percentage
C	0.38-0.43
Cr	0.7-0.9
Mn	0.6-0.8
Mo	0.2-0.3
Ni	1.65-2.0
P	0.035 max
Si	0.15-0.3
S	0.04 max
Fe	Balance



**Figure 1. Schematic view of the minimal fluid applicator.**

**Table 2. Input parameters and their levels.**

Pressure at fluid injector [Bar]		Frequency of pulsing [Pulses/min]		Rate of fluid application [ml/min]		Mode of fluid application		Composition of cutting fluid	
L1	L2	L1	L2	L1	L2	L1	L2	L1	L2
50	100	500	750	5	15	Single jet	Twin jet	10% oil	20% oil

L1-Level 1, L2-Level 2

In order to ensure better penetration of cutting fluid in to the rake face, an attempt was made to make use of more than one fluid jet. Accordingly a single jet configuration as in **Figure 2(a)** that corresponds to level-1 and a twin jet configuration as in **Figure 2(b)** which corresponds to level-2 were used in this investigation.

Two compositions of cutting fluid were considered in this investigation. The first composition contained 10% oil and the rest water (level-1) and the second contained 20% oil and the rest water (level-2).

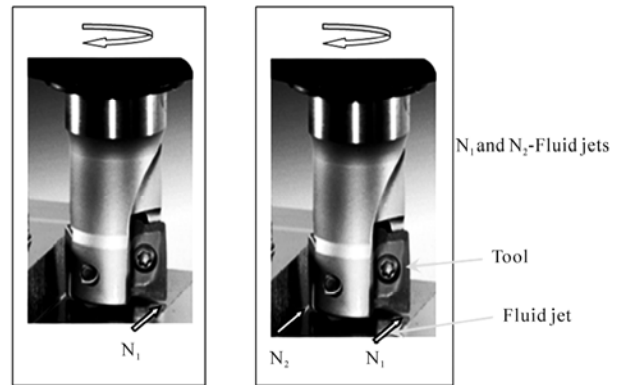
## 2.1. Mode of Analysis

Selection of the operating parameters for optimum performance was planned using Response Table Methodology [12]. A set of levels of operating parameters are to be determined to obtain minimum surface roughness, minimum flank wear and minimum cutting force. These operating parameters are to be used to compare the relative advantage of this method with respect to conventional wet milling and dry milling for the same tool-work machine tool system with constant cutting parameters such as cutting speed, feed and depth of cut which are shown in **Table 3**.

An 8 run experiment was designed based on Taguchi's techniques [12] and the design matrix is shown in **Table 4**. The experiments were conducted with two replications. Surface roughness, flank wear and main cutting force were considered as the performance parameters. With optimum cutting performance as the basis, it was sought to determine 1) the level of the rate of fluid application 2) the level of frequency of pulsing 3) the level of pressure at the fluid injector 4) the level of composition of the cutting fluid and 5) the level of number of fluid jets to be employed.

## 2.2. Experimental Details

Experiments were carried out on an HMT (model: FN1U) milling machine. A Kistler dynamometer was used for measuring cutting force. Surface roughness was measured using a stylus type Perthometer (Mahr make), flank wear measurement was done using a tool maker's microscope. The cutting speed, feed and depth of cut were set in the semi finish milling range for the tool-work combinations.

**Figure 2. Mode of fluid application (Single jet & twin jet).****Table 3. Parameters kept constant and their values.**

Parameter	Value
Cutting speed	45 m/min
Feed	0.14 mm/tooth
Depth of cut	0.4 mm

**Table 4. Basic design matrix for eight run two level experiment with five factors.**

Run No.	Factor columns				
	1	2	3	4	5
1	1	1	1	2	2
2	1	1	2	2	1
3	1	2	1	1	2
4	1	2	2	1	1
5	2	1	1	1	1
6	2	1	2	1	2
7	2	2	1	2	1
8	2	2	2	2	2

## 3. Results and Discussion

**Figure 3** presents the relative significance of the operating parameters (fluid application as well as the cutting fluid parameters) on attainable surface finish. The rela-



**Table 5. Summary of operating parameters for optimum performance.**

Sl. No	Output parameters	Objective	P	F	Q	N	C
1.	Surface roughness ( $\mu\text{m}$ )	To minimize surface roughness	100	500	5	Twin jet	20
2.	Flank wear (mm)	To minimize flank wear	100	500	5	Twin jet	20
3.	Cutting force (N)	To minimize cutting force	100	500	5	Twin jet	20

P-Pressure (bar), F-Frequency (Pulses/min), Q-Quantity (ml/min), N-Number of jets, C-Percentage composition of oil in water

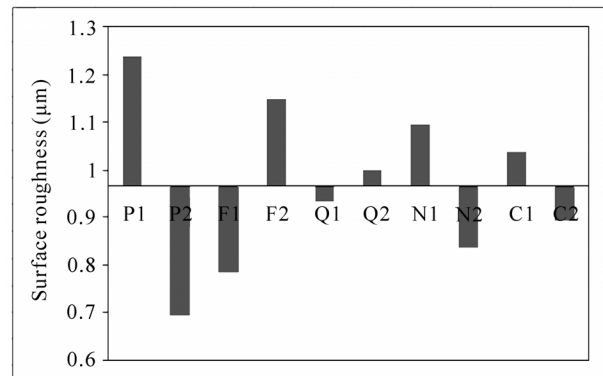
tive significance of operating parameters on flank wear is shown in **Figure 4** and the relative significance of the operating parameters on cutting force is presented in **Figure 5**. ANOVA analysis was also carried out using Qualitek-4 software to find out the percentage influence of individual parameters on surface roughness, flank wear and cutting force. From the ANOVA results, it was evident that pressure at the fluid injector forms the most significant parameter influencing the output parameters. It was also found that the interaction effects were not significant. The percentage of significance of pressure at the fluid injector on surface roughness, flank wear and cutting force were 54.203, 58.962, and 72.99 respectively. The results of the analysis which led to a set of levels of fluid application as well as cutting fluid parameters to minimize surface roughness, flank wear and cutting force are summarized in **Table 5**. The following parameter wise discussion is based on the results presented in **Table 5**.

### 3.1. Pressure at the Fluid Injector

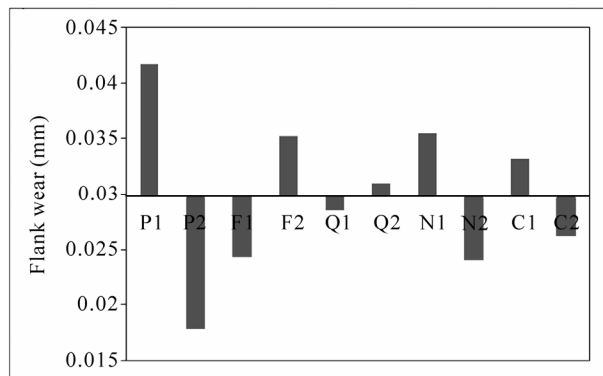
The pressure at the fluid injector kept at level-2(100 bar) favored lower flank wear and better surface finish. The penetration power of the fluid droplet is directly proportional to the exit velocity (approximately 70 m/s) [3] and the velocity varies as a function of the square root of the injection pressure [11] where as the size of the individual droplets is inversely proportional to the exit velocity [13]. The cutting force is directly related to the chip friction on the rake face. Any attempt to reduce friction on the rake face can bring forth lower cutting force, lower energy consumption, better surface finish and lower flank wear. When the pressure at the fluid injector is high, better penetration will be facilitated leading to better lubrication at the contact surfaces.

### 3.2. Mode of Fluid Application

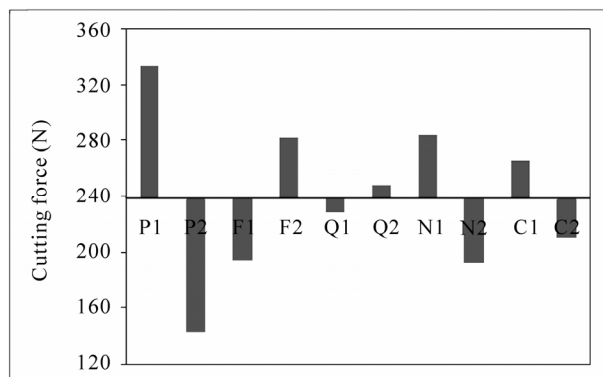
When the tool insert T is in location B as shown in **Figure 6(a)**, the direction of impingement of the fluid droplets from nozzle  $N_1$  is opposite to the direction of movement of the tool insert T and the fluid drops fall on the back side of the chip.



**Figure 3. Relative significance of levels of operating parameters on surface roughness.**



**Figure 4. Relative significance of levels of operating parameters on flank wear.**



**Figure 5. Relative significance of levels of operating parameters on cutting force.**



When the cutter rotates through  $180^\circ$  and assumes the location A, the scenario is as indicated in the **Figure 6(b)**. In this case, the direction of impingement of fluid droplets from the nozzle  $N_2$  is in the same direction as the direction of movement of tool insert T and the fluid droplets fall on the tool-work interface.

In the present investigation two configurations were used. The configuration as shown in **Figure 6(b)** forms level-1 and that in **Figure 6(c)** forms level-2 for the mode of fluid application as presented in **Table 2**. It was observed that the twin jet configuration as shown in **Figure 6(c)** gave better cutting performance when compared to the single jet configuration.

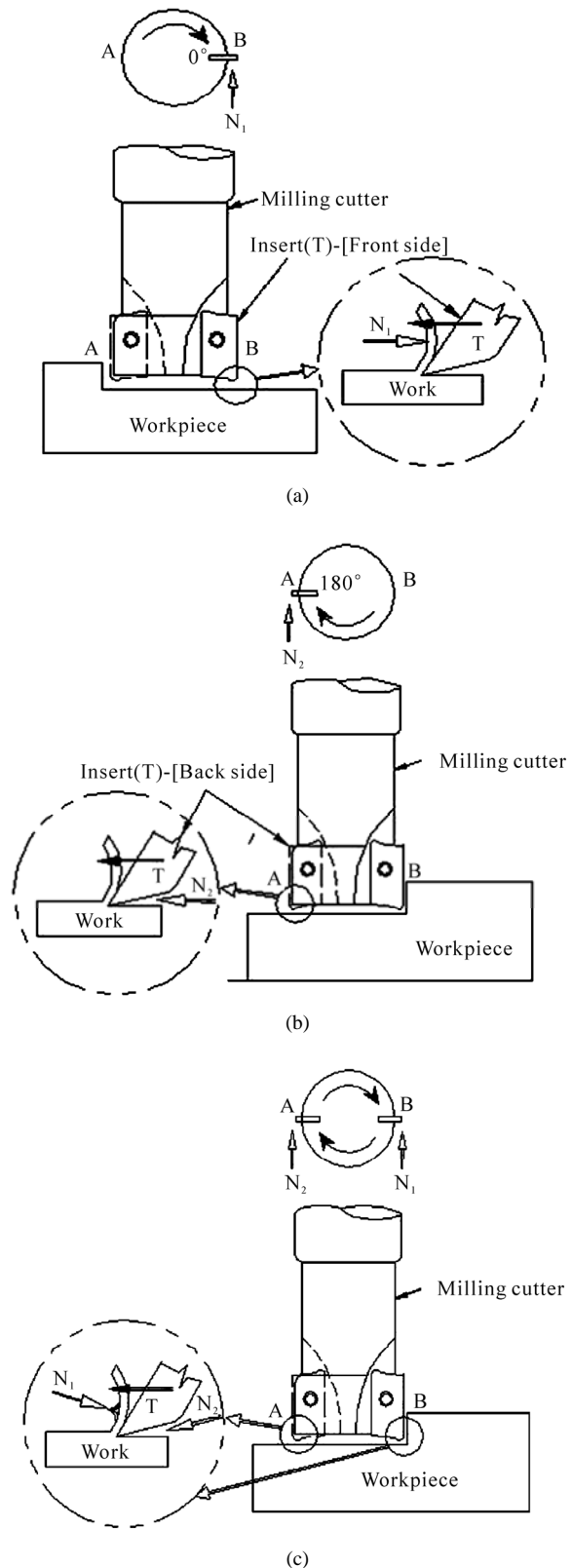
The single jet configuration was selected as level-1 based on earlier work and results [10] in which mention is made about the advantages of minimal fluid application on the tool-work interface during hard turning.

When a configuration as in **Figure 6(c)** is selected, fluid droplets are applied both on the back side of the chip as in **Figure 6(a)** and on the tool-work interface as in **Figure 6(b)**. When cutting fluid is applied on the back side of the chip, the fluid particles owing to their high velocity tend to adhere to the back side of the chip. These droplets evaporate taking the latent heat of vaporization from the chip. **Figure 7** shows the cooling of the back side of the chip which leads to its contraction where as the chip surface in contact with the rake face is hot and tends to elongate.

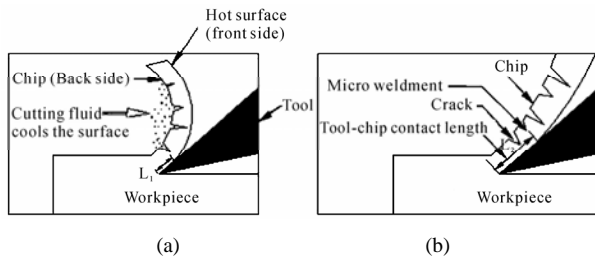
This leads to the curling of the chip away from the tool rake face resulting in the reduction of tool-chip contact length. Reduction in tool-chip contact length brings forth lower cutting force; lower flank wear and hence improved surface finish [10,14].

A chemical phenomenon can also occur at the tip of the micro cracks that formed on the back side of the chip. High velocity fluid droplets can penetrate on the back side of the chip and reach the tip of the micro cracks and stick on the surface owing to their high velocity. In the absence of cutting fluid, the nascent surface at the crack tip can coalesce due to the formation of micro weldments. The micro weldments can strengthen the back side of the chip thereby reducing the tendency of the chip to bend away from the rake face. But when a fluid droplet is present at the crack tip, it dopes the nascent surface and acts as a dielectric preventing the formation of micro weldments. This leads to the weakening of the back side of the chip and the chip tends to bend backwards, *i.e.*, away from the rake face resulting in the reduction in tool-chip contact length and hence lower cutting force [15]. Weakening of the back side also leads to its ultimate fracture resulting in the formation of fragmented chips that can be handled easily.

When cutting fluid is applied through the nozzle  $N_2$ ,



**Figure 6.** Location of fluid jet(s) (a)  $N_1$  in single jet configuration; (b)  $N_2$  in single jet configuration; (c)  $N_1$  and  $N_2$  in the twin jet configuration.

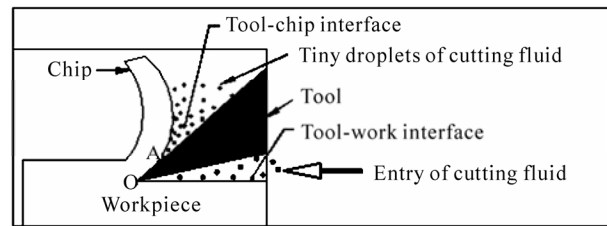


**Figure 7.** Effect of cooling the back side of the chip, (a) cooling of the back side of the chip; (b) no supply of cutting fluid.

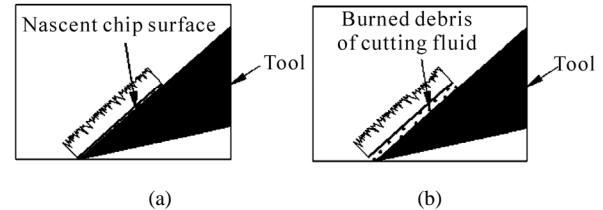
the high velocity fluid droplets can enter the tool-work interface as in **Figure 6(b)** and finally can make their way to the tool-chip interface as shown in **Figure 8** through the micro cracks near the root of the chip.

These fluid particles provide rake face lubrication by forming a film of lubricant that adheres strongly to the rake face of the tool which reduces friction and hence the cutting force. The extreme pressure that exists at the tool-chip interface prevents the easy entry of cutting fluid particles into the tool-chip interface. But when cutting fluid is applied at the tool-work interface, some cutting fluid particles can enter into the tool-chip interface through the small capillaries that exist at the root of the chip (**Figure 8**) which can permit passage of cutting fluid particles of smaller size if they possess sufficient kinetic energy by virtue of their high velocities. There is also a possibility of formation of a complex compound on the tool-chip interface which offers very low shear force and act as a lubricant owing to the extreme thermal conditions that exist in the rake face as proposed by Varadarajan *et al.* [9]. Moreover the presence of cutting fluid at the tool-chip interface can act as a dielectric preventing the intensity of surface interaction between the chip and the tool thereby transforming the condition in the region OA in **Figure 8** from sticking to one of sliding, leading to reduction in cutting force.

There is of course the possibility of burning of cutting fluid droplets at the tool-chip interface due to the severe thermal conditions that exist there. Even the burnt out fluid debris can act as a dielectric preventing inter molecular as well as inter atomic interaction between the tool and the chip (**Figure 9**) thereby preventing sticking of the chip on the rake face and this leads to reduction in cutting force. Moreover the fluid particles falling near the root of the chip can cause weakening of the cutting zone by creating zones of weakness on the work material and at the front side of the chip due to the embrittlement action of the cutting fluid. This action is based on Re-binder effect and involves micro cracks formation and healing [16]. Adsorbed film/burned debris of cutting fluid prevents closing of micro cracks. Each micro crack near the root of the chip act as a stress concentrator and



**Figure 8.** Passage of cutting fluid droplets into the tool-chip interface from tool-work interface.



**Figure 9.** Functioning of cutting fluid as a dielectric, (a) nascent chip surface tends to stick to the tool surface; (b) burned debris prevents surface interactions.

the energy needed for cutting gets reduced. In other words, penetration of foreign atoms from the cutting fluid decomposition produces an embrittlement effect near the root of the chip similar to hydrogen embrittlement which reduces the energy needed for cutting the material.

When cutting fluid is applied with two nozzles, performance improvement through reduction of cutting force is possible through two mechanisms namely reduction of tool-chip contact length and better rake face lubrication whereas when a single nozzle is employed only one mechanism namely reduction in tool-chip contact length is in operation. Hence a twin jet configuration can offer better cutting performance when compared to single jet configuration owing to the dual mechanisms of chip curl and rake face lubrication.

### 3.3. Rate of Application

It is observed that the rate of fluid application at low level is advantageous in terms of better surface finish, lower flank wear and lower cutting force. According to the empirical relationship developed by Hiroyasu and Kadota [13], the mean diameter  $D$  for a droplet size of cutting fluid injection is given by

$$D = K(\Delta P)^{-0.135} \rho^{0.121} V^{0.131}$$

where  $\Delta P$  is the mean pressure drop,  $\rho$  is the density of the medium in which injection of fluid takes place,  $V$  is the quantity of fluid delivered per pulse and  $K$  is a constant. With lower delivery rates, the size of individual droplets decreases. As explained earlier, these tiny droplets provide better lubrication leading to lower cutting

force, lower flank wear and better surface finish. Moreover the rate of fluid application can be kept at lower level (5 ml/min) which will also ensure efficient evaporative heat transfer, lower rates of fluid consumption and reduced mist formation that leads to a green environment on the shop floor.

During conventional wet turning, the quantity of heat extracted by convective heat transfer is given by

$$Q = mC_p\Delta T$$

where  $Q$  is the heat quantity in K cal,  $m$  is the mass of cutting fluid,  $C_p$  is the specific heat capacity and  $\Delta T$  is the temperature reduction brought about.

However, during minimal fluid application cooling occurs due to both convective and evaporative heat transfer. The evaporative heat transfer is facilitated by the increase in surface area caused by atomization and the quantity of heat removed is given by,

$$Q_1 = mC_p\Delta T + mL$$

where  $m$ ,  $C_p$  and  $\Delta T$  have the same notation as mentioned before.  $m$  is the mass of the fluid evaporated and  $L$  is the evaporation enthalpy. In the case of water the evaporation enthalpy is 2260 kJ/kg and in the case of mineral oil is about 210 kJ/kg. The specific heat capacity  $C_p$  for water is 4.2 kJ/kg K° and that for mineral oil is 1.9 kJ/kg K°. Since the evaporation enthalpy of water is very high, evaporation of even a very small quantity of water is sufficient to create better cooling. Moreover the cutting fluid droplets by virtue of their high velocity can puncture the blanket of vapor and reach the interfaces facilitating more efficient heat transfer which is not possible in conventional wet milling where the adherent film of lubricant retards the heat transfer.

Hence when the rate of fluid application is low, smaller will be the droplet sizes, which leads to increased surface area to facilitate evaporative heat transfer and high individual droplet velocities facilitate better penetration of fluid particles into the tool-chip interface.

### 3.4. Composition

It is seen that composition of cutting fluid comprising of 20% oil and the rest water corresponding to level-2 offered improved cutting performance when compared to a composition with 10% oil. During machining, cutting fluid acts as a coolant and as a lubricant. In case of oil in water emulsion as used in this investigation, water acts as a coolant and oil acts as a lubricant. During minimal fluid application, very small quantity of cutting fluid is expected to perform the dual functions of cooling and lubrication. It appears that a composition consisting of 10% oil is too lean to provide effective rake face lubrication at the tool-chip interface. A certain minimum quan-

tity of lubrication must be present in the cutting fluid to compensate for the possible losses as the fluid reaches the tool-chip interface through the tool-work interface.

### 3.5. Frequency of Pulsing

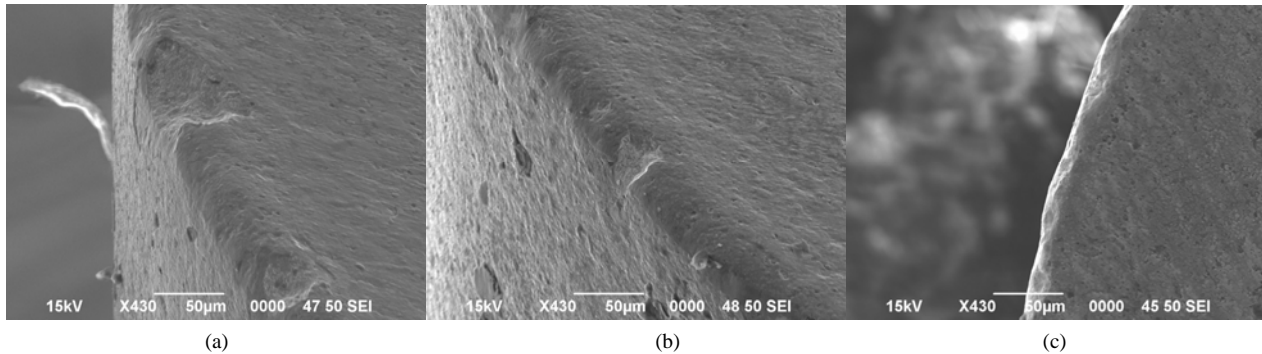
It is observed that frequency of pulsing of fluid application at low level favored better cutting performance. It is reported that the frictional forces between two sliding surfaces can be reduced considerably by rapidly fluctuating the width of the lubricant filled gap separating them [17].

When a pulsing jet is used, the width of the lubricant filled gap between the tool rake face and the chip fluctuates with a frequency equal to the frequency of pulsing of the fluid jet. The width will be maximum when the fluid slug falls at the gap and will be minimum when no particles fall on the gap during the pulsing cycle. This process continues as the fluid particles fall in the gap between the chip and the tool intermittently. When the frequency of pulsing ( $F$ ) is 750 pulses/min, the quantity of fluid delivered per pulse is very less when compared with the frequency of pulsing of 500 pulses/min for any fixed rate of fluid application. Hence the fluctuation in the width of the liquid film between the tool and the chip is less appreciable when the frequency of pulsing is 750 pulses/min when compared to that at a frequency of 500 pulses/min. A minimum quantity of cutting fluid should be delivered per pulse to get an appreciable fluctuation in the width. This leads to presence of fresh fluid droplets in to the tool-chip interface unlike in the case where a stagnant layer of cutting fluid is present when a continuous jet is employed [18]. The presence of fresh fluid droplets facilitates better filling of the gap on the tool-chip interface thereby providing better lubrication and enhanced cooling as the droplets evaporate.

Moreover, when the frequency of pulsing is very high, the individual particles will be small and may lack in kinetic energy to penetrate in to the tool-chip interface. This leads to less fluid particles reaching the rake face and hence less efficient rake face lubrication. It is also to be noted that the pulsing nature of the fluid delivery vanishes when the frequency of pulsing is very high and the fluid delivery tends to resemble a continuous jet, devoid of all the aforesaid advantages claimed for a pulsing jet.

### 3.6. Comparison of Flank Wear

Average flank wear was determined during dry, wet and minimal fluid application, keeping the cutting speed, feed and depth of cut at 45 m/min, 0.14 mm/tooth and 0.4 mm respectively. The flank wear was 0.127 mm during dry milling 0.031 mm during conventional wet mill-



**Figure 10.** SEM photographs on comparison of worn out insert edges during dry, wet and minimal fluid application, (a) dry milling; (b) wet milling; (c) milling with minimal fluid application. Cutting speed-45 m/min, Feed-0.14 mm/tooth, Depth of cut-0.4 mm, Cutting time-120 sec.

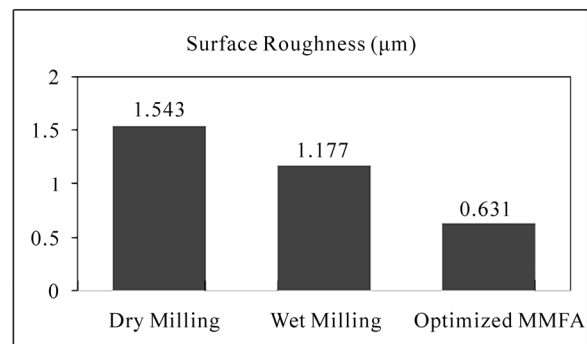
ing and 0.018 mm during optimized milling with minimal fluid application for a cutting time of 120 seconds. SEM photographs of tool flank wear during dry milling, conventional wet milling and milling with minimal fluid application are presented in **Figures 10(a), 10(b)** and **10(c)** respectively. It is observed that flank wear is minimum during milling with minimal fluid application in the optimized mode. Lower flank wear during minimal fluid application is attributed to better rake face lubrication and lower tool-chip contact length and better heat transfer due to evaporative cooling. The comparison of results of optimized milling with minimal fluid application with dry milling and conventional wet milling is presented in **Table 6** from which it is clear that milling with minimal fluid application can offer improved surface finish, lower flank wear and lower cutting force when compared to dry milling and conventional wet milling.

**Figures 11 to 13** presents a comparison of surface roughness, flank wear and cutting force during dry milling, wet milling and milling with minimal fluid application. It can be seen that milling with minimal fluid application with twin-jet configuration can bring forth better surface finish, lower flank wear and lower cutting force when compared to that during conventional wet milling and pure dry milling.

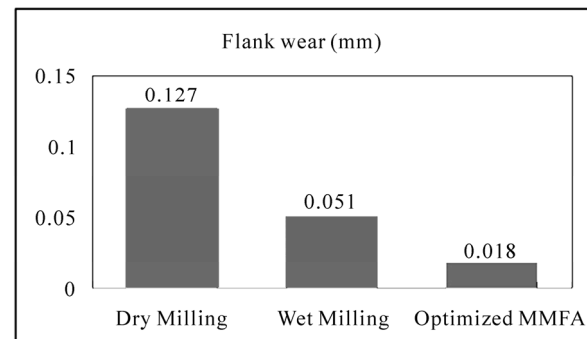
**Table 6.** Comparison of output parameters during wet, dry and milling with minimal fluid application.

Sl. No	Output parameters	Surface roughness Ra ( $\mu\text{m}$ )	Flank wear (mm)	Cutting force (N)
1.	Dry milling	1.543	0.127	471.73
2.	Wet milling	1.177	0.051	228.25
3.	Milling with minimal fluid application (Optimized mode)	0.631	0.018	105.79

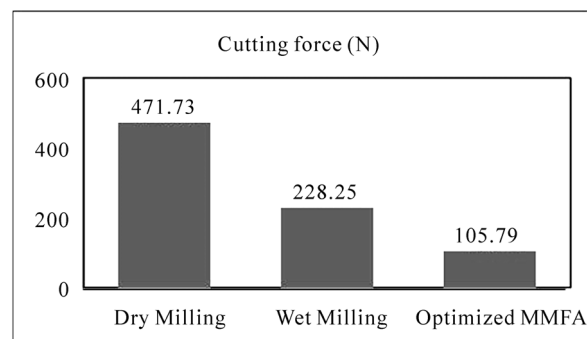
machining time = 120 seconds



**Figure 11.** Comparison of surface roughness (Ra).



**Figure 12.** Comparison of flank wear.



**Figure 13.** Comparison of cutting force.

## 4. Conclusions

It is observed that the fluid application parameters namely pressure of fluid injection, frequency of pulsing, direction of fluid application, composition and rate of fluid application have their own influence on the cutting performance during surface milling of hardened AISI4340 steel.

Results in this work indicated that milling with pulsed jet minimal fluid application holds promise for the development of a commercial environment friendly pulsed jet fluid application scheme with particular reference to surface milling of hardened steel.

## 5. Acknowledgements

The authors thank the authorities of the Centre for Research in Design and Manufacturing of the Karunya University for facilitating this project and M/s Taugetec India (P) Ltd. for supplying cutting tools at concessional rates.

## 6. References

- [1] A. S. Varadarajan, P. K. Philip and B. Ramamoorthy, "Investigations on Hard Turning with Minimal Cutting Fluid Application(HTMF) and its Comparison with Dry and Wet Turning," *International Journal of Machine Tool and Manufacture*, Vol. 42, No. 2, 2001, pp. 193-200.
- [2] A. S. Varadarajan, P. K. Philip and B. Ramamoorthy, "Neural Network Assisted Performance Prediction in Hard Turning with Minimal Quantities of Cooling Lubricants," *Proceedings of the 14th International Conference, CAD/CAM, Robotics and Factories of the Future*, PSG College of Technology, Coimbatore, India, 1998, pp. 654-658.
- [3] A. S. Varadarajan, P. K. Philip and B. Ramamoorthy, "Investigations on Hard Turning with Minimal Pulsed jet of Cutting Fluid," *Proceedings of the International Seminar on Manufacturing Technology beyond 2000*, Bangalore, India, 1999, pp. 173-179.
- [4] A. Attansio, M. Gelfi, C. Giardimi and C. Remino, "Minimal Quantity Lubrication in Turning: Effect on tool wear," *International Journal of Wear*, Vol. 260, No. 3, 2006, pp. 333-338.
- [5] A. S. Varadarajan, P. K. Philip and B. Ramamoorthy, "Optimization of Operating Parameters for the Cutting Performance during Hard Turning with Minimal Cutting Fluid," *Proceedings of the International Conference on Intelligent, Flexible, Autonomous Manufacturing Systems*, Coimbatore, India, 2000, pp. 717-725.
- [6] A. Raj, K. L. D. Wins, R. Gnanadurai and A. S. Varadarajan, "Investigations on Hard Milling with Minimal Fluid Application," *International Conference on Frontiers in Design and Manufacturing*, Karunya University, Coimbatore, 2008, pp. 183-187.
- [7] T. Thepsonthi, M. Hamdi and K. Mitsui, "Investigation into Minimal-Cutting Fluid Application in High-Speed Milling of Hardened Steel Using Carbide Mills," *International Journal of Machine Tools and Manufacture*, Vol. 49, No. 2, 2009, pp. 156-162.
- [8] M. Rahman, A. S. Kumar and M. U. Salam, "Experimental Evaluation on the Effect of Minimal Quantities of Lubricant in Milling," *International Journal of Machine Tools & Manufacture*, Vol. 42, No. 5, 2002, pp. 539-547.
- [9] A. S. Varadarajan, B. Ramamoorthy and P. K. Philip, "Formulation of a Cutting Fluid for Hard Turning with Minimal Fluid Application," *20th AIMTDR conference at Birla institute of Technology Ranchi*, India, 2002, pp. 89-95.
- [10] P. K. Philip, A. S. Varadarajan and B. Ramamoorthy, "Influence of Cutting Fluid Composition and Delivery Variables on Performance in Hard Turning Using Minimal Fluid in Pulsed Jet Form," *Journal of the Institution of Engineers (India)*, Vol. 82, No. 3, 2001, pp. 12-19.
- [11] J. B. Heywood, "Internal Combustion Engine Fundamentals," McGraw-Hill, New York, 1996.
- [12] R. H. Lochner and J. E. Matar, "Design for Quality," Chapman and Hall, London, 1990, pp. 77-95.
- [13] Hiroyasu and T. Kadota, "Fuel Drop Size Distribution in Diesel Combustion Chamber," SAE paper 740715, *SAE Transactions*, Vol. 83, 1974, pp. 715-721.
- [14] L. De Chiffre, "Function of Cutting Fluids in Machining," *Journal of the Society of Tribologists and Lubrication Engineers*, Vol. 44, No. 6, June 1998, p. 514.
- [15] Ball, "A Survey of Metal Working Fluid Mist in Manufacturing Plants," *Journal of the Tribologists and Lubrication engineers*, Vol. 53, No. 9, 1997, p. 18.
- [16] V. P. Astakhov, "Metal Cutting Theory Foundations of Near-Dry (MQL) Machining," *International Journal of Machining and Machinability of Materials*, Vol. 7, No. 1/2, 2010, pp. 1-16.
- [17] U. Landman, "'FRUSTRATED' lubricant molecules offer new strategy for reducing friction in mechanical devices," Georgia Tech – Research news. <http://gtresearchnews.gatech.edu/newsrelease/FRICTION.html>
- [18] R. Alexander, A. S. Varadarajan and P. K. Philip, "Hard Turning with Minimum Cutting Fluid – A Viable Green Alternative on the Shop Floor," *Proceedings of the 18th All India Manufacturing Technology Design and Research Conference*, Vol. 1, Kharagpur, 1998, pp. 183-187.
- [19] G. Boothroyd and W. A. Knight, "Fundamentals of Machining and Machine tools," 3rd Edition, CRC Taylor & Francis UK, 2006, pp. 69-100.

# Using Image Analysis for Structural and Mechanical Characterization of Nanoclay Reinforced Polypropylene Composites

**Turup Pandurangan Mohan, Krishnan Kanny\***

*Composites Research Group Department of Mechanical Engineering Durban University of Technology, Durban – South Africa*

*E-mail: [kannyk@dut.ac.za](mailto:kannyk@dut.ac.za)*

*Received July 9, 2010; revised September 1, 2010; accepted September 8, 2010*

## Abstract

This paper focuses on the micromechanical study of the tensile property of Polymer-Clay Nanocomposites (PCN). Polypropylene (PP) filled with nanoclay is chosen as the PCN. Measurements of optical dispersion parameters (as discussed by Basu *et al.*, namely, exfoliation number ( $\xi_n$ ), degree of dispersions ( $\chi$ ) and agglomerate %) in PCN system were carried out using Transmission Electron Microscopy (TEM) and Optical Microscopy (OM). The experimentally obtained tensile modulus is compared with theoretically obtained modulus values from the optical dispersion parameters and observed a close matching between these values. Also, the tensile values are compared with other standard theoretical models and observed that the results obtained from optical dispersion parameters are suited well with experimental results.

**Keywords:** Polymer Clay Nanocomposites, Transmission Electron Microscope, Optical Microscope, Intercalation/Exfoliation, Micromechanical Modeling

## 1. Introduction

Polymer filled with nanolayered silicate clay has become a significant research interest in recent past and continues to be an area of important focus because they exhibit dramatic improvement in properties at very low clay filler contents. Usually micron-Scale conventional fillers are added in polymer in the form of particles or fibres shaped additives. However, the addition of these particles in polymer imparts increased weight, brittleness, opacity etc. A polymer nanocomposite (in which at least one dimensions of reinforcement material in nanometer level  $\sim 100$  nm) on the other hand provides enhanced property benefits to polymer system at very low weight concentration level ( $\sim 3$  to 5 wt.%). Commonly used nanoparticles in polymer matrix are nanolayered clays, because of their ease availability and cost effectiveness [1-3].

The addition of nanoclay in polymer matrix result in the formation of two types of nanocomposites structures, namely, an intercalated or an exfoliated structure. The host polymer matrix enters into the interlayer spacing of nanoclay and increases the interlayer of clay more and

maintains the parallel arrangement of nanolayers of clay in matrix and this structure is called an intercalated structure. If the nanolayers of clays are randomly dispersed in matrix, then the structure is called an exfoliated structure. These intercalated and exfoliated structures can be examined by using TEM and X-ray diffraction (XRD) methods. In general, exfoliated structure provides improved properties than intercalated nanocomposite structure due to increase of net aspect ratio of clay nanolayers (length/thickness). However, if the concentration of clay is increased, the composite structure becomes intercalated structures and also some times leads to improved properties which are primarily due to the major contribution of clay property rather than nanoclay composite structure (exfoliated) [4-7]. Each nanolayer of clay constitute of elliptical disc like platelet shaped structure, of length and width varying from 100 nm to 2000 nm and thickness of about 1 nm.

It is well known fact that the property of PCN depends on degree of dispersions of clays. The properties are good if the dispersion of clays are proper and with no agglomeration [8-11]. This phenomenon suggests that there exists a link between dispersions and the property

of composites. The better the dispersion of nanolayers in polymer, better property enhancements can be obtained. However, the nanolayers are not easily dispersed in most polymers due to their preferred face-to-face stacking of clay platelets in agglomerated tactoids. Studying the characteristics of dispersions of particles (distribution, arrangement, orientation, etc) helps to understand the property of composites in better way. Basu *et al.* [12] has done image analysis using stereology of TEM and Optical Microscope (OM) pictures and studied the extent of dispersion of particles using dispersion parameters (namely: exfoliation number, interparticle distance and agglomeration %). In this work, we used these optical dispersion parameters and further extended these parameters to study the tensile property of composites. PCN system chosen in this study was polypropylene (PP) as matrix polymer material and reinforcement as nanoclay particles. The objective of this work is to measure the tensile modulus using optical dispersion parameters. The theoretically measured tensile modulus using optical dispersion parameters is then compared with experimentally obtained results and also with various standard micro-mechanical models. It is observed that the theoretical results measured using this optical dispersion parameters correlated well with that of experimental results than other standard models. The out come of the results are discussed in this paper.

## 2. Experiments

### 2.1. Materials and Manufacturing

Cloisite 15A is a natural montmorillonite organically modified with a quaternary ammonium salt and was obtained from Southern Clay Products, USA. Polypropylene pellets were procured from Chempro, South Africa.

The nanocomposite panel was manufactured using a melt-blend technique. In this technique, the polypropylene pellets and the nanoclay were combined in a REIFFENHAEUSER screw extruder. The extruder has a 40 mm diameter single rotating screw with a length/diameter ratio (L/D) of 24 and driven by a 7.5 kW motor. Three heating zones along the length of the screw were set up to gradually heat the pellet/clay mixture. The temperatures in these zones were as follows: Zone 1 (pellet loading end) was set at 170°C, Zone 2 (centre region of screw) was at 190°C, and Zone 3 (extrusion end) was maintained at 210°C. This temperature gradient setup was created to avoid thermal shock, (*i.e.*, the heating condition is fixed up in such a way that the melt polymer samples exhibits uniform gradient of temperature across the length of extrusion unit instead of sudden change of temperature).

## 2.2. Characterization

Microscopic investigation of selected nanocomposite specimens at the various weight compositions were conducted using a Philips CM120 BioTWIN transmission electron microscope with a 20 to 120 kV operating voltage. The cryo and low dose imaging TEM has BioTWIN objective lens that gives high contrast and a resolution of 0.34 nm. The specimens were prepared using a LKB/Wallac Type 8801 Ultramicrotome with Ultratome III 8802A Control Unit. Ultra thin transverse sections, approximately 80-100 nm in thickness were sliced at room temperature using a diamond coated blade. The sections were supported by 100 copper mesh grids.

3cm × 3 cm × 3mm specimen of PP-clay series were taken and cut into two across the mid portion of the specimen. The cut portion is viewed through optical microscope at 100x using ZEISS AXIO LAB optical microscope. Tensile tests were performed on virgin PP and the nanocomposite specimens using the LLOYDS Tensile Tester fitted with a 20 kN load cell. The tensile tests were performed at a crosshead speed of 1 mm/min in accordance with the ASTM D3039 standard.

## 3. Results and Discussions

### 3.1. Rules of Mixture and Halpin-Tsai Formulation

The parallel model (rules of mixture) has been applied for the prediction of Young's modulus and is given the Equation (1). Young's modulus of clay and PP are taken as 167 GPa and 1 GPa respectively.

$$E_c = E_m V_m + E_f V_f \quad (1)$$

Figure 1 shows the experimental and rules of mixture values. There is a large variation in experimental and theoretical values. Equation (1) shows that the theory does not account for the aspect ratio and the shape of the fillers.

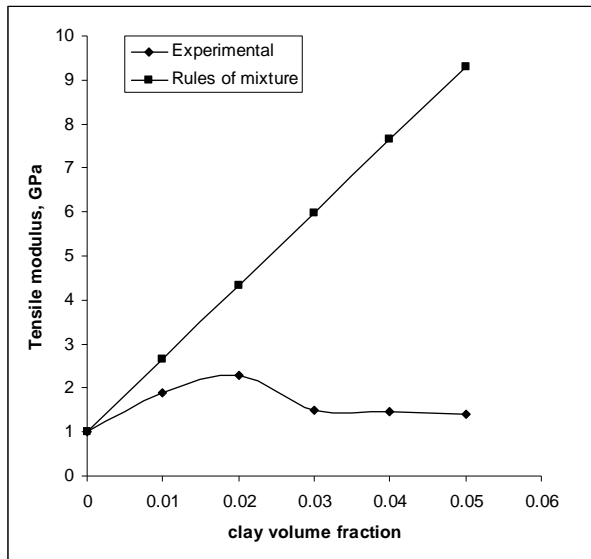
This theory is further improved by Halpin Tsai [13] which predicts the stiffness of particulate filled composites as a function of aspect ratio. The longitudinal and transverse moduli  $E_{11}$  and  $E_{22}$  are expressed in the general form as per Equation (2).

$$\frac{E_c}{E_m} = \frac{1 + \xi \eta V_f}{1 - \eta V_f} \quad (2)$$

Further  $\eta$  is given by

$$\eta = \frac{\frac{E_f}{E_m} - 1}{\frac{E_f}{E_m} + \xi} \quad (3)$$





**Figure 1.** Comparison of Rules of mixture and experimental results.

$\xi = 2(a/b)$  in which 'a' and 'b' are the length and thickness of the fibre. The effect of 'a' on modulus of composites is shown in **Figure 2**. At higher clay content, there is a large variation in experimental and theoretical results. The existence of agglomeration, intercalated structures, etc., of clay particles in matrix polymer might have reduced composite properties along the loading direction and this leads to the low modulus value than the theoretical values.

### 3.2. Stack Model

The polymer-clay nanocomposites consist of clay platelet reinforcement in variety of polymer matrices for the formation of either intercalated or exfoliated structure. However, in most cases exfoliation is thermodynamically unfavourable and most process techniques lead only to intercalated structures particularly at higher clay content [8-11]. Here an attempt is made to understand the influences of incomplete exfoliation on nanocomposite stiffness using composite theory. For this analysis, the stacking of clay platelets within a particle is treated in a very simple fashion, *i.e.* platelets of equal diameter are stacked directly one over the other and the load is applied parallel to the platelet edges, as shown in **Figure 3**. Matrix polymer is assumed to be present in the interlayer region of two clay nano platelets (layers).

The tensile modulus of a simple stack in the direction parallel to its platelets can be estimated by using the rule of mixture, as suggested elsewhere [14]. Stack modulus can be found out from rules of mixture as per Equation (4).

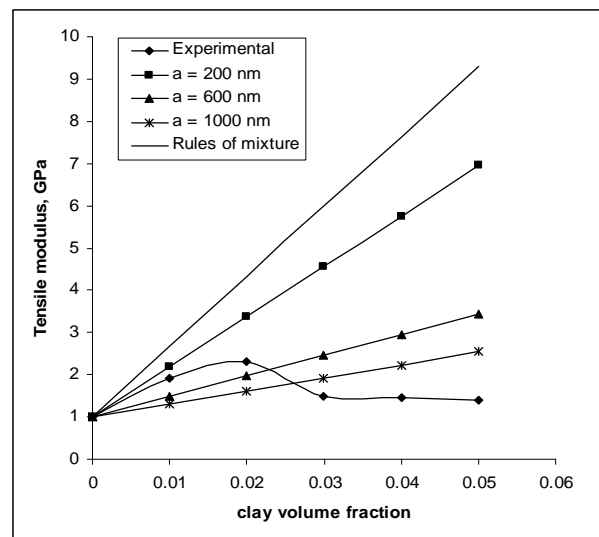
$$E_s = E_{mi}V_{mi} + E_{cl}V_{cl} \quad (4)$$

The stack modulus ( $E_s$ ) obtained from Equation (4) is substituted in Equation (1) in place of  $E_f$ . The matrix thickness in the stacks plays a significant role in the composite modulus. If matrix thickness in the clay interlayer region is more, then the effective clay volume fraction will reduce. **Figure 4** shows the effect of matrix thickness in interlayer region and their corresponding decrease in the clay volume fraction. Also, at given matrix thickness, the volume fraction of clay stack remains constant irrespective of number of stacks.

**Figure 5** show the comparison of experimental results with the theoretical values of stack model. It is observed that matching is good at clays volume fraction of 0.02 and 0.03, however at higher clay content the deviations is more. By altering stack thickness and thickness of matrix at interlayer ( $d_{ms}$ ), some matching can be expected. Even though at higher clay content, the structure becomes intercalated structure (stacking sequence), the theoretical and experimental results have not matched well. Possibly other factors like aspect ratio, interface property etc, could have influenced the experimental results.

### 3.3. Mori-Tanaka Theory

Mori-Tanaka micromechanical model have been proposed to predict the elastic constants of discontinuous fibre/flake composites [15]. This model depends on parameters including particle/matrix stiffness ratio; particle



**Figure 2.** Comparison of Halpin-Tsai theory and experimental results.



**Figure 3.** Tensile loading in stack model.

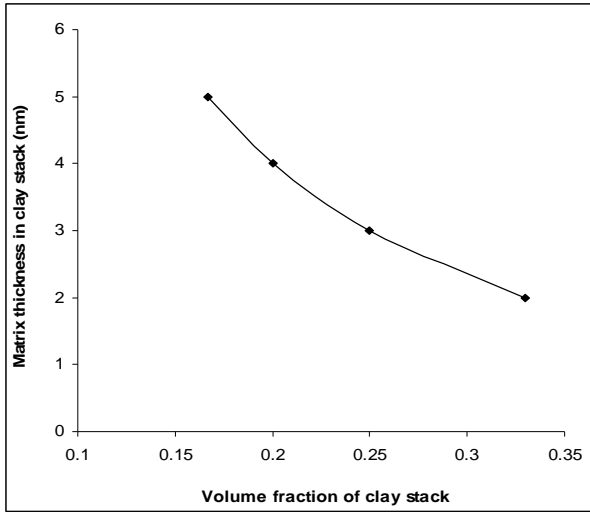


Figure 4. Effect of matrix thickness in clay nanolayer.

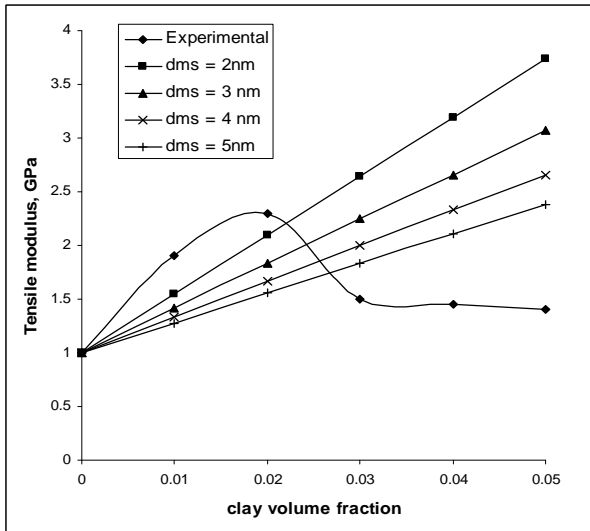


Figure 5. Comparison of tensile modulus of nanocomposites and stack model.

volume fraction; particle aspect ratio; and their orientation. In applications relevant to the present study, the particles and matrices are assumed to be linearly elastic, can be taken as isotropic or transversely isotropic. Here,  $E_p$  and  $E_m$  denote the elastic modulus of the particle and the matrix respectively. Later, Tucker *et al.* [16] provides a good review of the application of several classes of micromechanical models to discontinuous fibre reinforced polymers. It is noted that, of the existing models, the widely used Halpin-Tsai equations give reasonable estimates for effective stiffness, but the Mori-Tanaka type models give the best results for large aspect-ratio fillers. The present study is focused on the prediction of longitudinal stiffness,  $E_{11}$ ; for composites filled with

unidirectional disk-like particles. The Mori-Tanaka model is given by Equation (5).

$$\frac{E_{11}}{E_m} = 1 + 2(L/t)\eta V_f \quad (5)$$

$\eta$  is the shape factor which can be taken from Halpin-Tsai shape factor (Equation (3)),  $t$  is the thickness of the clay nanolayer (1 nm) and  $L$  is the length of the clay nanolayer (nm). Figure 6 shows the comparison of experimental values with theoretical results for different values of clay length. The thickness of nanolayer ' $t$ ' is taken as 1 nm.

The modulus values increase as the length of clay nanoparticle increases. The theoretical prediction of modulus up to low clay volume fraction is better, however, at higher clay concentrations, there exist large variations in the experimental values and Mori Tanaka result. This suggests that other parameters are influencing the experimental trend. The length of clay layers are not the function of clay concentrations since same species of clays are used. Hence it is understood that net aspect ratio (length/thickness) has affected the aspect ratio. Also, stacking of clay nanolayers is high at higher clay concentration (intercalated structure). All these factors could have reduced the modulus at higher clay content. Mori-Tanaka formulation considers only the size, shape, aspect ratio and volume fraction of fillers, however, it does not consider the effect of net aspect ratio of fillers (which is predominant at higher clay content). In Mori-Tanaka formulation, the behaviour of interface characteristics is also not considered, which is taken care in Takanayagi's phase model.

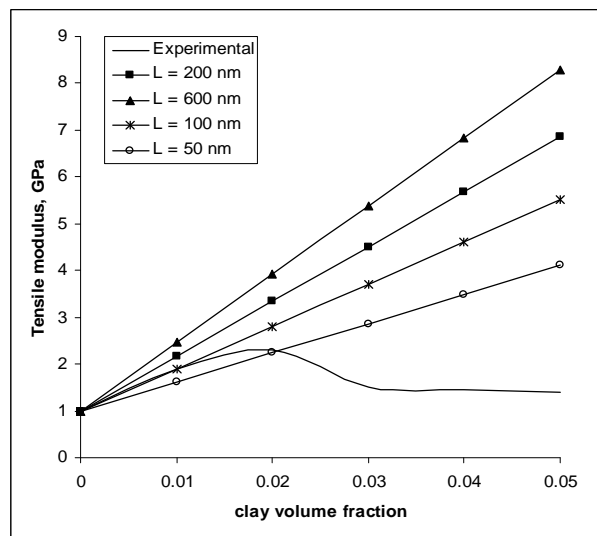


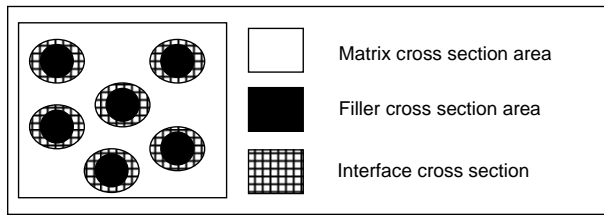
Figure 6. Comparison of modulus with Mori-Tanaka theory.

### 3.4. Takayanagi's Two Phase and Interface Model

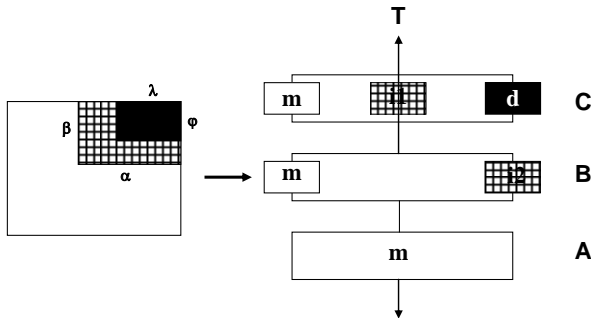
The phase model suggested by Takayanagi has widely been used to explain modulus of polymers, polymer blends and composites [16]. Two phase model describes the modulus of composites which consists of homogeneous rigid discontinuous phase and homogenous continuous matrix phase. When the dispersed particles approach a very small size, the specific surface area of the interfacial region is so large that it is comparable with or even larger than that of the dispersed phase. Recent work on polymer nanocomposites shows that the macromolecular chains intercalated in inorganic compounds are confined in a very small region and their behaviour is quite different from those in bulky polymers. It is found that these macromolecules are quite rigid. Based on this, an interface contribution of matrix and particle is taken in to account in Takayanagi's model.

The moduli of the matrix, dispersed phase, and interface are  $E_m$ ,  $E_d$  and  $E_i$  respectively, and their corresponding volume fractions are  $V_m$ ,  $V_d$  and  $V_i$  respectively. **Figure 7** shows the distribution of particles in the matrix. The schematic of filler/matrix interface is also depicted. The system can be explained as a three-phase model in which the three phases are connected to each other in series and in parallel. The response of these three phases to a stress is schematically shown in **Figure 8**.

The three phase model as shown in **Figure 8** is divided in to three regions which are connected in series as A, B and C. The elongation of these three regions under



**Figure 7. Schematic of cross-section view of polymer-particle filled composites.**



**Figure 8. Equivalent model under tensile response.**

the stress ( $T$ ) loaded on the specimen are  $\varepsilon_A$ ,  $\varepsilon_B$  and  $\varepsilon_C$ , respectively. In region A, only matrix with volume fraction  $V_{Am}$  exists. In region B, the interface with volume fraction  $V_{Bi}$  and matrix with volume fraction  $V_{Bm}$  coexist in a parallel arrangement. In region C, the matrix with volume fraction  $V_{Cm}$ , the interface with volume fraction  $V_{Ci}$  coexists in a parallel arrangement. It is known that  $V_{Am} + V_{Bm} + V_{Cm} = V_m$ ,  $V_{Bi} + V_{Ci} = V_i$ . The elongation in region A is

$$\varepsilon_A = \frac{T}{E_A} = \frac{T}{E_m} \quad (6)$$

where  $E_A$  is the modulus of the region A, i.e.,  $E_m$ .

The elongation in region B is:

$$\frac{T}{(1-\alpha)E_m + \alpha E_{Bi}} \quad (8)$$

The elongation in region C is

$$\frac{T}{(1-\alpha)E_m + (\alpha-\lambda)E_{Ci} + \lambda E_d} \quad (9)$$

The total elongation in these three regions is

$$\begin{aligned} \varepsilon_C &= (1-\beta)\varepsilon_A + (\beta-\phi)\varepsilon_B + \phi\varepsilon_C \\ &= \left( \frac{1-\beta}{E_m} + \frac{\beta-\phi}{(1-\alpha)E_m + \alpha E_{Bi}} + \frac{\phi}{(1-\alpha)E_m + (\alpha-\lambda)E_{Ci} + \lambda E_d} \right) \end{aligned} \quad (10)$$

$$\text{Where } \lambda\phi = V_d; \alpha\beta - \lambda\phi = V_i \quad (11)$$

Since  $\varepsilon_C/T = 1/E_c$ , where  $E_c$  is the modulus of the composites, Equation (10) becomes

$$\frac{1}{E_c} = \frac{1-\beta}{E_m} + \frac{\beta-\phi}{(1-\alpha)E_m + \alpha E_{Bi}} + \frac{\phi}{(1-\alpha)E_m + (\alpha-\lambda)E_{Ci} + \lambda E_d} \quad (12)$$

This equation can be understood by considering some special cases.

1) when  $\lambda\phi = V_d = 0$ , i.e. no dispersed phase and therefore no interfacial region, only a matrix exists, then  $E_c = E_m$

2) when  $1-\beta = 0$ ,  $1-\alpha = 0$ , i.e.,  $\beta = 1$ ,  $\alpha = 1$  and  $V_m = 0$ , i.e., the matrix phase does not exist. Here there is no interfacial region and dispersed phase giving  $E_c = E_d$

3) when  $\alpha - \lambda = \beta - \phi = 0$ , or  $\alpha = -\lambda$  and  $\beta = \phi$ , Equation (12) reduces to

$$\frac{1}{E_c} = \frac{1-\phi}{E_m} + \frac{\phi}{(1-\lambda) + \lambda E_d} \quad (13)$$

The Equation (13) describes the modulus of two-phase composites namely homogeneous rigid phase and ho-

mogeneous matrix phase. However, in nanoclay filled composites, the matrix particle interface has to be considered and this is given in 3-phase model.

### 3.4.1. Modulus of the Interfacial Region

The modulus of the interface in regions 1 and 2 are different from each other (shown in **Figure 8**). In the region 1, owing to the parallel arrangement of a number of volume units in the interfacial region, the modulus of this region could be expressed by:

$$E_{il} = E_{il}(l) \quad (14)$$

where  $E_{il}(l)$  is the modulus at region 1 with the distance  $l$  from the surface of the dispersed rigid phase. If a linear gradient distribution of the modulus along the normal direction of the surface is assumed, then

$$dE_{il}(l) = \frac{E_{il}(0) - E_m}{\tau} dl \quad (15)$$

After integration, the Equation (16) is obtained:

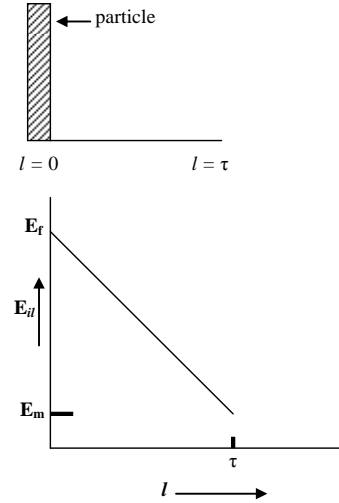
$$E_{il}(l) = E_{il}(0) - \frac{E_{il}(0) - E_m}{\tau} l \quad (16)$$

where  $E_{il}(0)$  is the modulus of the interface at the surface of the dispersed rigid phase and  $\tau$  is the thickness of the interface region. When  $l = 0$ ,  $E_{il}(0)$  stands for the modulus of the interface, close to the surface of the fillers and it is a constant. Alternately, when  $l = \tau$ ,  $E_{il}(\tau)$  represents the modulus at the edge of the interface next to the matrix, i.e.,  $E_m$  (**Figure 9**). If there exists linear decrease of  $E_f$  along  $l$ , then the modulus of the interface region  $l$  with thickness of  $\tau$  is then

$$E_{il} = \frac{E_{il}(0) + E_f}{2} \quad (17)$$

As seen in **Figure 8**, the region 2 (Block i2) connects with the dispersed phase at the top and connects with the matrix at the bottom. From top to bottom the modulus of these phase varies from  $E_{i2}(0)$  to  $E_m$ . Block i2 can be treated as a series arrangement of a number of volume units and the modulus in this region varies with  $l$ .

It should be noted that  $E_{Bi} = E_{i2}$ ,  $E_{Ci} = E_{il}$ .  $E_{il}$  or  $E_{i2}$  could be another type of function depending on the interaction of the macromolecules with the surface of dis-



**Figure 9.** Variation of interface modulus along the normal of particle surface.

persed phase. In the present case it is assumed that modulus  $E_{il}$  and  $E_{i2}$  are same.

### 3.4.2. Tensile Modulus of Polymer Nanocomposites

If the modulus in the interfacial region takes a linear gradient reduction along the normal direction of the surface of dispersed phase, Equation (13) would be

$$\frac{1}{E_c} = \frac{1 - \beta}{(1 - \alpha)E_m + \alpha[\ln(E_m / E_{i2}(0))[E_{i2}(0) - E_m]]} + \frac{\phi}{(1 - \alpha)E_m + (\alpha - \lambda)[E_{il}(0) + E_m] / 2 + \lambda E_d}$$

If a random orientation of the plate-like dispersed phase is considered with thickness =  $\lambda$ , length and width as  $\zeta$  and  $\zeta \gg 1$ , the following conditions are assumed, i.e.,  $\alpha = \beta$ ,  $\phi = \lambda$ . Each plate particle has two interface regions:  $V_d = \lambda$  and  $\alpha^2 - V_d = (2\tau/t)V_d$ , which can be arranged as

$$\alpha = [(2\tau/t + 1)V_d]^{1/2} \quad (19)$$

The modulus of interfacial region is assumed to be

$$E_{il}(0) = E_{i2}(0) = kE_m \quad (20)$$

Where  $k$  represents the modulus ratio ( $1 < k < [E_d/E_m]$ ) of the neighboring interface surface of a dispersed particle. Thus the equation obtained is

$$\begin{aligned} \frac{1}{E_c} = & \frac{1 - \sqrt{[2(\tau/t) + 1]V_d}}{E_m} \\ & + \frac{\sqrt{[2(\tau/t) + 1]V_d} - \sqrt{V_d}}{\{1 - \sqrt{[2(\tau/t) + 1]V_d}\}E_m + [\sqrt{[2(\tau/t) + 1]V_d}(k - 1)E_m / \ln k]} \\ & + \frac{\sqrt{V_d}}{\{1 - \sqrt{[2(\tau/t) + 1]V_d}\}E_m + \{\sqrt{[2(\tau/t) + 1]V_d} - \sqrt{V_d}\}(k + 1)E_m / 2 + \sqrt{V_d}E_d} \end{aligned} \quad (21)$$

Using the above equation the effects of particle size, particle shape, thickness of interfacial region, modulus ratio of dispersoid phase to the matrix, and the  $k$  value on nanocomposites is studied.

### 3.4.3. Effect of $k$ Value

$k$  is the modulus ratio of the particle surface adjacent to the matrix and is usually in the range of  $1 < k < (E_d/E_m)$ .  $E_c$  increases with the increase of  $k$  and the variation is shown in **Figure 10**. The result shows that for higher clay content the experimental values better with theoretical values. Also the curve suggests that the interfacial modulus has considerable effect on tensile modulus of composite. At lower clay concentration, possibly interfacial moduli are higher or the model may not suit with experimental results.

### 3.4.4. Effect of Particle Size and Interface Thickness

The effect of particle size on the modulus of nanocomposites is studied and the results are shown in **Figure 11**. The thicknesses of layers are varied from 1 nm to 30 nm. Here the interface thickness is assumed as 10 nm and  $k$  as 30. By altering these parameters possibly some match between experimental and theoretical can be expected. **Figure 12** shows the effect of interface thickness on composite modulus. This suggests interface thickness has some influence in nanocomposite modulus.

## 3.5. Optical Dispersion Parameters

The above discussed theoretical models consider mostly the geometry and composition of composites. To some extent, they consider the interface characteristics in predicting the modulus values of composite series. Hence, most likely experimental and theoretical results do not match each other. In this section, optical dispersion parameters (namely: Agglomeration %, Exfoliation number, degree of dispersion) are taken in to consideration for predicting modulus values. These parameters are measured by viewing the composite material through Optical microscope (**Figure 13**) and Transmission Electron Microscope (**Figure 14**).

In **Figure 13** of OM, the bright phase is the matrix phase and the dark phase is the particle phase. As the clay concentration increases the clay stacking becomes more and hence more aggregated clay phase is seen. **Figure 14** shows the bright field TEM of PP-clay nanocomposites. Matrix phase represents the bright region and the dark phase represents the particle (clay) regions.

Agglomeration % (Agg. %) is the proportion of micron size agglomerates in Optical microscope, micron-size agglomerates larger than 5 microns are considered. The area lesser than 5 microns was analyzed using TEM images.

The Agg. % were calculated using OM and using the Equation (22)

$$\text{Agg. \%} = \frac{(\text{total area of clay dispersed in matrix}) \times 100}{(\text{agglomerated area of } > 5 \text{ microns})} \quad (22)$$

It is observed that Agg. % increases as clay concentration increases in polymer matrix. The exfoliation number ( $\xi_\eta$ ) is calculated from TEM pictures (**Figure 14**) as per Equation (23).

$$\xi_\eta = \frac{100(S_v)_{p-c}}{(S_v)_{total}} \quad (23)$$

where  $(S_v)_{p-c}$  is the polymer-clay interfacial area per unit volume of the specimen and  $(S_v)_{total}$  is the total clay

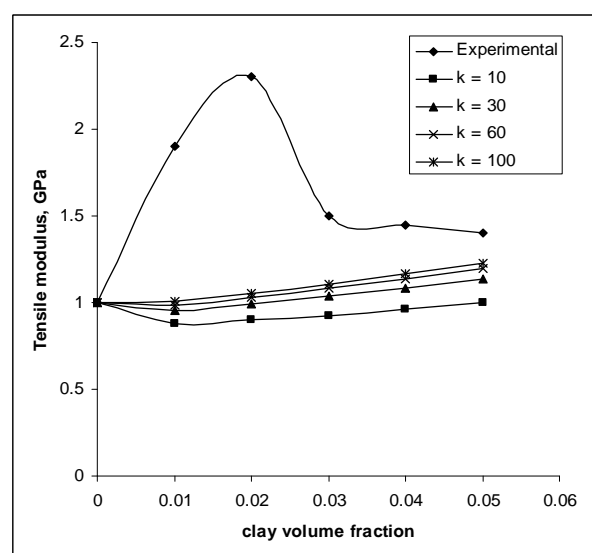


Figure 10. Effect of interface modulus.

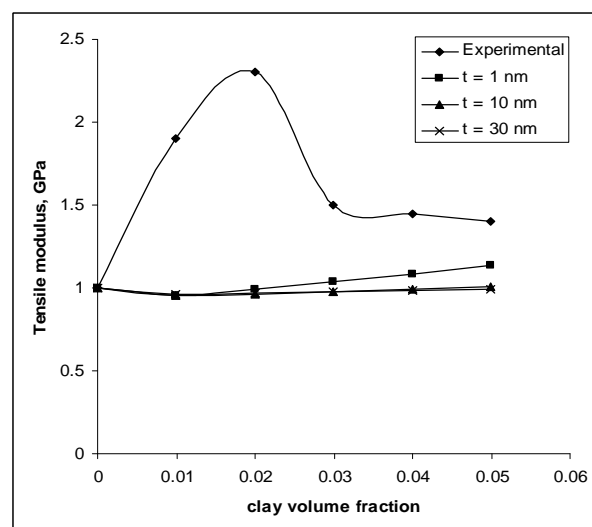


Figure 11. Effect of particle thickness.

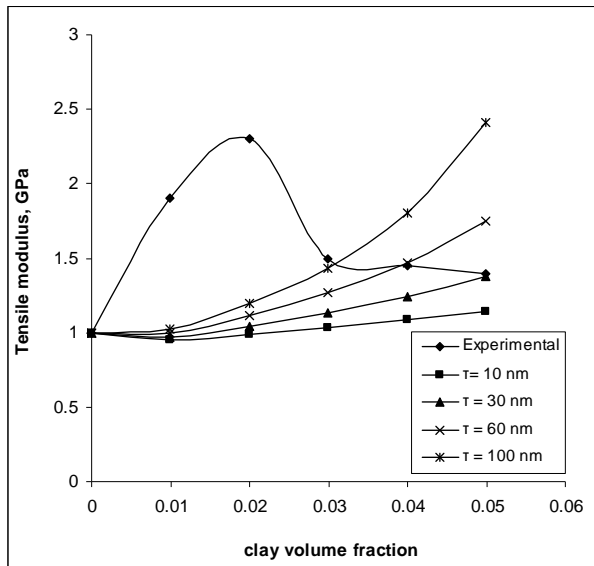
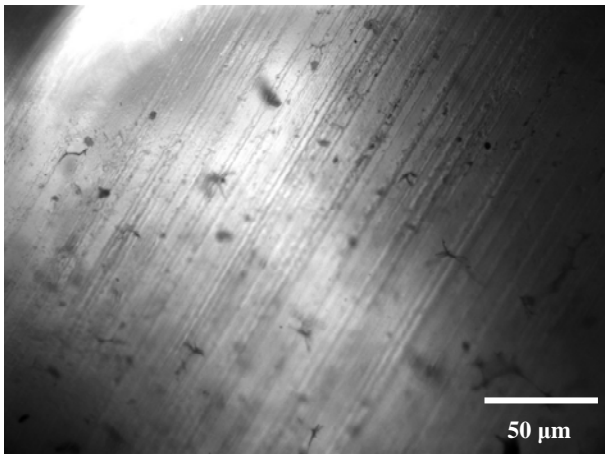
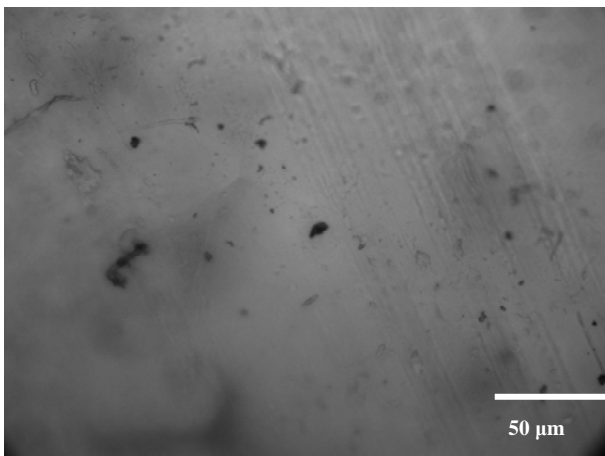


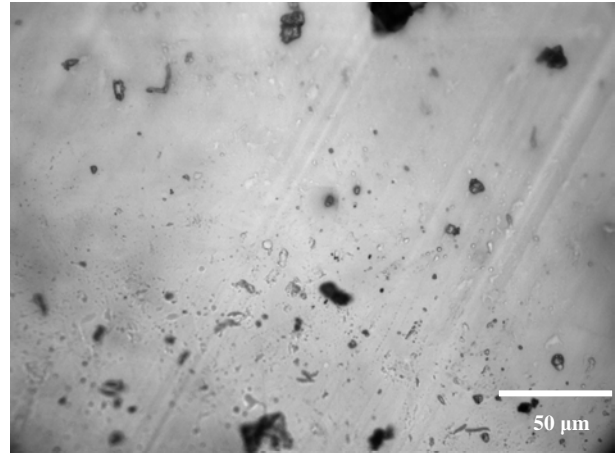
Figure 12. Effect of interface thickness.



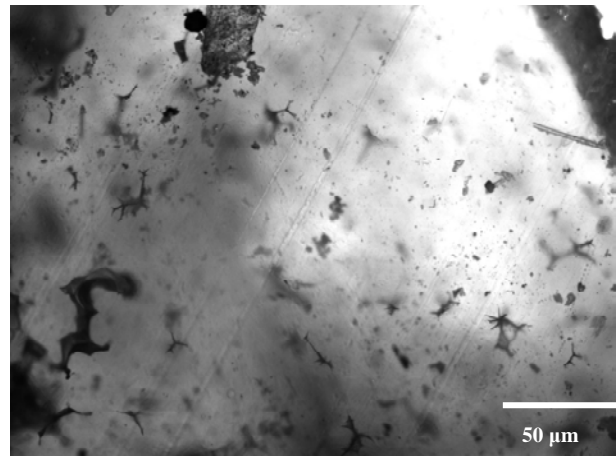
(a)



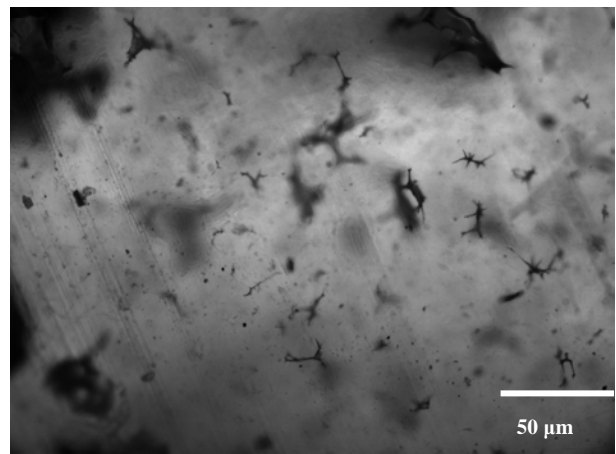
(b)



(c)

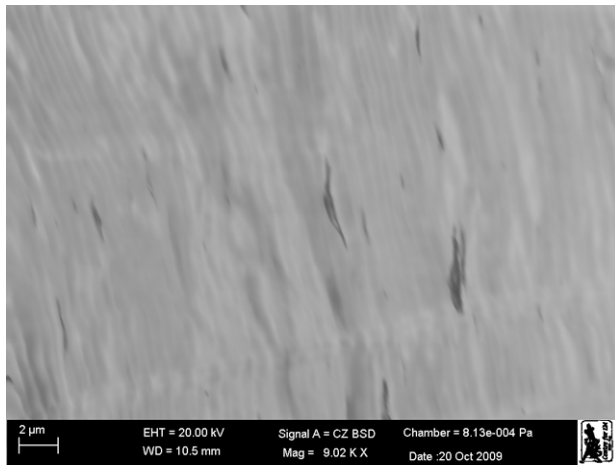


(d)

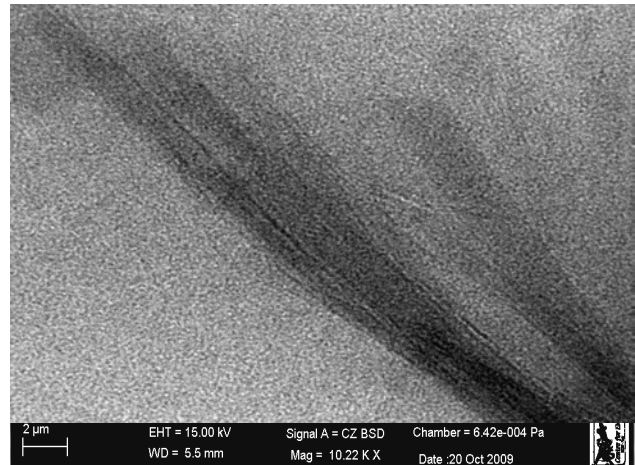


(e)

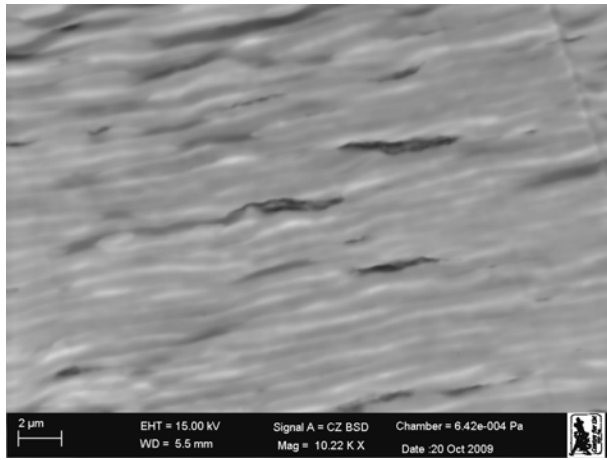
Figure 13. Optical microscope of PP with (a) 1%, (b) 2%, (c) 3%, (d) 4% and (d) 5% clay.



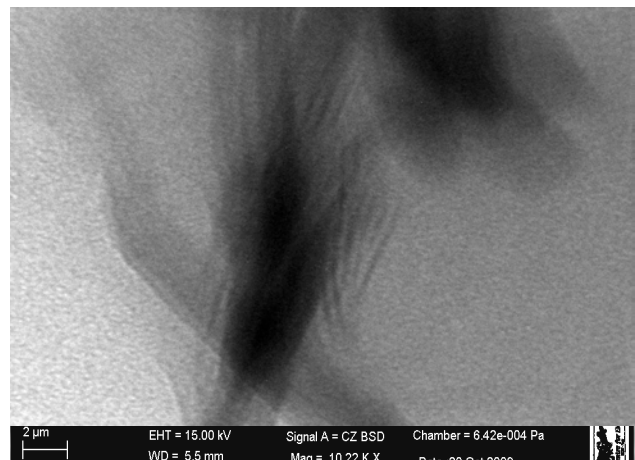
(a)



(d)



(b)



(e)

**Figure 14. TEM of PP with (a) 1%, (b) 2%, (c) 3%, (d) 4% and (e) 5% clay.**

$$(S_v)_{p-c} = \frac{4L_A}{\pi} \quad (24)$$

$$(S_v)_{total} = \frac{V_v}{0.94} \quad (25)$$

where  $L_A$  is the total length of perimeter of particles per unit area from TEM images,  $V_v$  is the volume fraction of clay estimated from the area fraction of all particles from TEM images. The degree of dispersions ( $\chi$ ) is calculated as per the Equation (26).

$$\chi = \xi_\eta (1 - \text{Agg.}\%) \quad (26)$$

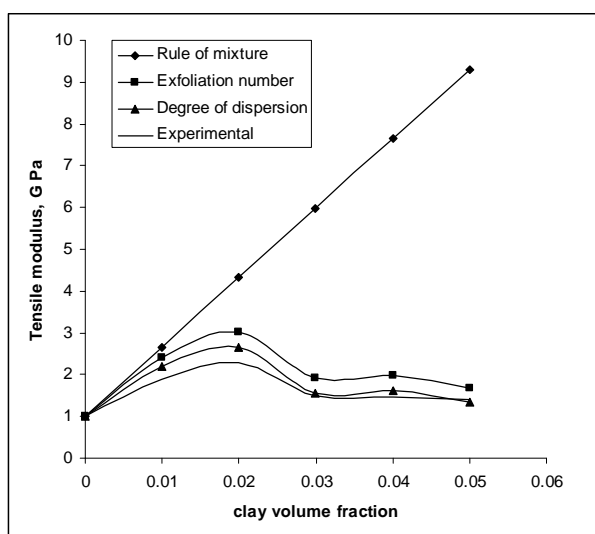
The values of these parameters are shown in **Table 1**. **Figure 15** shows the experimental values and values obtained from dispersion parameters. These parameter were compared and it is observed that these parameters fit well with experimental results. The resulted disper-

interfacial area exposed to the polymer matrix. 0 indicates no exfoliation and 100 indicate complete exfoliation.  $(S_v)_{p-c}$  and  $(S_v)_{total}$  are calculated as per Equations (24) and (25) respectively.



**Table 1. Nanocomposite dispersion data and property.**

Optical dispersion parameters	PP + 1% clay	PP + 2% clay	PP + 3% clay	PP + 4% clay	PP + 5% clay
Agg. %	8	12	18	19	20
Exfoliation No. ( $\xi_n$ )	90	70	32	26	18
Degree of dispersion ( $\chi$ )	83	62	26	21	14
Exptl. Tensile modulus, GPa	1.9	2.3	1.5	1.45	1.4

**Figure 15. Comparison of rules of mixtures, experimental obtained values and analytical dispersion parameters.**

sion parameter (Table 1) values are substituted with theoretical modulus from rules of mixtures and graphs are plotted. It is observed a close matching between dispersion parameters and experimental results.

#### 4. Conclusions

The structural changes that are taking place in PP- nano-clay systems are quantified as optical dispersion parameters and were measured using TEM and OM image analysis. The dispersion parameters measured were exfoliation number ( $\xi_n$ ), degree of dispersion ( $\chi$ ) and agglomerate concentration (Agg. %). These parameters were substituted in rules of mixtures (parallel model) to predict tensile modulus of nanocomposites and observed a good correlation between experimental and theoretical tensile modulus. Further, the modulus prediction by these optical dispersions method is better than other standard models. This good correlation of optical dispersion parameters with experimental results shows positive goal towards successfully measurement of tensile modulus.

#### 5. References

- [1] F. Perrin-Sarazin, M.-T. Ton-That, M. N. Bureau and J. Denault, "Micro- and Nano-Structure in Polypropylene /Clay Nanocomposites," *Polymer*, Vol. 46, No. 25, 2005, pp. 11624-11634.
- [2] B. Q. Chen and J. R.G. Evans, "Impact and Tensile Energies of Fracture in Polymer-Clay Nanocomposites," *Polymer*, Vol. 49, No. 23, 2008, pp. 5113-5118.
- [3] S. Pavlidou and C. D. Papaspyrides, "A Review on Polymer-Layered Silicate Nanocomposites," *Progress in Polymer Science*, Vol. 33, No. 12, 2008, pp. 1119-1198.
- [4] C. E. Powell and G. W. Beall, "Physical Properties of Polymer/Clay Nanocomposites," *Current Opinion in Solid State and Materials Science*, Vol. 10, No. 2, 2006, pp. 73-80.
- [5] N. Sheng, M. C. Boyce, D. M. Parks, G. C. Rutledge, J. I. Abes and R. E. Cohen, "Multiscale Micromechanical Modeling of Polymer/Clay Nanocomposites and the Effective Clay Particle," *Polymer*, Vol. 45, No. 2, 2004, pp. 487-506.
- [6] G. Scocchi, P. Posocco, A. Danani, S. Priol and M. O. Fermeiglia, "To the Nanoscale, and beyond: Multiscale Molecular Modeling of Polymer-Clay Nanocomposites," *Fluid Phase Equilibria*, Vol. 261, No. 1-2, 2007, pp. 366-374.
- [7] T. D. Fornes and D. R. Paul, "Modeling Properties of Nylon 6/Clay Nanocomposites Using Composite Theories," *Polymer*, Vol. 44, No. 17, 2003, pp. 4993-5013.
- [8] S. Boutaleb, F. Zaïri, A. Mesbah, M. Naït-Abdelaziz, J. M. Gloaguen, T. Boukharouba and J. M. Lefebvre, "Micromechanics-Based Modelling of Stiffness and Yield Stress for Silica/Polymer Nanocomposites," *International Journal of Solids and Structures*, Vol. 46, No. 7-8, 2009, pp. 1716-1726.
- [9] J.-J. Luo and I. M. Daniel, "Characterization and Modeling of Mechanical Behavior of Polymer/Clay Nanocomposites," *Composites Science and Technology*, Vol. 63, No. 11, 2003, pp. 1607-1616.
- [10] G. Tanaka and L. A. Goettler, "Predicting the Binding Energy for Nylon 6,6/Clay Nanocomposites by Molecular Modeling," *Polymer*, Vol. 43, No. 2, 2002, pp. 541-553.
- [11] Y.-P. Wu, Q.-X. Jia, D.-S. Yu and L.-Q. Zhang, "Modeling Young's Modulus of Rubber-Clay Nanocomposites Using Composite Theories," *Polymer Testing*, Vol. 23, No. 8, 2004, pp. 903-909.
- [12] S. K. Basu and Tewari, "Transmission Electron Microscopy Based Direct Mathematical Quantifiers for Dispersion in Nanocomposites," *Applied Physics Letters*, Vol. 91, No. 5, 2007, p. 053105.
- [13] J. C. Halpin and J. L. Kardos, "The Halping-Tsai Equations: A Review," *Polymer Engineering and Science*, Vol. 16, No. 5, 1976, pp. 344-352.
- [14] D. A. Bruce and J. Bicerano, "Micromechanics of Nanocomposites: Comparison of Tensile and Compressive Elastic Moduli, and Prediction of Effects of Incomplete

Exfoliation and Imperfect Alignment on Modulus," *Polymer*, No. 43, No. 2, 2002, pp. 269-287.

- [15] T. Mori and K. Tanaka, "Average Stress in Matrix and Average Elastic Energy of Materials with Misfitting In-

clusions," *Acta Metallurgica*, Vol. 21, No. 5, 1973, pp. 571-574.

- [16] L. J. Xiang, K. J. Jiao, W. Jiang and B. Z. Jiang, "Tensile Modulus of Polymer Nanocomposites," *Polymer Engineering and Science*, Vol. 42, No. 5, 2002, pp. 483-493.

## Notation

$\alpha$	length fraction of interface	$d_{ms}$	thickness of matrix in a stack
$\beta$	width fraction of interface	$E_c$	Young's modulus of composites
$\lambda$	length fraction of dispersoid	$E_m$	Young's modulus of matrix
$\varphi$	width fraction of dispersoid	$E_f$	Young's modulus of filler
$\chi$	degree of dispersions	$E_s$	Stack modulus
$\zeta$	shape factor of filler	$E_p$	Young's modulus of particle
$\eta$	modulus ratio factor	$V_f$	volume fraction of filler
$\tau$	interface thickness	$V_m$	volume fraction of matrix
$\xi_n$	exfoliation number	$E_{cl}$	clay modulus in stack
$\varepsilon_A, \varepsilon_B, \varepsilon_C$	elongation in region A, B and C respectively	$E_{mi}$	matrix modulus in stack
$a$	length of clay platelet	$V_{cl}$	volume fraction of clay in stack
$k$	interface modulus (modulus ratio)	$V_{mi}$	volume fraction of matrix in stack
$t$	nanoclay thickness	$L$	length of clay platelet
		$T$	applied load

# Nonlinear Control of an Induction Motor Using a Reduced-Order Extended Sliding Mode Observer for Rotor Flux and Speed Sensorless Estimation

Olivier Asseu<sup>1</sup>, Michel Abaka Kouacou<sup>1\*</sup>, Theophile Roch Ori<sup>1</sup>, Zié Yéo<sup>1</sup>, Malandon Koffi<sup>1</sup>,  
Xuefang Lin-Shi<sup>2</sup>

<sup>1</sup>Département Génie Electrique et Electronique, Institut National Polytechnique Houphouët Boigny  
(INP HB), BP 1093 Yamoussoukro Côte d'Ivoire

<sup>2</sup>Université de Lyon, AMPERE, INSA Lyon, CNRS UMR 5005, Villeurbanne 69621, France

E-mail: [abakaci@yahoo.fr](mailto:abakaci@yahoo.fr)

Received July 13, 2010; revised August 19, 2010; accepted August 21, 2010

## Abstract

This article proposes an innovative strategy to the problem of non-linear estimation of states for electrical machine systems. This method allows the estimation of variables that are difficult to access or that are simply impossible to measure. Thus, as compared with a full-order sliding mode observer, in order to reduce the execution time of the estimation, a reduced-order discrete-time Extended sliding mode observer is proposed for on-line estimation of rotor flux, speed and rotor resistance in an induction motor using a robust feedback linearization control. Simulations results on Matlab-Simulink environment for a 1.8 kW induction motor are presented to prove the effectiveness and high robustness of the proposed nonlinear control and observer against modeling uncertainty and measurement noise.

**Keywords:** Robust Nonlinear Control, Induction Motor, Reduced-Order Extended Sliding Mode Observers, Parameter Estimation

## 1. Introduction

The induction motors (IM) become very popular for motion control applications due to its reasonable cost, simple and reliable construction. However, the control of IM is proved very difficult since the dynamic systems are non linear, the electric rotor variables are not usually measurable or the transducers are expensive (such as torque, speed, flux transducers) and the physical parameters are often imprecisely known or variable. For instance, the rotor resistance drifts with the temperature of the rotor current frequency.

This naturally structure of non-linear and multivariable state of IM models induces the use of the non-linear control methods and in particular the robust feedback linearization strategy [1-3] to permit a decoupling, assure a good dynamic performance and stability of the IM.

However, a variation of the rotor resistance can induce a state-space “coupling” which can induce a degradation of the system. In order to achieve better dynamic performance, an on-line estimation of rotor fluxes, speed and rotor resistance is necessary. An approach proposed

in [4,5] to estimate with success the state variables in an IM is the use of the full-order Sliding Mode Observer (SMO). This latter, built from the dynamic model of the IM by adding corrector gains with switching terms, is used to provide not only the unmeasurable state variable estimation (rotor fluxes and speed) but also the estimation of the measurable parameters (stator currents). However the determination of the measurable parameters estimation imposes some estimation algorithms very long and usually sophisticated with an increase of the computational volume. Therefore, in order to reduce the accuracy and the computation rate of the estimation algorithms, the measured parameters estimation is not necessary.

Thus a Reduced-Order Discrete-Time Extended Sliding Mode Observer (RDESMO) for the IM is presented in this paper to solve only and specially the problem of the unmeasurable parameters estimation (rotor fluxes, speed and rotor time constant).

So after a brief review of the IM model, a robust input-output linearization and decoupling control of induction motor is presented in Section 2. A reduced-order

discrete-time Extended Sliding Mode Observer (ESMO) is developed in Section 3. Section 4 describes the simulation results carried out on a 1.8 kW IM drive system. Finally, conclusions are summarized in Section 5.

## 2. Induction Motor Model and Robust Feedback Control

By assuming that the saturation of the magnetic parts and the hysteresis phenomenon are neglected, the classical dynamic model of the IM in a  $(d, q)$  synchronous reference frame can be described by [6]:

$$\begin{cases} V_{ds} = R_s I_{ds} + \frac{d\Phi_{ds}}{dt} - \omega_s \Phi_{qs} \\ V_{qs} = R_s I_{qs} + \frac{d\Phi_{qs}}{dt} + \omega_s \Phi_{ds} \end{cases}; \begin{cases} \Phi_{ds} = \frac{L_m}{L_r} \Phi_{dr} + \sigma L_s I_{ds} \\ \Phi_{qs} = \frac{L_m}{L_r} \Phi_{qr} + \sigma L_s I_{qs} \end{cases} \quad (1.a)$$

$$\begin{bmatrix} \Phi_{ds} \\ \Phi_{dr} \end{bmatrix} = \begin{bmatrix} L_s & L_m \\ L_m & L_r \end{bmatrix} \begin{bmatrix} I_{ds} \\ I_{dr} \end{bmatrix}; \quad \begin{bmatrix} \Phi_{qs} \\ \Phi_{qr} \end{bmatrix} = \begin{bmatrix} L_s & L_m \\ L_m & L_r \end{bmatrix} \begin{bmatrix} I_{qs} \\ I_{qr} \end{bmatrix} \quad (1.b)$$

The load mechanical equation is:

$$\frac{J}{p} \frac{d\omega_r}{dt} + \frac{f}{J} \omega_r = C_{em} - C_r \quad \text{where} \quad C_{em} = p \cdot \frac{L_m}{L_r} (\Phi_{dr} I_{qs} - \Phi_{qr} I_{ds}) \quad (1.c)$$

The application of (1.a) to (1.c) returns a system of fifth-order non-linear differential equation, with as state variables the stator currents ( $I_{ds}, I_{qs}$ ), the rotor fluxes ( $\Phi_{dr}, \Phi_{qr}$ ) and the rotor pulsation ( $\omega_r$ ):

$$\begin{aligned} \dot{x}_c &= f_c(x_c) + g_c \cdot u \quad \text{where} \\ x_c &= [I_{ds} \ I_{qs} \ \Phi_{dr} \ \Phi_{qr} \ \omega_r]^t, u = [V_{ds} \ V_{qs}]^t \\ f_c(x_c) &= \begin{bmatrix} -\lambda I_{ds} + \omega_s I_{qs} + \sigma_r \beta \Phi_{dr} + \beta \omega_r \Phi_{qr} \\ -\omega_s I_{ds} - \lambda I_{qs} - \beta \omega_r \Phi_{dr} + \beta \sigma_r \Phi_{qr} \\ \sigma_r L_m I_{ds} - \sigma_r \Phi_{dr} + \omega_{sl} \Phi_{qr} \\ \sigma_r L_m I_{qs} - \omega_{sl} \Phi_{dr} - \sigma_r \Phi_{qr} \\ p^2 \cdot \frac{L_m}{L_r J} (\Phi_{dr} I_{qs} - \Phi_{qr} I_{ds}) - \frac{p}{J} C_r - \frac{f}{J} \omega_r \end{bmatrix}; \\ g_c &= \begin{bmatrix} \frac{1}{\sigma L_s} & 0 \\ 0 & \frac{1}{\sigma L_s} \\ 0 & 0 \\ 0 & 0 \\ 0 & 0 \end{bmatrix} \end{aligned} \quad (2)$$

$$\sigma_r = \frac{1}{T_r}; \quad \lambda = \lambda(\sigma_r) = \frac{1}{\sigma} \left( \frac{1}{T_s} + (1-\sigma)\sigma_r \right); \\ \beta = \frac{1-\sigma}{\sigma L_m}; \quad \sigma = 1 - \frac{L_m^2}{L_s L_r}$$

Moreover, by choosing a rotating reference frame  $(d, q)$  so that the direction of axe  $d$  is always coincident with the direction of the rotor flux representative vector (field orientation), it is well known that this rotor field orientation in a rotating synchronous reference frame realizes:

$$\Phi_{dr} = \Phi_r = \text{Constant and } \Phi_{qr} = 0 \quad (3)$$

Thus the dynamic model of the IM, completed with the output equation, can be rewritten as:

$$\dot{x} = f(x) + g \cdot u; \quad y = [h_1(x) \ h_2(x)]^t = [\Phi_r \ \omega_r]^t \quad \text{with} \\ x = [I_{ds} \ I_{qs} \ \Phi_r \ \omega_r]^t, u = [V_{ds} \ V_{qs}]^t$$

$$f(x) = \begin{bmatrix} -\lambda I_{ds} + \omega_s I_{qs} + \sigma_r \beta \Phi_r \\ -\omega_s I_{ds} - \lambda I_{qs} - \beta \omega_r \Phi_r \\ \sigma_r L_m I_{ds} - \sigma_r \Phi_r \\ p^2 \cdot \frac{L_m}{L_r J} \Phi_r I_{qs} - \frac{p}{J} C_r - \frac{f}{J} \omega_r \end{bmatrix}; \quad (4)$$

$$g = \begin{bmatrix} \frac{1}{\sigma L_s} & 0 \\ 0 & \frac{1}{\sigma L_s} \\ 0 & 0 \\ 0 & 0 \end{bmatrix}$$

From the expressions (2) and (3), one can write:

$$\begin{cases} \frac{dI_{mr}}{dt} = \sigma_r I_{ds} - \sigma_r I_{mr} \\ \sigma_r = \omega_{sl} \cdot \frac{I_{mr}}{I_{qs}} \\ C_{em} = \frac{p L_m}{L_r} \Phi_r I_{qs} \end{cases} \quad \text{with} \quad I_{mr} = \frac{\Phi_r}{L_m} \quad (5)$$

This relation (5) shows that the dynamic model of the IM can be represented as a non-linear function of the rotor time constant. A variation of this parameter can induce, for the IM, a lack of field orientation, performance and stability. Thus, to preserve the reliability, robustness performance and stability of the system under parameters variation (in particular the rotor time constant variations) and disturbances, we can use a robust feedback linearization strategy to regulate the motor states.

As a matter of fact, we can see that the system (4) has relative degree  $r_1 = r_2 = 2$  and can be transformed into a linear and controllable system by chosen [7]:

- a suitable change of coordinates given by:  
 $z_1 = h_1(x); \quad z_2 = L_f h_1(x); \quad z_3 = h_2(x);$

$$z_4 = L_f h_2(x);$$

- the feedback linearization control having the following form:

$$u = \begin{bmatrix} L_{g1}L_f h_1(x) & L_{g2}L_f h_1(x) \\ L_{g1}L_f h_2(x) & L_{g2}L_f h_2(x) \end{bmatrix}^{-1} \begin{bmatrix} v_1 - L_f^2 h_1(x) \\ v_2 - L_f^2 h_2(x) \end{bmatrix}$$

where  $v_1$  and  $v_2$  are the new inputs of the obtained decoupled systems

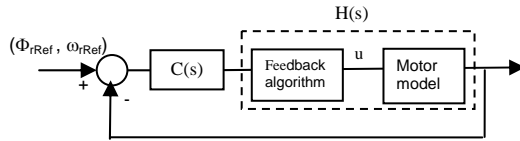
- and two robust controllers  $C(s)$  to provide a good regulation and convergence of the rotor flux ( $\Phi_r$ ) and speed ( $\omega_r$ ). On the other hand, in order to impose after a closed loop a second order dynamic behaviour defined by  $H(s)$ , the controller  $C(s)$  can be chosen by [8]:

$$C(s) = \frac{J(s)H(s)^{-1}}{1-J(s)}; \quad J(s) = \frac{1}{(1+t_0s)^2};$$

$$H(s) = \frac{1}{1 + \frac{2\xi_0}{\omega_0}s + \frac{1}{\omega_0^2}s^2} \quad (6)$$

where the real  $t_0$  is an adjusting positive parameter.

The block diagram structure for the control of ( $\Phi_r$ ,  $\omega_r$ ) is as follows:



Furthermore, as the control of an IM generally required the knowledge of the instantaneous flux of the rotor that is not measurable, a full-order SMO built from the model (2) by adding corrector gains with switching terms is widely used [7,9] with success for on-line estimation at one and the same time of rotor time constant, fluxes, currents or speed. The equivalent value of the switching function depends on the current errors given by the difference between the estimated currents to their real or measured values. However, as the currents are already measurable, their estimated values are not therefore necessary.

Thus in the next section, in order to reduce the execution time of the observation with respect to the rotor time constant variations, a RDESMO is proposed to provide only the unmeasurable parameters estimation (rotor fluxes, rotor time constant and speed). And the switching term of this reduced observer will be only function of the measurable parameters (voltage, currents...).

### 3. Reduced-Order Discrete-Time Extended Sliding Mode Observer

#### 3.1 Reduced-Order Sliding Mode Observer

Let us consider the dynamic model of the IM given by the system (2). Assume that among the state variable, the

stator currents ( $I_{ds}$ ,  $I_{qs}$ ) are measurable, therefore their on-line estimation is not necessary. Thus from the expression (2), in order to estimate only the rotor flux ( $\Phi_{dr}$ ,  $\Phi_{qr}$ ) and speed ( $\omega_r$ ), a reduced dimensional state vector defined by  $X_r = [\Phi_{dr} \ \Phi_{qr} \ \omega_r]^T = [x_1 \ x_2 \ x_3]^T$ , T can be introduced. The corresponding reduced-order state space equation becomes:

$$\dot{x}_r(t) = J_r(x_r(t), v(t))$$

Where  $v(t) = [I_{ds}, I_{qs}]^T$  is the new input.

$$J_r(x_r(t), v(t)) = \begin{pmatrix} -\sigma_r x_1 + \omega_{sl} x_2 + \sigma_r L_m I_{ds} \\ -\omega_{sl} x_1 - \sigma_r x_2 + \sigma_r L_m I_{qs} \\ p^2 \frac{L_m}{L_r J} (I_{qs} x_1 - I_{ds} x_2) - \frac{p}{J} C_r - \frac{f}{J} x_3 \end{pmatrix} \quad (7)$$

The fact that the state vector only consists of the rotor flux and speed offers an advantage namely the reduction of the computational volume and complexity. Thus the rotor flux and speed can be more easily and rapidly estimated. Denote  $\hat{x}_1$ ,  $\hat{x}_2$  and  $\hat{x}_3$  the estimates of the fluxes  $\Phi_{dr}$ ,  $\Phi_{qr}$  and  $\omega_r$ . The Reduced-order SMO is a copy of the model (7) by adding corrector gains with switching terms:

$$\begin{cases} \dot{\hat{x}}_1 = -\sigma_r \hat{x}_1 + \omega_{sl} \hat{x}_2 + \sigma_r L_m I_{ds} + \Gamma_1 I_s \\ \dot{\hat{x}}_2 = -\omega_{sl} \hat{x}_1 - \sigma_r \hat{x}_2 + \sigma_r L_m I_{qs} + \Gamma_2 I_s \\ \dot{\hat{x}}_3 = p^2 \frac{L_m}{L_r J} (I_{qs} \hat{x}_1 - I_{ds} \hat{x}_2) - \frac{p}{J} C_r - \frac{f}{J} x_3 + \Gamma_3 I_s \end{cases} \quad (8)$$

where  $\Gamma_1$ ,  $\Gamma_2$  and  $\Gamma_3$  are the observer gains. The switching "Is" is defined as

$$I_s = \begin{bmatrix} \text{sign}(s_1) \\ \text{sign}(s_2) \end{bmatrix}; \quad S = \begin{bmatrix} s_1 \\ s_2 \end{bmatrix} = M \tilde{Z}_r; \quad (9)$$

$$M = \begin{bmatrix} \beta \sigma_r & \beta \hat{x}_3 \\ -\beta \hat{x}_3 & \beta \sigma_r \end{bmatrix}^{-1}$$

where  $\tilde{Z}_r$  is a function depending on the parameters measurements (stator currents, voltages...).

Setting  $\tilde{x} = x - \hat{x}$ , the estimation error dynamics is given by:

$$\begin{cases} \dot{\tilde{x}}_1 = -\sigma_r \tilde{x}_1 + \omega_{sl} \tilde{x}_2 - \Gamma_1 I_s \\ \dot{\tilde{x}}_2 = -\omega_{sl} \tilde{x}_1 - \sigma_r \tilde{x}_2 - \Gamma_2 I_s \\ \dot{\tilde{x}}_3 = p^2 \frac{L_m}{L_r J} (\tilde{x}_1 I_{qs} - \tilde{x}_2 I_{ds}) - \frac{f}{J} \tilde{x}_3 - \Gamma_3 I_s \end{cases} \quad (10)$$

With the following observer gain matrices given by the expression (11), the estimation error  $[\tilde{x}_1, \tilde{x}_2, \tilde{x}_3]$  converges to zero.

$$\begin{bmatrix} \Gamma_1 \\ \Gamma_2 \\ \Gamma_3 \end{bmatrix} = \begin{bmatrix} r - \sigma_r & \omega_{sl} \\ -\omega_{sl} & r - \sigma_r \\ p^2 \cdot \frac{L_m I_{qs}}{L_r J} & -p^2 \cdot \frac{L_m I_{ds}}{L_r J} \end{bmatrix} \Delta; \quad \Delta = \begin{bmatrix} n & 0 \\ 0 & n \end{bmatrix} \quad (11)$$

where  $r$  and  $n$  are positive adjusting parameters which play a critical role in the stability and the velocity of the observer convergence.

### 3.2. Reduced-Order Extended Sliding Mode Observer

In order to estimate the rotor time constant, a reduced dimensional extended state vector defined by  $X_{re} = [\Phi_{dr} \ \Phi_{qr} \ \omega_r \ \sigma_r]^T = [x_1 \ x_2 \ x_3 \ x_4]^T$  has been introduced with  $\sigma_r = R_r/L_r$ . The corresponding reduced-order extended state equation becomes:

$$\dot{x}_{re}(t) = J_{re}(x_{re}(t), v(t)) \quad \text{where}$$

$$J_{re}(x_r(t), v(t)) = \begin{pmatrix} -x_4 \cdot x_1 + \omega_{sl} \cdot x_2 + x_4 \cdot L_m I_{ds} \\ -\omega_{sl} \cdot x_1 - x_4 \cdot x_2 + x_4 \cdot L_m I_{qs} \\ p^2 \cdot \frac{L_m}{L_r J} \cdot (I_{qs} \cdot x_1 - I_{ds} \cdot x_2) - \frac{p}{J} \cdot C_r - \frac{f}{J} \cdot x_3 \\ \varepsilon \end{pmatrix} \quad (12)$$

where  $\varepsilon$  presents the slow variation of  $\sigma_r$ . The proposed Reduced-order ESMO is:

$$\begin{cases} \dot{\hat{x}}_1 = -\hat{x}_4 \cdot \hat{x}_1 + \omega_{sl} \cdot \hat{x}_2 + \hat{x}_4 \cdot L_m I_{ds} + \Gamma_1 I_s \\ \dot{\hat{x}}_2 = -\omega_{sl} \cdot \hat{x}_1 - \hat{x}_4 \cdot \hat{x}_2 + \hat{x}_4 \cdot L_m I_{qs} + \Gamma_2 I_s \\ \dot{\hat{x}}_3 = p^2 \cdot \frac{L_m}{L_r J} \cdot (I_{qs} \cdot \hat{x}_1 - I_{ds} \cdot \hat{x}_2) - \frac{p}{J} \cdot C_r - \frac{f}{J} \cdot \hat{x}_3 + \Gamma_3 I_s \\ \dot{\hat{x}}_4 = \varepsilon + \Gamma_4 I_s \end{cases} \quad (13)$$

where is,  $\Gamma_1$ ,  $\Gamma_2$  and  $\Gamma_3$  are respectively defined by (9) and (11).

To determine observer gain  $\Gamma_4$ , it can be supposed that the observation errors of the fluxes converge to zero. The estimation errors of the fluxes  $\tilde{x}_i = x_i - \hat{x}_i = 0$  ( $i = 1, 2$ ) are then given by:

$$\begin{aligned} 0 &= -\tilde{x}_4 \cdot \hat{x}_1 + \hat{x}_4 \cdot \tilde{x}_1 + \omega_{sl} \cdot \tilde{x}_2 + L_m I_{ds} \cdot \tilde{x}_4 - \Gamma_1 I_s \\ 0 &= -\omega_{sl} \cdot \tilde{x}_1 - \tilde{x}_4 \cdot \hat{x}_2 + \hat{x}_4 \cdot \tilde{x}_2 + L_m I_{qs} \cdot \tilde{x}_4 - \Gamma_2 I_s \end{aligned} \quad (14)$$

By replacing the expressions of 1 and 2 in (14), the estimation error dynamics of the rotor time constant is given by:

$$\tilde{x}_4 = -\Gamma_4 I_s = -\Gamma_4 \Delta^{-1} \begin{bmatrix} \tilde{x}_1 \\ \tilde{x}_2 \end{bmatrix} = -\Gamma_4 \Delta^{-1} \cdot \frac{1}{r} \cdot \begin{bmatrix} L_m I_{ds} - \hat{x}_1 \\ L_m I_{qs} - \hat{x}_2 \end{bmatrix} \cdot \tilde{x}_4$$

We can see that this error dynamics is locally and exponentially stable by chosen:

$$\Gamma_4 = m \cdot r \cdot \begin{bmatrix} L_m I_{ds} - \hat{x}_1 \\ L_m I_{qs} - \hat{x}_2 \end{bmatrix}^T \cdot \Delta \quad \text{with } m > 0 \quad (15)$$

The parameter  $m$  is adjusted with respect to rotor time constant estimation.

Finally, from the expressions (11) and (15), it can be seen that there are three positive adjusting gains:  $r$ ,  $n$  and  $m$  which play a critical role in the stability and the velocity of the observer convergence. These three adjusting parameters must be chosen so that the reduced observer satisfies robustness properties, global or local stability, good accuracy and considerable rapidity.

In order to implement the reduced-order ESMO algorithm in a DSP for real-time applications, the corresponding reduced-dimension state space equation defined in (12) must be discretized using Euler approximation (1st order). Thus the new discrete-time varying model represented by a function depending on the stator current is given by:

$$\begin{cases} x_{re}(k+1) = x_{re}(k) + T_e \cdot J_{re}(x_{re}(k), v(k)) = x_{re}(k) + T_e \cdot q(x_{re}(k), v(k)) \\ y_{re}(k) = x_{re}(k) \end{cases}$$

with

$$q(x_{re}(k), v(k)) = \begin{bmatrix} -\sigma_r(k) \cdot \Phi_{dr}(k) + \omega_{sl}(k) \cdot \Phi_{qr}(k) + \sigma_r(k) \cdot L_m I_{ds}(k) \\ -\omega_{sl}(k) \cdot \Phi_{dr}(k) - \sigma_r(k) \cdot \Phi_{qr}(k) + \sigma_r(k) \cdot L_m I_{qs}(k) \\ p^2 \cdot \frac{L_m}{L_r J} \cdot [I_{qs}(k) \cdot \Phi_{dr}(k) - I_{ds}(k) \cdot \Phi_{qr}(k)] - \frac{p}{J} \cdot C_r - \frac{f}{J} \cdot \omega_1(k) \\ 0 \end{bmatrix}; \quad (16)$$

where  $k$  means the  $k$ th sampling time, i.e.  $t = k \cdot T_e$  with  $T_e$  the adequate sampling period chosen without failing the stability and the accuracy of the discrete-time model. The proposed RDESMO can be defined by the following equation:

$$\hat{x}_{re}(k+1) = \hat{x}_{re}(k) + T_e \cdot q(\hat{x}_{re}(k), v(k)) + G(k) \cdot I_s(k) \quad (17)$$

where the prediction vector is:

$$\tilde{x}_{re}(k+1) = \tilde{x}_{re}(k) + T_e \cdot q(\tilde{x}_{re}(k), v(k))$$

$$\text{with } \tilde{x}_{re}(k) = [\tilde{\Phi}_{dr}(k) \ \tilde{\Phi}_{qr}(k) \ \tilde{\omega}_r(k) \ \tilde{\sigma}_r(k)]^T$$

The switching vector  $I_s(k)$ , deduced from the continuous case given by (9), can be written as:

$$I_s(k) = \begin{bmatrix} \text{sign}(s_1(k)) \\ \text{sign}(s_2(k)) \end{bmatrix} \quad \text{with} \quad (18)$$

$$S = \begin{bmatrix} s_1(k) \\ s_2(k) \end{bmatrix} = T_e \cdot M(k) \cdot \tilde{Z}(k+1)$$

where

$$M(k) = \begin{pmatrix} -\hat{\sigma}_r(k) & \omega_{sl}(k) \\ -\omega_{sl}(k) & -\hat{\sigma}_r(k) \end{pmatrix},$$

$$\tilde{z}(k+1) = \begin{pmatrix} z_{rd}(k+1) - \hat{z}_{rd}(k+1) \\ z_{rq}(k+1) - \hat{z}_{rq}(k+1) \end{pmatrix}$$

Let us introduce the measure vector

$z_r(k+1) = [z_{rd}(k+1), z_{rq}(k+1)]T$  written as follows:

$$z_{rd}(k+1) = \Phi_{dr}(k+1) - \Phi_{dr}(k) - T_e \cdot \omega_s(k) \cdot \Phi_{qr}(k) \quad \text{and}$$

$$z_{rq}(k+1) = \Phi_{qr}(k+1) - \Phi_{qr}(k) + T_e \cdot \omega_s(k) \cdot \Phi_{dr}(k)$$

From the electrical Equation (1.a) of the IM, an approximate (1st order) discrete-time relation of the fluxes is given by:

$$\begin{cases} z_{rd}(k+1) = \frac{T_e L_r}{L_m} [V_{ds}(k) - R_s I_{ds}(k)] - \frac{\sigma L_s L_r}{L_m} [I_{ds}(k+1) - I_{ds}(k) - T_e \omega_s(k) I_{qs}(k)] \\ z_{rq}(k+1) = \frac{T_e L_r}{L_m} [V_{qs}(k) - R_s I_{qs}(k)] - \frac{\sigma L_s L_r}{L_m} [I_{qs}(k+1) - I_{qs}(k) + T_e \omega_s(k) I_{ds}(k)] \end{cases} \quad \text{and} \quad (19)$$

$$\begin{pmatrix} \hat{z}_{rd}(k+1) \\ \hat{z}_{rq}(k+1) \end{pmatrix} = \begin{pmatrix} \tilde{\Phi}_{dr}(k+1) - \tilde{\Phi}_{dr}(k) - T_e \omega_s(k) \cdot \tilde{\Phi}_{qr}(k) \\ \tilde{\Phi}_{qr}(k+1) - \tilde{\Phi}_{qr}(k) + T_e \omega_s(k) \cdot \tilde{\Phi}_{dr}(k) \end{pmatrix}$$

The proposed gain matrix representation  $G(k)$ , deduced from the continuous case given by (11) and (15),

can be defined as follows (discrete-time approach):

$$G_r(k) = \begin{pmatrix} \Gamma_1(k) \\ \Gamma_2(k) \\ \Gamma_3(k) \\ \Gamma_4(k) \end{pmatrix} = \begin{pmatrix} r - T_e \cdot \hat{\sigma}_r(k) & T_e \cdot \omega_{sl}(k) \\ -T_e \cdot \omega_{sl}(k) & r - T_e \cdot \hat{\sigma}_r(k) \\ T_e \cdot p^2 \cdot \frac{L_m \cdot I_{qs}}{L_r \cdot J} & T_e \cdot p^2 \cdot \frac{L_m \cdot I_{ds}}{L_r \cdot J} \\ T_e \cdot (m L_m I_{ds}(k) - \hat{\Phi}_{dr}(k)) & T_e \cdot (m L_m I_{qs}(k) - \hat{\Phi}_{qr}(k)) \end{pmatrix} \Delta \quad (20)$$

Once the fluxes are estimated, it is easy to deduce the estimated torque defined by:

$$\hat{C}_{em}(k) = p \cdot \frac{L_m}{L_r} (\hat{\Phi}_{dr}(k) \cdot I_{qs}(k) - \hat{\Phi}_{qr}(k) \cdot I_{ds}(k)) \quad (21)$$

## 4. Simulation Results

In order to verify the feasibility of the proposed RDESMO, the simulation on SIMULINK from Mathwork has been carried out for a 1.8 kW induction motor controlled with a robust linearization via feedback algorithm (**Figure 1**). The nominal parameters of the induction motor are given in the **Table 1**.

The RDESMO is implanted in a S\_function using C language. In order to evaluate its performances and effectiveness, the comparisons between the observed state variables and the simulated ones have been realized for several operating conditions with the presence of about 15% noise on the simulated currents ( $I_{ds}$ ,  $I_{qs}$ ) or speed. Thus, using a sampling period  $T_e = 1$  ms, the simulations are realized at first in the nominal case with the nominal parameters of the induction motor (**Table 1**) and then, in

the second case, with 50% variation of the nominal rotor time constant ( $\sigma_r = 1.5 \sigma_{rn}$ ) in order to verify the rotor time constant tracking and flux estimation.

**Figure 2** and **Figure 3** show the simulation results for a step input of the rotor speed and flux. One can see that in both nominal (**Figures 2(a), 2(c)**) or non-nominal (**Figures 3(a'), 3(c')**) cases, the estimated values of fluxes and torque converge very well to their simulated values.

The observed fluxes (**Figure 2(a)**) indicate the good orientation ( $\Phi_{dr}$  is constant and  $\Phi_{qr}$  converges to zero) which is due to a favorable rotor time constant estimation (**Figures 2(b), 3(b')**). The estimated torque (**Figure 2(c)**) is in good agreement with the simulated value.

Once the fluxes are estimated, we can deduce the algorithm of the feedback linearization control (**Figure 1**). The waveforms show the good uncoupling between the rotor flux and the speed because a step variation in  $\Phi_{dr}$  (**Figure 2(a)** and **Figure 3(a')**) can not generate a speed  $r$  change (**Figure 2(d)** and **Figure 3(d')**). Thus the field orientation and the synthesis of robust linearization and decoupling control are well verified.

All those results show the satisfying tuning, the excellent performance of the robust decoupling control and



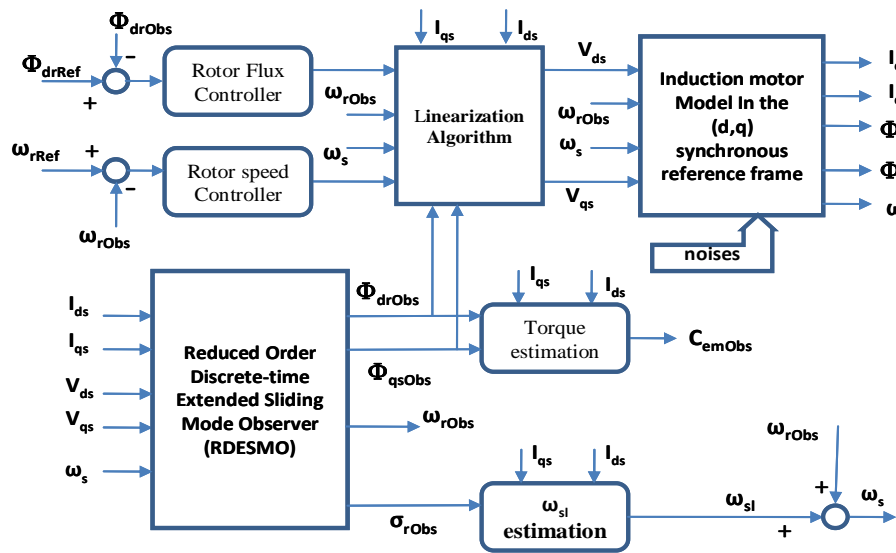
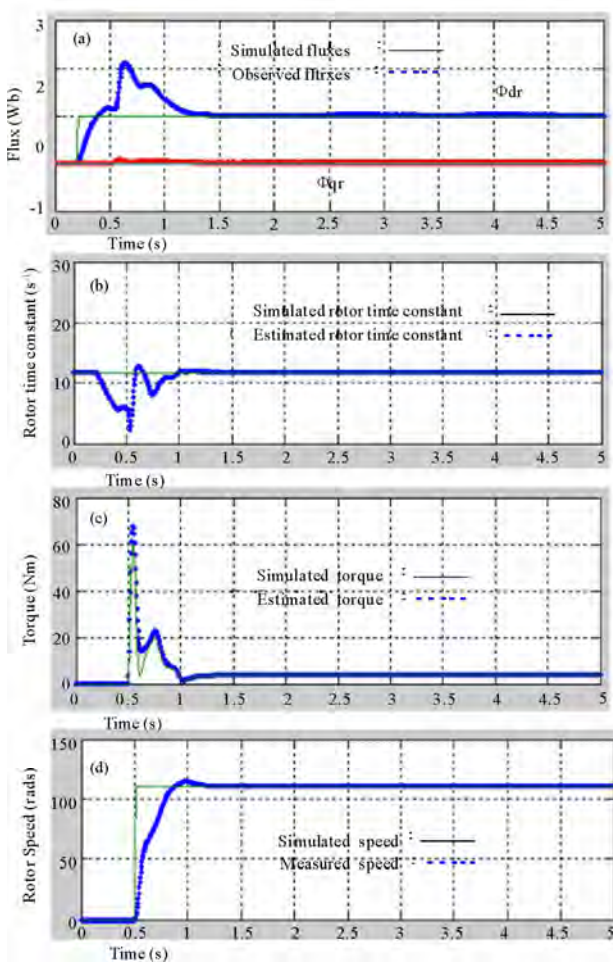
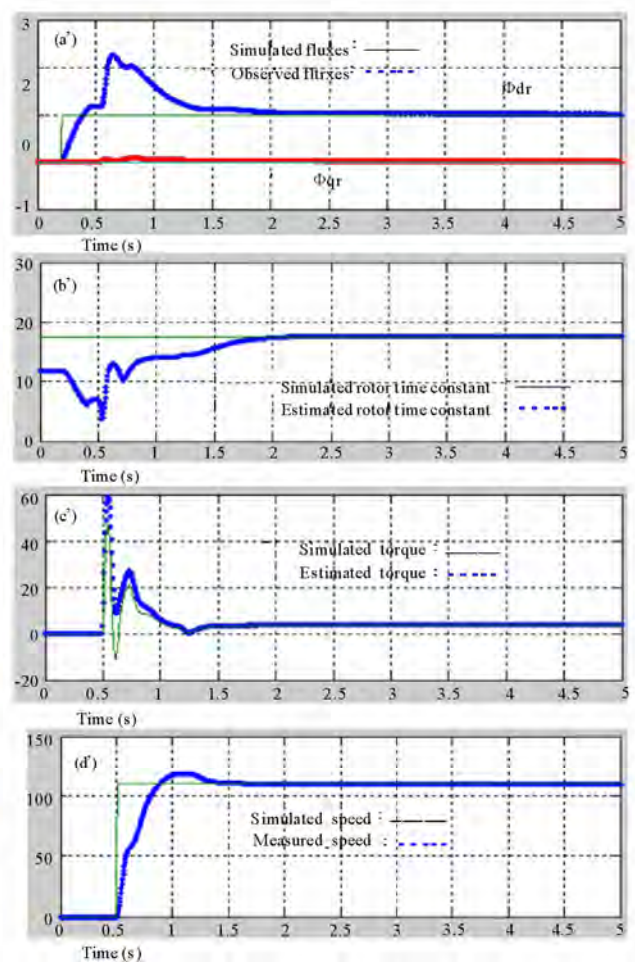


Figure 1. Simulation scheme of the system.

Figure 2. (a, b, c, d): Nominal case ( $R_r = R_{rn}$ ).Figure 3. (a', b', c', d'): Non nominal case ( $R_r = 1.5R_{rn}$ ).

**Table 1. Nominal parameters of the induction motor.**

$P_{mn} = 1.8 \text{ kW}$	$U_n = 220/380 \text{ V}$	$I_n = 20.8/12 \text{ A}$	$p = 2$
$F_n = 50 \text{ Hz}$	$n = 1420 \text{ rpm}$	$J_n = 0.15 \text{ kg.N/m}^2$	$f_n = 0.05 \text{ N.m.s/rad}$
$R_{sn} = 5.7$	$R_{rn} = 1.475$	$L_{sn} = 0.1766 \text{ H}$	$L_{rn} = 0.1262 \text{ H}$
$L_{m1} = 0.0504 \text{ H}$	$L_{m2} = 0.1262 \text{ H}$		

RDESMO against rotor resistance variations and perturbations or noises.

## 5. Conclusions

We have shown in this paper that a robust feedback linearization strategy and RDESMO are used to permit a regulation and observation for the Induction motor states in order to assure a good dynamic performance and stability of the global system. In order to reduce the observation execution time, this RDESMO, based on the full -order SMO principle, permit only and specially for the reconstruction of the parameters non measurable in an IM (the fluxes, speed and the rotor time constant estimation).

The interesting simulation results obtained on the induction motor show the effectiveness, the convergence and the stability of this robust decoupling control and RDESMO against rotor resistance variations, measured noises and load. Thus, in order to validate the robustness of this non-linear control and RDESMO, Experimental results on a testing bench for a 1.8 kW induction motor will be present in the next research project.

## 6. References

- [1] D. I. Krein, I. J. Ha, and M. S. Ko, "Control of Induction Motors via Feedback Linearization with Input-Output

Decoupling," *International Journal of Control*, Vol. 51, No. 4, 1989, p. 863-883.

- [2] K. B. Mohanty, N. K. De and A. Routray, "Sensorless Control of a Linearized and Decoupled Induction Motor Drive," *National Power Systems Conference, NPSC*, Kharagpur, India, December 2002, pp. 46-49.
- [3] R. Yazdanpanah, J. Soltani and G. R. A. Markadeh, "Nonlinear Torque and Stator Flux Controller for Induction Motor Drive Based on Adaptive Input-Output Feedback Linearization and Sliding Mode Control," *Energy Conversion and management*, Vol. 49, No. 4, 2008, pp. 541-550.
- [4] P. A. Bogdan and A. Keyhani, "Sliding-Mode Flux Observer with Online Rotor Parameter Estimation for Induction Motors," *IEEE Transactions on Industrial Electronics*, Vol. 54, No. 2, April 2007, pp. 716-723.
- [5] A. Derdiyok, "Speed-Sensorless Control of Induction Motor Using a Continuous Control Approach of Sliding-Mode and Flux Observer," *IEEE Transactions on Industrial Electronics*, Vol. 52, No. 4, August 2005, pp. 1170-1176.
- [6] D. F. Bernard and L. Jean-Paul, "Identification et observation des actionneurs électriques," Vol. 1 & 2, Hermes, Paris, 2007.
- [7] O. Asseu, Z. Yeo, M. Koffi, X. Lin-Shi, C. T. Haba and G. L. Loum, "Robust Decoupling Control and Extended Sliding Mode Observer for an Induction Motor," *News -Phys Chem*, Vol. 48, July 2009, pp. 1-8.
- [8] J. C. Doyle, B. A. Francis and A. R. Tannenbaum, "Feedback Control Theory," Maxwell MacMillan Internat, New York, 1992.
- [9] M. Tursini, R. Petrella and F. Parasiliti, "Adaptive Sliding Mode Observer for Speed Sensorless Control of Induction Motors," *IEEE Transactions on Industry Applications*, Vol. 36, No. 5, September/October 2000, pp. 1380-1387.

## Nomenclature

$C_{em}, C_l$ : Electromagnetic and load torques, N.m.  
 $f$ : friction coefficient, Nm.s/rad.  
 $I_{ds}, I_{qs}, I_{mr}$ : Stationary frame (d,q)-axis stator currents and rotor magnetizing current, A.  
 $J$ : inertia, kg.m<sup>2</sup>.  
 $L_r, L_s, L_m, L_f$ : rotor, stator, mutual and leakage inductances, H.

$p$ : pole pair number.

$R_s, R_r$ : stator and rotor referred resistance,  $\Omega$ .

$T_e, T_r, T_s$ : sampling period, rotor and stator time constant ( $T_r = L_r/R_r = 1/\sigma_r$ ;  $T_s = L_s/R_s$ ), s.

$V_{ds}, V_{qs}$ : Stationary frame d- and q-axis stator voltage, V.

$\Phi_{dr}, \Phi_{qr}$ : d-q components of rotor fluxes, Wb.

$\Phi_{ds}, \Phi_{qs}$ : d-q components of stator fluxes, Wb.

$\omega_s, \omega_r, \omega_{sl}$ : stator, rotor and slip pulsation (or speed), rad/s.

# A Fast Predicating of Nutrient Removal Efficiency in Five Steps Sequencing Batch Reactor System Using Fuzzy Logic Control Model

Saad Abualhail<sup>1</sup>, Rusul Naseer<sup>2</sup>, Ammar Ashor<sup>3</sup>, Xi-Wu Lu<sup>1\*</sup>

<sup>1</sup>Department of Environmental Science and Engineering, Southeast University, Nanjing, China

<sup>2</sup>Department of Chemical Engineering, Faculty of Engineering, Basrah, Iraq

<sup>3</sup>Department of Civil Engineering, Faculty of Engineering, Basrah, Iraq

E-mail: [saad.arab@yahoo.com](mailto:saad.arab@yahoo.com)

Received June 10, 2010; revised August 4, 2010; accepted August 6, 2010

## Abstract

Removal efficiency of COD, NH<sub>4</sub>-N and PO<sub>4</sub>-P and NO<sub>3</sub>-N in five step SBR processes is widely influenced by hydraulic retention time of Anaerobic/Anoxic/Aerobic/Anoxic/Aerobic step of this system where the hydraulic retention time in each step is influence directly on removal efficiency of this system therefore the operator of this system cannot control on this system without experience or a control model. The major objective of this paper is develop a control model (Fuzzy Logic Control Model) based on fuzzy logic rule to predict the maximum removal efficiency of COD, NH<sub>4</sub>-N, PO<sub>4</sub>-P and NO<sub>3</sub>-N and minimize hydraulic retention time in each step of SBR process where the controlled variables was the hydraulic retention times in the Anaerobic/Anoxic/Aerobic/Anoxic/Aerobic step respectively and the output variables was the COD, NH<sub>4</sub>-N, PO<sub>4</sub>-P and NO<sub>3</sub>-N removal efficiency at constant ratio of C/N/P and sludge age. As a results Fuzzy logic if-then rules were used and MIMO Model was built to control COD, NH<sub>4</sub>-N and PO<sub>4</sub>-P and NO<sub>3</sub>-N removal efficiency based on hydraulic retention time in each tank of five step SBR process where the three dimension results show that the influence of hydraulic residence time at each step of SBR system on removal efficiency COD, NH<sub>4</sub>-N, PO<sub>4</sub>-P and NO<sub>3</sub>-N. Fuzzy control model provide a suitable tool for control and fast predict of Hydraulic residence time effects on biological nutrient removal efficiency in five-step sequencing batch reactor.

**Keywords:** Fuzzy Logic Control, Hydraulic Retention Time and SBR System

## 1. Introduction

Conventional control methods are powerful when good analytical mathematical models are available to support their development and operation. This situation is uncommon in real processes. Particularly, the real-time control of wastewater treatment plants (WWTP) is a difficult but essential task, due to the lack of accurate dynamical models describing the process and reliable on-line instrumentation (Olsson and Newell, 1999). However, WWTP can be properly operated by specialized people, having knowledge about the process, though in practice, this know-how is essentially qualitative, empirical, and incomplete. The operation of a WWTP represents therefore a knowledge intensive task. In this regard, a

system capable of giving all the possible information about the state of the process must be available in order to establish the basis of a diagnosis system integrating all the possible knowledge. This requirement is an important step to have successful control

Decisions (Patry and Chapman, 1989). Applications of knowledge-based systems to activated sludge processes are being widely studied (Chapman et al., 1989, Barnett et al., 1992). Most of systems are off-line Knowledge-Based Expert Systems (KBES) mainly diagnostic and advising tools to help process Operators. An activated sludge wastewater treatment plant can be classified as a complex system due to its nonlinear dynamics, large uncertainty in uncontrolled inputs and in the model parameters and structure, multiple time scale of the dynamics, and multi input-output structure. Some KBES

\*Corresponding Author: Xi-Wu Lu, Southeast University

have been designed with the main purpose of online supervision, though the emphasis on real-time supervisor control is usually absent. Many researchers have studied the Operation characteristics and parameters of step feeding process by theoretical analysis and computer simulation S. Fujii, 1996. L. Larrea, A. Larrea, 2001. G. Zhu 2006. Some practical experiences were also drawn from extended; renewed or retrofitted Conventional activated sludge process, J. Fillos 1996. S. Schlegel 1992, E. Gorgun, 1996. S. Wang, 2006. During the last two decades, there were a variety of applications of fuzzy logic control in wastewater treatment plants to optimize operation and performance of bioprocesses. Fuzzy logic provides a language with a syntax and semantics to translate qualitative knowledge into numerical reasoning. In most engineering problems, information about the probabilities of various risk items is only vaguely known. The term computing with words has been introduced by Zadeh (1996) to explain the notion of reasoning linguistically rather than with numerical quantities. Fuzzy rule-based modeling is one of techniques that make use of human knowledge and deductive processes where the experience of operator is assisted to manage and operate biological wastewater treatment plant satisfactorily using operational observations. It is important to develop computer operational decision support systems that are able to play a similar role to the expert in daily operation in minimizing cost and increase performance of wastewater treatment processes. The control objective and parameters ranged from aeration T. J. Ferrer, 1998. T. Kalker, 1999. M. Fiter, 2005. Effluent suspended solid Y. Tsai, 1996. External carbon addition M. Yong, 2006 [17], and loading rate E. Murnleitner, 2002, to nitrification in Sequencing Batch Reactor (SBR) process Y. Peng, 2003, and dissolved oxygen concentration A. Traoré, 2004. A fuzzy control strategy was applied by Meyer *et al.* (2003) for the control of aeration in wastewater treatment plants with pre-denitrification. The implementation of expert systems based on fuzzy logic rules are described elsewhere (Carrasco *et al.*, 2002; Puñal *et al.*, 2002). Recently, especially attention to the expert supervision and control of anaerobic digestion processes is reported (Flores *et al.*, 2000; Polit *et al.*, 2002). Fuzzy control algorithms have been widely applied to pursue better effluent quality and higher economic efficiency on aerobic biological treatment processes (Irene *et al.*, 2008; Wu *et al.*, 2007; Murnleitner *et al.*, 2002. Marsili-Libelli (2006) developed fuzzy pattern recognition to control SBR switching. The switching strategy was from the indirect observation of process state through simple physicochemical measurements and the use of an inferential engine to determine the most appropriate switching schedule. In this study, fuzzy rule based model is developed to predict the maximum re-

moval efficiency of COD, NH<sub>4</sub>-N, PO<sub>4</sub>-P and NO<sub>3</sub>-N and minimize hydraulic retention time in each stage, Anaerobic-Anoxic (1)-Aerobic (1)-Anoxic (2)-Aerobic (2), of SBR system whereas the hydraulic retention time have direct influence on energy and operation cost of wastewater treatment plant. The fuzzy model is built based on if-then rules for hydraulic retention time and removal efficiency of COD, NH<sub>4</sub>-N, PO<sub>4</sub>-P and NO<sub>3</sub>-N based on experimental data that collected from the literature.

**Fuzzy control law:** The features of the fuzzy logic toolbox of MATLAB® constitute a support for the easy implementation of the set of rules, these being the main part of the control law developed in this study. The fuzzy methodology applied was Mamdani's fuzzy inference method (Mamdani and Assilian, 1975). In this method, the first and the second part of the fuzzy inference process consist in the fuzzification of the inputs and application of fuzzy operators. Based on acquired knowledge on the process, a set of rules handling the regulation of the COD, NH<sub>4</sub>-N, PO<sub>4</sub>-P and NO<sub>3</sub>-N removal efficiency in dependence on the hydraulic retention times of the reactors was set up. The output of the control law was the COD, NH<sub>4</sub>-N, PO<sub>4</sub>-P and NO<sub>3</sub>-N removal efficiency. The first step to build the control law was the translation of possible values of the different inputs and output variables into linguistic labels given by membership functions. The system configuration of RsFLC is shown in Figure 1.

## 2. Material and Methods

The experimental set up was fermenter (Bioflo IIC, New Brunswick) with a 5 L working volume was used as the SBR. The fermenter was microprocessor controlled for aeration, agitation, pH and dissolved oxygen (DO).

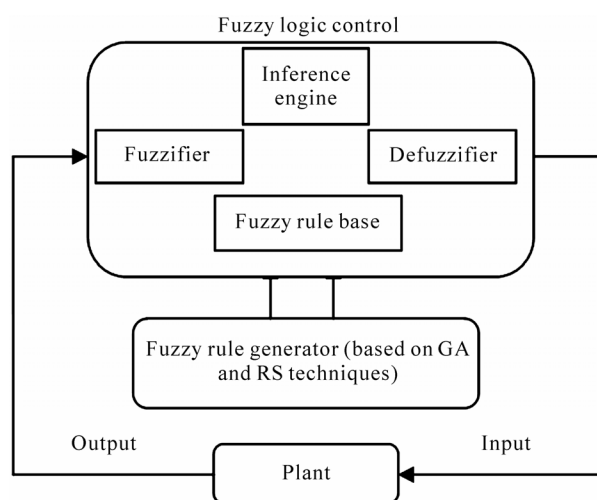


Figure 1. System configuration of RsFLC.

Aeration was provided by using an air pump and a sparger. Agitation speed was varied between 25 and 300 rpm. The pH, DO and ORP of the nutrient medium were continuously monitored by the relevant probes. The fermenter was used to investigate the effectiveness of Hydraulic retention time on the removal efficiency of COD, NH<sub>4</sub>-N, PO<sub>4</sub>-P and NO<sub>3</sub>-N. The effect of Hydraulic retention time on removal efficiency at constant sludge age (10 days) is shown in **Table 1**.

## 2.1. Fuzzy Rule Based Modeling

In fuzzy rule-based modeling, the relationships between variables are represented by means of fuzzy if-then rules of the form "If antecedent proposition then consequent proposition". The antecedent proposition is always a fuzzy proposition of the type "x is A" where x is a lin-

guistic variable and A is a linguistic constant term. The proposition's truth-value (a real number between 0 and 1) depends of degree of similarity between x and A.

Depending on the form of the consequent proposition, two main types of rule-based fuzzy models are commonly used:

- Linguistic fuzzy model: Both antecedent and the consequent are fuzzy propositions (e.g., Mamdani model)
- Takagi-Sugeno (TS) fuzzy model: the antecedent is a fuzzy proposition; the consequent is a crisp function

The linguistic model (Zadeh, 1973; Mamdani, 1977) has the capacity to capture qualitative and highly uncertain knowledge in the form of if-then rules:

$$R_i: \text{If } x \text{ is } A_i \text{ then } y \text{ is } B_i; i = 1, 2, \dots, K \quad (1)$$

**Table 1. Experimental data of removal efficiency and hydraulic retention time of five Step SBR system at (COD/N/P = 100/5/1.5).**

	Hydraulic retention time (h)				Removal efficiency (%)			
	Anaerobic	Anoxic	Anoxic	Oxic	COD	NH <sub>4</sub> -N	PO <sub>4</sub> -P	NO <sub>3</sub> -N
	step (1)	Oxic step (1)	step (2)	step (2)				
1	1.5	4.5	1.5	1.5	96	80	43	60
1.5	1.5	4.5	1.5	1.5	96	88	45	20
2	1.5	4.5	1.5	1.5	97	73	71	90
2.5	1.5	4.5	1.5	1.5	68	84	63	70
2	1.0	4.5	1.5	1.5	96	87	90	81
2	1.5	4.5	1.5	1.5	97	73	71	90
2	2.0	4.5	1.5	1.5	99	79	69	55
2	1.0	2.0	1.5	1.5	97	49	66	50
2	1.0	3.0	1.5	1.5	95	84	73	66
2	1.0	4.5	1.5	1.5	96	87	91	81
2	1.0	6.0	1.5	1.5	99	90	66	38
2	1.0	4.5	1.0	1.5	94	83	72	40
2	1.0	4.5	1.5	1.5	96	87	90	81
2	1.0	4.5	2.0	1.5	95	93	72	58
2	1.0	4.5	2.5	1.5	96	91	68	50
2	1.0	4.5	1.5	1.5	96	87	90	81
2	1.0	4.5	1.5	2.0	96	77	69	5
2	1.0	4.5	1.5	2.5	96	79	67	4
2	1.0	4.5	1.5	3.0	95	88	62	6

where,  $x$  is the input (antecedent) linguistic variable and  $A_i$  is the antecedent linguistic constants (the qualitatively defined functions). Similarly,  $y$  is the output (consequent) linguistic variable and  $B_i$  is the consequent linguistic constants. The values of  $x$  and  $y$  and  $A_i$  and  $B_i$  are fuzzy sets defined in the domains of their respective base variables. The linguistic terms  $A_i$  and  $B_i$  are usually selected from sets of predefined terms, such as small, medium, large. The rule base  $R = \{R_i/i = 1, 2, \dots, K\}$  and the sets  $A$  and  $B$  constitute the knowledge base of the linguistic model. Each rule is regarded as a fuzzy relation (fuzzy restriction on the simultaneous occurrences of values  $x$  and  $y$ ):  $R_i (X \times Y) \rightarrow [0,1]$ . This relation can be computed in two basic ways-by using:

- Fuzzy implications or
- Fuzzy conjunctions (Mamdani method). In this study, the Mamdani method was used, in which conjunction  $A \wedge B$  is computed by a minimum operator (a t-norm);

$$R_i = A_i \times B_i$$

$$i.e., \mu_{R_i}(x, y) = [\mu_{A_i}(x) \wedge \mu_{B_i}(y)] \quad (2)$$

The minimum operator is computed on the Cartesian product space of  $X$  and  $Y$ , i.e., for all possible pairs of  $x$  and  $y$ . The fuzzy relation  $R$  represents the entire model Equation (1) and is given by the disjunction (union or maximum, i.e., s-norms) of the  $K$  individual rule's relations,  $R_i$ :

$$K = \bigcup_{i=1}^K R_i, i.e., \mu_R(x, y) = \max_{1 \leq i \leq K} [\mu_{A_i}(x) \wedge \mu_{B_i}(y)] \quad (3)$$

Now the entire base is encoded in the fuzzy relation  $R$  and the output of the linguistic model can be computed.

By the max-min composition ( $\circ$ ):

$$y = x \circ R \quad (4)$$

Suppose an input fuzzy value  $x = A'$ , which has the output value  $B'$  given by the relational composition:

$$\mu_{B'}(y) = \max_x [\mu_{A'}(x) \wedge \mu_R(x, y)] \quad (5)$$

By substituting Equation (2) into Equation (5), get:

$$\mu_{B'}(y) = \max_x [\mu_{A'}(x) \wedge \max_{1 \leq i \leq K} [\mu_{A_i}(x) \wedge \mu_{B_i}(y)]] \quad (6)$$

Equation (6) can be written as follow:

$$\mu_{B'}(y) = \max_x [\mu_{A'}(x) \wedge \max_{1 \leq i \leq K} [\mu_{A_i}(x) \wedge \mu_{B_i}(y)]] \quad (7)$$

Equation (7) represents the output fuzzy Set of the linguistic model.

The most common methods used for defuzzification are: Yager (1980) centroidal method, is always used for

defuzzification due to its simplicity, that can be determined as:

- Yager (1980) centroidal method, is always used for defuzzification due to its simplicity, that can be determined as:

$$Defuzzified\ value = \frac{\int_a^b y \cdot \mu_{B'}(y) dy}{\int_a^b \mu_{B'}(y) dy} \quad (8)$$

where:

$a$  and  $b$  = The lower and upper limits of the integral which determines the validity domain of the membership function

$y$  = The centroidal distance from the origin;

- Chen (1985) ranking method
- Bertoluzza *et al.* (1995) method and
- Tran and Duckstein (2002) method

The above algorithm is the Mamdani inference that used as (SISO) single input and single output. It can be extended to Multiple Inputs and Single Output (MISO) and Multiple Outputs (MIMO). The MIMO model is a set of MISO models.

In the case of MIMO model  $R_i$  becomes as follow:

$R_i$ : If  $x_1$  is  $A_{1i}$  and  $x_2$  is  $A_{2i}$  and...

and  $x_p$  is  $A_{pi}$  then  $y_1$  is  $B_{1i}$  and  $y_2$  is  $B_{2i}$  and... (9)

and  $y_p$  is  $B_{pi}$ ,  $i = 1, 2, \dots, K$

The above model is the special case of Equation (1), as the set  $A_i$  and  $B_i$  is obtained by the Cartesian product of fuzzy sets:

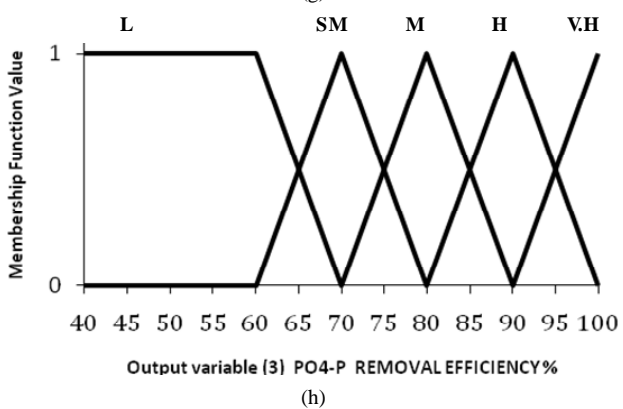
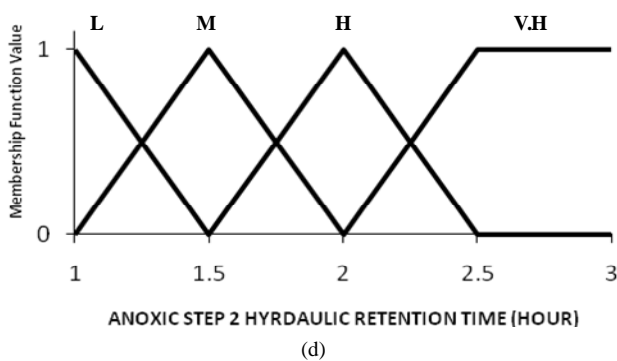
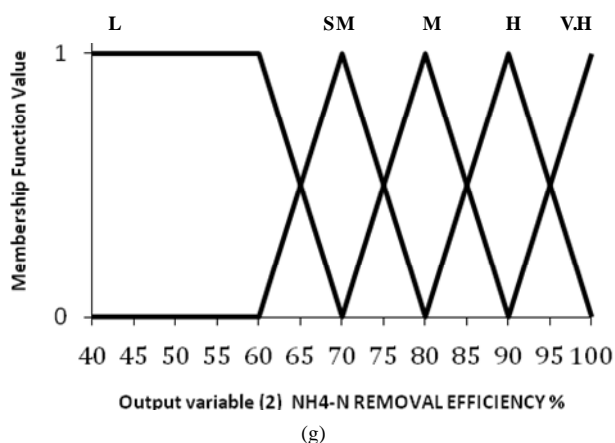
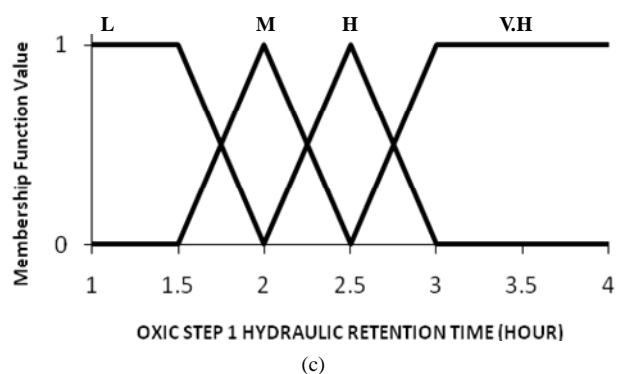
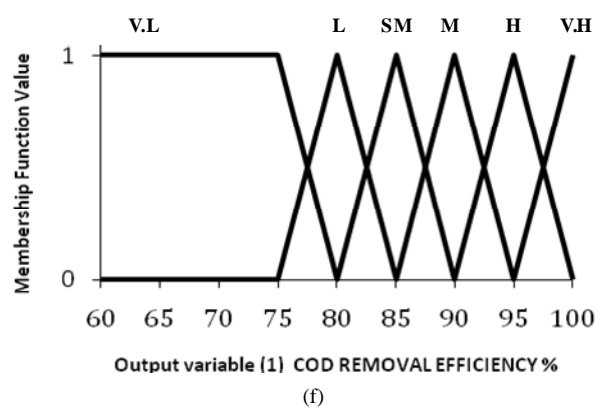
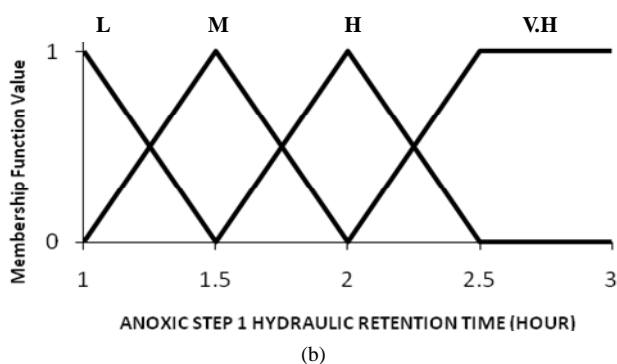
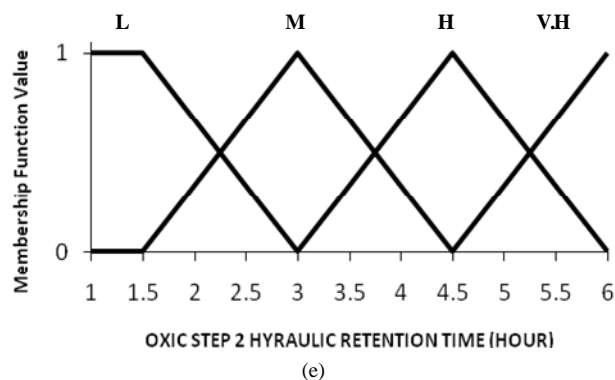
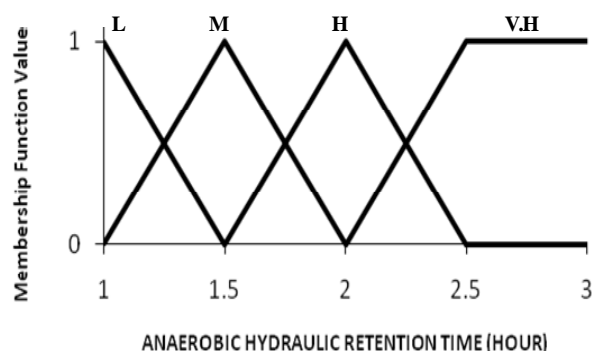
$$A_{ij} = A_{i1} \times A_{i2} \times A_{i3} \times \dots \times A_{ip} \quad (10)$$

$$B_{ik} = B_{i1} \times B_{i2} \times B_{i3} \times \dots \times B_{ip} \quad (11)$$

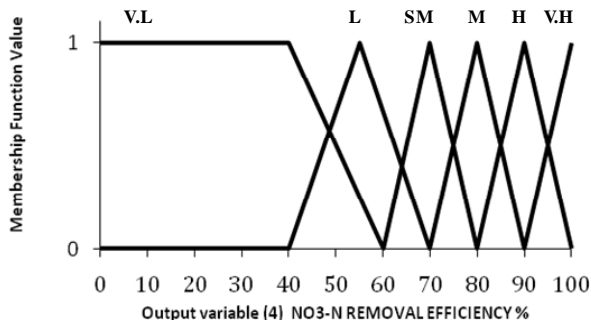
**Hydraulic retention time modeling:** The data collected for 17 operating conditions as shown in **Table 1** were used for developing a fuzzy rule-based model. The efficiency of multi-tank was assessed based on COD,  $NH_4$ -N and  $PO_4$ -P and  $NO_3$ -N removal efficiency. The control parameters of MIMO model are Anaerobic HRT, Anoxic step one HRT, Aerobic step one HRT, Anoxic step two HRT and Aerobic step two HRT were defined by qualitative scales as shown in **Figure 2**.

The variability in the input control parameters was used for fuzzification. A Hydraulic retention time were expressed by low, small medium, medium, high and very high scale in each tank (anaerobic, anoxic, aerobic, anoxic and aerobic).

The response of the model is the removal efficiency of COD,  $NH_4$ -N,  $PO_4$ -P and  $NO_3$ -N and for COD and  $NO_3$ -N output, a six granularity scale (very low (V.L),







(i)

**Figure 2.** The input and output of MIMO model in Mamdani inference fuzzy logic model.

low(L), small medium (S.M), medium(M), high (H), very high(V.H)) while for NH<sub>4</sub>-N and PO<sub>4</sub>-P output, a five granularity scale (low(L), small medium (SM), medium(M), high (H), very high(V.H)) were used as shown

in **Figure 2**. The fuzzy rule based model was developed with seventeen rules based on the collected data under each operating condition and expert judgment as shown in **Table 2**.

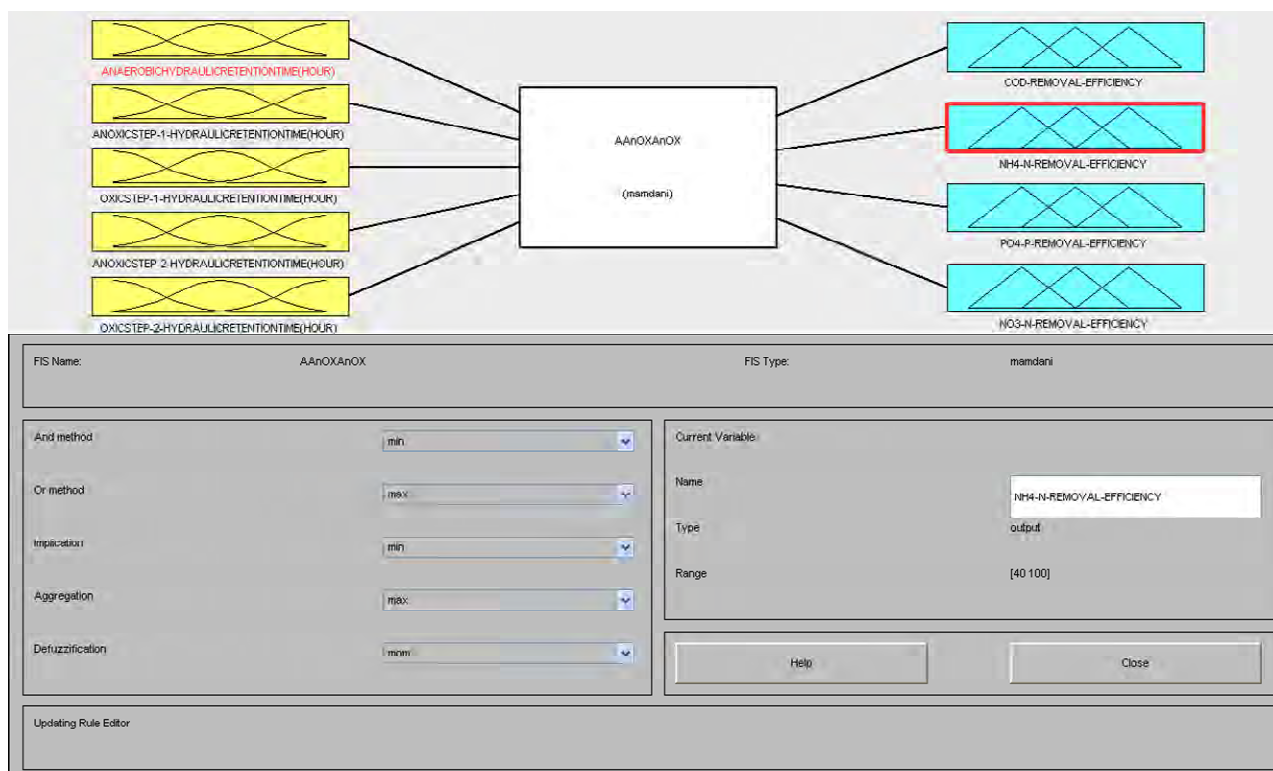
### 3. Results and Discussion

#### 3.1. Fuzzy Control Application

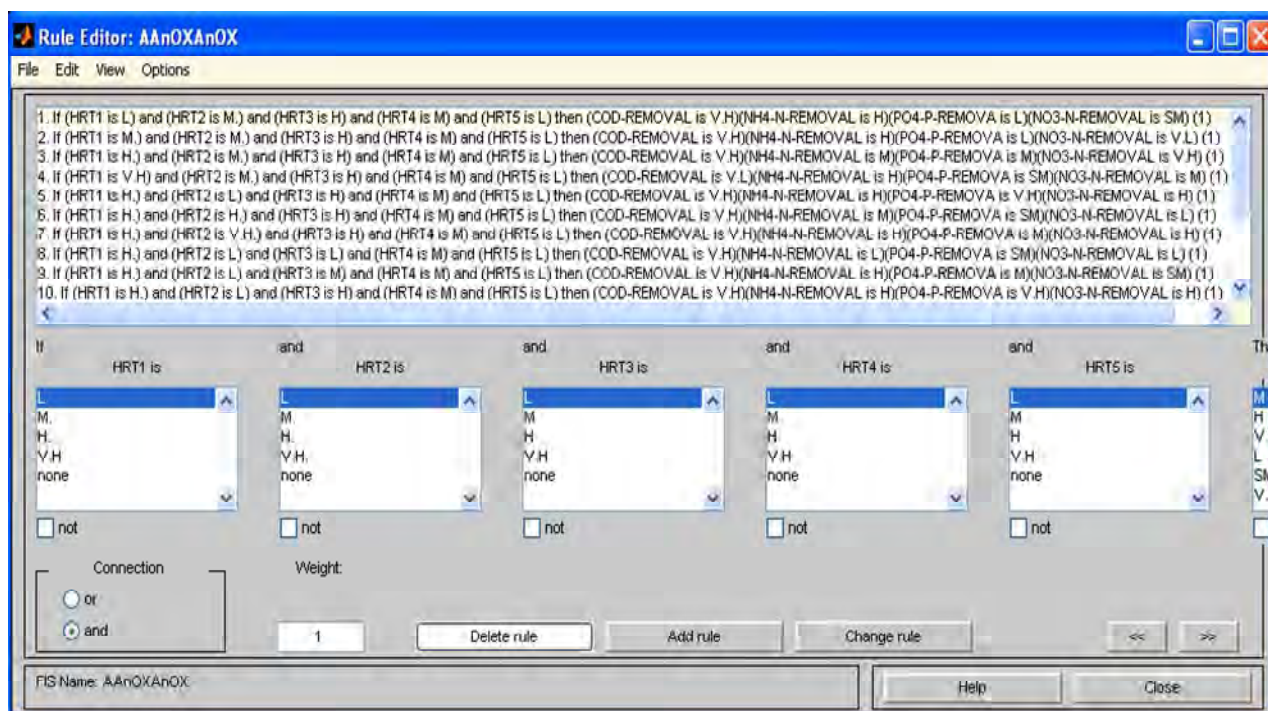
The Mamdani inference was established based on 17 fuzzy linguistic rules as shown in **Figure 3(b)**. The defuzzified results and graphical outputs can be derived as shown in **Figure 3(a)-(c)** whereas **Figure 3** illustrates an example of the surface viewer screen obtained from the fuzzy logic toolbox. Two- or three-dimensional graphic results of variables can be plotted and compared. The relationships between the nutrient concentrations of five step SBR system and the hydraulic retention time inputs of the model can be obtained as shown in **Figure 4**. **Figure 4** is shows that COD, NH<sub>4</sub>-N, PO<sub>4</sub>-P and NO<sub>3</sub>-N

**Table 2.** Fuzzy rule based model for hydraulic retention time and removal efficiency in SBR system at constant sludge age (MIMO model).

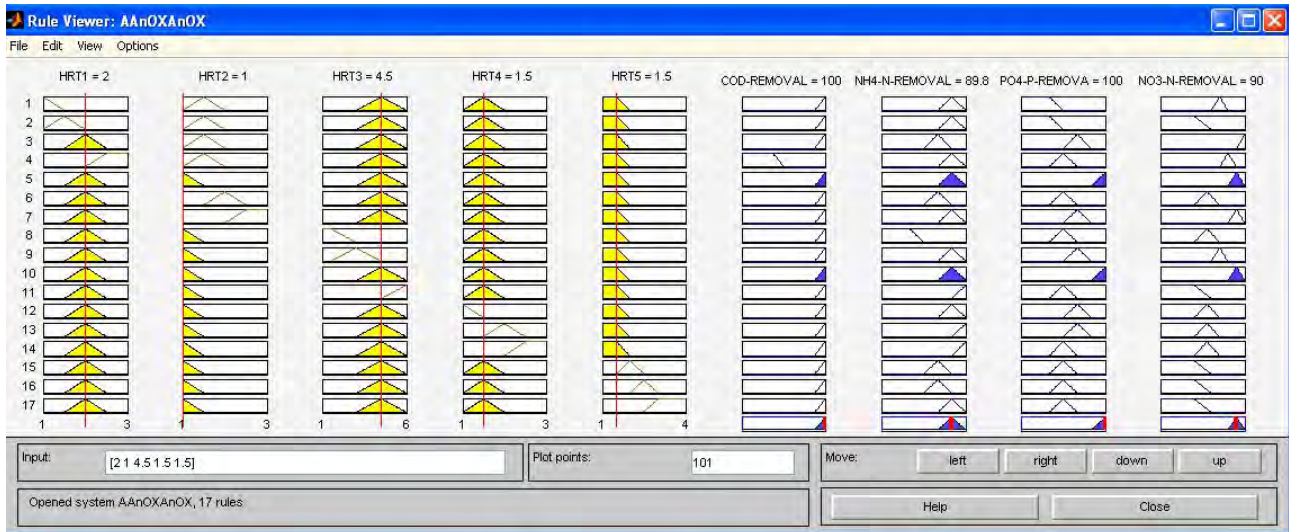
Rule			And or	Anoxic	And or	Oxic	And or	Anoxic	And or	Oxic			R.NH	R.PO	R.NO
no. (Ri)	If	Anaer	not	step (1)	not	Step (1)	not	step (2)	not	step (2)	Then	R.COD	4-N	4-P	3-N
R1	If	H	And	L	And	H	And	M	And	H	Then	V.H	M	SM	V.L
R2	If	H	And	V.H	And	H	And	M	And	L	Then	V.H	H	M	H
R3	If	H	And	L	And	H	And	M	And	V.H	Then	V.H	H	SM	V.L
R4	If	L	And	M	And	H	And	M	And	L	Then	V.H	H	L	SM
R5	If	H	And	M	And	H	And	M	And	L	Then	V.H	M	M	V.H
R6	If	H	And	H	And	H	And	M	And	L	Then	V.H	M	SM	L
R7	If	H	And	L	And	H	And	M	And	M	Then	V.H	M	SM	V.L
R8	If	H	And	L	And	L	And	M	And	L	Then	V.H	L	SM	L
R9	If	H	And	L	And	M	And	M	And	L	Then	V.H	H	M	SM
R10	If	V.H	And	M	And	H	And	M	And	L	Then	V.l	H	SM	M
R11	If	H	And	L	And	V.H	And	M	And	L	Then	V.H	V.H	SM	V.L
R12	If	H	And	L	And	H	And	L	And	L	Then	H	H	M	L
R13	If	H	And	M	And	H	And	M	And	L	Then	V.H	H	L	V.L
R14	If	H	And	L	And	H	And	H	And	L	Then	V.H	V.H	M	L
R15	If	H	And	L	And	H	And	V.H	And	L	Then	V.H	V.H	SM	L
R16	If	H	And	L	And	H	And	M	And	L	Then	V.H	H	V.H	H
R17	If	H	And	L	And	H	And	M	And	L	Then	V.H	H	V.H	H



(a)

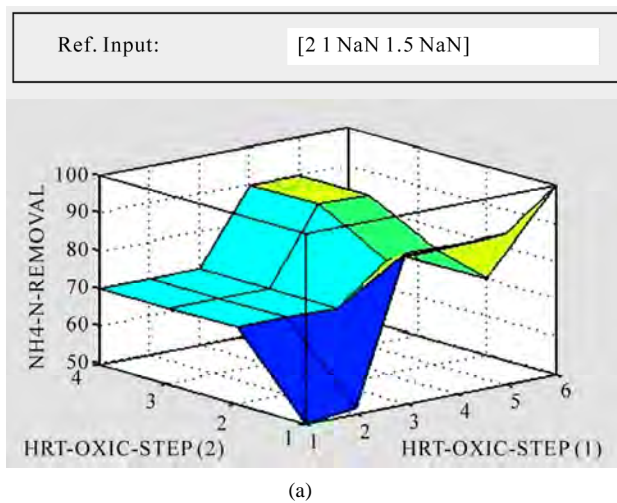


(b)

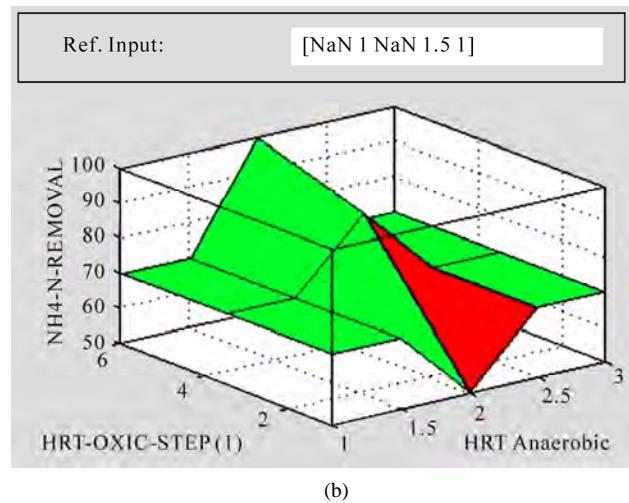


(c)

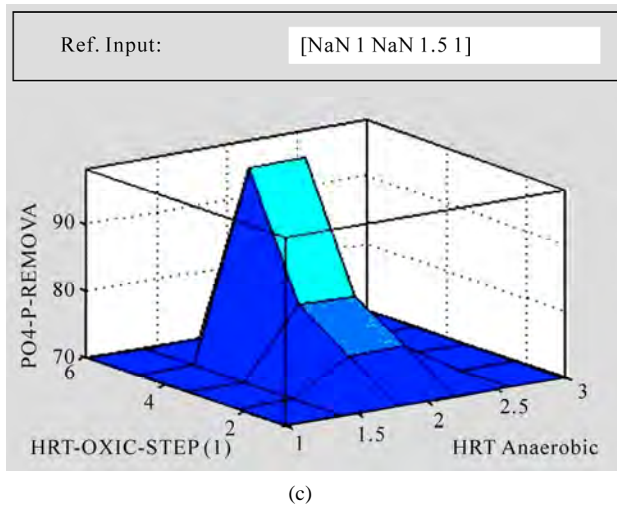
**Figure 3. Fuzzy inference system (a) FIS editor screen; (b) Rule editor of matlab-fuzzy and (c) Rule viewer screen to obtain defuzzified results.**



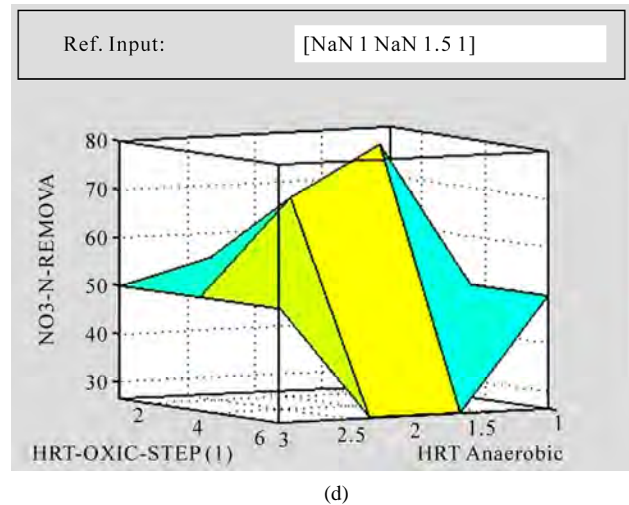
(a)



(b)



(c)



(d)



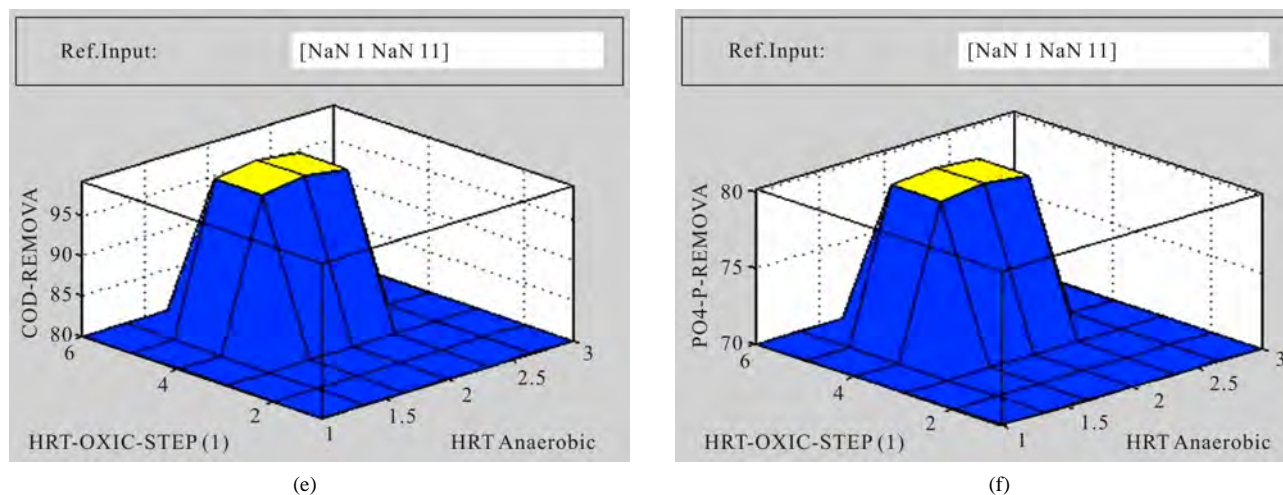


Figure 4. 3D response surface graph for output value under different hydraulic retention time (C/N/P = 100/5/1.5, sludge age (10) days).

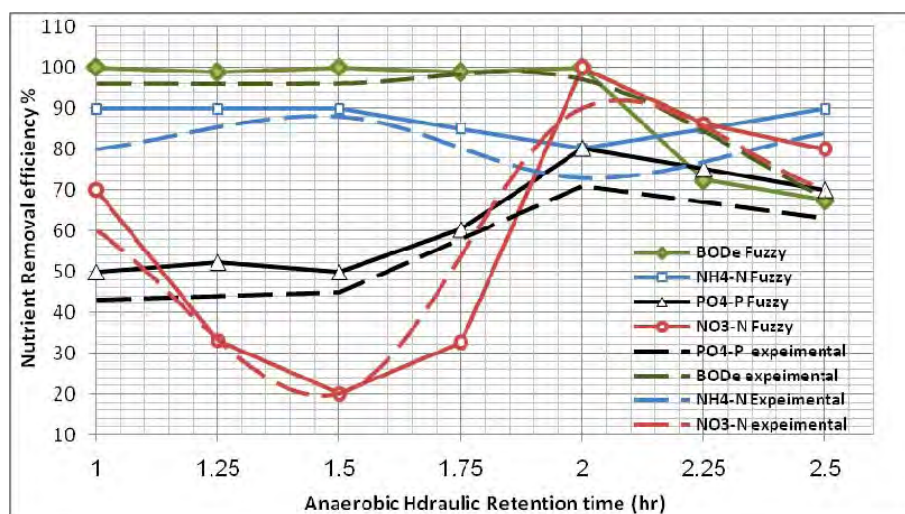


Figure 5. Overall nutrient percent removal at different hydraulic retention time of the anaerobic step.

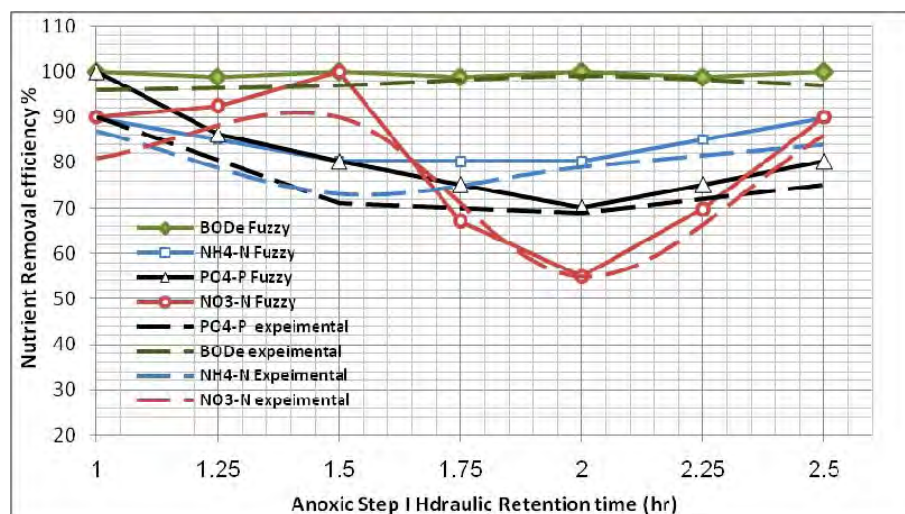


Figure 6. Overall nutrient percent removal at different hydraulic retention time of the anoxic step I.

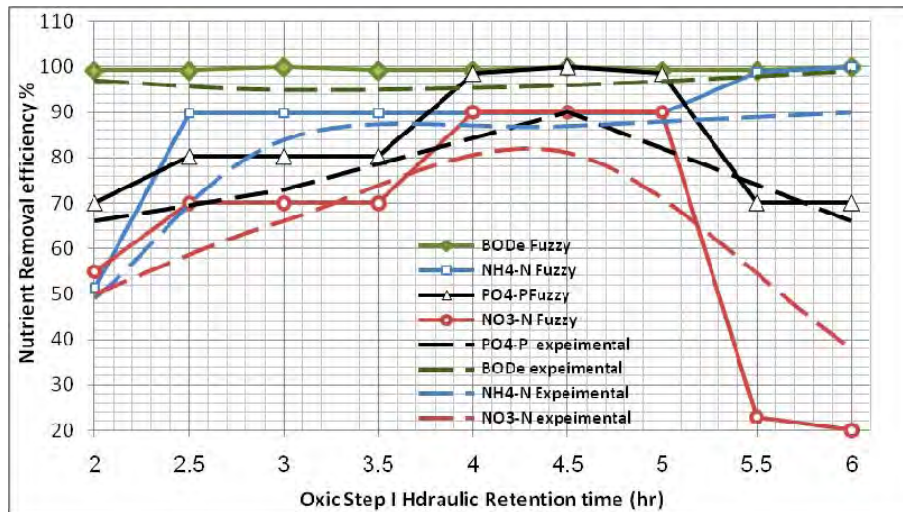


Figure 7. Overall nutrient percent removal at different hydraulic retention time of the oxyc step I.

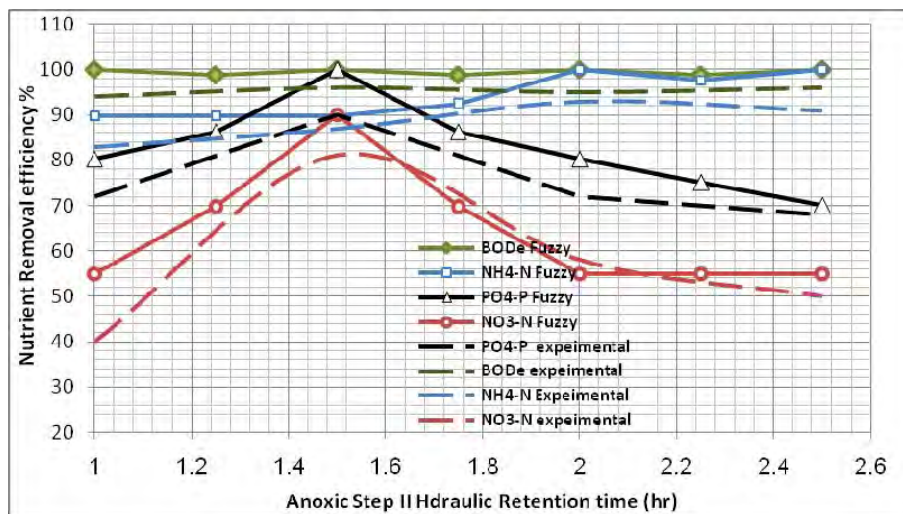


Figure 8. Overall nutrient percent removal at different hydraulic retention time of the anoxic step II.

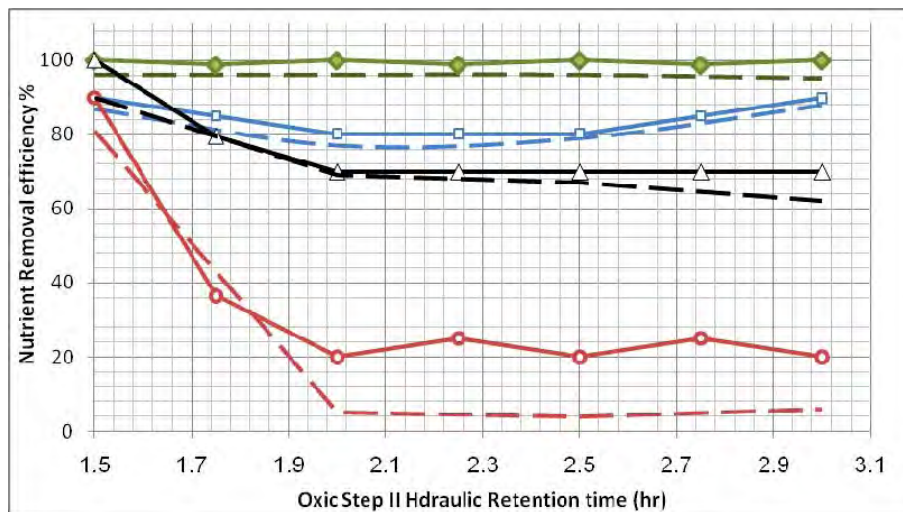


Figure 9. Overall nutrient percent removal at different hydraulic retention time of the oxyc step II.

removal efficiency of the system with the inputs Anaerobic, Anoxic, Aerobic, Anoxic and Aerobic hydraulic retention time of the model. **Figure 3(c)** shows the results of applied rules and their corresponding outputs according to the mass center of variables. Using the interface, defuzzified values for output variables can be derived changing input values manually. Different output values can be obtained through the rule viewer according to the given input values.

It is not flexible to get defuzzified output values for all the real input values using the interface. For that reason, a program is written using MATLAB codes to drive defuzzified output results in accordance with real input values.

### 3.2. Comparison with Experimental Data

The comparison results of Fuzzy logic model with Experimental data are shown in **Figures 5-9**. The results show that Fuzzy logic Control model is a good tool that can be used in Prediction Removal efficiency of five step SBR system whereas the comparison results indicated that the FLC model have a good convergence performance and the predictions of outflow nutrient removal efficiency coincided well with the experimental values.

## 4. Conclusions

Fuzzy logic model was built based on if-then rules (from collection data) for COD, NH<sub>4</sub>-N and PO<sub>4</sub>-P and NO<sub>3</sub>-N removal efficiency and hydraulic retention time in each step of five step SBR process. A control law based on fuzzy logic features was developed and validated for Hydraulic retention time in Anaerobic /Anoxic/Aerobic/Anoxic/Aerobic tank of SBR wastewater process. The controlled variables was the Hydraulic retention times in the Anaerobic/Anoxic/Aerobic/Anoxic/Aerobic tank respectively and the output variables was the COD, NH<sub>4</sub>-N, PO<sub>4</sub>-P and NO<sub>3</sub>-N removal efficiency. The model provides a new tool for control hydraulic residence time effects on biological nutrient removal efficiency in five-step sequencing batch reactor.

## 5. References

- [1] A. Uygur and F. Kargi, "Hydraulic Residence Time Effects in Biological Nutrient Removal Using Five-Step Sequencing Batch Reactor," *Enzyme and Microbial Technology*, Vol. 35, No. 2-3, 2004, pp. 167-172.
- [2] S. Fujii, "Theoretical Analysis on Nitrogen Removal of the Step-Feed Anoxic-Oxic Activated Sludge Process and its Application for the Optimal Operation," *Water Science and Technology*, Vol. 34, No. 1-2, 1996, pp. 459-466.
- [3] L. Larrea, A. Larrea, E. Ayesa, J. Rodrigo, M. Lopez-Carrasco and J. Cortacans, "Development and Verification of Design and Operation Criteria for the Step Feed Process with Nitrogen Removal," *Water Science and Technology*, Vol. 43, No. 1, 2001, pp. 261-268.
- [4] G. Zhu and Y. Peng, "Theoretical Evaluation on Nitrogen Removal of Step-Feed Anoxic/Oxic Activated Sludge Process," *Journal of Harbin Institute of Technology*, Vol. 13, No. 3, 2006, pp. 99-102.
- [5] J. Fillos, V. Diyamandoglu, L. Carrio and L. Robinson, "Full-Scale Evaluation of Biological Nitrogen Removal in the Step-Feed Activated Sludge Process," *Water Environment Research*, Vol. 68, No. 2, 1996, pp. 132-142.
- [6] S. Schlegel, "Operational Results of wastewater Treatment Plants with Biological N and P Elimination," *Water Science and Technology*, Vol. 25, No. 4-5, 1992, pp. 241-247.
- [7] E. Gorgun, N. Artan, D. Orhon and S. Sozen, "Evaluation of Nitrogen Removal by Step Feeding in Large Treatment Plants," *Water Science and Technology*, Vol. 34, No. 1-2, 1996, pp. 253-260.
- [8] S. Wang, L. Yu, G. Man, H. Zhu, D. Peng and X. Wang, "A Pilot Study on a Step-Feeding Anoxic/Oxic Activated Sludge System," *Water Science and Technology*, Vol. 53, No. 9, 2006, pp. 95-101.
- [9] T. Kalker, C. Van Goor, P. Roeleveld, M. Ruland and R. Babuska, "Fuzzy Control of Aeration in an Activated Sludge Wastewater Treatment Plant: Design, Simulation and Evaluation," *Water Science and Technology*, Vol. 39, No. 4, 1999, pp. 71-78.
- [10] M. Fiter, D. Guell, J. Comas, J. Colprim, M. Poch and I. Rodriguez-Roda, "Energy Saving in a Wastewater Treatment Process: An Application of Fuzzy Logic Control," *Environmental Technology*, Vol. 26, No. 11, 2005, pp. 1263-1270.
- [11] J. Ferrer, M. Rodrigo, A. Seco and J. Penya-Roja, "Energy Saving in the Aeration Process by Fuzzy Logic Control," *Water Science and Technology*, Vol. 38, No. 3, 1998, pp. 209-217.
- [12] Y. Tsai, C. Ouyang, M. Wu and W. Chiang, "Effluent Suspended Solid Control of Activated Sludge Process by Fuzzy Control Approach," *Water Environment Research*, Vol. 68, No. 6, 1996, pp. 1045-1053.
- [13] M. Yong, P. Yong-Zhen, W. Xiao-Lian, W. Shu-Ying, "Intelligent control aeration and external carbon addition for improving nitrogen removal, Environmental Modelling and Software, 21, 2006, pp. 821-828.
- [14] E. Murnleitner, T. Becker and A. Delgado, "State Detection and Control of Overloads in the Anaerobic Wastewater Treatment Using Fuzzy Logic," *Water Research*, Vol. 36, No. 1, 2002, pp. 201-211.
- [15] Y. Peng, J. Gao, S. Wang and M. Sui, "Use of pH as Fuzzy Control Parameter for Nitrification under Different Alkalinity in SBR Process," *Water Science and Technology*, Vol. 47, No. 11, 2003, pp. 77-84.
- [16] A. Traoré, S. Grieu, S. Puig, L. Corominas, F. Thiery, M. Polit and J. Colprim, "Fuzzy Control of Dissolved Oxy-

- gen in a Sequencing Batch Reactor Pilot Plant," *Chemical Engineering Journal*, Vol. 111, No. 1, 2005, pp. 13-19.
- [17] U. Meyer and H. J. Pöpel, "Fuzzy-Control for Improved Nitrogen Removal and Energy Saving in WWWT-Plants with Pre-Denitrification," *Water Science and Technology*, Vol. 47, No. 11, 2003, pp. 69-76.
- [18] E. F. Carrasco, J. Rodríguez, A. Puñal, E. C. Roca and J. M. Lema, "Rule-Based Diagnosis and Supervision of a Pilotscale Wastewater Treatment Plant Using Fuzzy Logic Techniques," *Expert Systems with Applications*, Vol. 22, No. 1, 2002, pp. 11-20.
- [19] A. Puñal, J. Rodríguez, E. F. Carrasco, E. Roca and J. M. Lema, "An Expert System for Monitoring and Diagnosis of Anaerobic Wastewater Treatment Plants," *Water Research*, Vol. 36, No. 10, 2002, pp. 2656-2666.
- [20] J. Flores, B. Arcay and J. Arias, "An Intelligent System for Distributed Control of an Anaerobic Wastewater Treatment Process," *Artificial Intelligence*, Vol. 13, No. 4, 2000, pp. 485-494.
- [21] M. Polit, M. Estaben and P. Labat, "A Fuzzy Model for an Anaerobic Digester, Comparison with Experimental Results," *Artificial Intelligence*, Vol. 15, No. 5, 2002, pp. 385-390.
- [22] L. A. Zadeh, "Fuzzy Logic Computing with Words," *IEEE Transactions—Fuzzy Systems*, Vol. 4, No. 2, 1996, pp. 103-111.
- [23] B. Olsson and B. Newell, "Wastewater Treatment Systems—Modelling, Diagnosis and Control," IWA Publishing, London, 1999.
- [24] G. G. Patry and D. Chapman, "Dynamic Modeling and Expert Systems in Wastewater Engineering," Lewis Publishers, Chelsea, 1989.
- [25] M. W. Barnett, G. G. Patry and M. Hiraoka, "Knowledge-Based (Expert) Systems for the Activated Sludge Process," In: J. F. Andrews, Ed., *Dynamics and Control of the Activated Sludge Process*, Technomic Publishing Company, Lancaster, 1992, pp. 231-243.
- [26] J. Irene, C. Julián, L. Javier and A. B. Juan, "Start-Up of a Nitrification System with Automatic Control to Treat Highly Concentrated Ammonium Wastewater: Experimental Results and Modeling," *Chemical Engineering Journal*, Vol. 144, No. 3, 2008, pp. 407-419.
- [27] C. Y. Wu, Z. Q. Chen, X. H. Liu and Y. Z. Peng, "Nitrification-Denitrification Via Nitrite in SBR Using Real-Time Control Strategy when Treating Domestic Wastewater," *Biochemical Engineering Journal*, Vol. 36, No. 2, 2007, pp. 87-92.
- [28] E. Murnleitner, T. M. Becker and A. Delgado, "State Detection and Control of Overloads in the Anaerobic Wastewater Treatment Using Fuzzy Logic," *Water Research*, Vol. 36, No. 1, 2002, pp. 201-211.
- [29] S. Marsili-Libelli, "Control of SBR Switching by Fuzzy Pattern Recognition," *Water Research*, Vol. 40, No. 5, 2006, pp. 1095-1107.
- [30] E. H. Mamdani, "Application of Fuzzy Logic to Approximate Reasoning Using Linguistic Systems," *Fuzzy Sets and Systems*, Vol. 26, No. 1, 1977, pp. 1182-1191.
- [31] L. A. Zadeh, "Outline of a New Approach to the Analysis of Complex Systems and Decision Process," *IEEE Transactions of Systems, Man and Cybernetics*, No. 1, 1973, pp. 28-44.
- [32] R. R. Yager, "A General Class of Fuzzy Connectives," *Fuzzy Sets and Systems*, Vol. 4, No. 3, 1980, pp. 235-242.
- [33] C. Betroluzza, N. Corral and A. Salas, "On a New Class of Distances between Fuzzy Numbers," *Mathware and Soft Computing*, Vol. 2, No. 2, 1995, pp. 71-84.
- [34] L. T. Tran and L. Duckstein, "Comparison of Fuzzy Numbers Using a Fuzzy Distance Measure," *Fuzzy Sets and Systems*, Vol. 130, No. 3, 2002, pp. 331-341.

## Nomenclature

*a*: The lower limits of the integral of the membership function

*b*: The upper limits of the integral of the membership function

*COD*: Chemical oxygen demand Concentration

*FIS*: Fuzzy Inference system

*FLC*: Fuzzy Logic Control

*i,j,k*: subscript symbols

*H*: High Value

*HRT*: Hydraulic Retention time

*L*: Low value

*M*: Medium

*MIMO*: Multi Input Multi Output model

*MISO*: Multi Input Single Output Model

*NH<sub>4</sub>-N*: Ammonia Nitrogen Concentration

*NO<sub>3</sub>-N*: Nitrate Nitrogen Concentration

*PO<sub>4</sub>-P*: Poly Phosphate concentration

*SM*: Small medium value

*V.H*: Very High Value

*VL*: very low value

*y*: The centroidal distance from the origin in output membership function.



# Effect of Periodic Variation of Sol-air Temperature on the Performance of Integrated Solar Collector Storage System

Nawaf H. Saeid, Tan Jun Wong

*Department of Mechanical, Manufacturing and Materials Engineering, The University of Nottingham Malaysia Campus, Semenyih, Selangor, Malaysia*

*E-mail: [nawaf.saeid@nottingham.edu.my](mailto:nawaf.saeid@nottingham.edu.my)*

*Received June 8, 2010; revised September 6, 2010; accepted September 29, 2010*

## Abstract

Parametric study is carried out in the present article to investigate the unsteady performance of solar energy gain and heat retention of two different integrated-collector-storage systems. The systems are the conventional rectangular-shaped storage tank and the modified tank shaped as rectangular cuboid with one semi-circular top. The two systems have the same absorber surface area and volume for water. The heat and fluid flow is assumed to be unsteady, two-dimensional, laminar and incompressible. The performances of the two systems are evaluated based on the maximum temperature in the system during daytime heating period and nighttime cooling period. For comprehensive study, 24-hours simulations for 3 cases with different wall boundary condition impose on the absorber plate are investigated. The simulation results show that the modified system has better heat retain than the conventional system. Periodic variations of both systems are investigated, and it is found that both systems show consistent results on different days. The modified system is able to store most of the thermal energy in the semi-circular top region with higher temperature than that of the conventional system.

**Keywords:** Heat Transfer, Integrated Solar Collector Storage, Buoyancy Driven Flow, Numerical Study

## 1. Introduction

Over the last two decades, interest has been growing for more effective utilize of renewable sources of energy. Many researchers have strongly promoted the use of solar energy as a viable source of energy. This is due to solar energy a sustainable and environmentally friendly source of energy. Water heating accounts for approximately 25% of the total energy used in a typical single-family home. An electric water heater is the single biggest energy user of all appliances in the home. Home solar heating can lead to savings of 85% on utility bills over the costs of electric water heating [1].

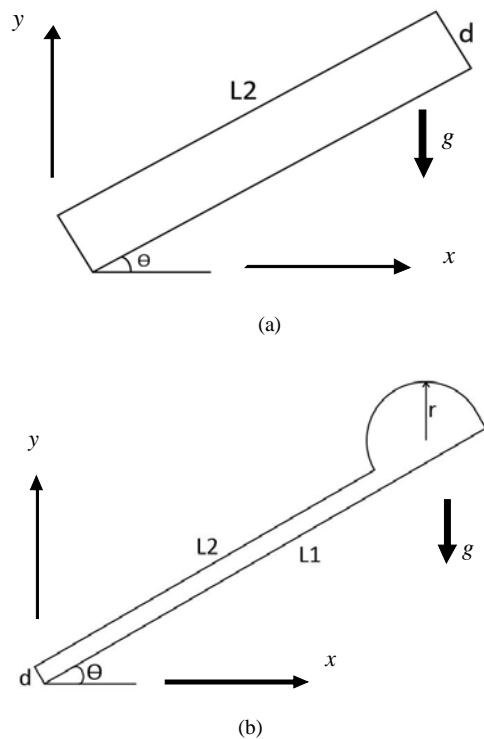
A simple solar water heater is usually consisting of a water tank, a dark absorber to capture the sun's radiation effectively, and a sheet of glass to create a greenhouse effect. Water enters at the bottom and is heated by the absorber. As it warms, hot water travels to the top of the tank due to its lower density. When the water is ready for use, cool water is supplied to the inlet and hot water flows out the top. The main disadvantage of the solar collector systems is the high thermal loss to the surroundings. In particular, the heat losses are greatest during the night and overcast days with low ambient temperature.

Kalogirou [2] presented a survey of the various types of solar thermal collectors and their applications. In this survey study, various types of collectors including flat -plate, compound parabolic, evacuated tube, parabolic trough, Fresnel lens, parabolic dish and heliostat field collectors were described. The storage of solar energy is necessary for an effective usage of this energy due to the fact that the solar energy has an unsteady characteristic during the day. The storage tank can be separated or integrated with the solar collector. The solar integrated-collector-storage (ICS) water heating system is combining the solar absorber panel and the storage tank in a single unit. This makes the system more cost effective and has less maintenance problems.

There are many different designs in the literature for ICS. Garnier *et al.* [3] considered a rectangular-shaped box incorporating the solar collector and storage tank into a single unit and was optimized for simulation in Scottish weather conditions. Kalogirou [4] compared the ICS with flat plate collector and reported that ICS is efficient and inexpensive. Optimization was carried out by considering three different configurations of a cusp concentrator for a cylindrical receiver. The main disadvantage of these collectors comes from the design of the

system, *i.e.* with the receiver of the collector being also the storage vessel, it is not possible to insulate it properly and there are significant heat losses during the night. Sridhar and Reddy [5] investigated a modified cuboid solar integrated-collector-storage (ICS) water heating system with transparent insulation material. The system consists of a tank shaped as rectangular cuboid with one semi-circular top. After numerical investigation to evolve optimum configuration, the system is designed, developed and tested for Indian weather conditions. Sridhar and Reddy [5] found that the modified ICS system is structurally supportive in storing of hot fluid in the storage region, after heating by the energy collected at the absorber plate. The design of any ICS system should consider the natural convection process in enclosures in general due to its effect on thermal performance of the ICS systems. Examples of such studies can be found in references [6-10].

The main objective of the present study is to investigate numerically the unsteady performance of solar energy gain and heat retention of two different integrated-collector-storage systems. The two ICS systems are shown in **Figure 1**, which are the conventional rectangular-shaped storage tank (**Figure 1(a)**) and the modified tank shaped as rectangular cuboid with one semi-circular top (**Figure 1(b)**).



**Figure 1. The physical model (a) Conventional rectangular-shaped storage tank; (b) Modified rectangular cuboid with one semi-circular top.**

In order to compare the performance of the two ICS systems, the absorber plate area  $L2$  and the total volume of both are considered the same. The values of the geometry parameters of the two ICS systems are given in **Table 1**.

## 2. Mathematical Model

Schematic diagrams of integrated-collector-storage systems are shown in **Figure 1**. The absorber surface  $L2$  for both ICS systems is exposed to the solar heat flux. The mathematical formulation of the present problem is based on the following assumptions:

- 1) The flow is unsteady, two-dimensional, laminar and incompressible;
- 2) The water properties are constant except for the density change with temperature, which gives rise to the buoyancy force; and
- 3) The viscous heating is neglected in the energy conservation.

Based on the above assumptions, the governing equations for the unsteady heat and fluid flow are as follows:

Mass conservation equation:

$$\frac{\partial u}{\partial x} + \frac{\partial v}{\partial y} = 0 \quad (1)$$

Momentum conservation equations:

$$\frac{\partial u}{\partial t} + u \frac{\partial u}{\partial x} + v \frac{\partial u}{\partial y} = -\frac{1}{\rho} \frac{\partial p}{\partial x} + \nu \left( \frac{\partial^2 u}{\partial x^2} + \frac{\partial^2 u}{\partial y^2} \right) - g\beta(T - T_o)\cos\theta \quad (2)$$

$$\frac{\partial v}{\partial t} + u \frac{\partial v}{\partial x} + v \frac{\partial v}{\partial y} = -\frac{1}{\rho} \frac{\partial p}{\partial y} + \nu \left( \frac{\partial^2 v}{\partial x^2} + \frac{\partial^2 v}{\partial y^2} \right) - g\beta(T - T_o)\sin\theta \quad (3)$$

Energy conservation equation:

$$\frac{\partial T}{\partial t} + u \frac{\partial T}{\partial x} + v \frac{\partial T}{\partial y} = \alpha \left( \frac{\partial^2 T}{\partial x^2} + \frac{\partial^2 T}{\partial y^2} \right) \quad (4)$$

where  $u$  and  $v$  are velocity components in  $x$  and  $y$  directions respectively,  $T$  is temperature,  $p$  is pressure,  $t$  is time,  $g$  is the acceleration due to gravity,  $\rho$ ,  $\nu$  and  $\alpha$  are density, kinematic viscosity and thermal diffusivity of the fluid respectively. The subscript  $o$  for reference

**Table 1. Geometry parameters of ICS systems.**

geometry parameters	Conventional ICS	Modified ICS
$d$ (cm)	14.415	5
$r$ (cm)	-	20.26
$L1$ (cm)	-	130.52
$L2$ (cm)	90	90
$\theta$	$30^\circ$	$30^\circ$

point and the Boussinesq approximation for the density-temperature relationship is defined as:

$$\rho \cong \rho_o [1 - \beta(T - T_o)] \quad (5)$$

Where  $\beta$  is the volumetric expansion coefficient, which appears in the body force term in Equations (2) and (3). All the surfaces of the two ICS systems are thermal insulated (zero heat flux boundary condition) except the absorber surface (L2) shown in **Figure 1**. The absorber surface (L2) is subjected to different conditions during heating and cooling periods as discussed in the next section.

## 2.1. Initial and Boundary Conditions

The initial and boundary conditions for the two ICS systems are:

At time = 0, the temperature of the stagnant water is 298 K everywhere.

For time > 0, three different boundary conditions on the absorber surface (L2) are used in the present study. They are:

**Case 1:** Constant heat flux of value 950 W/m for 2 hours of heating period followed by cooling period for 2 hours, where, a constant surface temperature is assumed on the absorber surface. The absorber surface temperature during the cooling period is assumed to be in the range 278 K to 298 K to reflect different weather conditions.

**Case 2:** Daily variation Sol-air temperature ( $T_{sol-air}$ ) is used as a boundary condition on the surface of the absorber. The  $T_{sol-air}$  is taken into account the outdoor ambient temperature and the solar heat flux. It is defined as:

$$T_{sol-air} = T_o + \frac{\alpha I - \Delta Q}{h_o} \quad (6)$$

Where  $T_o$  = outdoor surroundings' temperature [ $^{\circ}\text{C}$ ],  $\alpha$  = solar radiation absorptivity of a surface,  $I$  = global solar irradiance [ $\text{W/m}^2$ ],  $\Delta Q$  = extra infrared radiation due to difference between the external air temperature and the apparent sky temperature and  $h_o$  = heat transfer coefficient for radiation and convection [ $\text{W/m}^2\text{K}$ ].

**Case 3:** Periodic variation of sol-air temperature for duration of 4 continues days.

## 3. Numerical Solution Procedure

The solution domain for both ICS, shown in **Figure 1**, were created and meshed by divided it into non-uniform spacing quadrilateral cells. The mesh size refining or grid independence test study was carried out. The accuracy of the results is always a compromise between the number of cells and the computational cost. Therefore, after many simulation tests using different number of cells, it is found that 28,221 cells for the conventional ICS and

34,963 cells for the modified ICS are sufficient for the grid-ineffective mesh. The cells were clusters near the walls where steep variations in velocity and temperature are expected. FLUENT6.3 [11] is used as a tool for numerical solution of the governing Equations (1) to (4) based on finite-volume method. The segregated solver is used in the present study which solves conservation governing equations independently, and is applicable for the present incompressible flow problem. First Order Upwind discretization scheme [12,13] is selected for convection-diffusion formulation for momentum and energy equations. The central differencing scheme is used for the diffusion terms. The discretized equations were solved based on pressure correction method and uses PISO (pressure-implicit with splitting of operators) algorithm [14]. Relaxation factors are used to avoid divergence in the iteration. The typical relaxation factors were used as 0.7 for momentum equations, 0.3 for the pressure and 1.0 for the energy equation. For time integral the first order implicit scheme is used, which is unconditional stable. The time step is selected to be 600 seconds for both the heating and the cooling periods. The effect of the time step value on the accuracy of the results is tested. It is found that smaller time steps produce almost identical results. Therefore the time step and the mesh size defined above are fixed throughout the present study. The convergence criterion is based on the residual in the governing equations. The maximum residual in the energy equation was  $10^{-7}$  and the residual of other variables were lower than  $10^{-5}$  in the converged solution. In all the computational cases the global heat and mass balance are satisfied in the converged solution within  $\pm 10\text{-}3\%$ . Water is used as working fluid with constant physical properties. The values of the properties are: density  $\rho = 997 \text{ kg/m}^3$ , specific heat  $c_p = 4182 \text{ J/kgK}$ , thermal conductivity  $k = 0.6 \text{ W/mK}$  and viscosity  $\mu = 0.00089 \text{ kg/ms}$ .

## 4. Results and Discussion

The governing equations are solved under same initial conditions and different boundary conditions for the two ICS systems shown in **Figure 1**. The results under different boundary conditions are presented and discussed separately as follows.

### 4.1. Case 1: Constant Heat Flux and Constant Night Time Temperature

The simulations are carried out with constant heat flux of  $950 \text{ W/m}^2$  imposed on absorber surface for 2 hours. The performance of the two ICS systems are measured by the maximum temperature reached in the system. The temporal variations of the maximum temperature of the water

inside the ICS systems during the heating period are shown in **Figure 2**. The results of Sridhar and Reddy [5] are presented also in **Figure 2** for comparison. It can be observed from **Figure 2** that the discrepancy between the present results and those of Sridhar and Reddy [5] for the same modified ICS is negligible.

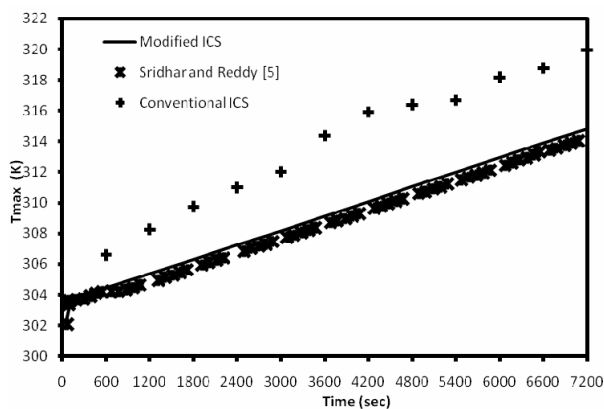
The results for the heating phase presented in **Figure 2** indicate better performance of the conventional ICS system against the modified ICS system. This is because the heated water in the conventional ICS system is confined in the rectangular shape and the maximum temperature occurs near the absorber surface. While in the modified ICS system the heated water is moving upwards to the semi-circular top region due to buoyancy forces and keeps the region near the absorber surface with lower temperature than that in the conventional ICS.

The contour plot of streamlines after one hour of heating of both the conventional and the modified ICS systems are presented in **Figure 3**. The streamline is a constant stream function line or it is the tangent line to the velocity vector of the flowing fluid. The stream function is defined as usual as:

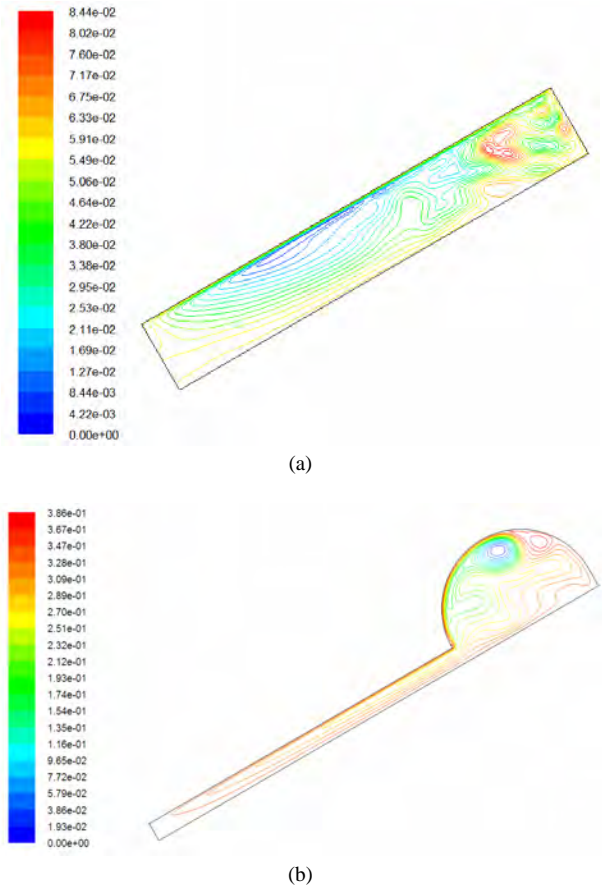
$$\rho u = \frac{\partial \psi}{\partial y}; \quad \rho v = -\frac{\partial \psi}{\partial x} \quad (7)$$

Where  $\psi$  is the stream function in kg/s. It can be seen in **Figure 3(a)** that the water is circulating and mixing in the whole system in the convectional ICS system. **Figure 3(b)** shows that the circulation of the water is mostly in the semi-circular top side of the modified ICS system. Comparing the range of the stream function of the streamlines presented in **Figure 3** indicate that the circulation in the modified ICS system is stronger than that of the conventional ICS system. The maximum value of the stream function in the conventional ICS is about  $8.44 \times 10^{-2}$  kg/s while that of the modified ICS is about  $3.86 \times 10^{-1}$  kg/s.

It is worth mentioning that the results presented in **Figure 3(b)** for the flow pattern of the present study and



**Figure 2.** Temporal variation of maximum temperature of water inside the ICS systems during heating period with constant heat flux of  $950 \text{ W/m}^2$ .



**Figure 3.** Streamlines in the systems after 1 hour of heating period with constant heat flux of  $950 \text{ W/m}^2$ . (a) convectional ICS; (b) modified ICS.

those of Sridhar and Reddy [5], (not shown here for briefly) are almost the same. This reflects the accuracy of the results in the present solution method.

The temporal variation of maximum temperature of water inside the ICS systems during cooling period with constant absorber temperature is shown in **Figure 4**. The absorber temperature during cooling period is assumed to be in a range of 278 K to 298 K, which simulates the night temperature at various conditions. Although the maximum temperature in the conventional ICS system is higher than that of the modified ICS system at the beginning of the cooling period, the modified system maintain higher temperatures compared to the conventional system. The results presented in **Figure 4** show the superior performance of the modified ICS system against the conventional ICS system for all values of absorber temperatures. This is because the modified ICS system saving most of the thermal energy in the semi-circular top region, which is thermally insulated. The hot water in this region will be approximately stationary during the cooling period since its density is lower than that in the rectangular lower region. While in the conventional system, the water will be

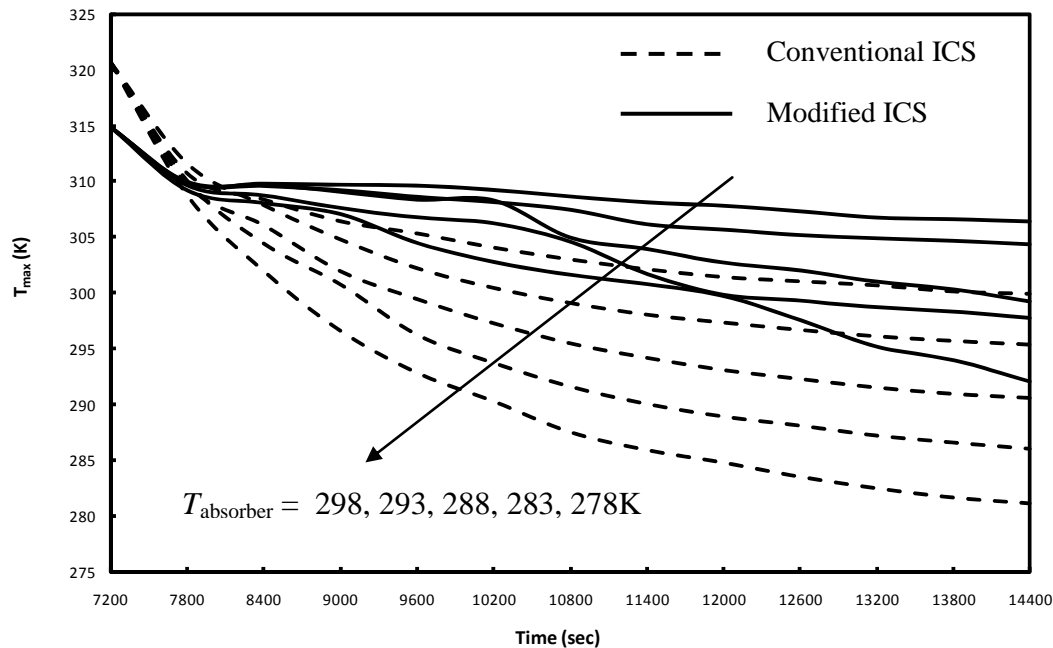


Figure 4. Temporal variation of maximum temperature of water inside the ICS systems during cooling period.

circulated in the whole system during the cooling period and continue losing heat to the outside environment.

The streamlines after two hours of cooling with constant absorber temperature of 288 K of both the conventional and the modified ICS systems are presented in **Figure 5**. **Figure 5(a)** shows that there are multi-cells circulations of water in the conventional system near the surface of the absorber. The circulation of water near the absorber surface indicating high heat lost during cooling period and therefore low maximum temperature in the system.

In the cooling period and after two hours of cooling with constant absorber temperature of 288 K of the modified ICS system the circulation of the water is again in the semi-circular top side and it is irregular. Note that the systems are thermally insulated except the absorber surface. Therefore the modified ICS keeping the water at the insulated semi-circular top region at high temperature and low density. **Figure 5(b)** shows that the water near the surface of the absorber is approximately stationary. It can be expected that the streamlines in the systems after the cooling period with other temperatures will be similar to those presented in **Figure 5**.

Comparing the results presented in **Figure 2** and **Figure 4** of the performance of the two systems after the successive two periods indicating better overall thermal performance of the modified ICS system. It is observed also that the difference in the maximum temperature in the systems after successive two periods is increased with the absorber temperature reduction. The maximum water

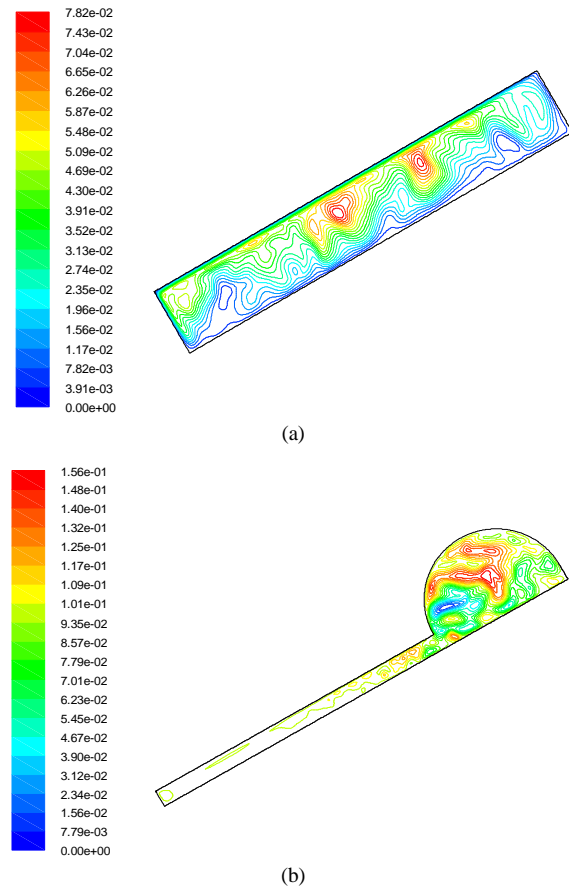
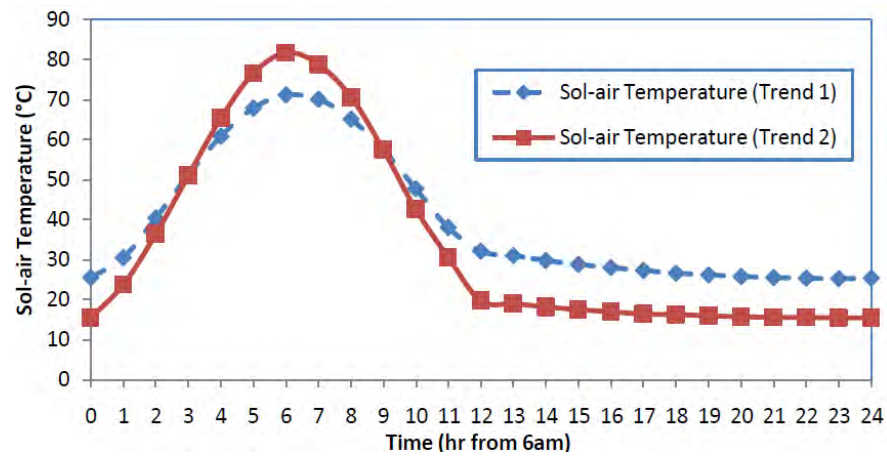
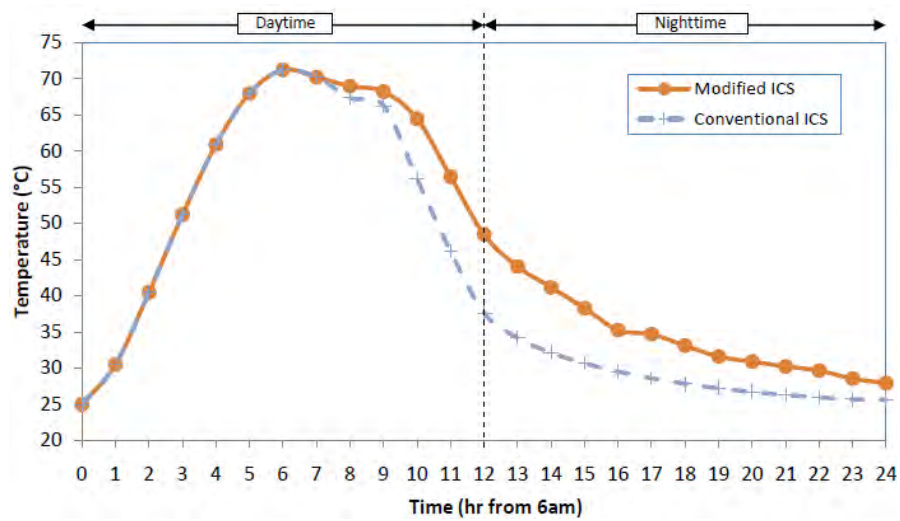


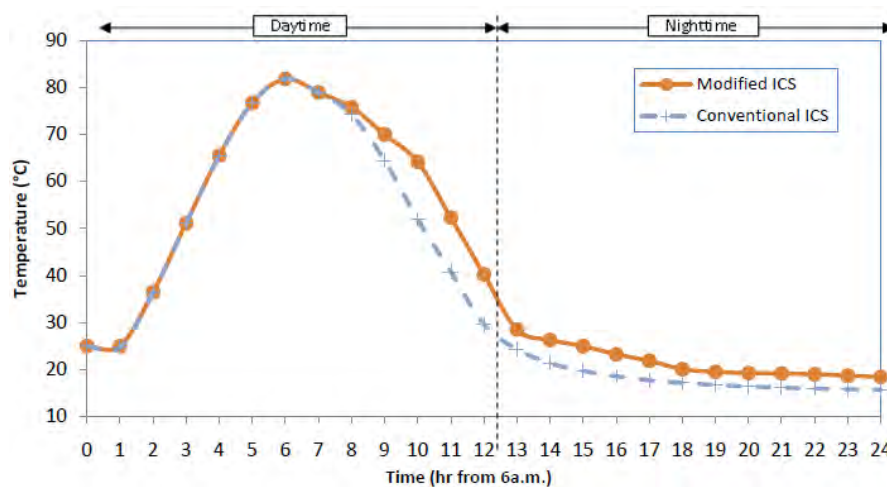
Figure 5. Streamlines in the systems after 2 hour of cooling period with constant absorber temperature of 288 K. (a) convectional ICS; (b) modified ICS.



(a)



(b)



(c)

Figure 6. (a) Daily Sol-air temperature variation for different trends; (b) The response of  $T_{\max}$  of the two ICS systems based on Trend 1 in 6(a); (c) The response of  $T_{\max}$  of the two ICS systems based on Trend 2 in 6(a).



temperature in the modified ICS system after the two periods is about 7 K to 11 K higher than that of the conventional ICS system.

#### 4.2. Case 2: Daily Variation of Sol-air Temperature

In this case, the 24 hours variation of the sol-air temperature defined in Equation (6) is used as boundary condition on absorber surface. It is well-known that the daily variation of the sol-air temperature depends on the season and many metrological parameters. Therefore, two different models are used for the daily variation of the sol-air temperature to evaluate the performance of the ICS systems.

The daily variations of the sol-air temperature for the two models are shown in **Figure 6(a)**. The condition for trend 2 is assumed to be harsher (higher amplitude) than trend 1. For trend 1, the minimum  $T_{sol-air}$  shows the value of 25.3°C, while that of trend 2 is 15.5°C. As for the maximum  $T_{sol-air}$ , trend 1 has the value of 71.2°C, while trend 2 shows the value of 81.8°C. It has the lower minimum  $T_{sol-air}$  and higher maximum  $T_{sol-air}$  as compared to trend 1. Thus, during daytime, this boundary condition may represent the hot weather. While during nighttime, it represents the cool weather.

The results are presented in **Figure 6(b)** show the effect of using trend 1 as boundary condition on the maximum temperature variation inside the two ICS systems. For the first 6 hours, the maximum temperatures of both systems are the same as the sol-air temperatures. This is due to the maximum temperature occurs near the absorber plate, which is the sol-air temperature during heating.

After 6 hours, the sol-air temperature is decreasing. This is when the cooling phase occurs. During the cooling phase, the maximum temperature will have a continuous reduction due to the cooling effect (heat loss). It can be observed from **Figure 6(b)** that the modified ICS has better heat retain since the maximum temperature has less reduction than that of the conventional ICS. The results show that there is a difference in the maximum temperature of 2°C-10°C between modified ICS and conventional ICS.

For the conventional ICS, the maximum temperature in the end of the simulations (say from 18-24 hours), is close to the sol-air temperature. This suggests that the inside of the conventional ICS is only left with cooled water, which is the same temperature as the outdoor temperature.

These results are justified by using a different trend of sol-air temperature as boundary condition. Different from trend 1 (which is the sol-air temperature previously used as boundary condition), the new trend has a varia-

tion of 15% of trend 1. The two trends are shown in **Figure 6(a)** for comparison. By using trend 2 sol-air temperature as boundary condition, the simulation procedure is repeated and the results of maximum temperature are obtained.

By using this condition (trend 2), the maximum temperature comparison in **Figure 6(c)** show that there would be 2°C-14°C difference in maximum temperature higher in modified ICS than that of the conventional ICS. Modified ICS shows a good heat retaining ability during nighttime. The results presented in **Figures 6(b)** and **(c)** show that the modified ICS system has much better performance than the conventional system when the sol-air temperature variation has higher amplitude.

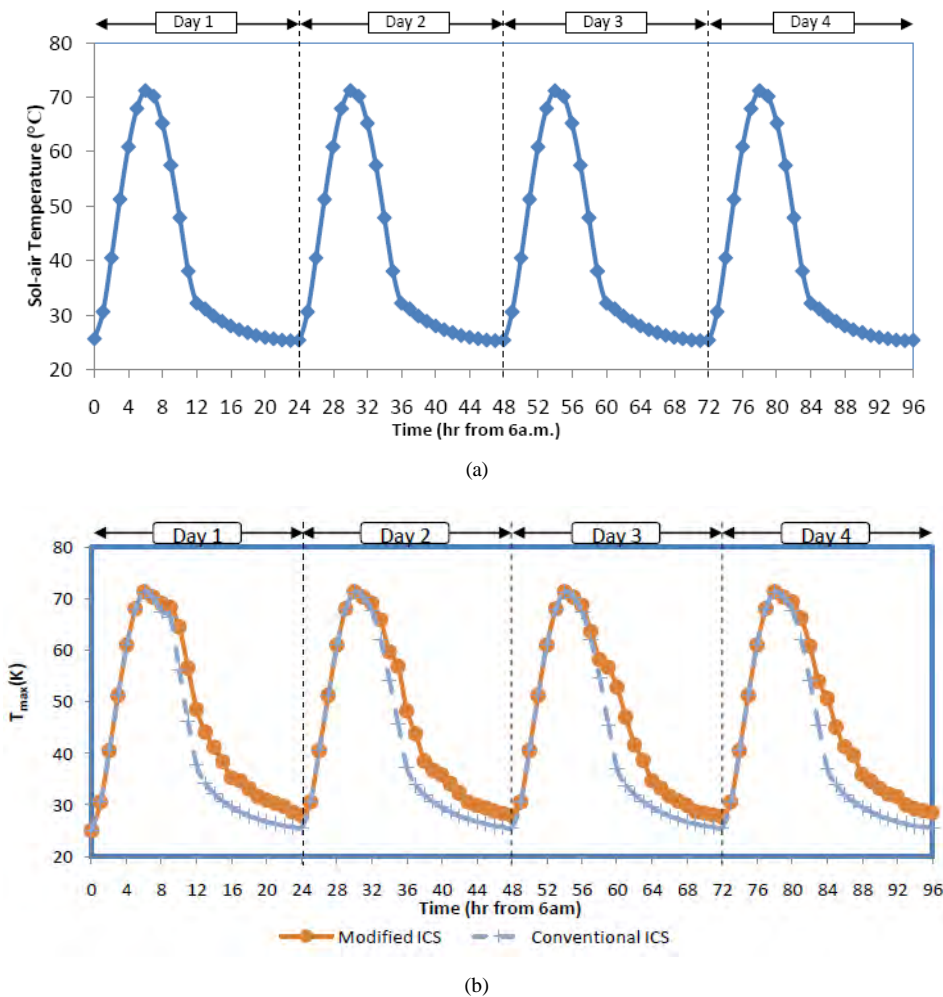
#### 4.3. Case 3: Periodic Variation of Sol-air Temperature

Although the results for 1 day show the great performance of the modified ICS system, the performance may be affected on the next day. Moreover it is important to eliminate the effect of the assumed initial condition. Therefore it is important to carry out the simulation of the performance of the ICS systems for more periods of sol-air temperature variation. To verify this, the periodic variation of the sol-air temperature boundary condition (trend 1 in **Figure 6(a)**) is assumed to be periodic and repeated for 4 successive days. This periodic variation of the sol-air temperature for 4 successive days is shown in **Figure 7(a)** and used as a boundary condition for the two ICS systems. The maximum temperature inside the ICS systems is used also to represent the performance of the systems. The results of the maximum temperature inside the ICS systems for the two systems are shown in **Figure 7(b)** during the 4 successive days. The results presented in **Figure 7(b)** show that the variation of the maximum temperature in the systems for the following days are almost the same as the first day. Thus, for the two systems, periodic variation does not have much effect on the maximum temperature. In general, the modified ICS system still shows a great result on the heat retaining.

### 5. Conclusions

The present study presents a numerical investigation of the unsteady thermal performance of two different integrated-collector-storage systems. The systems are the conventional rectangular-shaped storage tank and the modified tank shaped as rectangular cuboid with one semi-circular top. The two systems have the same absorber surface area and volume for water. The thermal performance of the two systems is tested by using 3 different cases based on dif-





**Figure 7. (a) Periodic variation of the Sol-air Temperature on the absorber surface; (b) the response of  $T_{\max}$  of the two ICS systems based on the boundary conditions in 7(a).**

ferent boundary conditions on the absorber plate. The results show that the shape of the integrated-collector-storage systems has a great importance on the natural convection heat and fluid flow inside the system. The numerical results recording during the daytime heating period and during nighttime cooling period shows that the overall performance (after the successive heating and cooling periods) of the modified system is better. The modified system is able to store the water with higher temperature in the semi-circular top region than that of the conventional system. This hits our main objectives on reducing nighttime thermal losses. Future work should be made on the effect of the unsteady hot water consumption, which is exit from the upper part of the system and the cold water inlet from the lower part of the system on the overall thermal performance.

## 6. References

- [1] Solarthermal.com (<http://solarthermal.com>).
- [2] S. A. Kalogirou, "Solar Thermal Collectors and Applications," *Progress in Energy and Combustion Science*, Vol. 30, No. 3, 2004, pp. 231-295.
- [3] C. Garnier, J. Currie and T. Muneer, "Integrated Collector Storage Solar Water Heater: Temperature Stratification," *Applied Energy*, Vol. 86, No. 9, 2009, pp. 1465-1469.
- [4] S. A. Kalogirou, "Design, Construction, Performance Evaluation and Economic Analysis of an Integrated Collector Storage System," *Renew Energy*, Vol. 12, No. 2, 1997, pp. 179-192.
- [5] A. Sridhar and K. S. Reddy, "Transient Analysis of Modified Cuboid Solar Integrated Collector-Storage System," *Applied Thermal Engineering*, Vol. 27, No. 2-3, 2007, pp. 330-346.
- [6] S. Ostrach, "Natural Convection in Enclosures," *ASME Journal of Heat Transfer*, Vol. 110, No. 4b, 1988, pp. 1175-1190.

- [7] D. Poulikakos, "Natural Convection in a Confined Fluid-Filled Space Driven by a Single Vertical Wall with Warm and Cold Regions," *ASME Journal of Heat Transfer*, Vol. 107, No. 4, 1985, pp. 867-876.
- [8] N. H. Saeid, "Computational Aspects for Natural Convection in a Cavity Using Vorticity-Stream Function Method," In: G. R. Liu *et al.*, Ed., *Computational Methods*, Springer, 2006, pp. 255-261.
- [9] N. H. Saeid and Y. Yaacob, "Natural Convection in a Square Cavity with Spatial Sidewall Temperature Variation," *Numerical Heat Transfer, Part A*, Vol. 49, No. 7, 2006, pp. 683-697.
- [10] N. H. Saeid, "Conjugate Natural Convection in a Porous Enclosure: Effect of Conduction in One of the Vertical Walls," *International Journal of Thermal Sciences*, Vol. 46, No. 6, 2007, pp. 531-539.
- [11] Fluent 6.3 User's Guide, Fluent Inc. <http://www.fluentusers.com>
- [12] H. K. Versteeg and W. Malalasekera, "An introduction to Computational Fluid Dynamics," Longman, New York, 1995.
- [13] S. V. Patankar, "Numerical Heat Transfer and Fluid Flow," McGraw-Hill, New York, 1980.
- [14] R. I. Issa, "Solution of the Implicitly Discretised Fluid Flow Equations by Operator Splitting," *Journal of Computational Physics*, Vol. 62, No. 1, 1986, pp. 40-65.

# Call for Papers

# ENGINEERING

A Journal Published by Scientific Research Publishing, USA

[www.scirp.org/journal/eng](http://www.scirp.org/journal/eng)

## Editor-in-Chief

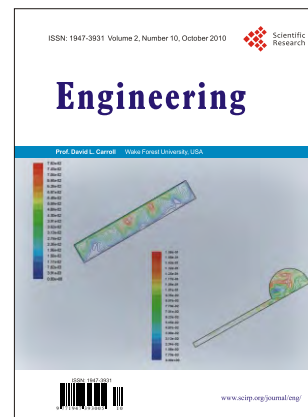
**Prof. David L. Carroll**

Wake Forest University, USA

## Editorial Board

Dr. Murad Y Abu-Farsakh  
Dr. Mohammad Al-Hwaiti  
Prof. Moh'd A. M. Al-Nimr  
Prof. Shahnor Basri  
Dr. Hengky Chandralahim  
Dr. Adinel Gavrus  
Dr. Krzysztof Górski  
Dr. Zhongwei Guan  
Dr. Kun Hadinoto  
Dr. Sung-Cheon Han  
Dr. Yunho Hwang  
Prof. Shouetsu Itou  
Dr. Sushil Kansal  
Prof. Jae Moung Kim  
Prof. Chui-Chi Lee  
Dr. Yiyang Li  
Dr. Durães Luisa  
Dr. Vandna Luthra  
Prof. Yong-Gang Lv  
Prof. Magdi Mahmoud  
Prof. Reinaldo Rodriguez Ramos  
Prof. Yuri Ribakov  
Dr. Arvind K. Srivastava  
Prof. Kune Y. Suh  
Prof. Hongbin Sun  
Dr. Costin D. Untaroiu  
Prof. Baolin Wang  
Dr. Rodrigo Sérgio Wiederkehr  
Dr. Yufei Wu  
Dr. Wei Yan  
Prof. Bo Yu  
Dr. Lei Zhang  
Dr. Ming Zhang

Louisiana State University, USA  
Al-Hussein Bin Talal University, Jordan  
Jordan University of Science and Technology, Jordan  
Putra University, Malaysia  
Swiss Federal Institute of Technology, Switzerland  
National Institut of Applied Sciences Rennes, France  
Technical University of Radom, Poland  
University of Liverpool, UK  
Nanyang Technological University, Singapore  
Daewon University College, Korea (South)  
University of Maryland, USA  
Kanagawa University, Japan  
Panjab University, India  
Inha University, Korea (South)  
She-Te University, Taiwan (China)  
The Chinese University of Hong Kong, China  
Universidade de Coimbra Pólo II, Portugal  
University of Delhi, India  
Chongqing University, China  
King Fahd University for Petroleum and Minerals, Iran  
University of Havana, Cuba  
Pariel University Center of Samaria, Israel  
NanoSonix Inc., USA  
Seoul National University, Korea (South)  
Tsinghua University, China  
University of Virginia, USA  
Harbin Institute of Technology, China  
University of Louisville, USA  
City University of Hong Kong, China  
Trend Micro, USA  
China University of Petroleum - Beijing, China  
University of Maryland, USA  
Smith International, Inc., Uruguay



ENGINEERING is an international journal dedicated to the latest advancement of engineering. The goal of this journal is to provide a platform for engineers and academicians all over the world to promote, share, and discuss various new issues and developments in different areas of engineering. All manuscripts must be prepared in English, and are subject to a rigorous and fair peer-review process. Accepted papers will immediately appear online followed by printed hard copy. The journal publishes original papers including but not limited to the following fields:

- Aerospace Engineering
- Agricultural Engineering
- Chemical Engineering
- Civil Engineering
- Electrical Engineering
- Environmental Engineering
- Industrial Engineering
- Materials Engineering
- Mechanical Engineering
- Mining Engineering
- Nanotechnology
- Nuclear Engineering
- Power Engineering
- Test Engineering
- Transportation Engineering

We are also interested in: 1) Short Reports—2-5 page papers where an author can either present an idea with theoretical background but has not yet completed the research needed for a complete paper or preliminary data; 2) Book Reviews—Comments and critiques.

## ★ Notes for Intending Authors

Submitted papers should not be previously published nor be currently under consideration for publication elsewhere. Paper submission will be handled electronically through the website. For more details, please access the website.

## ★ Website and E-Mail

<http://www.scirp.org/journal/eng>

[eng@scirp.org](mailto:eng@scirp.org)

## TABLE OF CONTENTS

**Volume 2 Number 10**

**October 2010**

<b>Influence of Cutting and Geometrical Parameters on the Cutting Force in Milling</b> H. Yangui, B. Zghal, A. Kessentini, G. Chevallier, A. Rivière, M. Haddar, C. Karra.....	751
<b>Modelling and Optimisation of a Spring-Supported Diaphragm Capacitive MEMS Microphone</b> N. Mohamad, P. Iovenitti, T. Vinay.....	762
<b>Analysis of the Manufactured Tolerances with the Three-Dimensional Method of Angular Chains of Dimensions Applied to a Cylinder Head of Car Engine</b> A. Mezghani, A. Bellacicco, J. Louati, A. Rivière, M. Haddar.....	771
<b>Geometric Inversion of Two-Dimensional Stokes Flows Application to the Flow between Parallel Planes</b> M. Hellou.....	780
<b>Surface Roughness Evaluation in Dry-Cutting of Magnesium Alloy by Air Pressure Coolant</b> J.-D. Kim, K.-B. Lee.....	788
<b>Optimization of Surface Milling of Hardened AISI4340 Steel with Minimal Fluid Application Using a High Velocity Narrow Pulsing Jet of Cutting Fluid</b> K. L. D. Wins, A. S. Varadarajan, B. Ramamoorthy.....	793
<b>Using Image Analysis for Structural and Mechanical Characterization of Nanoclay Reinforced Polypropylene Composites</b> T. P. Mohan, K. Kanny.....	802
<b>Nonlinear Control of an Induction Motor Using a Reduced-Order Extended Sliding Mode Observer for Rotor Flux and Speed Sensorless Estimation</b> O. Asseu, M. A. Kouacou, T. R. Ori, Z. Yéo, M. Koffi, X. Lin-Shi.....	813
<b>A Fast Predicating of Nutrient Removal Efficiency in Five Steps Sequencing Batch Reactor System Using Fuzzy Logic Control Model</b> S. Abualhail, R. Naseer, A. Ashor, X.-W. Lu.....	820
<b>Effect of Periodic Variation of Sol-Air Temperature on the Performance of Integrated Solar Collector Storage System</b> N. H. Saeid, T. J. Wong.....	832